



HAL
open science

Etude par microscopie à force atomique en mode non contact et microscopie à sonde de Kelvin, de matériaux modèles pour le photovoltaïque organique

Evan Spadafora

► **To cite this version:**

Evan Spadafora. Etude par microscopie à force atomique en mode non contact et microscopie à sonde de Kelvin, de matériaux modèles pour le photovoltaïque organique. Autre [cond-mat.other]. Université de Grenoble, 2011. Français. NNT : 2011GRENY050 . tel-00647312

HAL Id: tel-00647312

<https://theses.hal.science/tel-00647312v1>

Submitted on 1 Dec 2011

HAL is a multi-disciplinary open access archive for the deposit and dissemination of scientific research documents, whether they are published or not. The documents may come from teaching and research institutions in France or abroad, or from public or private research centers.

L'archive ouverte pluridisciplinaire **HAL**, est destinée au dépôt et à la diffusion de documents scientifiques de niveau recherche, publiés ou non, émanant des établissements d'enseignement et de recherche français ou étrangers, des laboratoires publics ou privés.

THÈSE

Pour obtenir le grade de

DOCTEUR DE L'UNIVERSITÉ DE GRENOBLE

Spécialité : **Nanophysique**

Arrêté ministériel : 7 août 2006

Présentée par

Evan J. SPADAFORA

Thèse dirigée par **Benjamin GRÉVIN**

préparée au sein du **Laboratoire d'Électronique Moléculaire
Organique et Hybride du CEA Grenoble**
dans l'**École Doctorale de Physique**

Étude par Microscopie à Force Atomique en mode non contact et Microscopie à sonde de Kelvin, de matériaux modèles pour le photovoltaïque organique

Thèse soutenue publiquement le **04 Novembre 2011**
devant le jury composé de :

M. Thierry MELIN

CNRS-IEMN (Lille, France), Rapporteur

M. Jacques COUSTY

CEA-IRAMIS/SPCSI (Saclay, France), Rapporteur

M. Frank PALMINO

Université de Franche-Comté (Besançon, France), Membre

M. Philippe LECLERE

FNRS Université de Mons (Mons, Belgique), Membre

M. Hervé COURTOIS

Université Joseph Fourier (Grenoble, France), Président

M. Benjamin GRÉVIN

CNRS-INAC/SPrAM (Grenoble, France), Directeur de Thèse



Thesis

submitted to the

University of Joseph Fourier in Grenoble

to obtain the degree of

Doctor of Philosophy

Subject: **Nanophysics**

Evan J. Spadafora

Ph. D. Advisor: **Dr. Benjamin Grévin**

**Investigations of model
organic materials and
photovoltaic devices using
noncontact atomic force
microscopy and Kelvin probe
force microscopy**

Thesis defended: **November 4, 2011**

Ph.D. thesis committee members:

Dr. Thierry Melin

CNRS-IEMN (Lille, France), Referee

Dr. Jacques Cousty

CEA-IRAMIS/SPCSI (Saclay, France), Referee

Professor Frank Palmino

University of Franche-Comté (Besançon, France), Member

Dr. Philippe Leclère

FNRS University of Mons (Mons, Belgium), Member

Professor Herve Courtois

University of Joseph Fourier (Grenoble, France), President

Dr. Benjamin Grévin

CNRS-INAC/SPrAM (Grenoble, France), Thesis Director



I believe in intuition and inspiration. Imagination is more important than knowledge. For knowledge is limited, whereas imagination embraces the entire world, stimulating progress, giving birth to evolution. It is, strictly speaking, a real factor in scientific research.

Albert Einstein
The Saturday Evening Post
October 26, 1929

Abstract

In this thesis, high resolution noncontact atomic force microscopy (NC-AFM) and Kelvin probe force microscopy (KPFM), under ultrahigh vacuum, has been applied to investigate the structure and electronic surface properties of model organic materials and photovoltaic devices at the nanoscale.

In the first experimental chapter, surface photovoltage measurements of nanoscale phase segregated P3HT:PCBM blends were resolved at the true nanometer scale using amplitude modulation KPFM (AM-KPFM).

Next, model self-assembled π -conjugated oligomers have been investigated, in order to obtain a deeper insight into the nature of the tip-surface interactions involved in KPFM. A crossover between the long-range (LR) and short-range (SR) electrostatic force regimes is observed by combining high resolution KPFM and damping spectroscopy. The influence of the LR forces is minimized by working at the onset of the damping.

Finally, using the same procedure, a multitechnique interdisciplinary investigation, using KPFM and ultraviolet photoelectron spectroscopy, was performed in order to characterize the work function of flexible transparent electrodes, based on functionalized carbon nanotubes using metallic nanoparticles.

Résumé

La nanostructure et les propriétés électroniques de matériaux modèles pour le photovoltaïque organique, ont été étudiées en utilisant la Microscopie à Force Atomique en mode non contact sous ultra-vide (NC-AFM) et la Microscopie à sonde de Kelvin (KPFM).

En utilisant le mode modulation d'amplitude (AM-KPFM), le potentiel de surface photogénéré dans des mélanges donneur-accepteur présentant une ségrégation de phase optimale a pu être visualisé à l'échelle du nanomètre.

Afin de préciser la nature des forces mises en jeu dans le processus d'imagerie KPFM, des oligomères π -conjugués auto-assemblés ont ensuite été étudiés. Une transition entre régimes à longue et à courte portée a ainsi été mise en évidence en combinant l'imagerie en haute résolution aux mesures de spectroscopie en distance. Ces mesures ont également démontré que l'influence des forces électrostatiques à courte portée peut être minimisée en travaillant au seuil du contraste de dissipation.

Enfin cette procédure a été utilisée, en combinaison avec les mesures de spectroscopie de photoélectrons UV, pour analyser la fonction de sortie locale d'électrodes transparentes à base de nanotubes de carbone fonctionnalisés.

Acknowledgements

First and foremost, I am greatly indebted to my PhD advisor, Dr. Benjamin Grévin. From the first week after arriving in France and being rushed out to the hospital, I felt like an enormous burden. However, he showed immense compassion, patience and understanding by helping me through my first few weeks as I struggled to adjust to the French environment. These characteristics were carried out throughout my 3 years as his research assistant. His scientific insight, enthusiasm about the research and experimental approach has allowed me to clearly shape and focus my ideas.

I am also very grateful to my fellow colleagues for their valuable feedback and suggestions, Dr. Renaud Demadrille, Dr. Patrice Rannou, Dr. Jean-Pierre Travers, Dr. James Hayton, Zaireen Yahya, Dr. Anne Forestier, Chiara Ottone, Elsa Couderc, and Yann Kervella, with whom I have worked closely and had brilliant discussions, especially those over lunch with topics ranging from science to politics and so on.

I would like to thank the collaborators that I have worked with that culminated in fruitful research topics; Dr. Jean-Pierre Simonato, Dr. Karell Saint-Aubin, Dr. Philippe Leclère, and Dr. Bernard Ratier.

I am also thankful to the staff at the CEA who have helped me at various times, including Isabelle Schuster and Céline Deleval.

I have been fortunate enough to meet some of the greatest friends during my time in France, without whom I would probably be lost. Particularly, I am very thankful to Rosalind Gay for her helpful efforts and tolerance throughout my writing process. I am also very appreciative of my friends from home, all of whom I miss dearly, their patience and support has been invaluable as I pursue my scientific and personal ambitions across the Atlantic.

I most certainly would not have lasted this long so far from home without the unwavering love and support of my Mom, Dad and sisters, Karen and Melissa. I love you and I will return home soon enough.

Finally, I thank the 1986 New York Mets, for their inspirational and miraculous win!



Contents

Abstract	vii
Acknowledgements	ix
List of Figures	xiii
List of Tables	xvii
Abbreviations	xix
1 Introduction	1
1.1 Thesis Outline	3
2 Organic Electronics & Optoelectronics	5
2.1 Conjugated Polymers	7
2.2 Organic Electronics	11
2.3 Organic Photovoltaics	13
2.3.1 Device Architectures	14
2.3.1.1 Biplanar Heterojunction	14
2.3.1.2 Bulk Heterojunction	15
2.3.1.3 Ordered Heterojunction	17
2.3.2 Operational Principle	18
2.4 Materials	22
3 Experimental Techniques	25
3.1 Atomic Force Microscopy (AFM)	26
3.1.1 Tip-Sample Forces	28
3.1.2 Vibrating Tip Dynamics	30
3.1.3 Frequency Modulation Atomic Force Microscopy (FM-AFM)	32
3.1.3.1 Beam Deflection	35
3.1.3.2 Self-Oscillation Loop	36
3.1.3.3 Damping Signal	37
3.2 Kelvin Probe Force Microscopy (KPFM)	38
3.2.1 Electrostatic Detection Methods	42
3.2.2 AM vs. FM KPFM	44
3.2.3 Cantilevers	46
3.3 Photoelectron Spectroscopy (PES)	48
3.3.1 Ultraviolet Photoelectron Spectroscopy (UPS)	53
3.3.2 X-Ray Photoelectron Spectroscopy (XPS)	54
3.4 Equipment Summary	55
3.4.1 Ultra-High Vacuum (UHV)	56

4	KPFM on Bulk Heterojunctions	59
4.1	Surface Photovoltage (SPV)	60
4.2	KPFM on organic solar cells	61
4.3	KPFM on an optimized P3HT:PCBM blend	65
4.3.1	P3HT:PCBM BHJ sample preparation and characterization	65
4.3.2	NC-AFM Topography Imaging	67
4.3.3	Kelvin Probe (CPD) Imaging	70
4.3.3.1	In Dark Contrast	72
4.3.3.2	Effect of Illumination	73
4.3.4	Surface Photovoltage	77
4.4	Conclusions	80
5	LCPD of Molecular Self-Assemblies	81
5.1	Local Contact Potential Difference (LCPD)	82
5.2	Molecular CPD of π -Conjugated Self-Assemblies	88
5.2.1	Materials & Sample Fabrication	89
5.2.2	QTF8 Topography on HOPG	90
5.2.3	QTF8 Modeling	91
5.2.4	FG1 Topography on HOPG	93
5.2.5	FG1 Modeling	95
5.2.6	Frequency Modulation KPFM	97
5.2.7	LCPD of QTF8 and FG1 Monolayers on HOPG	98
5.2.7.1	CPD Dependence vs. the Operating Set-Points	98
5.2.7.2	Molecular CPD Contrast	101
5.2.7.3	Distance Dependant Spectroscopy	105
5.3	Conclusions	107
6	Novel Transparent Electrodes	109
6.1	Novel Transparent Electrodes	110
6.2	Work Function Measurements	111
6.3	Functionalized CNTs	112
6.3.1	Materials & Sample Fabrication	113
6.3.2	KPFM of Functionalized CNTs	117
6.3.3	PES of Functionalized CNTs	120
6.3.3.1	Ultraviolet photoelectron spectroscopy (UPS)	120
6.3.3.2	X-Ray photoelectron spectroscopy (XPS)	123
6.3.4	KPFM & UPS Work Function Values	126
6.4	KPFM Conclusions	128
7	Conclusion	129
7.1	Future Perspectives	131
A	KPFM on FG1:PC₇₀BM BHJ	133
A.1	Materials & Sample Fabrication	133
A.2	Topography	133
A.3	Contact Potential Difference	135
	Bibliography	139

List of Figures

1.1	Thesis Outline	3
2.1	First Organic Device	6
2.2	π & σ bonds	7
2.3	Conductivity	8
2.4	Energy Band Diagram	9
2.5	Edge-On & Face-On Orientation	10
2.6	OFET Schematic	11
2.7	Photovoltaic Efficiencies	13
2.8	Polymeric solar cell heterojunctions	14
2.9	Organic BHJ Solar Cell	15
2.10	Organic Photovoltaic Energy Levels	16
2.11	P3HT Gradient	17
2.12	Organic Solar Cell Operation	19
2.13	Current-voltage (IV) curves of an organic solar cell	21
2.14	Organic Materials	22
3.1	Dynamic Mode AFM	27
3.2	Tip Forces	29
3.3	AFM Schematic	34
3.4	Beam Deflection AFM Schematic	36
3.5	FM-AFM Oscillation	37
3.6	KPFM Principle	40
3.7	Flexural modes of the cantilever	42
3.8	KPFM schematic	43
3.9	FM-KPFM Restrictions	44
3.10	SEM image of a Super Sharp Si tip	46
3.11	SSS Resonance Frequency Curve	47
3.12	SEM image of a PtIr ₅ coated Si tip	47
3.13	PtIr ₅ Resonance Curves	48
3.14	Omicron UPS and XPS Setup	49
3.15	UPS and XPS Process	50
3.16	Angle-Resolved XPS	52
3.17	UHV Setup	55
3.18	Omicron VT SPM, sample plates, and cantilever holder	56
3.19	Argon Ion Sputtering Gun	56
4.1	Surface Photovoltage (SPV)	61
4.2	KPFM of F8BT/PFB Blends	62

4.3	KPFM of MDMO-PPV:PCBM Blends	63
4.4	P3HT:PCBM	65
4.5	Absorption and IPCE of P3HT:PCBM	66
4.6	P3HT:PCBM TM-AFM Topography	67
4.7	P3HT:PCBM Topography	68
4.8	P3HT:PCBM	68
4.9	P3HT:PCBM Topography and Damping	69
4.10	FM-KPFM P3HT:PCBM in dark	70
4.11	P3HT:PCBM Topography, Damping, and Work Function in Dark	70
4.12	Histogram of CPD in Dark	72
4.13	Histogram of CPD under illumination	73
4.14	P3HT:PCBM Topography, Damping, and Work Function in Dark and under 532 nm Illumination	74
4.15	P3HT:PCBM Topography and Work Function	75
4.16	CPD in dark and under illumination	76
4.17	Calculated SPV of P3HT:PCBM	77
4.18	SPV of P3HT:PCBM	78
4.19	CPD Profile in dark and under illumination	79
5.1	LCPD on Si(111)7×7 surface	83
5.2	LCPD on KBr(001) using KPFM	84
5.3	LCPD of metallic adatom using KPFM	85
5.4	LCPD of CuPC on Au(111)	87
5.5	QTF8 and FG1 on HOPG Dipole Model	88
5.6	QTF8 Topography	90
5.7	QTF8 Molecular Modeling Conformations	92
5.8	QTF8 Modeling	93
5.9	FG1 molecular island on HOPG	94
5.10	FG1 Thiophene Modeling	95
5.11	FG1 Stacking Modeling	96
5.12	FG1 Stable Stacking Modeling	96
5.13	FM-KPFM on FG1	97
5.14	Δf change of AM-KPFM on FG1	98
5.15	FG1 3D Z, Damping and CPD as a function of Δf	99
5.16	Δ CPD spectroscopy on FG1:HOPG	100
5.17	Δf change of LCPD on FG1	102
5.18	FG1 Topography, Damping, and CPD	103
5.19	QTF8 Topography, Damping and CPD	104
5.20	CPD of QTF8 and FG1 with Damping contrast	104
5.21	QTF8 Wire on HOPG	105
5.22	QTF8 distance spectroscopy on HOPG	106
6.1	KPFM of ITO surface under UV exposure	111
6.2	CNT Network fabrication	114
6.3	SEM images of the CNT networks	116
6.4	KPFM of the CNT networks before and after exposure	118
6.5	CPD Histograms of the CNT networks before and after exposure	119
6.6	Full UPS Spectra of the CNT networks	121

6.7	UPS Fermi edge and Secondary cut-off of the CNT networks	122
6.8	XPS of the nanoparticle functionalized CNT networks	124
6.9	XPS Magnified peaks of the nanoparticle functionalized CNT networks	125
6.10	Work functions of the CNT networks	127
7.1	Thesis Conclusion	130
7.2	D-A Co-Oligomer	131
7.3	Au Nanoparticle Network	132
A.1	FG1:PCBM Morphology	134
A.2	FG1:PCBM Morphology and Damping	134
A.3	Pure FG1 and FG1:PCBM Morphology Comparison	135
A.4	Absorption and IPCE of FG1:PC ₇₀ BM	135
A.5	FG1:PCBM Global SPV	136
A.6	FG1:PCBM Magnified SPV	137

List of Tables

3.1	FM vs. AM KPFM	45
3.2	List of cantilever characteristics	46
3.3	Analyser operating parameters and resolution	53
3.4	Vacuum levels	57
6.1	Work function values of metals	115
6.2	CPD values of the CNT networks	119
6.3	UPS Fermi edge, Secondary cut-off, and ϕ_S values of the CNT networks	123
6.4	Work function values of the CNT networks	126

Abbreviations

AGC	Automatic Gain Control
AFM	Atomic Force Microscope
AM	Amplitude Modulation
AR-PES	Angle Resolved PES
BHJ	Bulk Heterojunction
CAE	Constant Analyzer Energy
CHA	Concentric Hemispherical Analyzer
CNT	Carbon Nanotube
(L)CPD	(Local) Contact Potential Difference
CRR	Constant Retard Ratio
FFT	Fast Fourier Transform
FM	Frequency Modulation
FWHM	Full Width Half Maximum
HOMO	Highest Occupied Molecular Orbital
HOPG	Highly Oriented Pyrolytic Graphite
IMFP	Inelastic Mean Free Path
IPCE	Incident Photon Current Efficiency
ITO	Indium-Tin Oxide
KPFM	Kelvin Probe Force Microscope
LUMO	Lowest Unoccupied Molecular Orbital
MD	Molecular Dynamics
MM	Molecular Mechanics
NC-AFM	Noncontact AFM
OFTF	Organic Thin Film Transistor
OSC	Organic Solar Cell
PES	Photoelectron (or Photoemission) Spectroscopy

PLL	Phase-Locked Loop
PSD	Photo Sensitive Diode
SCR	Space Charge Region
SEM	Scanning Electron Microscope
SPM	Scanning Probe Microscope
SPV	Surface Photo Voltage
SRE	Short-Range Electrostatic
SSS	Super Sharp Silicon
STM	Scanning Tunneling Microscope
SWNT	Single-wall Nanotube
TCO	Transparent Conductive Oxide
TEM	Transmission Electron Microscope
TF-AFM	Tuning-Fork AFM
TSP	Titanium Sublimation Pump
UHV	Ultra High Vacuum
UPS	Ultraviolet Photoelectron Spectroscopy
vdW	van der Waals
XPS	X-ray Photoelectron Spectroscopy

*Dedicated to my Mom, Dad, Melissa, Karen
and my late dog, Snickers . . .*


Introduction:

Motivation

Outline

An atom is a body which cannot be cut in two. A molecule is the smallest possible portion of a particular substance. No one has ever seen or handled a single molecule. Molecular science, therefore, is one of those branches of study which deal with things invisible and imperceptible by our senses, and which cannot be subjected to direct experiment.

-James Clerk Maxwell, 1873

n any given day, the Earth receives a vast amount of energy from the sun of about 6.26×10^{20} Joules per hour. As the global energy consumption in 2008 amounted to 4.74×10^{20} J, the Earth receives enough energy to fulfill the yearly demand for energy in less than one hour. Nevertheless, harnessing this source of energy in a cost effective way is not an easy task. Based on the photovoltaic effect, solar cells convert sunlight directly into electrical energy. At the moment, the photovoltaic industry is dominated by inorganic, silicon based, solar cells. As of 2011, a record power conversion efficiency of 43.5% has been achieved.[1] However, these systems have their drawbacks, the most notable of which being the high cost of fabrication. Nowadays, a great attention is focused on organic solar cells as a low cost alternative to conventional silicon-based photovoltaic devices.[2, 3]

Photovoltaic devices based on thin polymer films are particularly attractive mainly due to their ease of processing, mechanical flexibility, and substantial potential for low cost fabrication over large areas. Organic photovoltaics (OPVs) have the added benefit of being easily customized by tailoring the chemical makeup and material properties compared to traditional silicon based solar cells. In the last fifteen years, the power-conversion efficiency (PCE) of bulk heterojunctions, where p-type conjugated polymers are combined with n-type fullerenes, has continuously been improved, starting from relatively modest values to reach 5% in the well-known P3HT-PCBM couple, [4, 5] and as high as 8.3% in blends incorporating new small band gap (donor-acceptor) semi-conducting polymers.[6–8] However, in order to warrant their commercial viability, the efficiency of OPV devices needs further improvement. The control of the nanoscale morphology of the donor-acceptor blend is one of the critical parameters mobilizing

the efforts of physicists, chemists, and material scientists. The challenge is to obtain crystalline percolating networks of the donor and acceptor materials, interpenetrating at the scale of the mean diffusion length of excitons, to maximize the carrier generation at the interfaces and ensure their efficient transport to the electrodes. Therefore, high resolution characterization tools with nanometer resolution are needed to probe the morphology and the electronic properties of relevant samples for photovoltaic applications.

Unfortunately for August Kekulé, his vision of benzene as a cyclic molecule could not be confirmed while he was alive in 1865.[9] Fast forward almost 150 years, technological advancements have improved so much so that individual carbon rings of a pentacene molecule and the position of the hydrogen atoms around these rings, can be imaged by an atomic force microscope (AFM).[10] Furthermore, atomic resolution is routinely achieved by AFM on various kinds of surfaces.[11–13] The invention of AFM boosted the development of nanostructural devices as a direct method to map the topography of surfaces as well as to unveil a variety of physical and chemical properties down to the nanometer regime. In combination with AFM, scanning Kelvin force probe microscopy (KPFM) has become a very popular technique to map the electric surface potential of organic thin films and devices.[14–19] KPFM has already proven its ability to map contact potential differences (CPD) at the nanometer scale. Recently, local CPD (LCPD) atomic contrast has been achieved and modeled on several reference surfaces.[20, 21]

Despite these remarkable advancements, the spatial resolution reported for organic photovoltaic blends has typically been limited to a few tens of nanometers. Resolving structural and potential differences at the sub-10 nm scale has been beyond the limits of resolution even in the case of investigations carried out by noncontact AFM (nc-AFM) in ultrahigh vacuum (UHV).

Therefore, the main goal of this work is to use nc-AFM/KPFM to investigate the local structure and electronic properties of model organic materials and photovoltaic devices. The objective of this investigation is threefold:

- (i) To refine and resolve KPFM measurements at the nanoscale in order to map the surface photovoltage of nanoscale phase segregated bulk heterojunction photovoltaic devices.
- (ii) To investigate model self-assembled π -conjugated oligomers in order to obtain a deeper insight into the nature of the tip-surface interactions involved in the nc-AFM/KPFM imaging process.
- (iii) To confirm that single pass KPFM with small tip-surface separations (where short range forces can contribute to the KPFM imaging process) can still be used for quantitative investigations of the surface work function.

1.1 Thesis Outline

Therefore, this manuscript will be organized as follows:

In chapter 2, a brief overview of the field of organic electronics and optoelectronics is given. Specifically, a concise review of the fundamental principles for charge generation in organic heterojunctions is discussed.

In chapter 3, a comprehensive description of the working principles of the characterization methods used in this report is given: noncontact AFM (nc-AFM), KPFM, and photoelectron spectroscopy.

The next three chapters are devoted to the significant experimental results obtained throughout the duration of this thesis using nc-AFM and KPFM on key elements comprising a typical organic bulk heterojunction photovoltaic device.

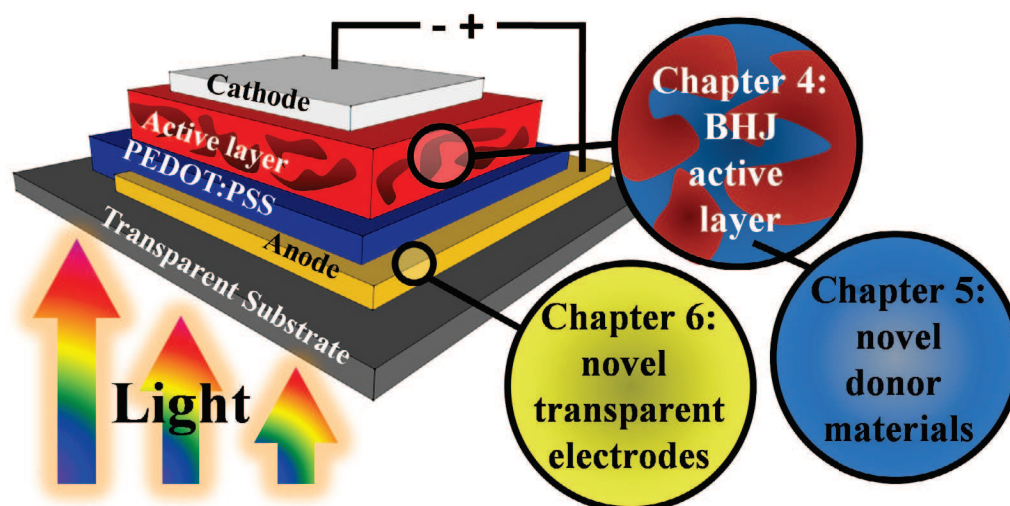


FIGURE 1.1

In chapter 4, we present nc-AFM/KPFM investigations carried out on a high efficient nanoscale phase segregated photovoltaic blend of the benchmark P3HT:PCBM. Our main goals are:

- (i) to clearly identify the networks of the donor and acceptor materials and,
- (ii) to visualize the charge carrier generation induced under selective illumination.

In chapter 5, the occurrence and nature of CPD contrasts at the molecular scale is investigated on two related model oligomers forming self-assembled π -stacked nanowires on highly oriented pyrolytic graphite (HOPG). For these edge-on stacks, a surface potential modulations correlated with the topography are expected due to the existence of molecular electric dipoles at the fluorenone cores.

In chapter 6, KPFM is used to characterize the surface potential of a series of flexible transparent electrodes, based on functionalized carbon nanotubes using metallic nanoparticles. These results are compared with the work function values deduced from ultraviolet photoelectron spectroscopy (UPS) measurements. In view of this comparison, the validity of work function values deduced from single pass KPFM experiments in the close proximity regime is discussed.

In chapter 7, we draw our conclusions and future perspectives.

Finally in appendix A, KPFM investigations of a novel donor-acceptor BHJ photovoltaic device is briefly presented. The behavior of the contact potential difference in dark and under illumination is addressed at the global scale.

Organic Electronics & Optoelectronics:

Conjugated Oligomers and Polymers
Organic Photovoltaics
Materials

Ce chapitre a pour objectif d'introduire le domaine de l'électronique et de l'opto-électronique organique, en présentant certaines notions essentielles relatives aux propriétés des molécules et polymères pi-conjugués. Le concept d'hétéro-jonction volumique est plus particulièrement décrit. Les matériaux étudiés dans ce travail sont également présentés.

In this chapter, a brief introduction into the field of organic electronics is given, outlining the properties of conjugated polymers and small molecules. Organic photovoltaics, specifically the concept of bulk heterojunction, is introduced. A detailed list of the materials investigated in this thesis is presented.

Typically, a plastic material isn't thought of as a conductive material. In fact, for most applications it is regarded as an insulator, such as for the protection around conductive wiring in order to insulate it and us from short circuits. However, in 1977, Alan J. Heeger, Alan G. MacDiarmid and Hideki Shirakawa discovered that a polymer, polyacetylene (as seen in figure 2.1), can be made conductive.[22–24] This discovery earned them the Nobel Prize in Chemistry in 2000.

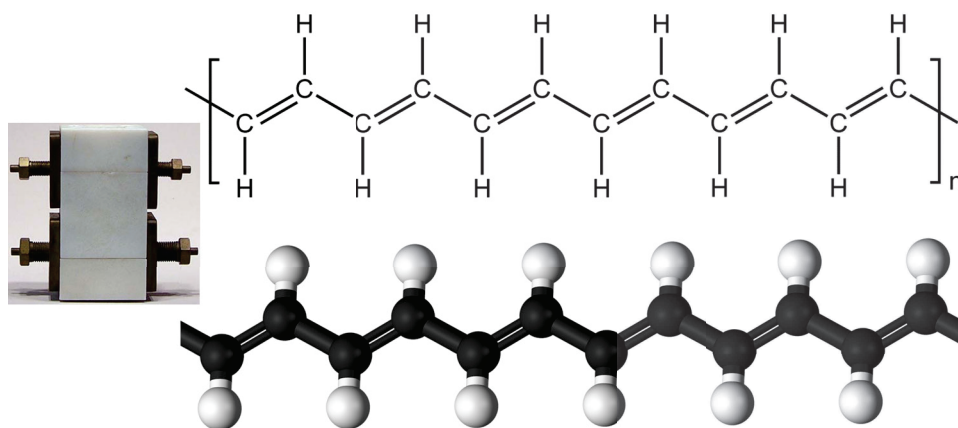


FIGURE 2.1: Voltage-controlled switch (left), an “active” organic polymer electronic device using melanin, a typical polyacetylene (chemical structure shown to the right), from 1974. Now in the Smithsonian Chip collection at the National Museum of American History in Washington D.C., USA.

However, conductive plastics were studied even earlier. In 1974, John McGinness and his coworkers described the “first experimental demonstration of an operating molecular electronic device”, as seen in figure 2.1. This “active” organic-polymer electronic device was a voltage-controlled bistable switch, with an active element being polyacetylene. The “ON” state of this device exhibited almost metallic conductivity, and exhibited low conductivity with switching, with as much as five orders of magnitude shifts in current.[25, 26]

Today, conductive plastics are being used for a number of applications, incorporated for use into commercial displays, batteries, diodes, electronic paper, transistors, solar cells etc. Conductive polymers are a desirable alternative in many applications because they are lighter, more flexible, and less expensive than inorganic conductors. New applications that would be impossible using copper or silicon are also possible.[27–31]

2.1 Conjugated Polymers

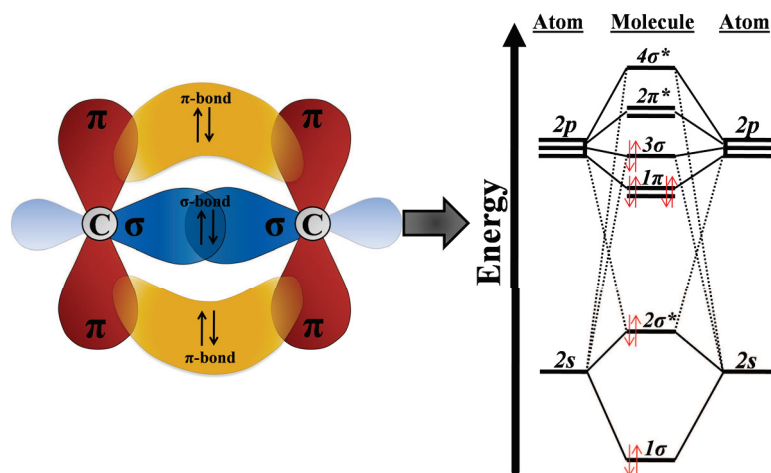


FIGURE 2.2: Pictorial representation (left) of the π & σ orbitals between two adjacent C atoms. The molecular orbital energy-level diagram (right) for diatomic molecules showing that $2p$ orbitals overlap to form bonding (π) and antibonding (π^*) orbitals.

Polymers, or plastics, are carbon-based macromolecules that are composed of repeating covalently bonded structural units, or monomers. Conjugated polymers have attracted a great deal of attention due to their remarkable electronic and optical properties arising from their unique structures consisting of alternating single bonds, and double or triple bonds. As a result, the π electron orbital overlaps between each connecting covalent or σ bond, as seen in figure 2.2. All conductive organic molecules conduct electrons through π bonds. A π bond is made by the addition of adjacent π -orbitals. They always have a node along the axis between the bound atoms. Most of the electron density in a π bond is above and below the plane of the connected atoms.

The bonding orbital (lower energy) has a node along the bond axis (π orbital). It is formed when the phases of the two π -orbitals match. The antibonding (π^*) orbital has a node along the axis and a node in the middle of the bond axis, between the nuclei of the two bound atoms. The simplest example of a π -conjugated chain is polyacetylene, which has the chemical structure shown in 2.1.

The band gap refers to the energy spacing between the highest occupied and the lowest unoccupied bands. The lowest unoccupied band is called the conduction band (inorganic semiconductors) or LUMO¹ (organic semiconductors) and the highest occupied band is called the valence band (inorganic semiconductors) or HOMO² (organic semiconductors).

¹Lowest Unoccupied Molecular Orbital

²Highest Occupied Molecular Orbital

The difference between HOMO and LUMO levels is reduced in the presence of π bonds which is at the origin of the semiconducting behavior of π conjugated materials. Materials comprising only sigma bonds (so called saturated systems) will display a larger HOMO-LUMO gap and behave as insulators.

Although the chemical structures of polymers are represented by alternating single bonds and double bonds, in reality, the electrons that contribute to the π bonds are mostly delocalized over three to four repeating units. For small molecules, the π bonds and corresponding π^* bonds have discrete energy levels. By increasing the number of carbon atoms, and thus increasing the length of delocalization, the π orbitals (and corresponding π^* orbitals) become closer. In a polymer, with a large number of carbon atoms, individual energy levels can no longer be distinguished.

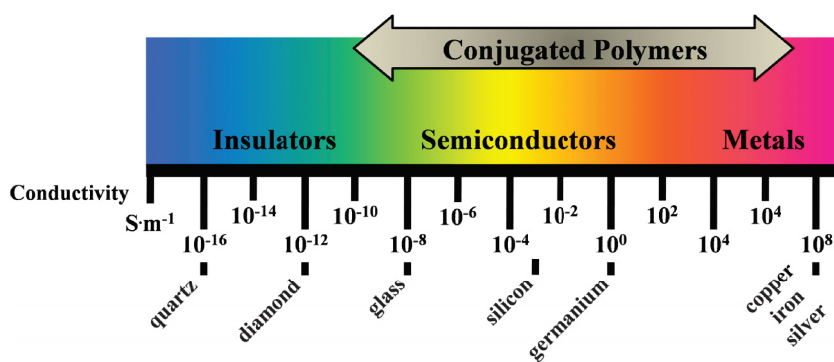


FIGURE 2.3: Conductivity of conjugated polymers compared to those of other materials, from quartz (insulator) to copper (conductor).

Much like inorganic semiconductors, where the level of conductivity is dictated by dopant materials, organic semiconductors work in a similar manner. The conjugated polymers in their undoped, pristine state are semiconductors or insulators, where the energy gap can be > 2 eV. Therefore, undoped conjugated polymers, such as polythiophenes and polyacetylenes display a low electrical conductivity (10^{-10} to $10^{-8} S \cdot m^{-1}$).

When the material is “doped” by oxidation, extra charge carriers are created (i.e. holes). Even with a very low level of doping ($< 1\%$), electrical conductivity increases by several orders of magnitude up to values of around $0.1 S \cdot m^{-1}$. Furthermore, any subsequent doping will eventually saturate the electrical conductivity, at values around 0.1 - $10 kS \cdot m^{-1}$ for different polymers. In practice, most organic conductors are doped by oxidation to give a p-type material. Shirakawa et al. reported high conductivity, $\sim 10^5 S \cdot m^{-1}$, in oxidized and iodine-doped polyacetylene.[23, 24]

However, in organic field effect transistors (OFETs) or polymer light emitting diodes, electrostatic doping is used to accumulate charges at the organic semiconductor/insulator interface, as pictured in figure 2.6.

In hole transporting OFET devices, a negative voltage is applied to the gate. By applying a second negative bias to the drain, the charges move along the channel and are collected at the drain.[32]

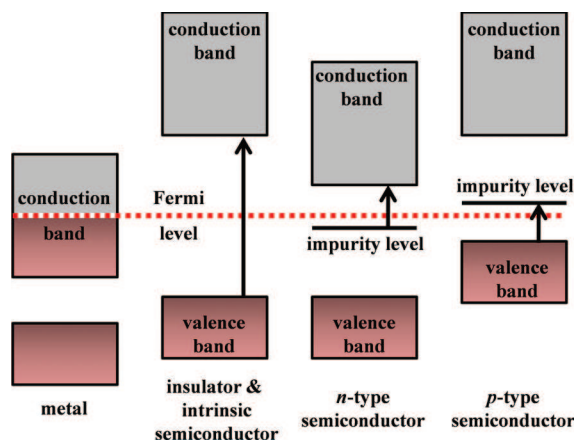


FIGURE 2.4: Energy diagram of a metal, an insulator, and n and p types extrinsic semiconductors.

The electrical properties of a material are determined by its electronic structure. Conductivity depends on the number density of charge carriers (number of electrons n) and how fast they can move in the material (mobility μ):

$$\sigma = n \mu e, \quad (2.1)$$

where e is the electron charge. In a metal, there is a high density of electronic states composed of electrons with relatively low binding energies, and these “free electrons” are able to move easily from atom to atom under an applied electric field. For example, the conductivity for metallic copper has been measured at around $10^8 \text{ S}\cdot\text{m}^{-1}$.

One mechanism proposed to account for conductivity in polymers is by charge hopping between different polymer chains, where an electron jumps between localized states on adjacent polymer chains. However, the bulk conductivity in the polymer is limited by the need for the electrons to jump from one chain to the next. In molecular terms, this is limited by an intermolecular charge transfer reaction, and also by macroscopic factors such as poor connection between different crystalline domains within the material.

The properties of conjugated polymers are strongly influenced by disorder effects which can take place at various scales. Intrachain, as well as interchain defects can indeed severely limit the charge transport. However, due to their high molecular weight and semicrystalline character, controlling the structural organization of π conjugated

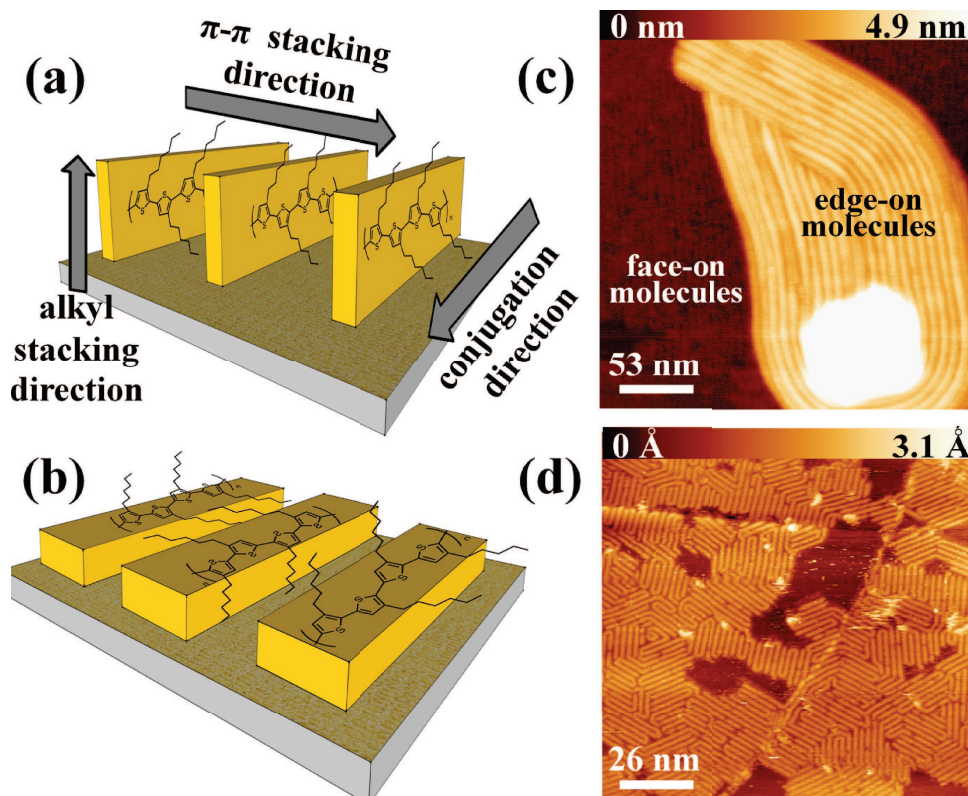


FIGURE 2.5: Schematic of edge-on (a) and face-on (b) orientations represented in the case of regioregular poly(3-hexylthiophene) (P3HT). In the case of OFETs the π - π stacking direction in (a) facilitates charge transport. (c,d) Scanning probe microscopy images of π conjugated oligomers and polymers self assembled on HOPG. (c) Topographic FM-AFM images of QTF8 edge-on stacks grown on a buffer layer of face-on molecules.[33] (d) STM topographic image of a face-on P3DDT film after *in-situ* annealing.[34]

polymers is challenging. Nowadays, a well-established approach to overcome this issue relies on the use of self-assembly and self-organization processes on surfaces.

Among π -conjugated materials, solution-processed regioregular poly(3-alkylthiophene-2,5-diyl)s (P3ATs), stand as a model system because of their remarkable self-organization properties on surfaces and high carrier mobilities under field effect doping. Poly(3-hexylthiophene) (P3HT) is a prototypical polymer among the P3AT family that is used for device applications, in part due to its ability to form self-assembled crystalline fibrils or nanorods. When deposited on a surface, P3HT can generally adopt two preferential orientations which are depicted in figure 2.5a and b. For edge-on assemblies (figure 2.5a), the interchain π -stacking direction is parallel to the plane of the substrate. On the other hand, the π conjugated cycles lie flat on the surface in the case of face-on assemblies (figure 2.5b). Frequency-modulation AFM and STM images of both kinds of assemblies are given in figures 2.5c and d, respectively.

For polymeric field effect transistors (PFET), it has been shown that the orientation of the crystalline domains dramatically influences the carrier mobility.[35] More precisely, the edge-on orientation promotes an efficient charge transport, since the π stacking direction is parallel to the channel at the organic-insulating interface.[36–39]

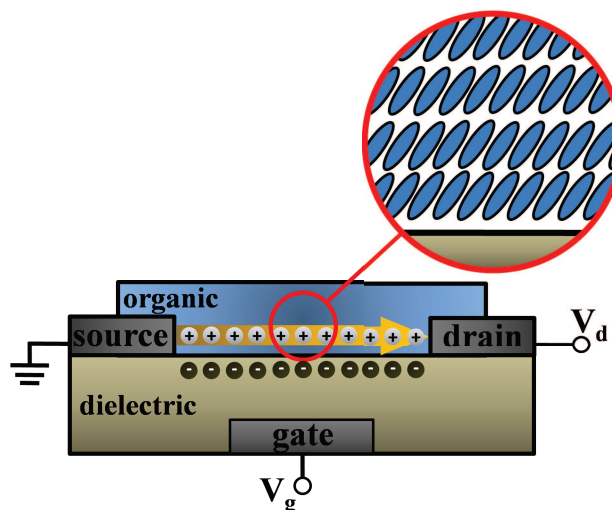


FIGURE 2.6: Basic schematic of a conventional organic field effect transistor (OFET) showing the arrangement of the molecules in the conducting channel made of short conjugated molecule.

2.2 Organic Electronics

Today, nanofabrication techniques can be broken down into two approaches, top-down and bottom-up. First termed by the Foresight Institute³ in 1989, these two approaches distinguish between conventional mass-production manufacturing techniques and molecular manufacturing. Top-down approaches use traditional microfabrication methods, such as photolithography, to create desired shapes and orders, analogous to carving the final structure from a larger block of matter. Conversely, bottom-up techniques use the chemical properties of molecules to produce the desired shape and properties for device applications. The bottom-up approach utilizes molecular self-assembly, described above, which is a key concept in supramolecular chemistry.[40–42] In this thesis, π - π interactions, caused by the overlapping π orbitals, as previously described, plays a major role in the supramolecular assembly.

Programmer design self-assembly of π -conjugated oligomers has been achieved using supramolecular techniques. Jean-Marie Lehn defines supramolecular chemistry as

³Foresight Institute www.foresight.org

‘chemistry beyond the molecule’, that is the chemistry of molecular assemblies leading to the design of supramolecular materials whose buildup and properties are controlled through the self assembly of suitable units.[43]

The organic materials used in electronic devices are generally split into two groups: small molecules and polymers. Polymers are usually processed from solution and have a molecular weight distribution that is described by the polydispersity of the material. On the other hand, small molecules, including oligomers, can be deposited by vapor methods or solution based processes and have a well-defined and highly reproducible molecular weight.[27] While typical polymers used for electronic applications are commercially available, with a variety of properties such as molecular weight, small molecules have to be synthesized in the lab.[44]

The synthesis, solubility/purification, and intrinsic electronic properties of polymers pose a significant problem to organic device applications because the regioregularity, molecular weight, and polydispersity have been shown to significantly affect the performance of devices.[45, 46] In fact, considerable differences in device performances have been observed when fabricated with the same polymer from different commercial sources, implying that the control of structural variables and purity is crucial.[44]

A possible solution to this problem is to replace the π -conjugated polymer with soluble small conjugated molecules, for example, as the donor material in organic solar cells. As Roncali points out in reference [44], this would have several potential advantages over polymers:

- ▷ defined chemical structure (therefore a defined regioregularity, molecular weight, and monodispersity),
- ▷ easier purification,
- ▷ a generally higher charge-carrier mobility and,
- ▷ a straightforward relationship between the chemical structure, electronic properties and device performances.

Exciting results have been obtained with plastic electronic devices based on polymers and small organic molecules. As discussed, both semiconducting materials have their pros and cons in which the processability and high ordering of organic thin layers are the unique features of both systems.

2.3 Organic Photovoltaics

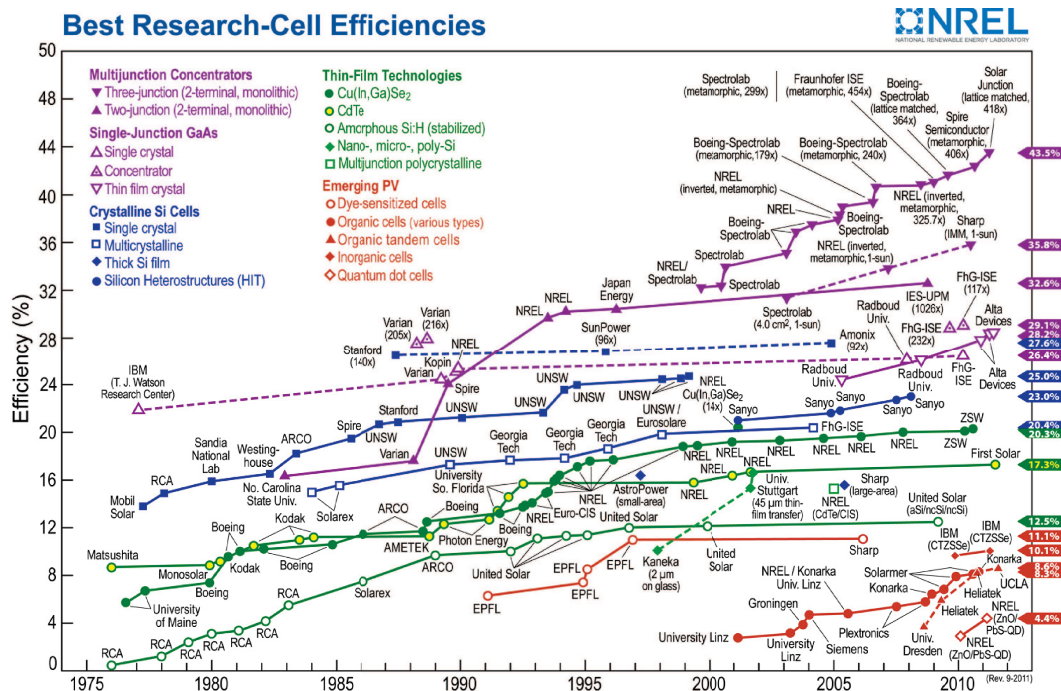


FIGURE 2.7: Progress of research-scale photovoltaic device efficiencies, under an air mass of 1.5, according to 9/2011 data from National Renewable Energy Laboratory (NREL).

Currently, a vast majority of commercial solar cells are made from highly purified and refined silicon crystal. However, due to the high cost and complex manufacturing process, interest in developing alternative photovoltaic technologies has increased. Within the last 20 years, organic materials gained broader interest for photovoltaic applications.[47–51]

Since the report of the first organic thin film solar cell by Tang [48], several architecture concepts have been presented using small molecules [48, 49], conjugated polymers [52], conjugated polymer blends [51, 53, 54], polymer-small molecule bilayers [55, 56], and blends [50, 57, 58] or combinations of organic-inorganic materials.[59, 60]

Using organic materials provides several benefits such as low cost synthesis, large optical absorption coefficients [61], and comparably easy manufacturing of thin film devices by either vacuum evaporation or solution cast processes. In addition, organic solar cells benefit from being able to be fabricated on mechanically flexible substrates. With the recent report of 8.3 % efficiency by Konarka (also certified by NREL⁴), organic photovoltaics are about to become a competitive option for solar energy conversion.[8]

⁴National Renewable Energy Laboratory (NREL) www.nrel.gov

Unlike conventional solar cells, that rely on the large built-in electric field of a p-n junction to separate the electrons and holes created when photons are absorbed, charge generation within an organic photovoltaic device relies on an interface between two different materials (electron donor and acceptor materials). A photon is converted into an electron–hole pair, typically in the donor material which is typically a polymer or small molecule. These charges tend to remain Coulombic bound in the form of an exciton. When the exciton diffuses within the donor material and reaches a donor-acceptor interface, charge separation can take place.[3]

In the following, three basic device architectures that can be used to realize a full organic photovoltaic device are presented: biplanar heterojunction, bulk heterojunction, and the ordered heterojunction, pictured in figure 2.8.

2.3.1 Device Architectures

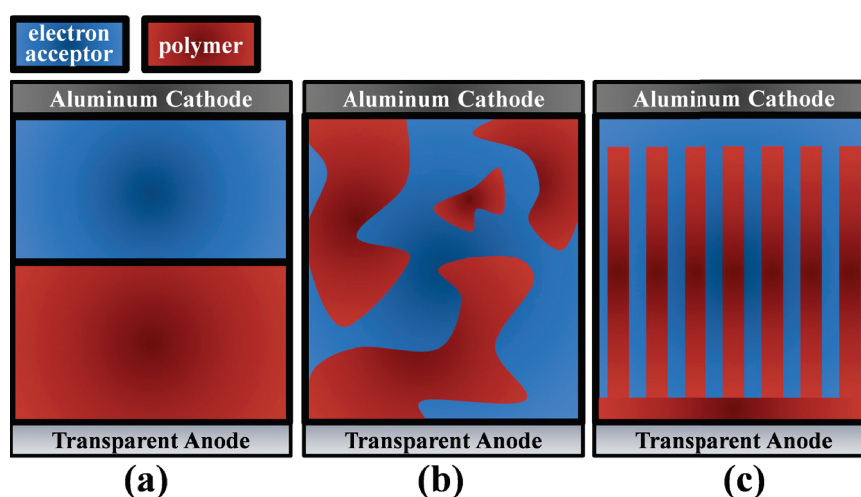


FIGURE 2.8: Three organic solar cell device architectures: (a) biplanar heterojunction, (b) bulk heterojunction and (c) ordered heterojunction.

2.3.1.1 Biplanar Heterojunction

The simplest device architecture one can conceive, that also promotes exciton separation, is a biplanar heterojunction (Figure 2.8a), in which the active layer is sandwiched between a transparent anode and a metallic cathode. However, the efficiency of the biplanar heterojunction device is primarily limited by the exciton diffusion length within these materials. The distance over which excitons travel before undergoing recombination is $\sim 3\text{--}10$ nm in most organic semiconductors. Therefore, any excitons formed

at a location further from the heterojunction interface than that of the exciton diffusion length have a very low probability of being dissociated. Thus, the active volume of this architecture is only limited to a very thin region close to the interface. Unfortunately, a very thin active area (< 100 nm) is not enough to adsorb most of the solar radiation flux in these types of materials.

This has inspired researchers of nanostructuring the materials such that the domain size is on the order of twice the diffusion length in order to overcome this limitation, as shown in the following.[62]

2.3.1.2 Bulk Heterojunction

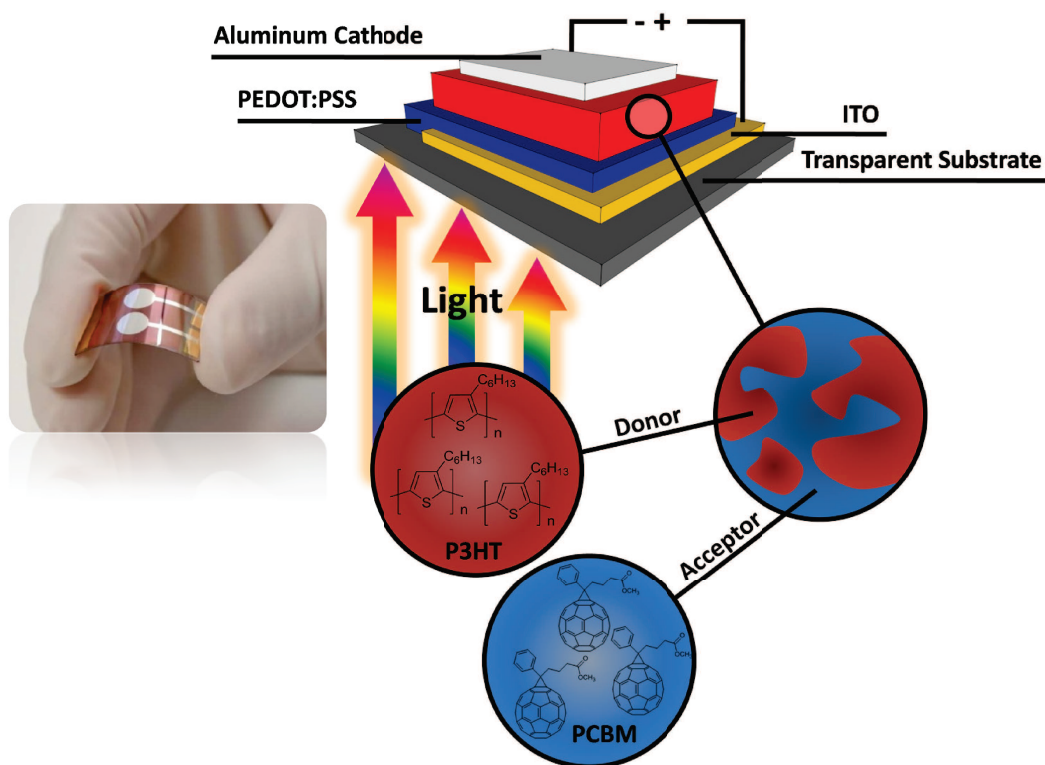


FIGURE 2.9: Normal geometry of a bulk-heterojunction solar cell. PEDOT:PSS: Poly(3,4-ethylenedioxythiophene) poly(styrenesulfonate). ITO: Indium tin oxide. P3HT: poly(3-hexylthiophene). PCBM: Phenyl-C61-butyric acid methyl ester.

In a bulk heterojunction (BHJ) architecture the electron donor and acceptor materials form two percolating intermixed networks, which maximizes the interface area where charge transfer can occur.

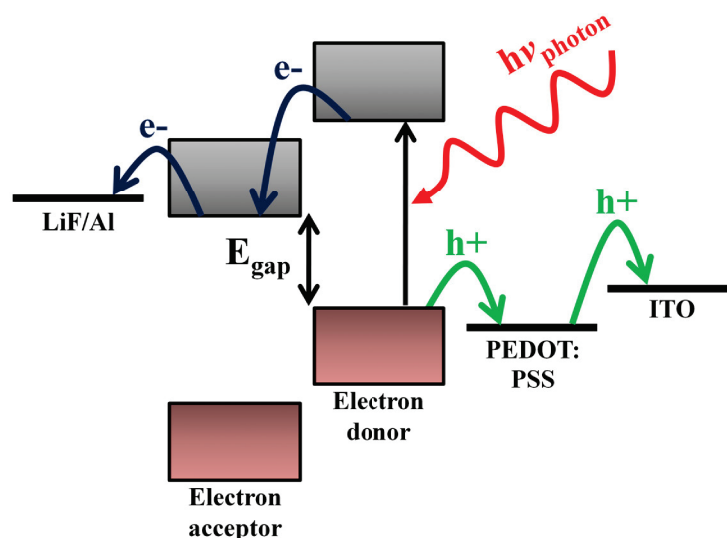


FIGURE 2.10: Schematic of the energy levels of the electron donor and acceptor materials. After charge separation, the electron and hole are transported through the respective materials and collected by the electrodes. Poly(3,4-ethylenedioxythiophene):poly(styrenesulfonate) (PEDOT:PSS) deposited on top of indium tin oxide (ITO) is used as the hole collecting anode, while lithium fluoride and aluminum are used as the electron collecting cathode.

The device geometry of a typical BHJ solar cell can be seen in figure 2.9. In this case, the transparent substrate (typically glass) is coated with indium-tin-oxide (ITO), a transparent conductive electrode with a high work function, suitable to act as a hole collecting anode. With the aim to reduce the roughness of this ITO layer and further increase the work function, a very thin layer of poly(3,4-ethylene dioxythiophene): poly(styrene sulfonate) (PEDOT:PSS) is spin cast on top. This is subsequently followed by the active layer. The top electrode usually consists of a low work function metal or lithium fluoride (LiF), topped with a layer of aluminum, all of which are deposited by thermal deposition in vacuum through a shadow mask. One of the most promising combinations of materials within the active layer is composed of a blend of a semiconducting polymer as a donor and a fullerene, C_{60} , derivative as the acceptor.[50]

In order to achieve an effective charge transport, the morphology of the active layer is critical. Both the donor and acceptor materials should ideally form crystalline, interpenetrated and percolating networks connected to the respective electrodes. Moreover, the length scale of the phase segregation between the two materials should be on the order of the mean exciton diffusion length (typically ≤ 10 nm).[50, 53, 63, 64] Achieving an ideal morphology is therefore highly challenging. Shaheen et al. have shown that the choice of solvent has a profound effect on the morphology and performance of BHJ photovoltaic device.[57] Furthermore, thermal annealing has been

frequently used to improve the crystallinity of the polymer domains resulting in better device efficiencies.[63, 65–68]

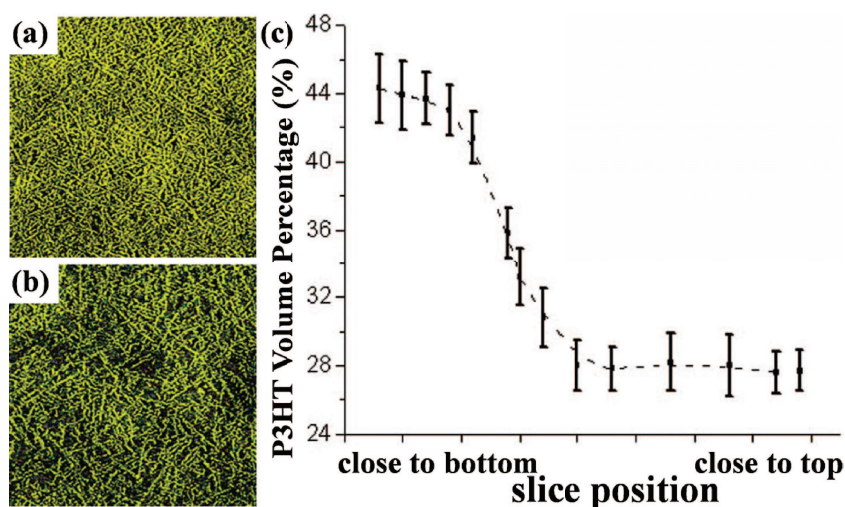


FIGURE 2.11: Images (a) and (b) are original slices taken out of the reconstructed volume of a P3HT:PCBM film, with a slice (a) located close to the bottom of the film and (b) close to the top of the film. Dimensions of the slices are $1700\text{ nm} \times 1700\text{ nm}$. A threshold was set up such that the crystalline P3HT nanorods are yellow in color. The relative area occupied by (yellow) P3HT in each slice can thus be determined for all slices through the whole thickness of the P3HT/PCBM film and plotted depending on a slice position (c). Image modified from reference [68].

In addition, in the case of the benchmark P3HT:PCBM tandem, electron tomography experiments have revealed a favorable concentration gradient of the electron donor material through the thickness of the active layer. In other words, the density of the P3HT fibrils is larger at the interface with the anode, which enhances the hole collection process, as seen in figure 2.11.[68].

2.3.1.3 Ordered Heterojunction

As already stated, in order to improve sufficient charge transport to the electrodes, it is vital to obtain an interpenetrating and percolating network of the donor and acceptor materials at the nanoscale. However, this can lead to the formation of a random network, that can possibly limit the efficiency of the BHJ architecture. Vastly different morphologies which may have dead ends and isolated domains can severely affect the charge transport by trapping charge carriers, preventing them from being extracted. Therefore, structuring one of the components into vertically aligned rods or pores with a diameter on the order of the exciton diffusion length would alleviate this problem, as seen in figure 2.8c.[62] This device structure is aiming to adapt the advantages of

both the biplanar and bulk heterojunction architectures, an enlarged donor-acceptor interface and an spatially uninterrupted pathway for the opposite charge carriers to their corresponding electrodes.

Unfortunately, so far, poor efficiencies have been achieved with ordered heterojunction architectures. Fabricating nanostructures with small pore sizes (on the order of the exciton diffusion length ~ 10 nm) and high aspect ratios has proven difficult.[62]

In summary, as Coakley et al. [64] describe, the path to improve the efficiency of OPV devices can be accomplished if:

- (i) a method is developed for patterning high aspect ratio nanostructures; for example, 20 nm wide straight holes that are 200 nm deep in a suitable semiconductor,
- (ii) the bandgap of the materials is reduced in order to absorb more light,
- (iii) the energy loss associated with electron transfer is reduced,
- (iv) the charge carrier mobility is improved and the interface is engineered to almost eliminate recombination,
- (v) and lastly, OPV cells of different bandgaps are stacked in order to harvest more of the solar energy.

2.3.2 Operational Principle

The basic operational principles of a BHJ organic solar cell can be broken down into four distinct processes, as seen in figure 2.12.

Light Absorption \Rightarrow Exciton Generation Light is mainly absorbed in the so-called electron donor material, which is typically a hole conducting small molecule or a conjugated polymer. Excitons, or the Coulombic bound electron-hole pairs, are generated on the polymer chain. The optical absorption coefficient for typical organic molecules is quite high. Therefore, a large amount of light can be absorbed within a relatively small amount of materials.[61] Whereas further increasing the layer thickness is advantageous for light absorption, it also burdens the charge transport. However, a drawback is that organic polymers tend to have a narrow absorption band within the solar spectrum.[69, 70]

Exciton Diffusion \Rightarrow to Acceptor Interface Due to the low dielectric constant in organic materials, the photogenerated excitons are strongly Coulombic bound. Electrically neutral excitons can only move by diffusion. For efficient charge generation, an exciton photogenerated anywhere in the blend has to reach the donor-acceptor interface within its lifetime. When the mobility of the exciton is too low or the active layer is too thick, the needed transit time of photogenerated charges to reach the donor-acceptor

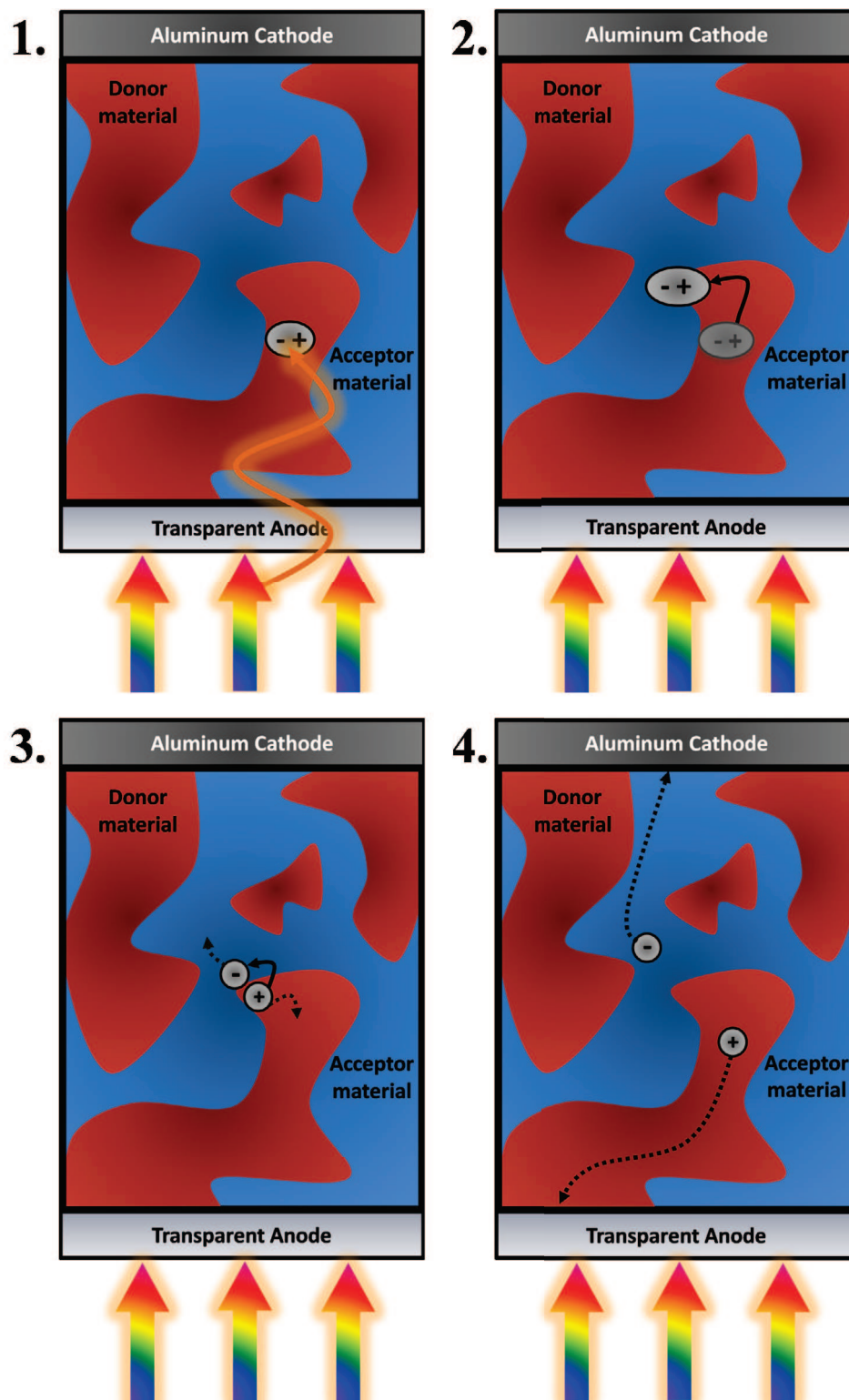


FIGURE 2.12: Pictorial representation of the operation of a BHJ organic solar cell:
 Step 1: Light Absorption ⇒ Exciton Generation.
 Step 2: Exciton Diffusion ⇒ to Acceptor Interface.
 Step 3: Exciton Dissociation ⇒ Free Electron-Hole Pair Generation.
 Step 4: Free Electron-Hole Pair Dissociation ⇒ Charge Transport ⇒ Photocurrent!

interface becomes longer than the lifetime. The exciton decays and the charges recombine. Therefore, the maximum of the allowed phase separation is determined by the diffusion length of the exciton. In most organic materials, the exciton diffusion length is limited to 5–10 nm by the relatively fast intrinsic decay process of the photoexcited molecules.[66, 71]

Exciton Dissociation \Rightarrow Free Electron-Hole Pair Generation Excitons can only be dissociated at energetically favorable acceptor molecules, such as fullerenes. This is because the energy gain is larger than the exciton binding energy. Afterwards, the electron or charge transfer can take place, in which the exciton dissociates into an electron on the fullerene acceptor and a hole which remains in the polymer. However, this electron-hole pair is still Coulombic bound, and is called geminate pair or polaron pair. This polaron pair also needs to be dissociated, this time by an electric field (built-in voltage + applied voltage). Therefore, the photocurrent in organic solar cells depends strongly on the applied voltage. This is a major loss mechanism in organic solar cells.[72, 73] In 1992, Sariciftci et al. demonstrated that the electron transfer from a conjugated polymer to C_{60} is ultrafast (sub-picosecond). This has demonstrated the great potential of fullerenes as acceptor materials.[47, 74]

Free Electron-Hole Pair Dissociation \Rightarrow Charge Transport The electrons and holes are transported to the respective electrodes, driven by the electric field, and moved by a hopping transport process. Surprisingly, the lifetime of the resulting charge-separated state in BHJ blends extends into the millisecond time domain. This long lifetime allows the photogenerated charges to diffuse away from the donor–acceptor interface (assisted by the internal electric field in the device) and be collected at their respective electrodes.[75, 76] However, the morphology and structural properties of the donor and acceptor materials play a major role in this step as well. A high degree of structural organization of the self-assembled polymers/oligomers and percolating networks throughout the active layer and an improved contact to the electrodes ensures high carrier mobility and charge collection. Thereby, the device performance and efficiency is optimized by lowering the series resistance of the polymer solar cells.[5, 65]

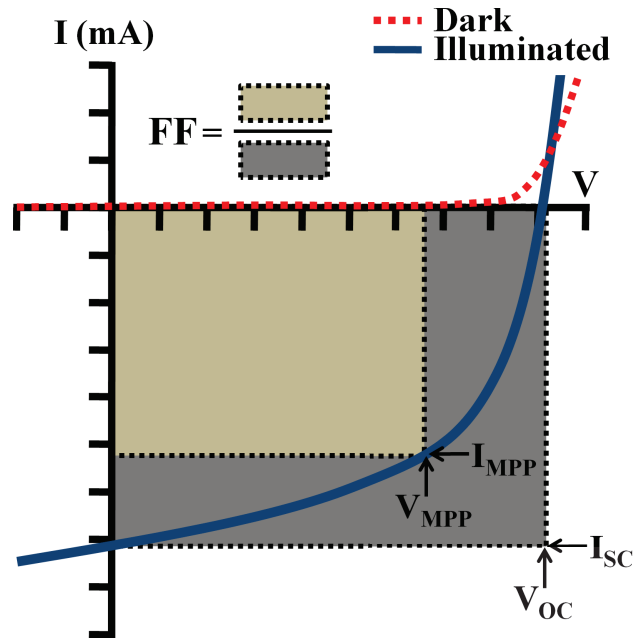


FIGURE 2.13: Typical behavior of the current-voltage (IV) measurements of an organic solar cell in dark (red dashed line) and under illumination (solid blue line).

Solar Cell Parameters The photovoltaic power conversion efficiency η_e is a measure of the degree of incident sunlight being converted into electricity and is defined as:

$$\eta_e = \frac{V_{OC} I_{SC} FF}{P_{in}}, \quad (2.2)$$

where V_{OC} is the open circuit voltage, I_{SC} is the short circuit current in A/m^2 , and P_{in} is the incident light power in W/m^2 . The fill factor (FF) is the ratio of the actual maximum obtainable power to the maximum theoretical power, defined as:

$$FF = \frac{I_{mpp} V_{mpp}}{V_{OC} I_{SC}}, \quad (2.3)$$

where I_{mpp} and V_{mpp} are the current and voltage at the maximum power point.[71] The trend of power conversion efficiencies of various types of solar cells, from the National Renewable Energy Laboratory (NREL), is shown in figure 2.7. According to Scharber et al. (2006), a power conversion efficiency exceeding 10% should be possible by controlling the morphology along with the size of the band gap and the LUMO offset.[77]

2.4 Materials

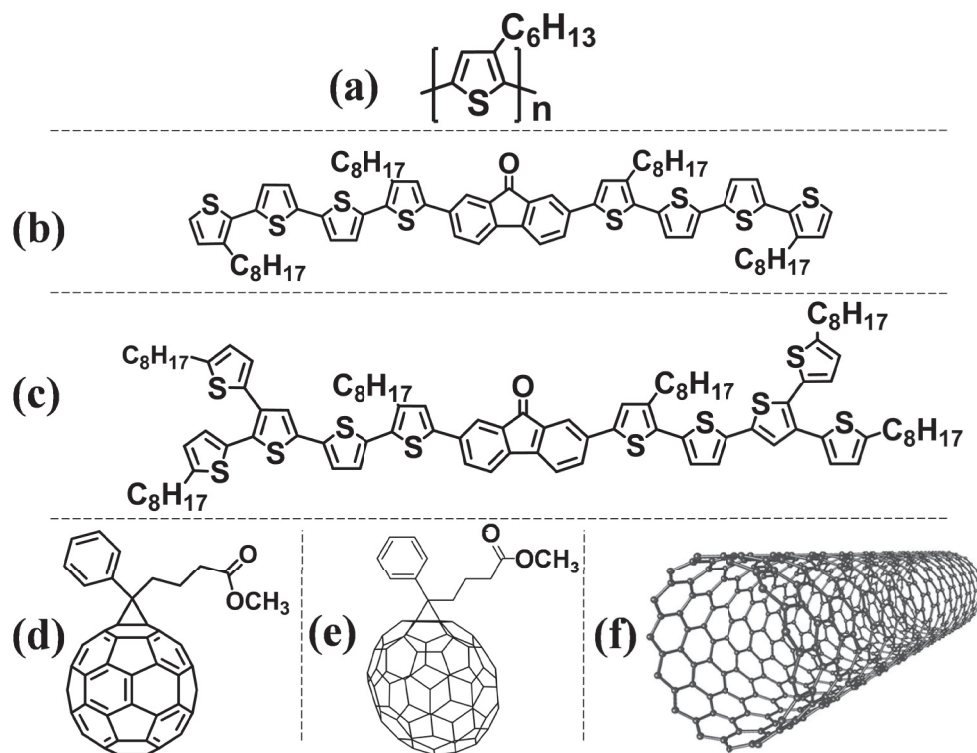


FIGURE 2.14: (a) polymer, poly(3-hexylthiophene) [P3HT], (b) QTF8, (c) FG1, (d) Phenyl- C_x -butiric acid methyl ester, PC_{60}BM and (e) PC_{70}BM . (f) Single wall carbon nanotube SWCNT.

In this thesis, six organic materials were investigated.

The well-known conjugated polymer, regioregular poly(3-hexylthiophene) (P3HT), was used in this thesis in combination with the fullerene PC_{60}BM . P3HT consists of stiff π -conjugated backbone with hexyl side chains that allow solubilization and processing for technological purposes.

Two novel small molecules (oligomers), abbreviated as QTF8 [78] and FG1 [79], seen in figure 2.14b and c, respectively, have been synthesized by fellow colleagues for photovoltaic applications. Both molecules contain a fluorenone central unit symmetrically coupled to oligothiophene segments. These novel oligomers were investigated for their intrinsic self-assembly properties.

Moreover, a comparison was carried out between the results obtained for the benchmark P3HT: PC_{60}BM with the ones achieved for an FG1: PC_{70}BM BHJ photovoltaic device (presented in appendix A).[79]

Fullerenes C_{60} and C_{70} itself are rather insoluble. Therefore, side groups are attached to increase their solubility for solution processing. The most widely used C_{60} and C_{70} derivative in solar cell devices is 1-(3-methoxycarbonyl)propyl-1-phenyl-[6,6] methanofullerene, PCBM, seen in figure 2.14d and 2.14e for C_{60} and C_{70} , respectively. This has shown increased solubility in organic solvents and is excellent electron acceptor material.[80]

Single wall carbon nanotubes (SWCNTs) are members of the fullerene family, seen in figure 2.14f. Extensive research and applications have been developed regarding the properties of these structures since their discovery in 1991.[81–83] In the context of this thesis, they have been incorporated as a network for use as a flexible transparent conductive electrode for photovoltaic applications.

Experimental Techniques: Noncontact Atomic Force Microscopy (NC-AFM) Kelvin Probe Force Microscopy (KPFM) Photoelectron Spectroscopy (PES) Cantilevers & Equipment

Les techniques expérimentales utilisées dans ce travail sont présentées dans ce chapitre, à savoir la microscopie à force atomique non contact en modulation de fréquence (FM-AFM), la microscopie à sonde de Kelvin (KPFM) et les techniques de spectroscopie de photo-électrons (PES). Nous montrerons en quoi la spectroscopie de photo-électrons UV (UPS) et la microscopie à sonde de Kelvin sont deux techniques complémentaires pour estimer la fonction de sortie d'un échantillon, et comment la spectroscopie de photo-électrons X (XPS) peut être utilisée pour analyser la composition chimique en surface. Les avantages et limitations de chacune de ces techniques seront détaillés en sus des principes opératoires de base. Les deux principales méthodes pouvant être utilisées pour réaliser des mesures de microscopie à sonde de Kelvin seront comparées: le mode modulation d'amplitude (AM-KPFM) et le mode modulation de fréquence (FM-KPFM). Enfin, nous donnerons une description détaillée du dispositif expérimental utilisé pour nos études.

A detailed overview of the principle techniques of this thesis will be outlined: Non-contact frequency modulation atomic force microscopy (FM-AFM), Kelvin probe force microscopy (KPFM), and Photoelectron Spectroscopy (PES). Ultraviolet photoelectron spectroscopy (UPS) is used complementary to KPFM to determine the work function ϕ_s of the sample and X-ray photoelectron spectroscopy (XPS) is used for surface composition analysis. Fundamental aspects of each technique will be addressed including the advantages and limitations. Regarding KPFM, a comparative overview of the two principle methods, Amplitude Modulated KPFM (AM-KPFM) and Frequency Modulated KPFM (FM-KPFM), will be provided. An in-depth experimental apparatus description will also be given.

In March 1981, G. Binnig, H. Rohrer, Ch. Gerber and E. Weibel at the IBM Zürich Research Laboratory observed vacuum tunneling of electrons between a sharp tungsten tip and a platinum sample.[84–86] Combined with the ability to scan the tip against the sample surface, the scanning tunneling microscope (STM), and consequently the field of scanning probe microscopy (SPM), was born. This development earned Binnig and Rohrer the Nobel Prize for Physics in 1986. Since then, advances in scanning probe microscopy have progressed rapidly, easily achieving atomic resolution.[87, 88] While the STM is an innovative tool allowing access to the world at the atomic scale, the basic operating principles of the STM are quite straightforward and has been covered extensively in many books and review articles.[11, 12, 89–93]

Despite of the great success of the STM, it is obvious that STM has a fundamental disadvantage. That is, with STM only the conductive or conductive layers coated samples can be investigated. To overcome this limitation, Binnig invented the AFM [94] in 1985 and it was introduced by Binning, Quate and Gerber as a spin-off to the STM.[95] This came about due to the apparent forces which act between the tip of the STM and the sample, causing elastic deformations of the tip which inevitably was put to use in the AFM.

3.1 Atomic Force Microscopy (AFM)

In atomic force microscopy (AFM) a flexible tip-cantilever assembly is scanned across a surface tracing the topographical contours. Forces, such as inter-atomic, frictional, magnetic and electrostatic, can either attract or repel the tip. AFM operates in two fundamental modes, in which the cantilever is used as a:

- ▷ static probe in contact mode, or
- ▷ as a resonator in the dynamic modes (intermittent and noncontact).

In contact mode, or static operation, the cantilever is dragged across the surface of the sample. The topography of the surface is measured directly using the deflection of the cantilever, which is proportional to the normal force F_N . Thus, the topography is regulated by the normal force acted on the cantilever by the sample surface. The force setpoint of the cantilever is added externally and may be either positive or negative, in which:

- ▷ $F_{set} > 0 \Rightarrow$ repulsive force
- ▷ $F_{set} < 0 \Rightarrow$ attractive force

Primarily, a positive force setpoint is applied but a negative force setpoint can be used on adhesive samples and for force spectroscopy.[96]

However, in this thesis, the primary method of operation is in dynamic mode, specifically using noncontact atomic force microscopy (NC-AFM), see section 3.1.3. Pioneered by Martin et al. [97], in dynamic mode, the cantilever is a harmonic oscillator and is externally oscillated at or close to its fundamental resonance frequency. When the cantilever is in close proximity to the surface, the oscillation amplitude, phase, and resonance frequency are modified by the interaction forces between the tip and sample. These changes in oscillation with respect to an external reference oscillation are used as a feedback signal to provide information about the sample's surface topography. Typically, changes in oscillation amplitude (amplitude modulation AFM) are employed in intermittent contact mode (also referred to as tapping mode), widely used in ambient conditions. Changes in the resonance frequency (frequency modulation AFM) are utilized in ultrahigh vacuum (UHV) and is commonly referred to as NC-AFM.[97] Frequency and amplitude modulation (FM and AM) AFM is illustrated in figure 3.1.

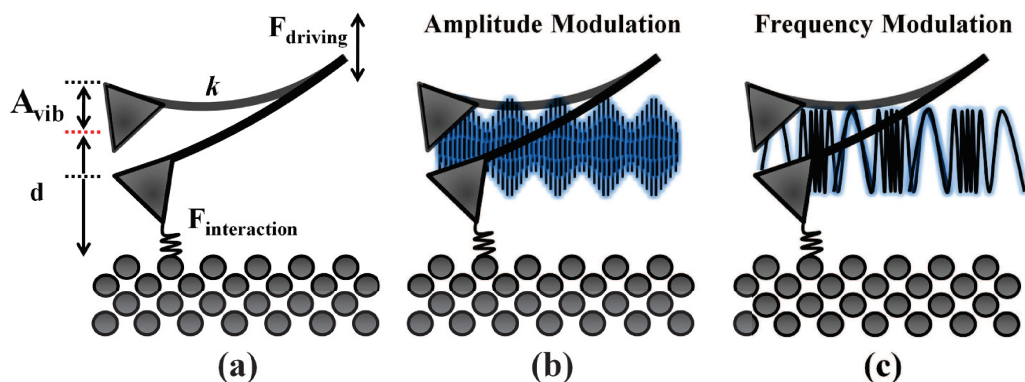


FIGURE 3.1: Driving force and tip-surface interaction force upon a vibrating cantilever (a) with a normal mode spring constant k expressed in equation 3.13, and vibrational amplitude, A_{vib} . Schematic representations of amplitude (b) and frequency modulation (c) AFM.

3.1.1 Tip-Sample Forces

Before we can discuss the operating mechanisms behind FM-AFM/NC-AFM, used in this thesis, it is important to consider the forces between an AFM cantilever and the surface. The potential energy between an AFM tip and the surface V_{ts} causes a z component of the tip sample force, simply given as:

$$F_{ts} = -\frac{\delta V_{ts}}{\delta z}. \quad (3.1)$$

The tip-sample spring constant for cantilever is defined as:

$$k_{ts} = -\frac{\delta F_{ts}}{\delta z}. \quad (3.2)$$

The frequency shift used to regulate the z-position, is either proportional to F_{ts} or its gradient depending of the amplitude regime.[13]

The range of forces between the tip and sample can be regarded as either long-range or short-range. In vacuum, there are short-ranged chemical forces (up to a few nm) while at the long-range there are van der Waals, electrostatic and magnetic forces (up to ~ 100 nm), which often overwhelm the short range chemical interaction responsible for atomic resolution.

Van der Waals interactions are caused by electric dipole moment fluctuations of atoms or molecules and their polarization on a sample surface. The form of the van der Waals potential for a spherical tip with radius R and an infinite plane is given by:

$$V_{vdW} = -\frac{A_H R}{6z}, \quad (3.3)$$

where A_H is the Hamaker constant which encapsulates the effects of the atomic polarizability and density and is a property of the materials of the tip and sample, typically of the order of 1 eV.[98] This gives rise to a force:

$$F_{vdW} = -\frac{A_H R}{6z^2}. \quad (3.4)$$

The van der Waals force can be a major disturbance in scanning probe microscopy because the force can be quite large.[13]

Additionally, with typical tip and sample materials, there exists an electrostatic potential difference, $U_{ts} \neq 0$. The electrostatic force on the cantilever can be generally expressed in terms of the capacitance gradient and the potential difference between tip

and sample:

$$F_{el} = -\frac{1}{2} \frac{\delta C_{ts}}{\delta z} V_{ts}^2, \quad (3.5)$$

where V is an external bias applied to the tip.[13] This will be discussed in more detail within the frame of Kelvin probe force microscopy, in section 3.2. Nonetheless, this suggests that even with no external bias applied to the tip and no trapped charges present there may be an electrostatic force present due to the difference in work function between tip and sample materials. However, by applying the appropriate bias the electrostatic force can be nulled, and this is often done for FM-AFM imaging. Assuming a spherical tip at a distance z above an infinite plane, the electrostatic force reduces to:

$$F_{el} = -\pi \epsilon_0 \left(\frac{R^2}{z(z+R)} \right) U_{ts}^2 \approx -\frac{\pi \epsilon_0 R U_{ts}^2}{z}, \quad (3.6)$$

where R is the radius of the spherical tip, U_{ts} is the potential between tip and sample and ϵ_0 is the permittivity of free space. Like van der Waals interactions, electrostatic interactions can cause large forces. Giessibl et al. [99] explain that in contrast to van der Waals forces, where short-range interactions can lead to large long-range tip-sample forces ($\propto 1/z^6$), electrostatic forces can contribute in the opposite direction. That is, the electrostatic field has a short-range exponential distance dependence.

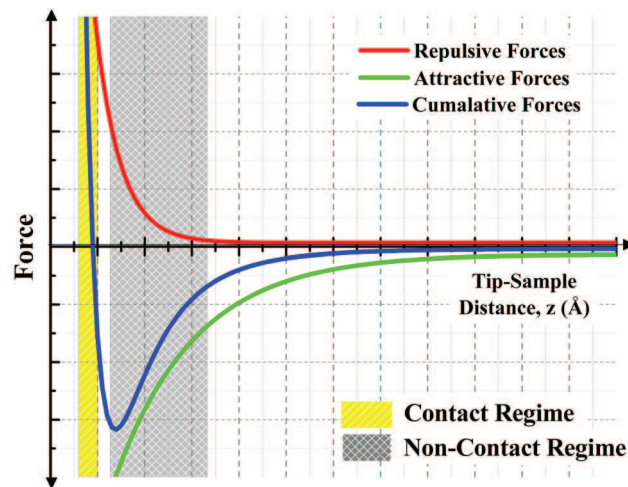


FIGURE 3.2: Force curve of an AFM tip as a function of surface distance, as well as operating regimes of contact and noncontact AFM modes.

Excluding long-range electrostatic and magnetic forces, a variety of different theories exist for empirically modeling the chemical/short range interactions. The two most common are the Lennard-Jones potential [11, 100] (which models the long-range van der Waals attractive force and Pauli repulsion, and is also used to demonstrate the force curve in figure 3.2) and the Morse potential (which in this form models short-range repulsive and attractive bonding forces), both of which can be expressed in terms of a

bond energy E_{bond} (typically, on the order of 10^{-18} J) and an equilibrium distance σ (on the order of the Å).[13] The Lennard-Jones potential is given by:

$$V_{LJ} = -E_{bond} \left[2 \left(\frac{\alpha}{z} \right)^6 - \left(\frac{\alpha}{z} \right)^{12} \right], \quad (3.7)$$

which gives rise to a force:

$$F_{LJ} = -12 \frac{-E_{bond}}{\sigma} \left[2 \left(\frac{\alpha}{z} \right)^7 - \left(\frac{\alpha}{z} \right)^{13} \right], \quad (3.8)$$

The Morse potential describes the covalent bonding dependence as an exponential decay:

$$V_{Morse} = -E_{bond} \left[2e^{-\kappa(z-\alpha)} - e^{-2\kappa(z-\alpha)} \right], \quad (3.9)$$

where κ is the characteristic inverse decay length [98, 101–103], which gives rise to a force:

$$F_{Morse} = -2\kappa E_{bond} \left[2e^{-\kappa(z-\alpha)} - e^{-2\kappa(z-\alpha)} \right], \quad (3.10)$$

Although, measured force curves may differ from this simplified model due to tip geometry or inhomogeneities in the sample.[104]

In order to obtain high resolution, the tip must probe close to the surface, such that it can access the short-range chemical forces.[105] As the force (and force gradient) between the tip and sample in the region we want to probe is so great that if we place the tip in this position in a static environment it will be pulled into contact with the surface (i.e. a so called ‘jump to contact’ into the repulsive regime where the tip-sample force will become much greater) due to the finite stiffness of the cantilever. If we want to work in the region where we are able to detect the short-range forces, without being drawn into the region where the tip and/or the sample is damaged or modified, it becomes necessary to use so-called dynamic AFM techniques.

3.1.2 Vibrating Tip Dynamics

In dynamic modes of AFM, a cantilever with a sharp tip is positioned in close proximity to the surface to be investigated and is mechanically excited at or near resonance. The equation of motion of such a driven cantilever in the presence of a tip-surface interaction force can be expressed by the equation of motion of a forced harmonic oscillator with

damping:

$$\underbrace{k z(t)}_{\text{Restoring force}} + \underbrace{\gamma_0 \dot{z}(t)}_{\text{Intrinsic damping}} + m^* \ddot{z}(t) = \underbrace{F_{ts}(x)}_{\text{Interaction force}} + \underbrace{F_0 \cos(\omega t)}_{\text{Driving force}}, \quad (3.11)$$

$$\text{where } \gamma_0 = \left(\frac{m^* \omega_0}{Q} \right).$$

Here, the restoring force of the cantilever spring, intrinsic damping of the cantilever, the tip-sample interaction force and the driving force used to excite the cantilever are included. In equation 3.11, k and m^* are the normal mode spring constant and effective mass of the cantilever, respectively; F_0 and ω are the amplitude and angular frequency of the driving force, respectively; and finally Q and ω_0 are the quality factor and angular resonance frequency, respectively.

In the absence of the tip-sample interaction $F_{ts}(z) = 0$, the natural resonant frequency (or fundamental eigenfrequency) of the cantilever with damping is given by:

$$f_0 = \frac{1}{2\pi} \sqrt{\frac{k}{m^*}} \simeq \frac{1.8373^2 t}{4\sqrt{3}\pi L^2} \sqrt{\frac{Y}{\rho}}, \quad (3.12)$$

where k and m^* are the normal mode spring constant and effective mass of the cantilever, respectively. For rectangular cantilevers, f_0 can be written in terms of the length, L , and thickness, t of the cantilever and the Young's modulus, Y and density, ρ of the material of the cantilever. Similarly, the normal mode spring constant of the cantilever can be expressed as:

$$k = \frac{Y w t^3}{4L^3}, \quad (3.13)$$

where w is the width of the cantilever.[106] In principle, the spring constant can be determined from these parameters, or measured directly (see table 3.2 for specific values of the cantilevers used).[107, 108] However, in FM-AFM, k varies by orders of magnitude during one oscillation cycle and a more complicated approach, utilizing canonical perturbation theory, is needed to calculate the frequency shift.[13, 98]

Quality Factor The resolution of an AFM is dependent on the quality factor of the vibrating cantilever. The quality factor (Q -factor) of an AFM cantilever is a dimensionless parameter that describes the damping coefficient of the cantilever. It characterizes the bandwidth of the resonance curve $[A(f)]$ relative to its resonant frequency (f_0). A higher Q -factor indicates a low rate of energy loss relative to the stored energy of the oscillator (or cantilever).[109] The Q -factor of the cantilever is defined as the ratio between the

cantilever's resonant frequency and its frequency change. It is measured directly from the resonance frequency curves, recorded here using a lock-in amplifier, see figure 3.11 and 3.13, using:

$$Q = \frac{f_0}{\text{FWHM}} = \frac{f_0}{f_b - f_a}. \quad (3.14)$$

In air, the Q -factor of the cantilever can reach several hundreds. However, in vacuum, due to the decrease of viscous friction, the Q -factor can be on the order of 10^4 .

Amplitude changes, used for imaging in AM-AFM, occur at a timescale of:

$$\tau_{AM} \approx \frac{2Q}{f_0}. \quad (3.15)$$

Although using high Q -factor cantilevers in AM-AFM reduces noise, they consequently make imaging slow. For example, in UHV with a Q -factor cantilever ($Q \sim 50,000$) at a resonant frequency of 50 kHz, a reliable amplitude measurement will take 2 seconds, making slope detection unsuitable for most vacuum applications.

The FM mode has achieved increased sensitivity through the use of higher Q -factor cantilevers without any restrictions on bandwidth. As in the case for AM-AFM, tip-sample interactions cause changes to the resonance frequency of the cantilever and in FM-AFM the resonance frequency is directly measured to produce an image. Unlike AM-AFM, the timescale for changes in the eigenfrequency of the cantilever in FM-AFM does not depend on the Q -factor and responds according to:

$$\tau_{FM} \approx \frac{1}{f_0}. \quad (3.16)$$

Therefore, high Q -factor cantilevers, and consequently high scan rates, can be used in FM-AFM.[110]

3.1.3 Frequency Modulation Atomic Force Microscopy (FM-AFM)

Frequency modulation AFM has proven to be a more accurate way of controlling and thereby minimizing probe-sample forces. Unlike tapping mode, it relies on instantaneous changes in the cantilever oscillation (its resonance frequency) and it allows a clear separation between elastic and dissipative interactions.[110] It is the method of choice for AFM in ultrahigh vacuum, where atomic resolution has been achieved on many different surfaces.[98]

Furthermore, as described above, the cantilever oscillates at its resonant frequency with a constant amplitude, A_0 . A feedback loop generates the driving signal of the

cantilever oscillation. The a.c. signal coming from the cantilever motion detector is amplified, phase shifted and then used as the excitation signal. The amplification is adjusted by an automatic gain control (AGC) to keep the vibrational amplitude constant (see block diagram of FM-AFM in figure 3.3). The topographical images in FM-AFM represent a map of constant frequency shift over the surface. This is because during the scan, the tip-sample distance is varied in order to achieve a set value for Δf . The measured frequency variation Δf_1 at the first resonance frequency of the cantilever f_1 is approximately proportional to the force gradient given by:

$$\frac{\Delta f_1}{f_1} = \sqrt{1 + \frac{1}{C} \cdot \frac{\delta F}{\delta z}} - 1 \approx \frac{1}{2k} \frac{\delta F}{\delta z}, \quad (3.17)$$

where F is the force acting on the cantilever and k is the cantilever spring constant.[98, 111, 112] The minimum force gradient detectable in FM-AFM, shown by Albrecht et al.[110], depends on the cantilever parameters (stiffness k and quality factor Q) and the detection bandwidth B , and is given by:

$$F'_{min} = \left. \frac{\delta F}{\delta z} \right|_{min} = \sqrt{\frac{4k(k_B T)B}{2\pi f_0 Q A_0^2}}, \quad (3.18)$$

where A_0^2 is the mean-square amplitude of the driven cantilever vibration and $k_B T$ is the thermal energy at temperature T . B is the FM detector bandwidth (in our case, ≈ 2 kHz), which is given by Carson's rule:

$$B \approx 2(\Delta + f_{max\ mod}), \quad (3.19)$$

where Δ is the deviation of the frequency setpoint and $f_{max\ mod}$ is the maximum modulation frequency.[113] Practically, B is a measure of the scanning speed, in which a small B implies long acquisition times. For example, a $10\text{ nm} \times 10\text{ nm}$ image with 512×512 pixels at a scan speed of $40\text{ nm} \cdot \text{s}^{-1}$ (4 lines per second), implies $B = 4 \times 512 \sim 10^3$ Hz bandwidth. This shows that essentially, AM and FM modes have the same sensitivity with the same set of parameters. However, in FM mode, the sensitivity can be increased by using high Q -factor cantilevers.

As seen in figure 3.3, there are two fundamental feedback systems in FM-AFM, amplitude and frequency regulation electronic feedback loops. The amplitude regulation feedback loop maintains a constant vibrational amplitude of the AFM cantilever. On the other hand, the frequency regulation feedback loop tracks and maintains a constant frequency shift by adjusting the z-position of the AFM tip. The frequency shift is the difference between the cantilever's oscillation frequency and the user-defined setpoint

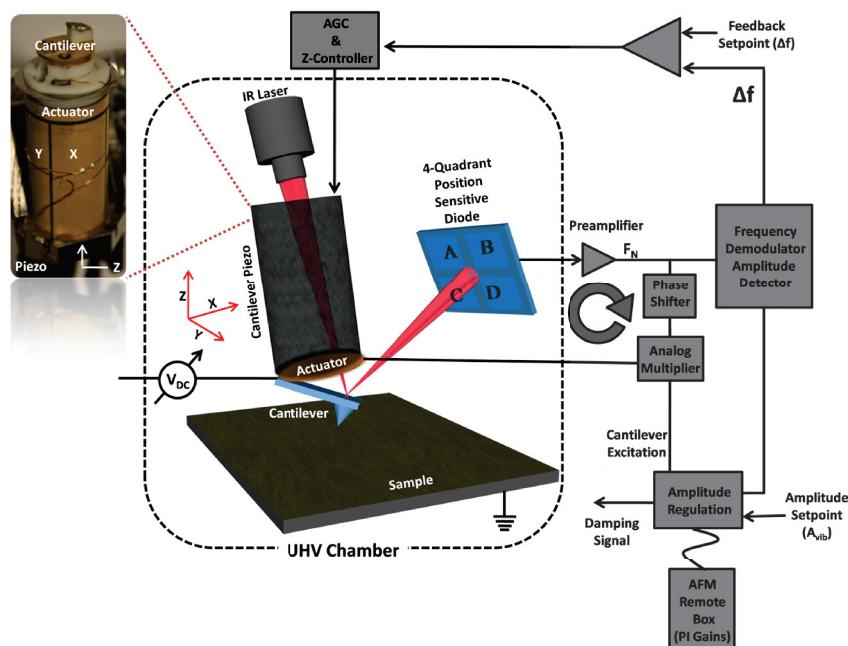


FIGURE 3.3: Omicron VT AFM schematic, refer to Figure 3.4 for more details to the beam deflection principles.

frequency. As discussed in more detail in the next section, the oscillation of the cantilever is monitored by the movement of a laser that is reflected onto a position sensitive diode (PSD). After which, a pre-amplifier amplifies the signal from the PSD where the amplitude signal of the cantilever's oscillation feeds directly into the amplitude regulation feedback loop. The amplitude regulation feedback loop consists of a positive feedback amplifier, a phase shifter, and proportional/integral output gains. These are used to detect an amplitude peak and subsequently generate an excitation signal for the cantilever's oscillation. The frequency regulation feedback loop consists of a multiplier, band pass filter (455 kHz) and frequency demodulator, where an intermittent frequency method is used for frequency evaluation.

Vibrational Amplitude As Giessibl stated in [11], there are six parameters needed to characterize an FM-AFM experiment:

- (a) the spring constant of the cantilever k ,
- (b) the eigenfrequency of the cantilever f_0 ,
- (c) the quality factor of the cantilever Q ,
- (d) the oscillation (or vibrational) amplitude A_0 (A_{vib}),
- (e) the frequency shift of the cantilever Δf ,
- (f) the bias voltage between the tip and sample V_{ts} .

It has been shown for a wide range of experimental conditions that two of the key parameters, listed in section 3.1.3, that are freely chosen; the oscillation amplitude A_0 and

the frequency shift Δf , may in fact be combined into what has been termed the ‘normalized frequency shift’ for oscillation amplitudes that are large compared to the range of the tip-sample force ($A \gg \gamma$), implicating that the tip should only interact mainly with short-ranged forces (close to the surface). Whereas for small amplitudes, the frequency shift is independent of the vibrational amplitude. Instead, it is proportional to the tip-sample force gradient. The normalized frequency shift parameter is in many ways a more useful physical quantity by which to compare experiments, since it essentially provides a standardized measure of how close the tip approaches to the sample. The normalized frequency shift γ [98] is defined as:

$$\gamma(z, A) = \frac{kA^{3/2}}{f_0} \Delta f(z, A). \quad (3.20)$$

It is also a useful nondestructive method for calibrating the cantilever’s physical oscillation amplitude with respect to the electrical excitation applied to the piezoelectric actuator, since, as mentioned, it provides a “fixed point” against which the physical position of the tip may be measured as the oscillation amplitude is varied.[114]

However, a second method was also used to determine the physical cantilever amplitude, based on calculating the amplitude from the PSD setpoint for the Omicron VT AFM from:

$$A_{vib} = 2l_{CL} \tan\left(\frac{2\pi}{360} \frac{A_{PSD}}{52I_{tot}}\right), \quad (3.21)$$

where l_{CL} , A_{PSD} , and I_{tot} is the length of the cantilever in nm (determined from the manufacturer in table 3.2, amplitude from the PSD in volts, and the total intensity of the PSD in volts, respectively. Both A_{PSD} and I_{tot} can be user-controlled through Omicron Matrix software.

3.1.3.1 Beam Deflection

The first AFM used by Binnig and coworkers, used an STM tip on the backside of the cantilever to measure deflections.[95] While this method was potentially sensitive, it was practically problematic. The most widely used method to measure the deflection of the cantilever is by detecting a laser beam reflected off the back of the cantilever onto a position sensitive diode (PSD). In the beam deflection setup, used in this thesis, the deflection of the cantilever is tracked by a continuous wave (cw) infrared laser (830 nm), at a power < 7 mW. An optical fiber passes the beam through the base flange, threading through the scanner piezo tube, and up to the AFM stage, where it hits the cantilever such that it is deflected onto a four quadrant position sensitive photo diode, as seen

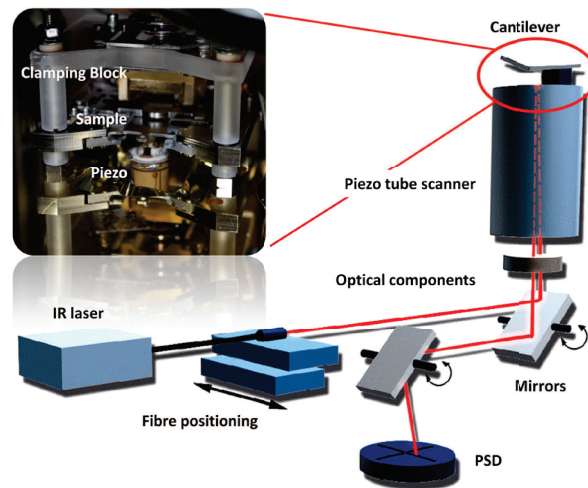


FIGURE 3.4: Working principle of the Omicron beam deflection AFM. Clamping block is used for low temperature studies with a cooling sample holder. Please note: sample is facing down. Basis for image modified from Omicron¹.

in 3.4¹, at maximum intensity. The laser beam position is adjusted by controlling the coarse and fine movements of two mirrors. The PSD yields various different signals, a normal force signal, F_N , moves the reflected beam vertically and a lateral force signal, F_L , moves the reflected beam horizontally across the PSD. These signals are adjusted according to cantilever specifications, because the manufacturing tolerances allow a rather large variation in the vertical positioning F_N . In addition, large area photodiodes typically have a bandwidth limitation and in our system the limitation of the PSD is approximately 500 kHz.

3.1.3.2 Self-Oscillation Loop

The scheme for our Omicron VT-AFM employs an analogue electronic system, involving self-excitation, automatic gain control (AGC), a FM demodulator and a phase shifter.[112] The output of the phase shifter that follows AGC is used as an excitation signal of the cantilever in order to properly track the resonance frequency. If the phase shift ϕ between the mechanical excitation generated at the actuator is $\phi = \pi/2$ (as seen in figure 3.5), the loop oscillates at $f = f_0$. Thus, a change in the resonance frequency Δf and the control signal of the AGC as a measure of tip-sample dissipation can be observed.[115] The self excitation setup has a high intrinsic stability for stochastic changes of the tip-sample force due to instabilities of the positions of the atoms involved in the tip-sample interaction. However, the self excitation setup has limitations concerning noise, particularly when using small amplitudes. It is confined

¹Omicron NanoTechnology GmbH www.omicron.de

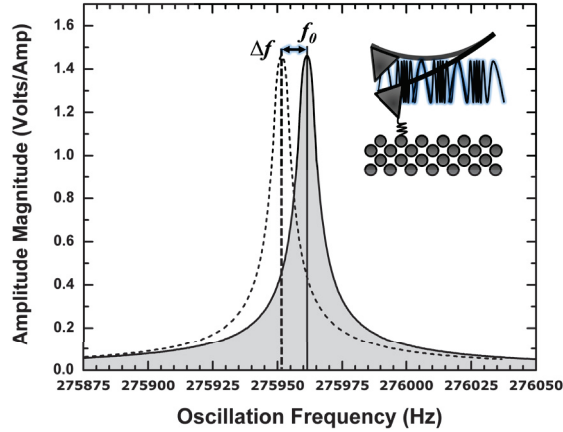


FIGURE 3.5: FM-AFM: by maintaining a constant $-\pi/2$ phase shift between the cantilever and the excitation signal, the resonance frequency of the cantilever under the external force provided by the tip-sample interaction can be tracked.[112]

to excitation of fundamental mode, except if used with an adjustable narrow bandpass filter.[116–118] This is important for application with Kelvin probe force microscopy at the second resonant frequency of the cantilever.[119]

3.1.3.3 Damping Signal

In NC-AFM, dissipative (or damping) forces take place in which a part of the work done by the forces upon the AFM cantilever is lost, ie. converted into heat. Therefore, it is common in NC-AFM imaging to use an additional feedback loop to maintain a constant amplitude of oscillation by modifying the drive signal. In this case, the change in drive signal required to maintain the constant amplitude of the cantilever is often interpreted as being related to the energy dissipated per cycle of the cantilever oscillation [11, 12, 120]:

$$E_{ts} = E_0 \left(\frac{A}{A_0} - \frac{f}{f_0} \right), \quad (3.22)$$

where E_{ts} is the dissipated energy, A and A_0 is the amplitude of the drive signal required to maintain the amplitude setpoint during imaging and far from the sample, respectively. E_0 is the intrinsic damping of the cantilever and is given by:

$$E_0 = \frac{\pi k A^2}{Q}, \quad (3.23)$$

where k and Q are, as before, the normal spring constant of the cantilever and the intrinsic quality factor of the oscillator, and A is the amplitude which is maintained constant. The damping signal value must stay positive, as it is a regenerative loop.[120–123].

3.2 Kelvin Probe Force Microscopy (KPFM)

Sir William Thomson, later known as Lord Kelvin, the renowned Scottish scientist, first postulated the Kelvin method in 1898. He presented a public lecture to the British Institution entitled “*the contact electrification of metals.*”[124] His method was straightforward and simple. Two conducting materials are allowed to come into electrical contact. Any flow of charge from one material to the other is monitored. Lord Kelvin used two large metal plates of zinc and copper and a gold leaf electroscope to demonstrate the surface charging effect. He showed that a potential is generated between the surfaces of two conductors when they are brought into electrical contact. Further modification of his original setup, including the introduction into vacuum, was made in 1932 by William A. Zisman at Harvard University.[125] Zisman mounted a vibrating reference tip over a surface. He noticed that as the tip vibrates the output voltage varies periodically. The peak-to-peak measured voltage depends upon the difference between the contact potential and the external voltage. The major improvement of this new method is that the surfaces do not need to touch each other. Therefore, only very weak electric fields are required, which are not likely to influence the electrical or chemical structure of the material. Over a century later, Lord Kelvin’s original idea is a widely used method for material research.

Kelvin probe force microscopy (KPFM) was introduced as a noncontact variant of AFM in 1991 by Nonnenmacher et al.[126] Differing from Zisman’s method, KPFM is a scanning probe technique where the potential offset arising from a capacitance between a probe tip and a surface can be measured, instead of measuring the current. Since the AFM tip provides only a small area, the resulting currents would be too small for a reasonable detection. The tip, when in close vicinity of the surface, is used as a reference electrode that forms a capacitor with the surface as it is scanned over it. The capacitance junction forms a drop in potential, called the contact potential difference (CPD).

KPFM is often used to measure the work function of the surface of materials with high spatial resolution.[127] The concept of work function (ϕ), in its simplest definition, is defined as the minimal amount of energy needed to remove an electron from its electronic ground state within a given material. In a metal, the work function ϕ , as described by the free electron model, is defined as the difference in energy of an electron in the vacuum state and an electron at the Fermi energy, as seen figure 3.6(a). In materials such as semiconductors and insulators, the work function ϕ is regarded as the difference in energy of an electron in the vacuum state and in the most loosely bound electrons in the solid.[101, 128]

A modulating bias voltage, V_{ac} , plus a DC voltage, V_{dc} , is applied between the cantilever and the surface.

$$V_{bias} = V_{dc} + V_{ac} \sin(\omega t). \quad (3.24)$$

As the tip approaches the sample, the total potential difference between the tip and the sample is expressed by:

$$V_{ts} = (V_{dc} \pm V_{CPD}) + V_{ac} \sin(\omega t). \quad (3.25)$$

The difference (\pm) is dependant upon whether the bias (V_{dc}) is applied either to the sample (+) or to the tip (-).[129] In order to derive an expression for the electrostatic force between the tip and the sample, we assume a parallel plate capacitor geometry (other geometries can be considered, but require more complicated models, such as that described by Nony et al. for atomic contrast KPFM [130]), in which the energy is expressed by:

$$V_C = \frac{1}{2} C_{ts} \Delta V_{ts}^2. \quad (3.26)$$

where C_{ts} is the capacitance between the tip and surface, which is influenced by the geometry of the tip and surface.[104, 131] The modulation bias, V_{ac} , generates oscillating electrical forces. The V_{dc} nullifies the resulting oscillating electrical forces that originates from the contact potential difference (CPD) between the tip and surface. The resulting electrostatic force can be written as:

$$\begin{aligned} F_{es}(t) &= \frac{\delta V_C}{\delta z} \\ &= \frac{1}{2} \frac{\delta C_{ts}}{\delta z} V_{ts}^2 \\ &= \frac{1}{2} \frac{\delta C_{ts}}{\delta z} [(V_{dc} \pm V_{CPD}) + V_{ac} \sin(\omega t)]^2, \end{aligned} \quad (3.27)$$

Subsequently, the electrostatic forces can be expanded into three spectral components [132], as follows:

$$F_{dc} = \frac{\delta C_{ts}}{\delta z} \left[\frac{1}{2} (V_{dc} \pm V_{CPD})^2 + \frac{V_{ac}^2}{4} \right] \quad (3.28)$$

$$F_{\omega} = \frac{\delta C_{ts}}{\delta z} (V_{dc} \pm V_{CPD}) V_{ac} \sin(\omega t) \quad (3.29)$$

$$F_{\omega_2} = \frac{\delta C_{ts}}{\delta z} \frac{V_{ac}^2}{4} \cos(2\omega t). \quad (3.30)$$

By compensating the contact potential, in which $V_{dc} = V_{CPD}$, the first harmonic F_{ω} nullifies the electrostatic force, with a frequency at ω , and is used to measure the CPD. Consequently, the dc part of the force, F_{dc} , is proportional to V_{ac}^2 resulting in a minimal static force and a constant bending of the cantilever. The second harmonic contains the

capacitance gradient $\delta C_{ts}/\delta z$ and can therefore be used to perform capacitance spectroscopy at ω_2 . [133, 134]

However, KPFM directly measures the contact potential difference (CPD) between the conductive AFM cantilever and the sample. When the bias V_{dc} is applied to the tip, the relationship between the CPD and the work function is defined as:

$$V_{CPD} = \frac{\phi_{tip} - \phi_{sample}}{|e|}, \quad (3.31)$$

where ϕ_{tip} and ϕ_{sample} are the work functions of the tip and sample, respectively, and e is the electronic charge (-1.60219×10^{-19} C).

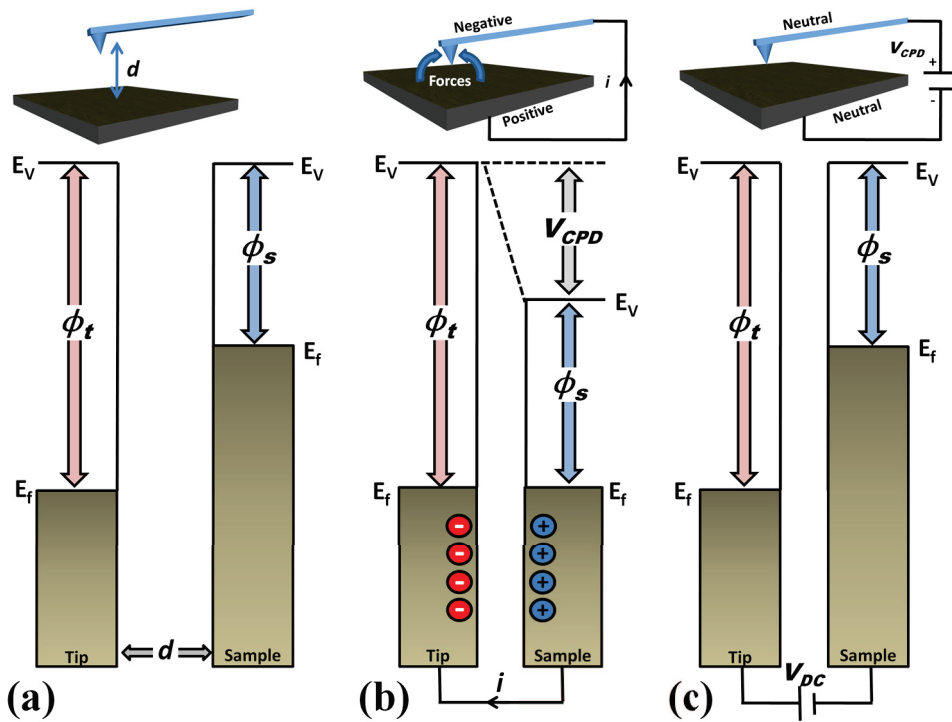


FIGURE 3.6: Energy levels of the sample and AFM tip for three cases: (a) the tip and sample are separated at a distance d with no electrical contact, (b) the tip and is in electrical contact with the sample, and (c) an external bias (V_{DC}) is applied between the AFM tip and sample in order to nullify the CPD and, therefore, the tip-sample force. E_v and E_f are the vacuum energy levels and the Fermi energy levels of the sample and tip, respectively.

The basic principle of KPFM relies on when an AFM tip is brought close to the sample surface. In which case, due to the differences in their Fermi energy levels, an electrical force is generated between the AFM tip and the sample surface. Figure 3.6 shows the energy level diagram of the tip and sample surface when ϕ_{tip} is greater than ϕ_{sample} . Figure 3.6(a) depicts the energy levels of the tip and sample surface when separated at a distance d . In this case, they are not electrically connected and the vacuum levels

are aligned but the Fermi energy levels are different. When the tip and sample surface are close, equilibrium requires the Fermi levels to line-up. Upon electrical contact, the Fermi levels will align through electron current flow. The system will reach an equilibrium state, as depicted in Figure 3.6(b). Both the tip and the sample surface will be charged. Here the Fermi energy levels of the tip and the sample are aligned but the vacuum energy levels are no longer the same. This forms a V_{CPD} between the tip and sample. This results in an electrical force that acts on the contact area between the tip and sample, due to the V_{CPD} . As shown in figure 3.6(c), this force is thereby nullified by applying an external bias (V_{dc}) with the same magnitude as the V_{CPD} but with an opposite charge. This applied voltage eliminates the surface charge. The applied external bias (V_{dc}) used to nullify the electrical force (due to the V_{CPD}) is proportional to the work function difference between the AFM tip and sample.

Lift-mode Operation Practically, KPFM can be operated in two ways: lift-mode and single-pass mode. In lift-mode KPFM, the measurements of the topography and CPD are separated by scanning over the surface in two distinct tracing steps, usually in ambient conditions. The first trace measures the sample topography, while the second trace measures the CPD, thus minimizing any cross-talk effects between their signals. During the second trace, the tip is lifted up over the same line at a preset lift height distance from the sample surface. Normally the set lift height is in the range of 10–50 nm. Thus, the CPD measurements are based on long-range electrostatic forces. The mechanical driving signal is turned off so that the cantilever is driven by an external bias, equation 3.24, where V_{ac} is usually 2–5 V. Most lift-mode KPFM configurations set the electrical driving frequency ω_e to the resonant or mechanical driving ω_m frequency used in the first trace. However, the two-pass technique requires twice more time for imaging. Another disadvantage is that a remote position of the probe is needed during the second pass. This reduces the resolution and sensitivity of electric imaging. Furthermore, by working in air, adsorbates contaminate the surface, resulting in a modified work function.[135]

However, topography and electrostatic measurements can be made simultaneously in the single scan operational mode. This approach has definite advantages compared to the lift-mode or two-pass mode: the improved sensitivity, higher spatial and energy resolution and a reduced experiment time. Additionally, to obtain absolute work function values, operation in ultrahigh vacuum (UHV) is essential. Within the single pass mode, the CPD can be measured using two different techniques: frequency modulation (FM-KPFM) and amplitude modulation (AM-KPFM). The electrostatic force can be detected either via $\Delta f(\omega_1)$ in the frequency modulation or $A(\omega_2)$ in the amplitude modulation mode, as described hereafter.

3.2.1 Electrostatic Force detection using AM or FM KPFM

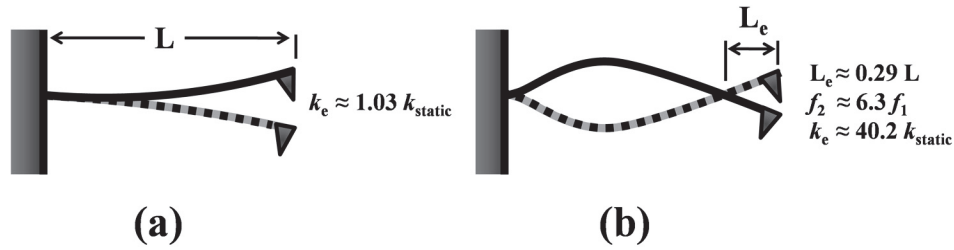


FIGURE 3.7: Predicted geometry, effective length, effective static stiffness, and resonant frequency for the first (a) and second (b) flexural modes of a rectangular cantilever, excluding effects associated with the mass and position of the cantilever tip.[12]

The UHV-KPFM was developed by Kikukawa et al. in 1995.[136, 137] AM mode KPFM measures the electrostatic force F_{es} directly from the amplitude of the cantilever oscillation at the second resonance frequency ω_2 (seen above in figure 3.7) induced by V_{CPD} and V_{ac} . The second resonance frequency peak is used for CPD measurement because the sensitivity of the potential measurement is improved at the ac frequency ω_2 . [138] A vibration amplitude-frequency characteristic of a cantilever used for AM-KPFM including the second resonance frequency f_2 is shown in figure 3.13. Typically, the second resonance peak is broader than the first and the amplitude and Q -factor is less than one-third. The less sensitive resonance frequency shift, due to forces acting upon the cantilever, also occurs at the second frequency. Thus the first resonance is employed for tip height control and the second for CPD measurement.[137] The limiting factor in the AM mode is the bandwidth of the photodiode used for detection of the cantilever oscillations. Due to the maximum bandwidth of approximately 500 kHz in our setup, as previously described in section 3.1.3.1, the stiffest cantilevers used in the AM mode have a first resonance frequency in the range of 60–80 kHz. Therefore, due to cantilever geometry, the second resonance frequency is in the range of 380–450 kHz, where $f_2 \approx 6.3 f_1$.

A block diagram of the KPFM schematic within the FM-AFM scheme is shown in figure 3.8. In the AM mode, the normal force signal F_N passes through a band pass filter, where it is separated into two. The low frequency goes to the z regulator for the topography imaging. The high frequency (CPD measurements) is fed directly into the lock-in amplifier. After which, the lock-in amplifier reference signal voltage output (OSC out) is used to apply V_{ac} to the tip. The signal is subsequently fed to the Kelvin probe control unit (KPCU), where it measures the CPD and applies a V_{dc} offset to nullify the lock-in output signal.

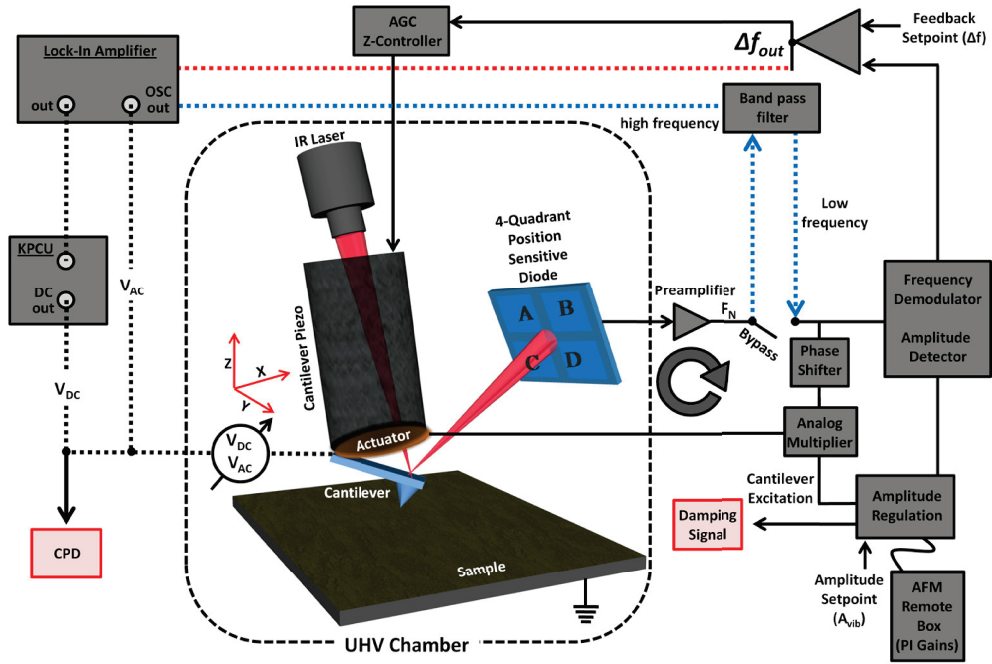


FIGURE 3.8: Schematic diagram showing FM (red) and AM (blue) KPFM modes within an FM-AFM system, as shown in figure 3.3.

In the FM mode, the applied ac voltage V_{ac} induces a modulation of the electrostatic force. This is detected by the oscillation at ω of the frequency variation of f_1 . In order to reduce crosstalk, the topographical signal is separated from the V_{CPD} measurement by modulating V_{ac} at a higher frequency, on the order of several kHz, than the bandwidth of the topography feedback.[139, 140] The measured signal is approximately proportional to the force gradient, deduced from equations 3.17 and 3.29, in which:

$$\begin{aligned} \Delta f_1(\omega) &\propto \frac{\delta F_\omega}{\delta z} \\ &= \frac{\delta^2 C}{\delta z^2} (V_{dc} - V_{CPD}) \times V_{ac} \sin(\omega t), \end{aligned} \quad (3.32)$$

in which the frequency ω is chosen in an appropriate range. The lower limit is dictated by an increasing cross-talk to the topography signal in which the tip-sample distance oscillates at ω . The upper limit is dictated by the bandwidth of the frequency demodulator.[138]

Glatzel et al. plotted the amplitude at ω of the oscillation of Δf_1 and the oscillation of the piezo-voltage U_z , that controls the tip-sample distance, seen in figure 3.9. It is clear that with increasing frequency ω the cross-talk with the topography signal decreases but also the signal intensity of the electrostatic force decreases due to the restricted bandwidth of the frequency demodulator.[138] Typically, modulation frequencies are used

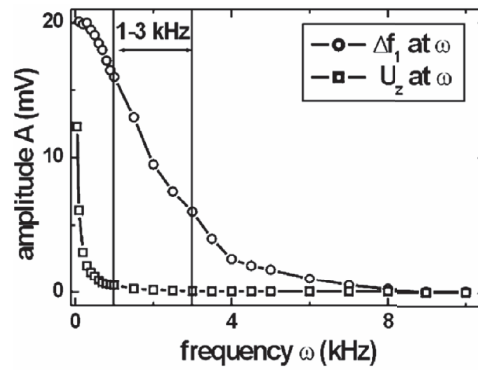


FIGURE 3.9: Restrictions in FM-KPFM. Dependence of the frequency shift Δf_1 and the height control signal of the topography U_z at the frequency ω of the ac voltage. Taken from [138] where the measurements were obtained with a Park Scientific Instruments' Si cantilever on a HOPG substrate.

in the range of 1–3 kHz. Glatzel concludes that this behavior is independent of the type of cantilever.

3.2.2 AM vs. FM KPFM

Since ac voltages contribute quadratically to the topography signal (see equation 3.28) and on semiconducting samples a voltage induced band-bending is possible [141], ac voltages as low as possible are used. In the AM mode, the main benefit of using the second resonant detection is the very high sensitivity even using a modulation bias V_{ac} as low as 100 mV peak-to-peak. While in the FM mode, ac voltages of 2 V peak-to-peak are necessary for sufficient sensitivity.

Theoretically, the AM-KPFM spatial resolution is not as high as in FM-KPFM, because in FM-KPFM the frequency shift of the cantilever oscillation is used to detect the force gradient.[138, 142] In AM-KPFM, long range interactions from the sample causes an electrostatic interaction both on the tip and the cantilever. As a result, the averaging effect from the tip and cantilever reduces the spatial resolution of AM-KPFM. However, AM-KPFM has been demonstrated to record atomic scale resolution [143], suggesting that short-range interaction forces become significant in both modes of KPFM at the nanometer regime. Therefore, the spatial resolution limitation of AM-KPFM is the same as FM-KPFM.[130] This will be discussed in detail in chapter 4.

The force gradient (used in FM-KPFM) has a shorter detection range than the force itself (used in AM-KPFM), as seen in the inter-atomic force distance curve in figure 3.2. In the attractive regime, the force gradient (which is the derivative of the force distance curve) becomes larger when inter-atomic distance is small. However, as the tip-surface

distance increases, the force gradient becomes insignificant. Therefore, most of the detection in the FM mode takes place at the tip apex, suggesting that the detection of the electrostatic force gradient is short-ranged detection. Therefore, in theory, the spatial resolution in the FM mode is approximately equal to the dimension of the tip apex.

Furthermore, in AM-KPFM the energy resolution of V_{CPD} is higher than in FM mode. Measurements in the AM mode detect V_{CPD} from the resonance peak of the oscillating cantilever. This greatly enhances the signal-to-noise ratio [130, 141], with a typical energy resolution of 5 meV.

Contrary to AM mode, FM-KPFM does not rely on soft cantilevers, but allows the use of stiff cantilevers with spring constants in the range of several tens of N/m. The decreased sensitivity of stiff cantilevers is partially compensated by the possibility to approach closer to the surface where the force gradient is larger. Furthermore, stiffer cantilevers provide a more stable topographical imaging.[142] Meanwhile, the energy resolution is usually a few 10 meV and the scan speed is limited by a rather large noise signal as compared to the AM mode (in most cases, a 20 dB damping plug is needed to reduce input amplitude due to a lock-in overload).

	Frequency Modulation	Amplitude Modulation
V_{ac} [138, 144, 145]	2 V	100 mV
f_{mod} [138, 144, 145]	1–3 kHz	$=f_2$
Cantilever Force Constant	$42 \text{ N}\cdot\text{m}^{-1}$	$2.8 \text{ N}\cdot\text{m}^{-1}$
Energy Resolution[138, 145]	$\geq 10 \text{ meV}$	5 meV
Spatial Resolution[130, 146]	\approx tip apex	same as FM

TABLE 3.1: A comparison of the principle parameters and achievable resolutions in FM and AM KPFM. Sub-nanometer spatial resolution of both FM and AM KPFM is observed in [145, 146, 146].

Table 3.1 lists the principal parameters and achievable resolutions in AM and FM KPFM. The force constant of the cantilever in AM-KPFM is governed by bandwidth limitation of the PSD. Also, the modulation frequency f_{mod} in FM-KPFM is governed by the bandwidth limitation of the frequency demodulator.

3.2.3 Cantilevers

For this thesis, four types of cantilevers were primarily used. The characteristics from the manufacturer are displayed in table 3.2. A scanning electron microscope (SEM) was used to image the cantilever and tip apex of the SSS and PtIr₅ coated cantilevers, the types used in this thesis, see figure 3.10 and 3.12.

Mode	Type	Length (μm)	Width (μm)	Force Constant ($\text{N}\cdot\text{m}^{-1}$)	Resonance Frequency (Hz)	Tip Radius (nm)
NC-AFM Topography	SSS	125 ± 5	30 ± 5	21 – 78, 42	250 – 390, 320	<5, 2
		225 ± 10	28 ± 7.5	0.5 – 9.5, 2.8	45 – 115, 75	
FM-KPFM	PtIr ₅ *	125 ± 10	30 ± 7.5	10 – 130, 42	204 – 497, 330	<35
AM-KPFM	coated Si	225 ± 10	28 ± 7.5	0.5 – 9.5, 2.8	45 – 115, 75	

TABLE 3.2: Cantilever characteristics from NanosensorsTM with **red numbers** indicating nominal values. Additionally, the thickness of SSS and PtIr₅ cantilevers are ~ 4 and $3 \mu\text{m}$, respectively. *25 nm thick double layer of chromium and PtIr₅ on both sides of the cantilever.

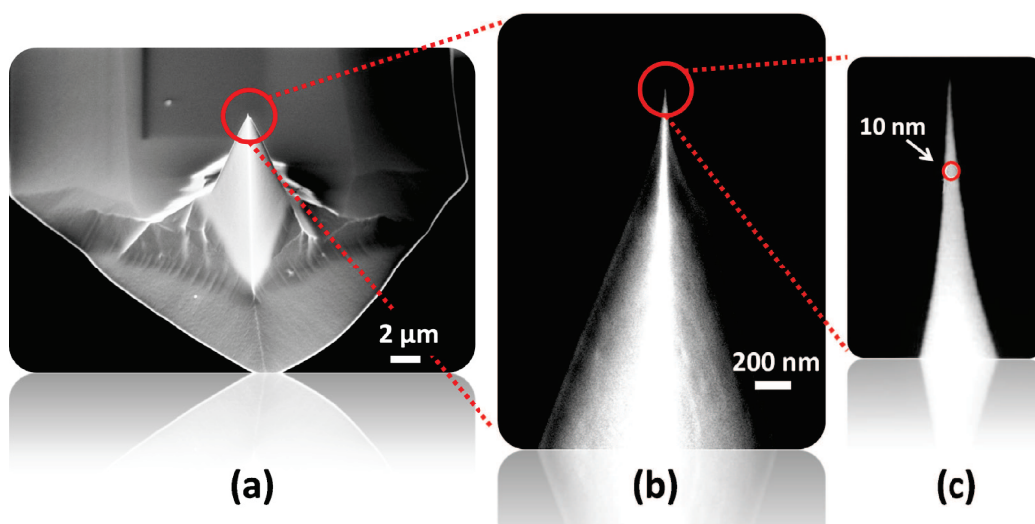


FIGURE 3.10: SEM image of Nanosensor's Super Sharp Si cantilever (a), zoom of the tip (b), and tip apex (c), with the red circle indicating 10 nm diameter. Image (c) reproduced from NanosensorsTM.

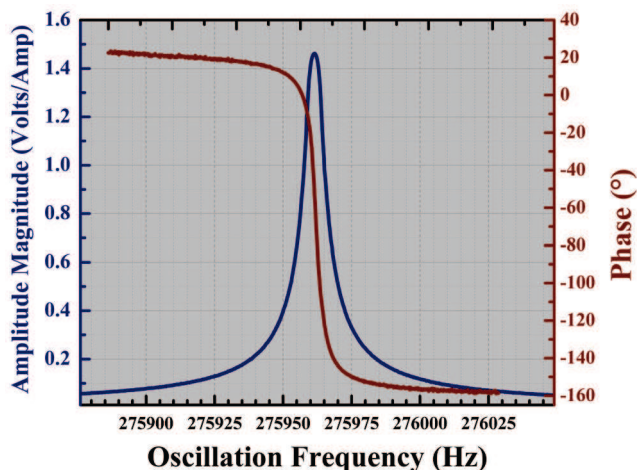


FIGURE 3.11: Resonance frequency curve and phase for a SSS tip. The Q-factor was measured using equation 3.14. $Q \simeq 35,000$.

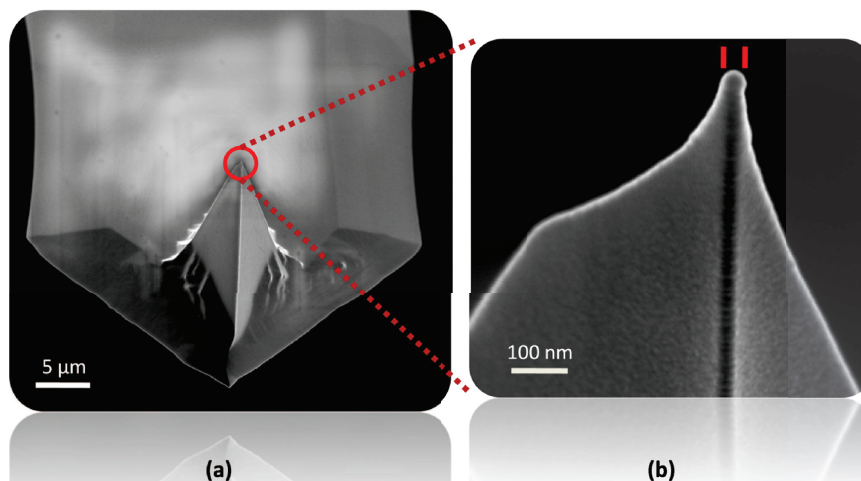


FIGURE 3.12: SEM image of Nanosensor's PtIr₅ coated Si cantilever (a) and zoom of the tip apex (b) with a 32 nm diameter, indicated by the red bars.

Tip Preparation The PtIr₅ coated Si cantilevers, purchased from Nanosensors, were used for KPFM measurements as conductive tips were mandatory for high resolution imaging.[144, 147] AFM tip preparation was performed *in-situ* in a separate UHV chamber following a similar procedure to those reported for high resolution AFM and KPFM.[147] PtIr₅ coated Si tips, used for KPFM, were thermally annealed at 300°C for 3 hours. Super sharp Si (SSS) tips were treated by combining argon sputtering, the apparatus seen in figure 3.19, at ~5 keV for 15 minutes and subsequently thermally annealed 300°C for 3 hours, suggesting that the oxide layer was completely desorbed.[148, 149]

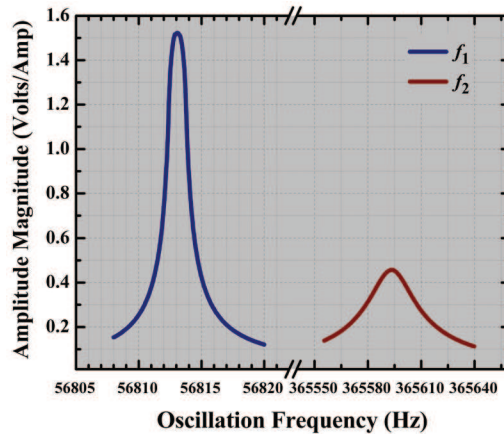


FIGURE 3.13: First, $f_1 = 56,813$ Hz, (a) and second, $f_2 = 365,593$ Hz, (b) resonance curves for a PtIr₅ tip. The Q-factor was measured using equation 3.14.

$$Q_{f_1} \simeq 32,000, \quad Q_{f_2} \simeq 11,000.$$

3.3 Photoelectron Spectroscopy (PES)

In this thesis, photoelectron spectroscopy (PES), sometimes referred to as photoemission spectroscopy, was used in conjunction with KPFM for quantitative measurements of samples. PES allows a comparative measurement of the work function ϕ_s through ultraviolet photoelectron spectroscopy (UPS) and analysis of surface composition (including surface contaminants) through x-ray photoelectron spectroscopy (XPS), which is also called electron spectroscopy for chemical analysis (ESCA).

The phenomenon of photoemission was first detected in 1887 by Heinrich Hertz.[150] Hertz observed and then showed that electrodes illuminated with ultraviolet light create electric sparks more easily. In the following years, experiments were refined to explain the nature of photoemission, such as the thorough investigation by Philipp Lenard in 1902 when he observed that the energy of individual emitted electrons increased with the frequency.[151]. In 1905, Einstein was able to explain their systematics by invoking the quantum nature of light.[152, 153]

The photons of a light beam have a characteristic energy determined by the frequency of the light. When radiation with energy $E = h\nu$, where h is Planck's constant and ν is the frequency of radiation, is incident on a metal surface, photoelectrons are produced, provided that $h\nu \geq \phi_s$, where ϕ_s is the work function of the sample.[154] If the photon energy is too low, the electron has insufficient kinetic energy to overcome the work function of the sample. Increasing the intensity of the light beam increases the number of photons in the light beam, and thus increases the number of electrons excited. However, the energy that each electron possesses is not affected. The electrons emitted have a characteristic energy that does not depend on the intensity of the incoming light,

but only on the energy or frequency of the individual photons. If the sample is at earth potential, electrons ejected from a state with binding energy E_b are emitted from the sample with a true kinetic energy E_k given by:

$$E_k = h\nu - E_b - \phi_s, \quad (3.33)$$

where ϕ_s is the work function of the sample. A schematic spectrum of electrons ejected by X-rays or UV radiation is shown in figure 3.15. The energy distribution of the emitted electrons has a high and low energy cutoff regions. The low energy cut off is at $E_k = \phi_s$, as described above. The high energy cut off occurs when electrons are ejected from the Fermi energy, where E_b is defined to be zero (at $E_k = h\nu - \phi_s$).

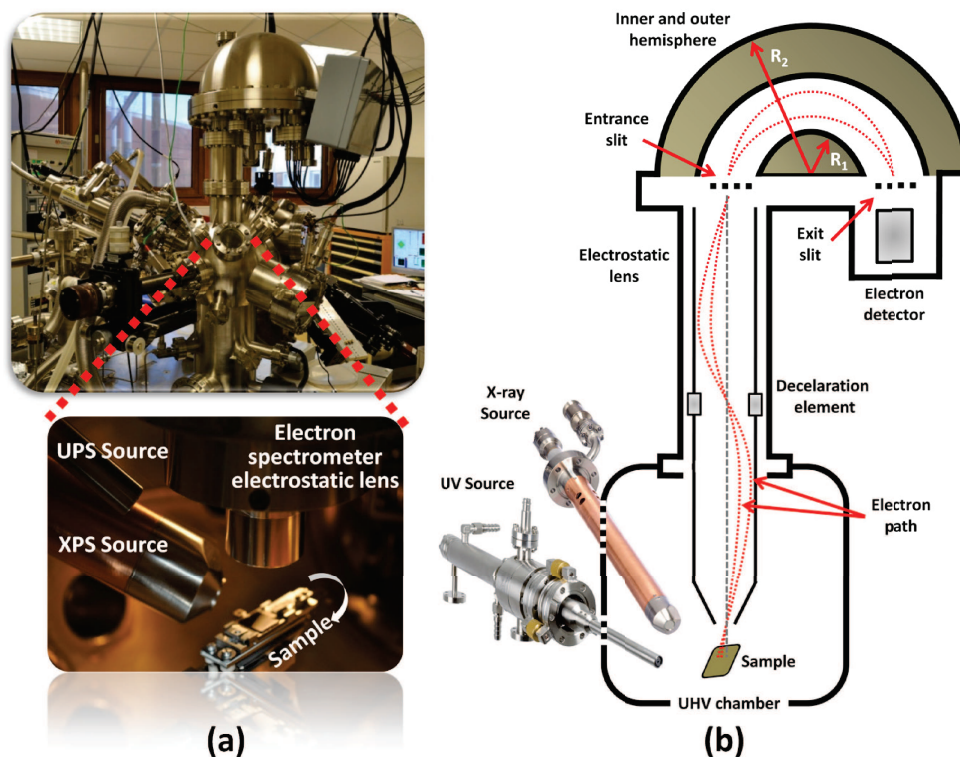


FIGURE 3.14: Image of the Omicron EA 125 electron spectrometer setup and through the view-port within the UHV chamber showing a tiltable sample (a) and schematic diagram of the concentric hemispherical analyzer (CHA) with an Omicron DAR 400 twin-anode high intensity x-ray source and HIS 13 ultraviolet photon source (b).

The emitted electrons pass through the first lens element and then are retarded by an amount R , determined by lens voltage, before entering the analyzer. The lenses enable two operating modes: constant retard ratio (CRR) and constant analysis energy (CAE). In the CAE mode, the electric field in the analyzer, and thus the analyzer pass energy, is kept constant, and a variable retarding voltage is applied to the deceleration element

in the transfer lens of the concentric hemispherical analyzer (CHA), seen in figure 3.14. In this way, only electrons that leave the sample with a certain energy E are allowed to pass through the analyzer before they can be detected. By recording the number of detected electrons as a function of the retarding voltage the electron spectrum is obtained. Alternatively, with CRR mode, the electrons are slowed down by an amount which a constant ratio of the electron energy to be analyzed. The retard ratio, k , is defined as:

$$k \approx \frac{E_k}{E_p}, \quad (3.34)$$

where E_p is the pass energy. Since the spatial divergence of the electron trajectories in the analyzer increases with decreasing pass energy, the energy resolution in the CRR mode is proportional to the detected energy, whereas in the CAE mode the energy resolution is constant over the entire spectrum. In other words, the CRR mode gives constant resolving power and the CAE mode gives constant energy resolution.[155]

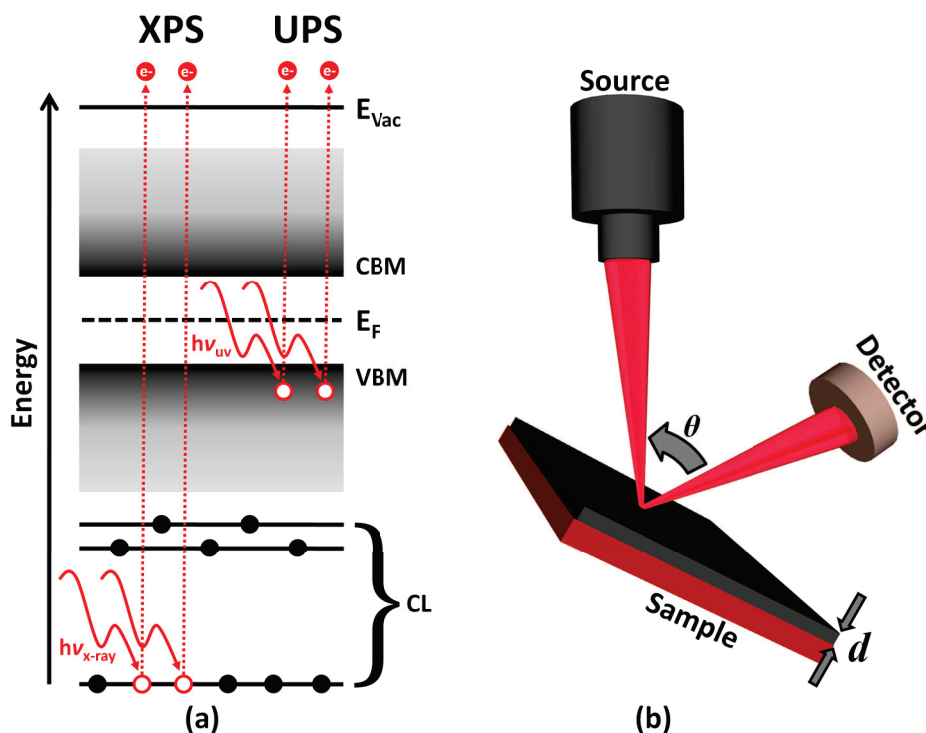


FIGURE 3.15: Schematic representation of the processes involved in XPS and UPS: (a) x-ray and ultraviolet photons kick out an electron in the core level (CL) and valence band, respectively, and (b) a pictorial schematic displaying an increase near-surface sensitivity for the escape depth, d , based on the IMFP λ , of electrons by adjusting the tilt of the sample, θ , according to equation 3.36. VBM: Valence band maximum. CBM: Conduction band minimum.

The analyzer is a band pass filter, where only electrons with energy very near to the pass energy E_p are transmitted, which are then stopped in the detector. Therefore, electrons which have been transmitted by the analyzer with a retardation R have a kinetic

energy of:

$$E_k = R + E_p + \phi_a = h\nu - E_b, \quad (3.35)$$

where ϕ_a is the work function of the analyzer, with a typical value in the range of 4.2–4.8 eV. In this work, the work function of the analyzer was calibrated using a clean Au(111) surface, $\phi_{\text{Au}} = 5.3$ eV so that $\phi_{\text{analyzer}} \approx 4.28$ eV. Note that this is independent of the sample work function ϕ_s . [155]

Angle Resolved PES (AR-PES) Additionally, the photocurrent, produced from photons from a PES experiment that impinge upon a surface, is a function of the depth (relative to the surface) within a sample. Neglecting elastic scattering events, the electron inelastic mean free path (IMFP) can be defined as the distance over which the probability of an electron escaping without a significant energy loss drops to e^{-1} of its original value. Therefore, the photocurrent can be described as:

$$I = I_0 e^{\left(\frac{-d}{\lambda \cos(\theta)}\right)} \quad (3.36)$$

where λ is the electron IMFP within the material, θ is the take-off angle measured from the sample normal, I_0 is the incident current and d is the escape depth, as seen in figure 3.15. For a given electron energy, varying the emission angle changes the effective mean escape depth. So as the emission angle (θ) is increased, $\cos(\theta)$ decreases, the analyzed region becomes more surface localized and the surface sensitivity is increased. This can also be used to determine the thickness of a deposited thin film (provided that the spectra are acquired before and after deposition of the deposited film). [154, 156, 157] Typically, for a photon energy of about 1400 eV (used in XPS) impinging the surface at 90° , ejected electrons from depths greater than 10 nm have a low probability of leaving the surface without undergoing through an energy loss event. Therefore, if escaped and subsequently detected, they would contribute to the background signal rather than well defined peaks. [158]

An example of an angle-resolved XPS spectra on a Si(100) substrate, with the native oxide intact, is shown in figure 3.16. The two peaks shown are for Si 2p surface oxide (left, ~ 104 eV) and the elemental Si substrate peak (right, ~ 100 eV). It is clear that data recorded at $\sim 45^\circ$ favors the surface oxide layer, while at $\sim 90^\circ$ the elemental substrate is dominate. [158]

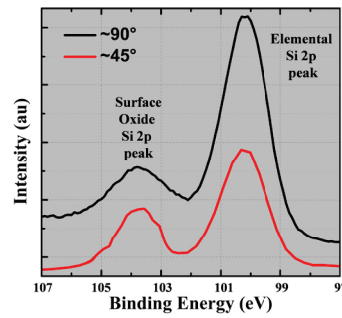


FIGURE 3.16: Angle resolved Si 2p spectra showing an increase in near-surface sensitivity for the escape depth, d , of electrons by adjusting the tilt of the sample, θ , according to equation 3.36.

Concentric Hemispherical Analyzer (CHA) The actual selection of the electron energy or speed is done through an electrostatic analyzer, in this thesis a concentric hemispherical analyzer (CHA). In a CHA, an electrostatic field is applied between an inner and outer hemispheres. Electrons injected through the entrance slit tangentially to the median hemispherical surface with an energy equal to that of the pass energy, are transferred from the entrance slit to the detector. They then describe a circular trajectory within the median hemispherical surface. The potential difference between the hemispheres determines the pass energy. The voltages on the inner and outer hemispheres are given by:

$$V_{inner} = E_p \left(2 \frac{R_0}{R_1} - 1 \right) \quad (3.37)$$

$$V_{outer} = E_p \left(2 \frac{R_0}{R_2} - 1 \right) \quad (3.38)$$

where R_0 is the median radius of the electron orbit and R_1 and R_2 are the radius of curvature for the inner and outer hemispheres, respectively, as seen in figure 3.14. The radius and the width of the slits at the analyzer entrance and exit determines the energy resolution of the CHA. Electrons are transferred from the sample to the entrance slit via electrostatic lens. The electron optics in the transfer lens assembly also contain an element that retards or accelerates electrons of a given energy to the pass energy.[155, 157, 159] Typical parameters for XPS and UPS measurements are given in table 3.3.

A variety of photon sources are used in PES studies, comprising the standard Mg $K\alpha$ / Al $K\alpha$ twin anode laboratory source (used in this thesis and shown in the Figure 3.14), monochromated anode sources, UV lamps, or synchrotron light sources.[160] Depending on the source of excited radiation, PES is also called ultraviolet photoelectron spectroscopy (UPS) or x-ray photoelectron spectroscopy (XPS) (electron spectroscopy for

Technique	Pass Energy, E_p (eV)	Effective* slit width (mm)	Kinetic Energy range, E_k (eV)	Calculated analyser resolution, ΔE (eV)	Step size (eV)	Dwell time (s)
XPS Broadscan	50	6	100 – 1500	1.5	0.5	0.2
XPS Narrowscan	20	6	20	0.6	0.05	0.5
UPS Fermi Edge	5	1	0.5	0.03	0.002	1

TABLE 3.3: Analyzer operating parameters and resolution. *Average of both the entrance and exit slit widths.

chemical analysis (ESCA)[161]).

3.3.1 Ultraviolet Photoelectron Spectroscopy (UPS)

Ultraviolet photoelectron spectroscopy (UPS) refers to the measurement of the kinetic energy spectra of photoelectrons ejected from a material by the ultraviolet photons. UPS was developed by David Turner at Imperial College in the 1960's, after the development of XPS.[162] Using a Helium lamp emitting at $h\nu=21.22$ eV (He I radiation) or $h\nu=40.8$ eV (He II radiation), only photoelectrons emitted from the valence band or shallow core levels are accessible, as seen in figure 3.15. Therefore, deep core electron levels cannot be excited. Although it can be used to study band structure, in this thesis, it is dedicated as a comparative measurement technique to KPFM to quantify the work function of the material.[163] UPS measures the lowest work function patch on the surface, even it is only a small fraction of the surface.[164] The work function is calculated from the UPS spectrum by subtracting the energy of the incident beam from the difference between the Fermi edge and the low-energy cut-off of secondary electrons.[165, 166] From the UPS spectra, one can calculate the work function of the sample by:

$$\phi_s = h\nu - (E_s - E_f), \quad (3.39)$$

where E_s and E_f is the energy of the secondary electron cutoff and the Fermi energy, respectively.

Vacuum Ultraviolet (VUV) Source The high intensity UV source (HIS 13) provided by Omicron is principally a cold cathode capillary discharge lamp. There is a windowless connection between the discharge area and the target sample within the UHV

chamber, as seen in figure 3.14(a). The discharge current is electronically stabilized and the lamp is water cooled to allow for a high discharge current (up to 300 mA). When a potential is applied to the ends of an insulating tube, filled with highly pure He gas (99.999 %) at a pressure of about 1 mbar, a spontaneous breakthrough occurs leading to continuous discharge. Additionally, due to the source being continuously pumped with gas, a differential pumping system is needed in order to maintain a pressure in the range of 10^{-9} to 10^{-10} mbar when the lamp is in operation. The differential pumping system requires the use of 3 oil based roughing rotary pumps and 2 turbomolecular pumps.

3.3.2 X-Ray Photoelectron Spectroscopy (XPS)

X-ray photoelectron spectroscopy (XPS) is used in research, development and manufacturing. This technique is able to obtain the chemical composition of various material surfaces up to 1 nm depth. Most of the elements can be detected except hydrogen. XPS was developed in the mid 1960's by K. Siegbahn and his research group in Uppsala, Sweden.[161] K. Siegbahn was awarded the Nobel Prize for Physics in 1981 for his work in XPS. For every element, there is a characteristic binding energy associated with each core atomic orbital, so that each element will give rise to a characteristic set of peaks in the photoelectron spectrum at kinetic energies (or corresponding binding energies) determined by the photon energy. Therefore, peaks at particular energies indicate the presence of a specific element in the sample under study. A database of the energies of many photoelectron and Auger-electron spectral lines is available from the National Institute of Standards and Technology (NIST)².

X-ray Source The Omicron DAR 400 twin-anode high intensity x-ray source, shown in the Figure 3.14, contains an Al/Mg twin-anode which is bombarded by electrons emitted from a filament that is held at ground potential. The anode is positively biased up to ~ 15 keV, in this way accelerating nearby electrons towards it. These electrons produce core holes in the anode target, either from an Al $K\alpha$ ($E_x = 1486.6$ eV, FWHM = 0.85 eV) or Mg $K\alpha$ ($E_x = 1253.6$ eV, FWHM = 0.7 eV) target material, by electron impact ionization. The vacancies can relax by emission of characteristic x-rays that illuminate the sample. The observed line width is a consequence of the different x-ray lines contributing. A thin Al-window prevents secondary and backscattered electrons to reach the sample. Since considerable power is dissipated in the anode (100–1000 W), the anode needs to be water cooled and must therefore be a good heat conductor (e.g. a metal). The anode top is silver coated to prevent Cu x-rays ghost lines from complicating the spectra when the anode material gets thin over time.

²National Institute of Standards and Technology (NIST) X-ray Photoelectron Spectroscopy Database srdata.nist.gov/xps

3.4 Equipment Summary

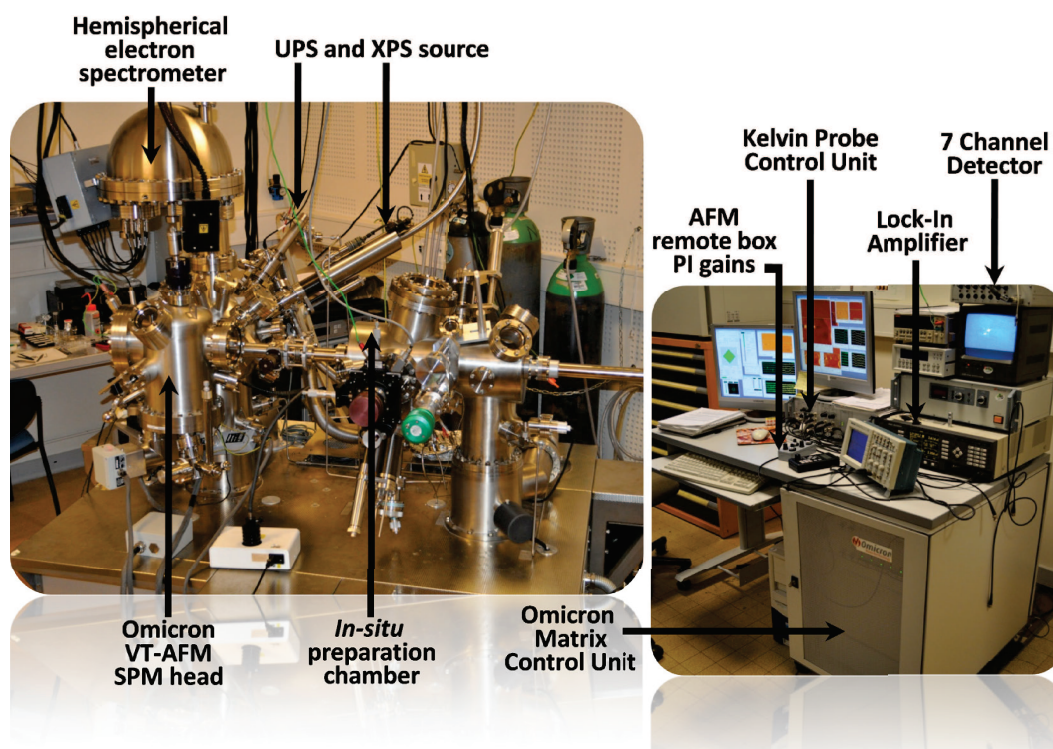


FIGURE 3.17: Omicron ultrahigh vacuum scanning probe microscope setup.

Omicron VT SPM The Omicron VT SPM is a commercial UHV microscope capable of both STM and AFM operation. An image of the UHV setup and control computers is shown in figure 3.17, combined *in-situ* with XPS and UPS analysis, as well as sample annealing. It is capable of covering a temperature range from 25 K to 1500 K, and uses dedicated sample plates for different temperature ranges, as seen in figure 3.18(c). The scanner tube has a scan range (*xyz*) of $10\ \mu\text{m} \times 10\ \mu\text{m} \times 1.5\ \mu\text{m}$. The tips are exchangeable *in-situ*. It uses remote controlled mirror motors for beam adjustment and a position sensitive photo diode detector. Operation modes include contact mode with normal force/lateral force detection and non-contact modes (NC-AFM, KPFM). It is also equipped with a long focal length optical microscope for sensor navigation. It is vibrational isolated using an internal eddy current damping system.

Most of the work in this thesis was carried out using standard $15\ \text{mm} \times 18\ \text{mm}$ stainless steel sample plate, which allows a maximum sample size of approximately $11\ \text{mm} \times 11\ \text{mm}$. All cantilevers were mounted on an exchangeable tip carrier, as seen in figure 3.18. The SPM was controlled using an Omicron Matrix control unit, a multi-processor modular unit. Data management was performed using Omicron vernissage software, and data treatment was performed using WSxM software.[167]

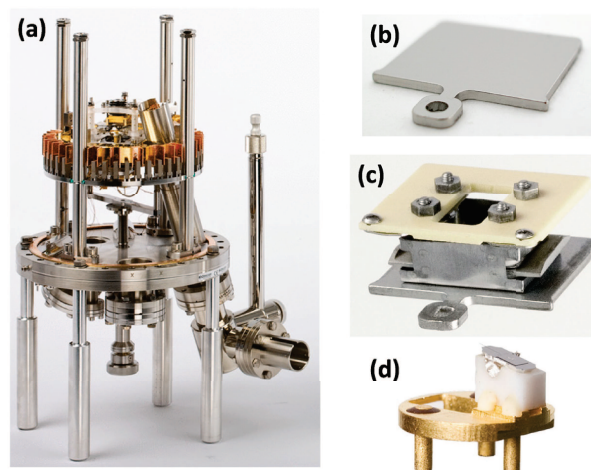


FIGURE 3.18: Omicron VT SPM with eddy current vibration isolation system (a), standard 15 mm \times 18 mm stainless steel sample plate (b), VT sample plate with modified top plate for temperature readout at the sample (c), and a cantilever mounted on an exchangeable tip carrier (d). All images taken from Omicron².

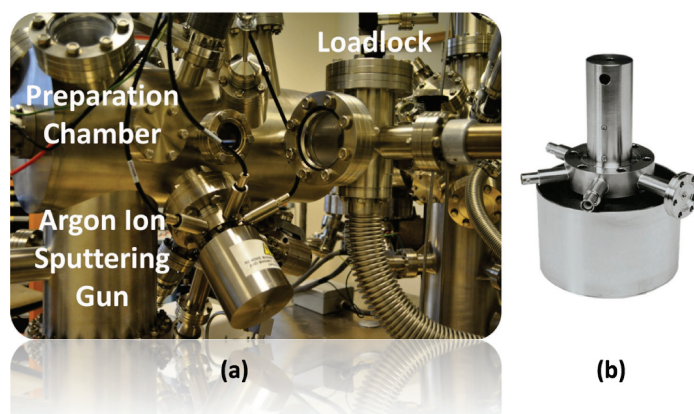


FIGURE 3.19: Image of the loadlock, preparation chamber and Argon ion sputtering gun setup (a). Image from Omicron² of the ISE 5, used as the Argon sputtering source.

3.4.1 Ultra-High Vacuum (UHV)

In order to achieve sufficient vacuum for UHV SPM operation, various pumps were used, as seen in table 3.4. Samples were placed into the loadlock, seen in figure 3.19, which was first pumped with a rotary roughing pump and a turbomolecular pump in order to bring the vacuum down to $\sim 10^{-8}$ mbar, in which case the sample was transferred into the preparation chamber. A turbomolecular pump employs multiple stages of rotors

to give gas enough momentum to guide it to the exhaust, thus creating a vacuum capable of pressures down to $\sim 10^{-8}$ mbar. The preparation and analysis chambers were pumped down to UHV using both an ion and titanium sublimation pump. An ion pump works by ionizing gases within a strong potential field, between 3–7 kV, in order to accelerate them into a solid cathode. Thus, a net pumping action is created capable of reaching pressures down to $\sim 10^{-11}$ mbar. An ion pump is important for use with scanning probe microscopy because there are no moving parts and there is no need for oil. Therefore, they are clean and low-maintenance, and most importantly, produce no vibration. However, over some time, due to the operational mechanism of an ion pump, a fraction of the energetic gas molecules are able to escape the cathode. Thus, the vacuum degrades over time. Therefore, in order to maintain UHV, especially throughout the course of several months where no break in UHV is required, a titanium sublimation pump (TSP) is employed. A TSP is simply a titanium filament placed just above the ion pump within both chambers, close to bare chamber walls. When a sufficiently high current, typically ~ 48 Amps, passes through the filament, titanium is sublimated into the chamber. The gaseous titanium atoms have a very short mean free path within the vacuum and are deposited onto the nearby chamber walls. The clean thin film of titanium on the chamber walls is highly reactive. When the residual gases within the chamber, including hydrogen but not noble gases, come into contact with the titanium on the chamber walls, they react to form a stable product. Typically, in our setup, a clean film of titanium was deposited every 32 hours. Thus, a net pumping action is achieved capable of pressures as low as in the high 10^{-12} mbar range. Additionally, both of the TSPs in our setup consist of 3 filaments, due to the finite lifetime of the filament.[159, 168] Table 3.4 summarizes types of pumps needed to achieve the corresponding pressure.

	Pressure (mbar)	Pump
Atmospheric pressure	1,013.25	...
Medium vacuum	$\geq 10^{-3}$	Roughing pump
High vacuum	$\geq 10^{-9}$	Turbomolecular pump
Ultra-high vacuum	$\geq 10^{-12}$	Ion pump and Titanium sublimation pump

TABLE 3.4: Common vacuum levels and pump needed to achieve it.

KPFM on Bulk Heterojunctions:

Surface Photovoltage & Space Charge Region

KPFM on Bulk Heterojunctions Review

Results on a Nano-Phase Segregated P3HT:PCBM OPV

Ce chapitre présente les résultats obtenus par microscopie à sonde de Kelvin sur des couches minces optimisées du tandem photovoltaïque P3HT:PCBM présentant une séparation de phase aux échelles nanométriques. Nous montrerons qu'une image claire des deux réseaux interpénétrés formés par les matériaux donneur et accepteur d'électrons peut être obtenue en combinant la topographie au signal de dissipation. Nous expliquerons comment nous avons pu mettre en évidence de manière directe la photo-génération des porteurs aux interfaces donneur-accepteur, en réalisant des images du potentiel de surface avec une résolution nanométrique, et en comparant les contrastes obtenus dans le noir et sous éclairage.

In this chapter, Kelvin probe force microscopy has been applied to a high efficient nanoscale phase segregated photovoltaic blend of P3HT:PCBM. Topography and damping images reveal the surface morphology of the interpenetrated network, clearly resolving each component of the blend. Direct visualization of the of the carrier generation at the donor-acceptor interface has been accomplished by resolving KPFM images of the blend in dark and under illumination at the nanoscale.

Nowadays, a great deal of attention is focused on organic solar cells with the goal of making them a competitive low cost alternative to conventional silicon-based photovoltaic devices.[2, 3] While organic photovoltaic device performances have undoubtedly improved, silicon-based cells still remain the most affordable, performance-efficient forms of solar energy conversion on the market today. Despite their fundamental difference in the charge-generation processes, there are many key operational concepts that can be used to describe the operation of silicon-based and organic photovoltaic devices. In the following, two key concepts are briefly introduced: the surface photovoltage and the space charge region.

4.1 Surface Photovoltage (SPV)

The surface photovoltage (SPV) can be defined as the change of potential of a semiconducting surface due to charge carriers generation under illumination. Illumination-induced changes in the surface potential can be analyzed using the conventional contactless Kelvin probe.[169, 170] More recently, Kelvin probe force microscopy has been applied for local investigations of the SPV both in the case of inorganic and organic semiconducting thin films and devices. SPV in photovoltaic blends is defined as the processes of photon absorption and exciton dissociation and the presence of opposite charges in the electron acceptor and donor phases which leads to local changes in surface potential (SP). As the work function of the metallic AFM tip does not change under illumination and therefore, the surface photovoltage [169–171] is deduced from:

$$\begin{aligned}
 |e| \cdot V_{\text{CPD(Light)}} &= \phi_{\text{tip}} - \phi_{\text{sample(Light)}} \\
 |e| \cdot V_{\text{CPD(Dark)}} &= \phi_{\text{tip}} - \phi_{\text{sample(Dark)}} \\
 \phi_{\text{sample(Light)}} - \phi_{\text{sample(Dark)}} &= V_{\text{CPD(Dark)}} - V_{\text{CPD(Light)}} \cdot |e| \\
 \Rightarrow \text{SPV} &= \Delta\phi_{\text{sample(Light-Dark)}}.
 \end{aligned} \tag{4.1}$$

KPFM is nowadays widely applied to investigate the SPV of various kinds of semiconductors and devices. As an example, it has been used to gain a deeper insight in the work function modification induced by surface states. In the case of CGSe thin films, Glatzel et al. showed that the work function differs for untreated, annealed, and sputtered samples, revealing the influence of surface states on the local electronic properties.[172] Combining SPV and KPFM is highly useful to quantify the band bending resulting from surface states, and determine the best surface preparation procedure.

Space Charge Region (SCR) In semiconductor physics the space charge region (also referred to as the depletion region) is an insulating region where the mobile charge

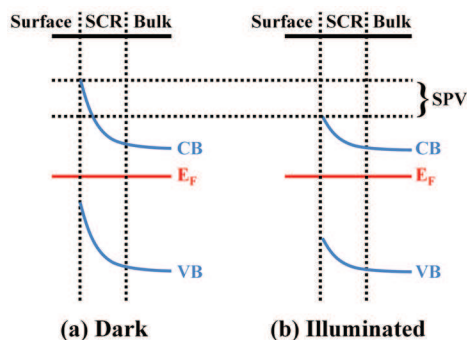


FIGURE 4.1: Two energy band diagrams illustrating SPV. In dark (a), surface defects cause the formation of a space charge region (SCR) where the conduction band that is the origin of majority carriers is bent away from the Fermi level at the surface. Under illumination (b), the influx of minority carriers screens surface charges and flattens the bands. The SPV is the change in potential at the surface due to illumination. Image recreated from Alison Chaiken at HP Laboratory.

carriers have diffused away or been forced away by an electric field. In response to the varying electric field in that region, band bending is closely associated to that phenomenon, seen in figure 4.1. The SCR can be used to describe the physics at the surface of a thin film or at the interfaces between two different semiconductors. In the first case, the electric field in the SCR causes excess electrons to be swept away from the surface. This serves to reduce the density of surface trapped electrons and decreases the band-bending.[169] Within a solar cell, it is generally regarded as the area between the p and n doped materials (or in organic photovoltaics, the donor and acceptor materials).[173] According to Brabec et al., efficient charge separation in an OPV occurs close to the donor-acceptor (D/A) interface, either within the exciton diffusion path or within the space charge region, due to the molecular nature of the heterojunction. Therefore, photoexcited states created far from the D/A interface recombine prior to diffusing to the heterojunction.[174]

4.2 KPFM on organic solar cells

Understanding the relationship between local film morphology, processing parameters, and device performance is critical if efficiencies are to be improved. A wide range of characterization techniques can provide complementary information about the effects of processing on the BHJ film morphology that paints different sections to the overall picture. KPFM is a powerful noncontact technique for studying these systems, especially the band offset, electronic surface properties, and transport properties at the surface. KPFM provides a noninvasive measurement of the surface potential (SP) distribution in

photovoltaic devices. The SP of a sample is regarded as the work function of the sample by taking into account effects due to the surface polarizability as well as band bending. By analyzing the local potential at donor-acceptor interfaces, KPFM can determine the space charge width with high accuracy.[175–177] Furthermore, in the case of thick organic layers ($d > 100$ nm) the influence of the underlying substrate can normally be neglected.

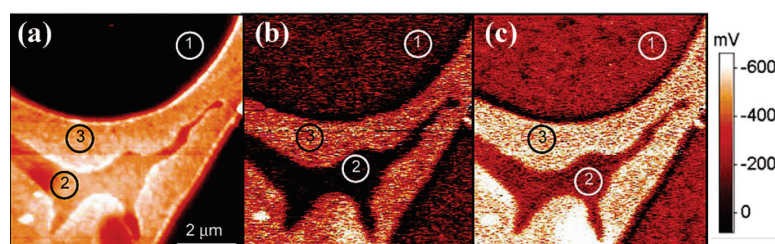


FIGURE 4.2: KPFM images of thin films of F8BT/PFB blends on top of the ITO anode prepared by spin coating in a saturated solvent atmosphere. Topography (a) and surface potential measured in the dark (b) and illuminated with a $7 \text{ mW}\cdot\text{cm}^{-2}$ 473 nm laser (c). Regions marked 1, 2, and 3 are, respectively PFB-rich, “bulk” and “interfacial” F8BT-rich phases. Image adapted from reference [17].

In the past decade, KPFM has been widely applied to investigate BHJ OPVs. Chiesa et al. have investigated all-polymer BHJ solar cells composed of F8BT:PFB¹ donor/acceptor blends, as seen in figure 4.2.[17] By directly showing the presence of a capping layer at the polymer/air interface which blocks the transport of photogenerated electrons to the surface, they suggest that charge trapping effects limit the efficiency of their devices.

Samori and coworkers studied blends of PDI/P3HT² using KPFM in dark and under illumination.[176, 178, 179] Although excitons are generated by light absorption in all the PDI clusters, their results prove that only the ones which are in physical contact with P3HT matrix exhibit an appreciable charge transfer because of the existence of a complementary electron donor phase. In addition, the KPFM results on submonolayer thick polymeric bundles of the electron-accepting PDI wires and bundles of electron-donating P3HT chains was shown to exhibit nanoscale photovoltaic activity.

They have also studied all-thiophene photovoltaic blends, composed of T5OHM³ oligomers as the electron acceptor and P3HT as the electron donor. They performed time resolved measurements revealing the dynamics of charging and discharging within the donor and acceptor domains of the blend.

¹F8BTB: poly-(9,9'-dioctylfluorene-co-benzothiadiazole) / PFB: poly-(9,9'-dioctylfluorene-co-bis-N,N'-(4-butylphenyl)-bis-N,N'-phenyl-1,4-phenylenediamine)

²PDI: perylenebis(dicarboximides) / P3HT: poly(3-hexylthiophene)

³T5OHM: 3''-methyl-4''-hexyl-2,2':5',2'':5'',2''':5''',2''''-quinquethiophene-1'',1''-dioxide

Martens et al. investigated organic BHJ solar cells comprised of MDMO-PPV:PCBM⁴ as the donor/acceptor materials.[180] These investigations showed that the phase separated domains had different electronic properties than the matrix, specifically showing a reduction of the work function of PCBM clusters. PCBM, when compared to the electron donor (in this case MDMO-PPV), is a good electron conductor and a less effective hole conductor. Therefore, PCBM should have a reduced work function under illumination. Hoppe and coworkers have used KPFM in conjunction with SEM to examine the active layers of 1:4 MDMO-PPV:PCBM spincast from chlorobenzene and toluene.[16, 181] Locally resolved SPV measurements, as well as annealing studies, helped to identify the distribution of PCBM and MDMO-PPV in only the toluene-cast films, as seen in figure 4.3.

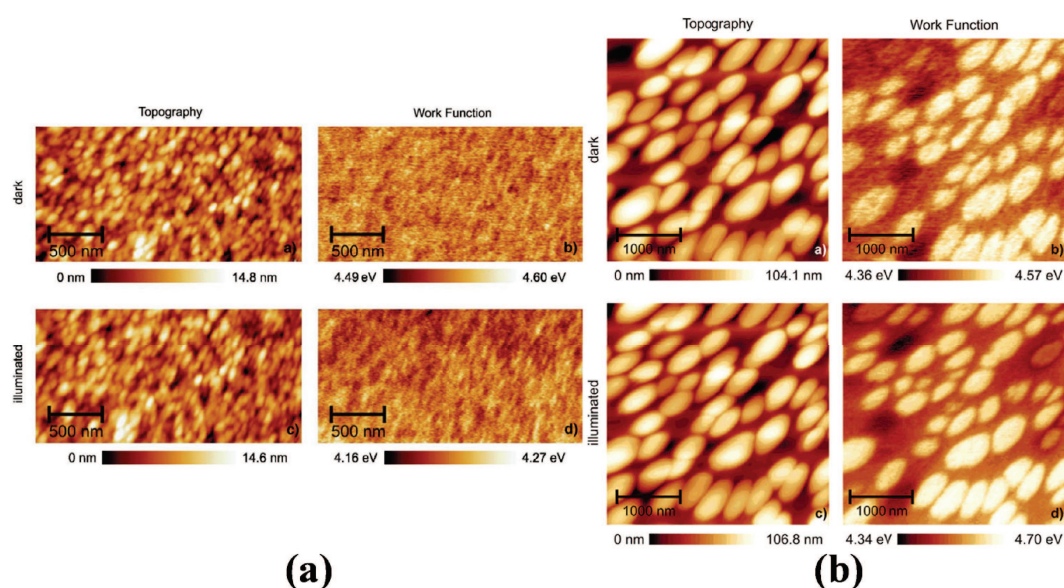


FIGURE 4.3: Topography and work function of a (a) chlorobenzene and a (b) toluene-cast blend film of MDMO-PPV/PCBM, measured in the dark and under 442 nm cw laser illumination. Image adapted from reference [16].

Their results showed that casting from toluene produced a thin layer on top of the film that prevented electron propagation to the electrode. The presence of the polymer skin layer around the fullerene clusters represents a severe loss mechanism of the photocurrent for two reasons: a) electrons, which are accelerated to the top aluminum electrode, have to penetrate this hole-rich layer and suffer recombination and b) holes in the polymer skin, which survive the recombination by the electrons in the polymer skin, would have to travel too far around the fullerene clusters to reach the hole collecting PEDOT:PSS electrode. On the other end, it was impossible to resolve

⁴MDMO-PPV: poly-[2-(3,7-dimethyloctyloxy)-5-methyloxy]- para-phenylene-vinylene / PCBM: [6,6]-phenyl-C₆₁-butyric acid methyl ester

the nanophase segregation in chlorobenzene cast films, neither in the CPD nor in the topography images.[182]

Maturová et al. have studied a similar MDMO-PPV:PCBM system and have found evidence of electron accumulation in both the polymer rich and fullerene phases.[18] Combining their data with a drift device model, they concluded that lateral electron transport can be a limiting process.

Recently, Su and coworkers have characterized hybrid solar cells based on P3HT:TiO₂ nanorod BHJ blends.[183, 184] Unlike Hoppe and coworkers on MDMO-PPV:PCBM BHJs, Su and coworkers conclude that simply changing the processing solvent does not yield better performances. Instead, a change of the surface ligands on the TiO₂ nanorods has a dramatic effect on the power conversion efficiency. Their results indicate that the function of ligands not only assists the separation and transport of charge carriers, but also reduces the recombination of charge carriers very effectively.[184] Likewise, they also conclude that a TiO₂ nanorod layer deposited on top of the active region can selectively collect electrons while blocking holes near the electrode.[183]

Last, Liu et al. have reported results on P3HT:PCBM BHJs incorporating single walled carbon nanotubes (SWCNT) [185, 186] based on a previous report by Su and coworkers on multi-wall CNTs blended within a P3HT film.[187] However, Su and coworkers results made it hard to distinguish the nanotubes from the P3HT matrix because the nanotubes imbedded within the polymer may not have been exposed at the surface. Therefore, Liu et al. have incorporated the SWCNTs by coating them on top of the active layer. Their results indicate that SWCNTs act as an electron donor material, increasing hole mobility when compared to PEDOT:PSS.

In summary, it was shown that KPFM is a useful technique to probe the electronic surface properties of BHJ solar cells and thin films. However, most of these reports have shown that it is difficult to establish a straightforward relation between the molecular energy levels of the donor and acceptor domains and the CPD measured by KPFM. In most cases, band bending effects should be taken into account, which requires an appropriate modeling. So far, a clear picture taking into account band bending both at the organic electrode and at the donor/acceptor interfaces is still missing.

Another issue concerns the current limits of resolution of the KPFM technique when applied to BHJ organic thin films. So far, to the best of our knowledge, the nanophase segregation in optimized samples has not been resolved even when combining nc-AFM and KPFM in UHV. This limited the application of KPFM to case studies, using samples with large scale phase segregation, as in the case of the films studied by Chiesa and coworkers in figure 4.2 [17] and by Hoppe and coworkers in figure 4.3.[16]

4.3 KPFM on an optimized P3HT:PCBM blend

In the field of polymer-based photovoltaic cells, P3HT and PCBM (chemical structure seen in figure 4.4) remain amongst the most studied active tandem materials. In the last 10 years, power-conversion efficiencies (PCE) have been continuously improved, starting from relatively modest PCE values up to approximately 5%, as seen in figure 2.7.[188] Even if some new polymers exhibit much higher performances, P3HT:PCBM remains a benchmark to study the relationship between the morphology and device performances.

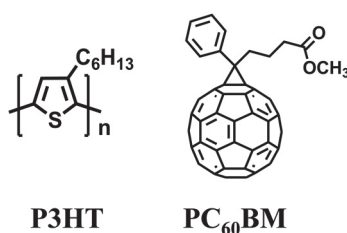


FIGURE 4.4: Chemical structure of P3HT and PC₆₀BM.

4.3.1 P3HT:PCBM BHJ sample preparation and characterization

For this study [189], P3HT:PCBM OPV devices were obtained from Professor Bernard Ratier and coworkers at the Université de Limoges. In order to optimize the sample morphology, Ratier and coworkers varied the concentration of the active layer components in the liquid phase before film deposition.[190] Following that process, they obtained optimized blends exhibiting both slow recombination and high photocurrent generation associated with an overall power conversion efficiency (η_e) of 4.25% under 100 mW·cm⁻² illumination.

Our optimized sample was composed of a 100 nm thick film of P3HT:PCBM blended in a 1:0.8 mass ratio, issued from two solutions in chlorobenzene whose concentration are 30 and 24 mg/mL, respectively. The active layer was spin coated on an indium tin oxide (ITO) coated glass substrate with a 30 nm thick topcoat layer of poly(3,4-ethylenedioxythiophene)-poly(styrenesulfonate) (PEDOT:PSS). The cathode was an aluminum layer (100 nm thick) deposited by vacuum evaporation onto the surface of the P3HT:PCBM film. The sample geometry can be seen in figure 2.9.

A post deposition annealing was performed on the complete device on a hot plate under an inert atmosphere at 100°C for 10 min. The annealing conditions were optimized such that the device performances improved dramatically, consistent with the picture

that better polymer chain ordering within the film allows for higher charge carrier mobility. In other words, the higher cell efficiency is attributed to thermally induced modification of the morphology by inducing P3HT crystallization and improving transport across the active layer-electrode interface.[190]

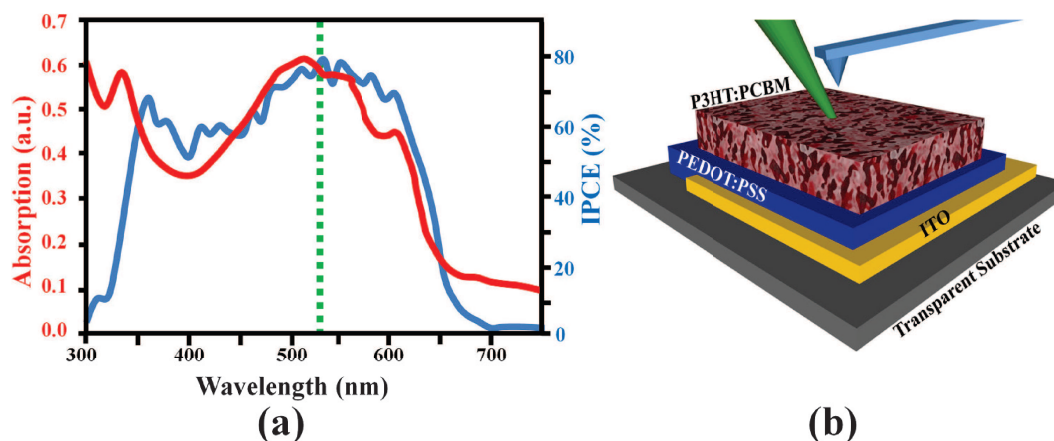


FIGURE 4.5: (a) Absorption spectra (red) and IPCE (blue) of annealed P3HT:PCBM (1:0.8) film at 100°C for 10 minutes. Laser illumination at 532 nm (green-dashed line). Image modified from reference [190]. (b) Experimental schematic depicting KPFM imaging under 532 nm (green) laser illumination.

The absorption spectra of the annealed films revealed peaks at 336 nm, due to the PCBM, and at 512, 554 and 604 nm, due to the P3HT. The incident photon to current efficiency (IPCE) of photo-generated charge carriers are given by the ratio between the number of electrons produced in the outer circuit and that of incident photons. The IPCE increased significantly after annealing and revealed peaks at ca. 540 nm. This indicates a peak charge carrier mobility. Absorption spectra and IPCE measurements, modified from reference [190], are shown in figure 4.5a.

4.3.2 NC-AFM Topography Imaging

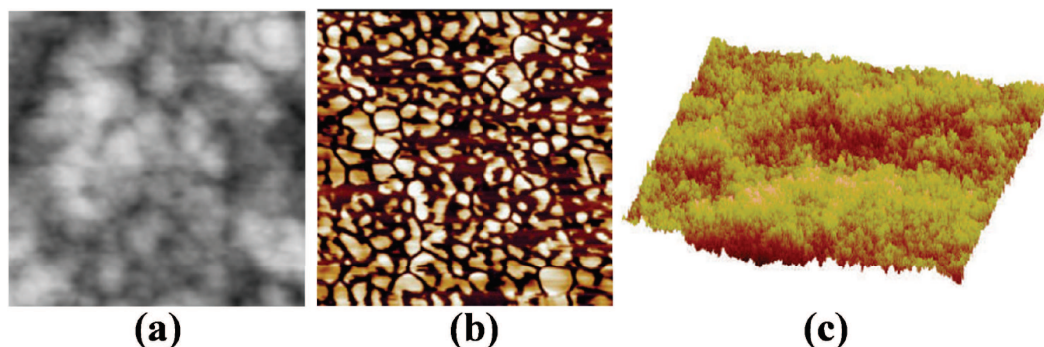


FIGURE 4.6: (a) P3HT/PCBM TM-AFM topography in ambient conditions, modified from reference [190]. (b) P3HT/PCBM TM-AFM phase image in ambient conditions, adapted from reference [5]. Images (a) and (b) $500\text{ nm} \times 500\text{ nm}$. (c) TM-AFM height image of a P3HT/PCBM composite films ($5\text{ }\mu\text{m} \times 5\text{ }\mu\text{m}$), adapted from reference [4].

To the best of our knowledge, few AFM-based reports have been able to clearly resolve the nanoscale morphology of optimized P3HT:PCBM blends. Figure 4.6b is a TM-AFM phase image of an optimized blend by Heeger and coworkers, clearly revealing both components.[5] However, a previous work by Loos and coworkers [68], using electron tomography (a transmission electron microscope based technique) revealed the 3-dimensional nanoscale organization in the photoactive layers, in which the nanoscale networks form high crystalline order and favorable concentration gradients of P3HT and PCBM through the thickness of the photoactive layer, as seen in figure 2.11.

In this work, a comparable level of resolution was achieved by using FM-AFM. A typical FM-AFM image of the P3HT:PCBM surface is shown in figure 4.7 and at higher magnification in figure 4.9a. At the mesoscopic scale, the active layer displays a flat surface with an effective roughness of less than 1 nm, consistent with previous AFM investigations in ambient conditions on this sample.[190] At smaller scales, seen in figure 4.9a, well-defined features are clearly visible emerging from the background in the form of elongated objects with the majority having moderate aspect ratios (typically from 2:1 to 4:1) and lengths from ten to a few tens of nanometers. From the comparison with aforementioned electron-tomography images reported on similar samples [68], we attribute these objects to P3HT nanocrystallites, formed upon the post deposition annealing performed at a moderate temperature. In our case, the mean length of the P3HT nanofibers is smaller than the one previously reported by Loos et al., consistent with the difference in the annealing processes (100°C for 10 min, instead of 130°C for 20 minutes).[68] The UHV FM-AFM image in our report [189] displays a morphology in which the P3HT concentration may be somewhere in between the ones revealed through electron tomography, as seen in figure 4.8.

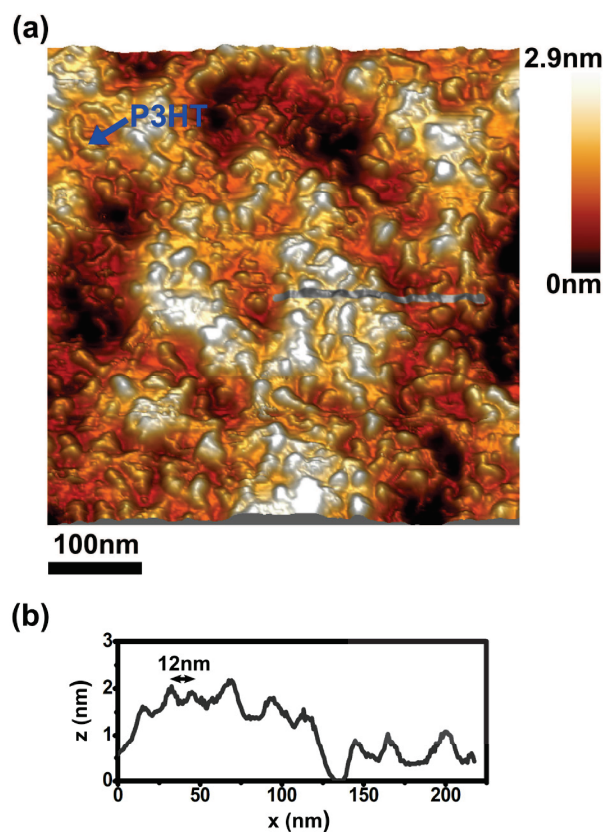


FIGURE 4.7: (a) FM-AFM (UHV, 300K) 3D topographic image ($500\text{ nm}\times 500\text{ nm}$, 600×600 pixels) of the P3HT:PCBM sample ($\Delta f = -19\text{ Hz}$, $A_{vib} = 44\text{ nm}$, scan speed = 50 ms per pixel). The rms roughness is 0.66 nm . (b) Topographic profile from image (a) in which the z -values correspond to the gray line in the image.

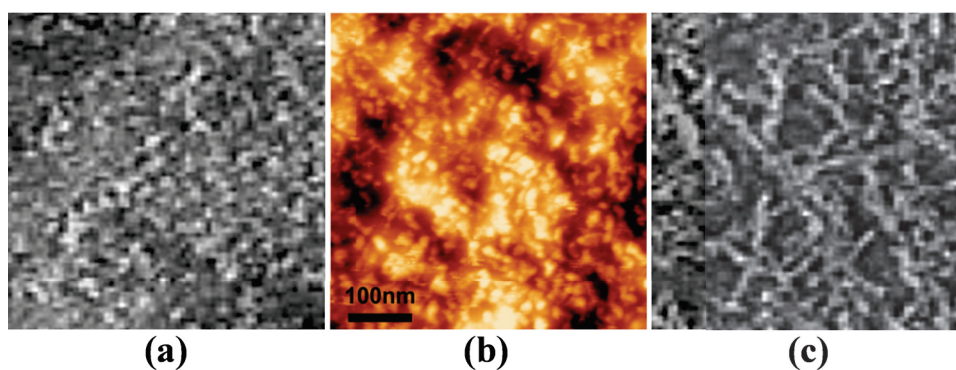


FIGURE 4.8: (a) Electron tomography of a P3HT:PCBM sample close to the surface as spin-casted. (b) FM-AFM (UHV, 300K) 2D topographic image of the P3HT:PCBM sample used in this report ($\Delta f = -19\text{ Hz}$, $A_{vib} = 44\text{ nm}$, scan speed = 50 ms per pixel). (c) Electron tomography of a P3HT:PCBM sample close to the surface after thermal annealing 130°C for 20 minutes. All images $500\text{ nm}\times 500\text{ nm}$. Images (a,c) modified from reference [68].

The nature of the P3HT and PCBM networks becomes even more obvious if one considers the damping images [33], which can be used to fully comprehend images (Figure 4.9b) by incorporating the 3D topography (z-levels) with dissipation data (color). The damping contrast is affected by the local chemical nature at the surface, and higher values are recorded over the P3HT crystallites. In a mechanistic picture, one may assume that a higher energy is dissipated in the tip-surface interaction over the most flexible component of the blend. However, a detailed modeling of the damping interaction would be needed for a quantitative analysis, as described in a previous report.[120] The exact mechanism at the origin of the damping may be more complex, and would require complementary investigations and modeling beyond the scope of this work. Furthermore, the composite images suggest the presence of nearly buried P3HT crystallites, partially or totally covered by an ultrathin layer of PCBM, giving rise to a slight damping contrast. In summary, this is in very good agreement with what is commonly expected for these blends [68, 190] with a phase segregation at a scale on the order of 10 nm.

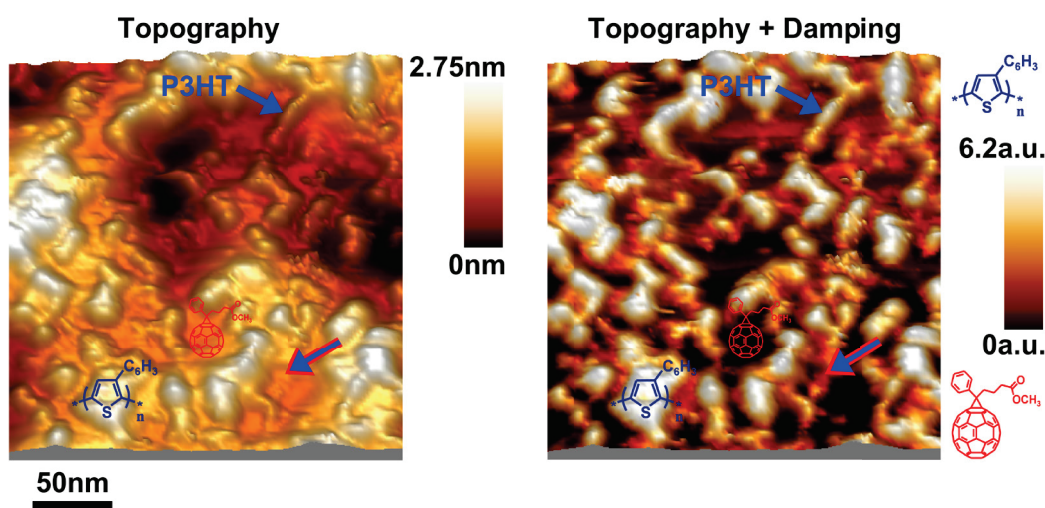


FIGURE 4.9: (a) FM-AFM (UHV, 300K) 3D topographic image ($250 \text{ nm} \times 250 \text{ nm}$, 300×300 pixels) of the P3HT-PCBM sample $\Delta f = -19 \text{ Hz}$, $A_{vib} = 44 \text{ nm}$, scan speed = 50 ms per pixel). (b) Composite image of topography (z-levels displayed in (a)) and damping signal (color). The damping level is lower over the stiffer PCBM. The blue and red-blue arrows in (a) and (b) pinpoint an emerged and nearly buried P3HT crystallite, respectively.

4.3.3 Kelvin Probe (CPD) Imaging

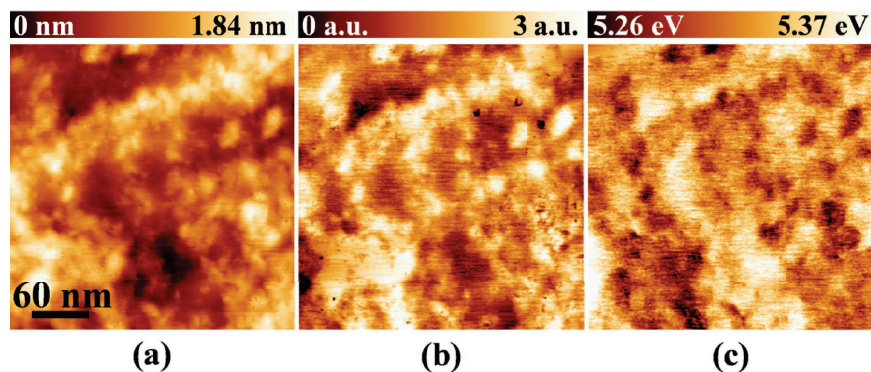


FIGURE 4.10: FM-AFM (UHV, 300K) 2D images ($300\text{ nm} \times 300\text{ nm}$, 300×300 pixels, $\Delta f = -29\text{ Hz}$, $A_{vib} = 30\text{ nm}$, scan speed = 100 ms per pixel) of the P3HT:PCBM sample recorded in dark of the topography (a), damping (b) and FM-KPFM work function (c) using the “FM-KPFM” cantilever described in table 3.2.

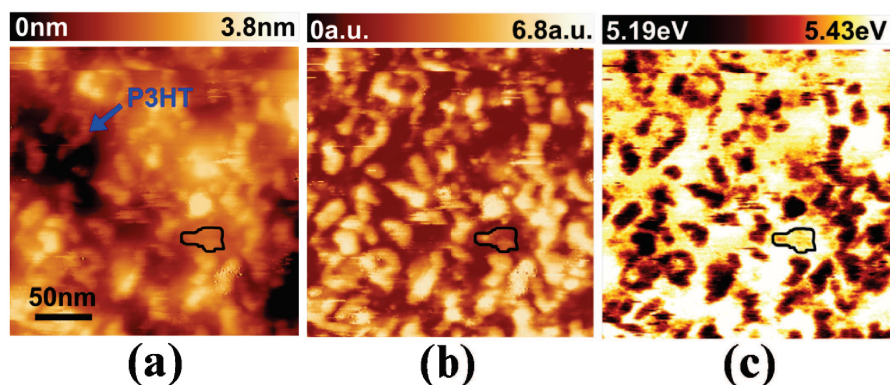


FIGURE 4.11: FM-AFM (UHV, 300K) 2D images ($250\text{ nm} \times 250\text{ nm}$, 300×300 pixels, $\Delta f = -19\text{ Hz}$, $A_{vib} = 44\text{ nm}$, scan speed = 50 ms per pixel) of the P3HT:PCBM sample recorded in dark. (a) topography, (b) damping, and (c) work function calculated from the Kelvin compensation potential. The dark-blue arrow in (a) indicates a P3HT crystallite. A nearly buried P3HT crystallite (partially or totally covered by a ultrathin layer of PCBM) is outlined in black.

To investigate the surface electronic properties with sub-10 nm resolution, comparative frequency modulated KPFM (FM-KPFM), seen in figure 4.10, and amplitude modulated KPFM (AM-KPFM), seen in figure 4.11, measurements have been carried out. Frequency modulated KPFM images were recorded in dark, with the view ports covered and the ion gauge turned off, using PtIr₅ coated Si cantilevers at a resonant frequency of 338 kHz, a modulation frequency of 1.3 kHz, and at a scan rate of 100 ms per pixel ($10\text{ nm} \cdot \text{s}^{-1}$), which corresponds to an imaging time of 5 hours per image. The scan speed was limited primarily due to a rather low signal to noise ratio. Therefore, a high frequency shift setpoint (close tip-sample distance) of -29 Hz was used in combination

with a 20 dB damping attenuator in order to reduce input amplitude. FM-KPFM was first used because of the assumption that AM-KPFM resolution may suffer as a result of the sensitivity to the electrostatic force, rather than the force gradient used in FM-KPFM.[142, 191] A lower work function level is associated to P3HT crystallites, also seen in the AM-KPFM measurements. Although FM-KPFM was able to distinguish features at the nanoscale, the signal was quite noisy (as seen in the work function image in image 4.10) and hard to stabilize through the course of the long imaging process. Therefore, with the goal to improve resolution and stability, AM-KPFM was employed.

To begin AM-KPFM investigations, in order to calculate the local work function of the sample surface, according to equation 3.31, the PtIr₅ cantilever tip had to be calibrated. KPFM data was collected on a set of reference samples including Pt, Al, and Ru thin films deposited by PVD on Si substrates provided by D. Mariolle and N. Chevalier from LETI-MINATEC (CEA, Grenoble), who also confirmed the value of the PtIr₅ mean work function by comparative KPFM measurements. A work function (ϕ_t) of 5.3 ± 0.1 eV was obtained for the PtIr₅ cantilever, which is consistent with the values reported from several other works for PtIr₅-coated cantilevers.[192] However, as tip changes can occur between measurements on different samples, the work function scales may be shifted by a few hundred of meV.

Amplitude modulated KPFM images were first recorded in dark, with the view ports covered and the ion gauge turned off, using PtIr₅ coated Si cantilevers (as described in table 3.2) at a resonant frequency (f_0) of 61.3 kHz and at a scan rate of 50 ms per pixel ($\sim 17 \text{ nm}\cdot\text{s}^{-1}$), which corresponds to an imaging time of ~ 7 hours per image based on an image recorded with dimensions 500×500 pixels. The scan speed in AM-KPFM was limited primarily due to the large quality factor of the cantilever in UHV, which means that the measured amplitude changes are slow (according to equation 3.15). The modulation frequency (f_{mod}) was tuned to the second resonance frequency at $\sim 6.3f_0 = 392.324$ kHz. Based on previous experimental [20, 21] and theoretical [21] investigations of sub-nanometer KPFM contrast, the lateral resolution was gradually improved by progressively reducing the tip-surface separation (i.e. lowering Δf). An optimal lateral resolution was achieved when the tip-surface separation (or Δf) at a constant physical amplitude is slightly lower than the onset of damping contrast. This implies a non negligible contribution of short-ranged electrostatic (SRE) forces, which will be discussed in the forthcoming chapter 5.[21] The optimization process reveals a spatial resolution of a few nm in the CPD (presented here in terms in work function) images.

4.3.3.1 In Dark Contrast

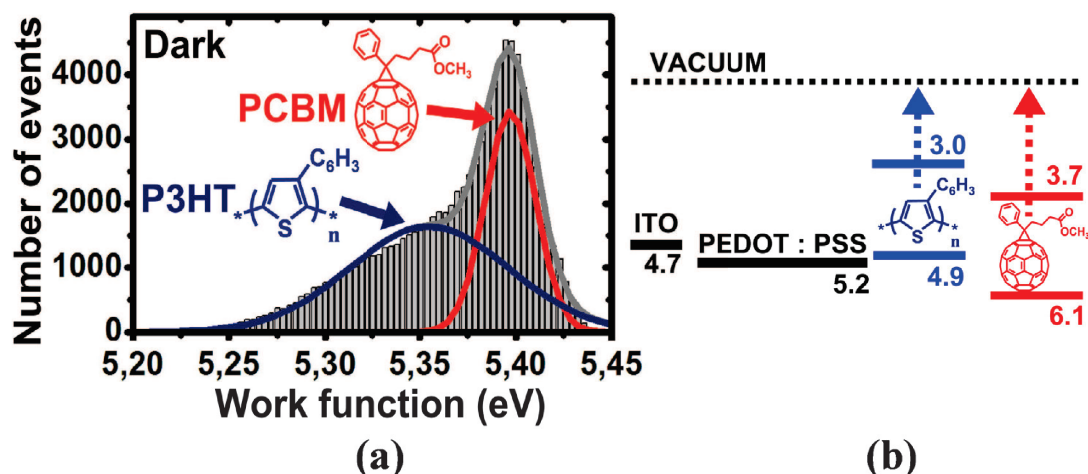


FIGURE 4.12: (a) Histogram distribution of the work function values extracted from KPFM images in dark and under illumination at 532 nm. P3HT (blue), PCBM (red in dark). (b) Simplified flat band energy diagram.

The KPFM images recorded in dark, as seen in figure 4.11, reveal a one-to-one correspondence of the topography (figure 4.11a) and the damping image (figure 4.11b), which were recorded simultaneously. A lower work function level, in average approximately 42 ± 4 mV, is associated to P3HT crystallites.

The magnitude of the full scale contrast in dark of approximately 200 mV is consistent with previous KPFM reports on organic blends described previously [16–18], as well as FM-KPFM data, described above in figure 4.10. The mean work function level is remarkably close to that expected for the bottom PEDOT:PSS electrode (ca. 5.2 eV).

The bottom hole collecting anode is composed of a 30 nm thick layer of PEDOT-PSS, whose work function can be as high as 5.2 eV [193], coated onto an ITO covered glass substrate whose work function is ca. 4.7 eV [194].

As described by Maturová and coworkers, the presence of charges in dark are thought to be absent in these pristine, undoped organic semiconductors, and the SP should be determined by the work function difference between the tip and the PEDOT:PSS bottom electrode.[18] However, the HOMO levels of the donor and acceptor materials are aligned with the Fermi level of the bottom electrode, as expected from a flat band model depicted in figure 4.12b. By diffusion, charge carriers will penetrate into the organic layer from the bottom PEDOT-PSS/ITO electrode, causing band bending.[195] As a result, the surface potential is shifted accordingly.[18] However, such a picture cannot fully account for the existence of a dark contrast between the donor and acceptor components of the active layer.

Following the conclusions of that previous report [18], we attribute the “in dark” contrast between P3HT and PCBM to band bending of the donor-acceptor blend at the PEDOT:PSS interface. In the relatively thin (~ 100 nm) blend, the lower work function detected over P3HT is consistent with the relative position of the energy levels in the system.[196, 197]

4.3.3.2 Effect of Illumination

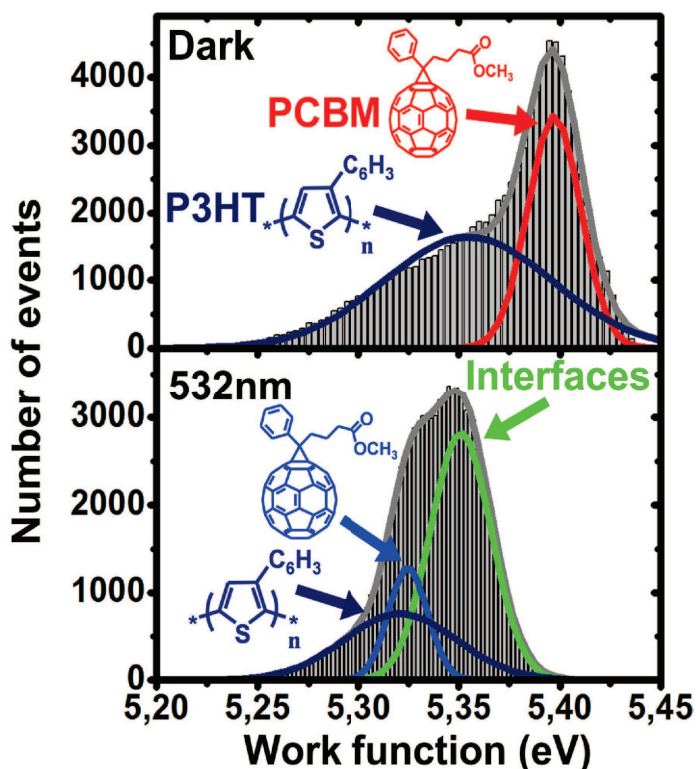


FIGURE 4.13: Histogram distribution of the work function values extracted from KPFM images in dark and under illumination at 532 nm. The Gaussian curves obtained from the decomposition of the histograms have been accordingly attributed to the contributions from the P3HT (blue), PCBM (red in dark, light blue under illumination), and at the D/A interfaces (green under illumination).

The choice of wavelength for illumination was based on the absorption spectra and IPCE data, see figure 4.5a and reference [190]. A well-defined peak in both data measurements occurred at roughly 530 nm. Therefore, for this study, continuous-wave (cw) laser illumination at a wavelength of 532 nm was chosen using a commercial diode-pumped solid state laser at 5 mW, with an effective intensity on the surface of the order of $50 \text{ mW}\cdot\text{cm}^{-2}$.

It is noteworthy to mention that the spot width of the AFM detection laser (wavelength $\lambda = 830$ nm) is approximately $20 \mu\text{m}$ and therefore the sample is not illuminated by

the AFM laser because it is effectively blocked by the cantilever (width $\approx 28 \mu\text{m}$). In addition, the AFM detection laser wavelength ($\lambda = 830 \text{ nm}$) falls well above the absorption band spectra for the P3HT:PCBM blend, as seen in figure 4.5a.[190]

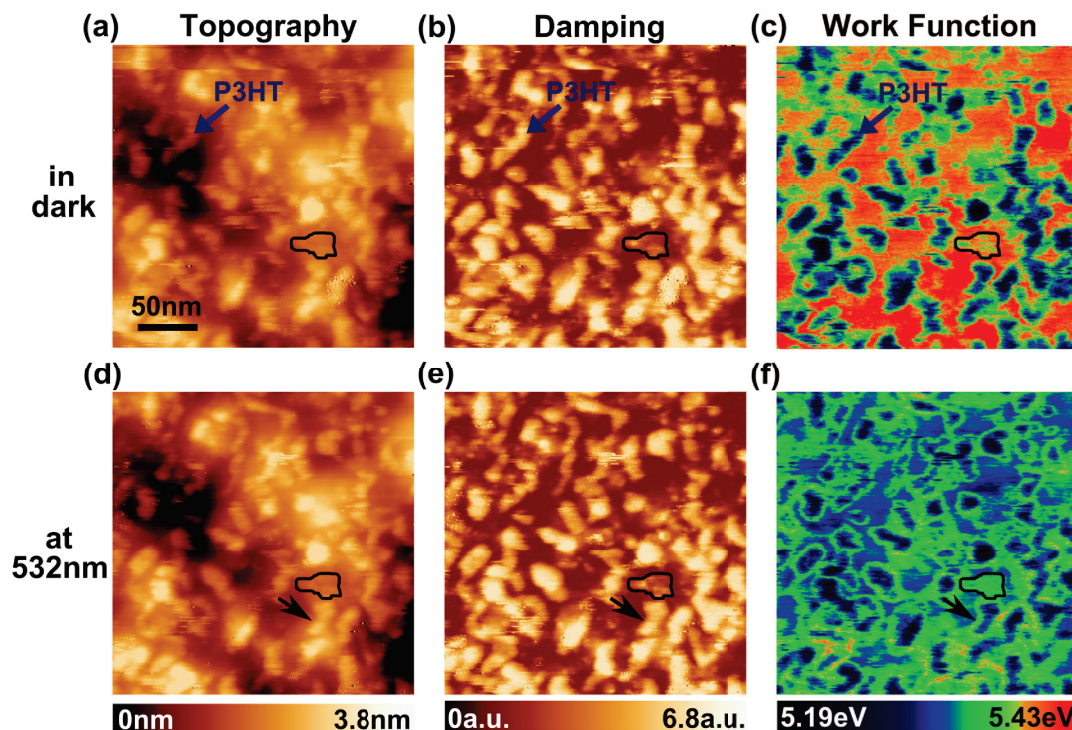


FIGURE 4.14: (a-f) FM-AFM (UHV, 300K) 2D images ($250 \text{ nm} \times 250 \text{ nm}$, 300×300 pixels, $\Delta f = -19 \text{ Hz}$, $A_{vib} = 44 \text{ nm}$, scan speed = 50 ms per pixel) of the P3HT:PCBM sample recorded in dark (a-c) and under illumination at 532 nm (d-f). (a,d) topography, (b,e) damping, and (c,f) work function calculated from the Kelvin compensation potential. For a direct comparison, the z-values have been coded by using the same color scales in (a,d), (b,e), and (c,f). The dark-blue arrows in (a-c) indicate a P3HT crystallite. The dark arrows in (d-f) pinpoint the interface between an emerging P3HT crystallite and the surrounding PCBM. A nearly buried P3HT crystallite (partially or totally covered by a ultrathin layer of PCBM) is outlined in black.

The surface potential is dramatically modified under illumination at 532 nm , as shown in figure 4.13 and by the comparison between figure 4.14c and f, which present KPFM images recorded at the same location before and under illumination. As a proof of the stability of the system, one can easily establish a good correspondence between the full set of images in dark and under illumination in figure 4.14. Both the topography and damping images remain unchanged after illumination. The absence of artifacts is also apparent in Figure 4.16a, which displays an image for which the top and bottom halves have been recorded in dark and under illumination, respectively. From the work function histograms (Figure 4.13a and b), it can be clearly seen that there is a redistribution of spectral weight toward lower values at 532 nm , revealing a net accumulation of negatively charged carriers at the surface.

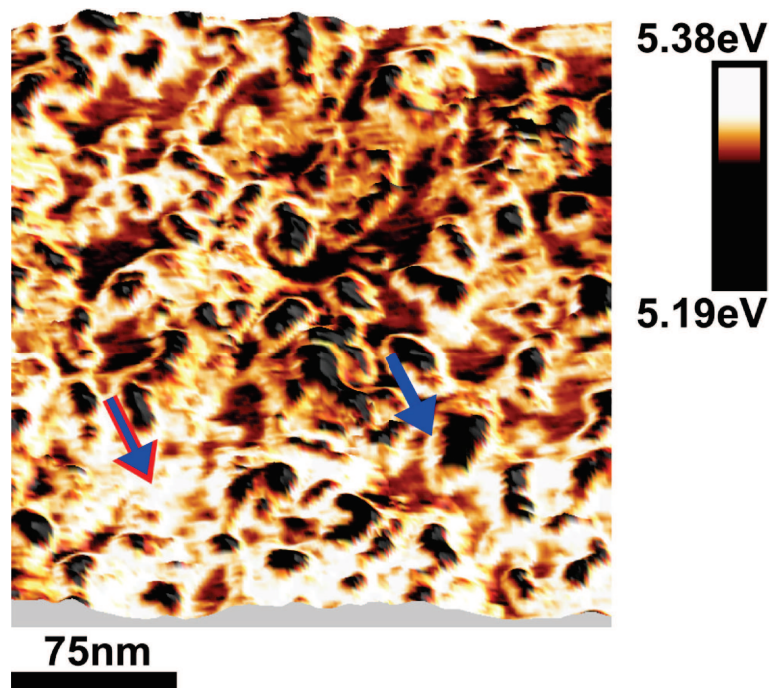


FIGURE 4.15: FM-AFM (UHV, 300K) composite image ($275\text{ nm}\times 275\text{ nm}$, 330×330 pixels) of topography (z levels) and Work function image under illumination at 532 nm. The color code has been selected to highlight some specific features. The blue arrow pinpoints the location of the interface between an emerging P3HT crystallite and the surrounding PCBM matrix. The bicolor red-blue arrow highlights a second kind of interface, between a nearly buried P3HT crystallite and its ultrathin PCBM capping layer.

We underline that a global negative shift of the work function has also been reported by Glatzel et al. in the case of nanophase segregated MDMO-PPV:PCBM blends.[16, 171] In this work, this effect was also confirmed by carrying complementary investigations on novel BHJ blends, as shown in the appendix A.

More precisely, the mean work function decreases strongly over the PCBM domains and to a lesser extent over P3HT crystallites, which can also be seen on the profile given in Figure 4.16b. Remarkably, under illumination, a well defined work function level is associated to the donor–acceptor interfaces, which appears either in the form of “halos” surrounding the emerging P3HT crystallites or as patches over the nearly buried interfaces (Figure 4.14f and Figure 4.15). The 1:1 correlation between the donor–acceptor interfaces and this signal can be confirmed by combining the topographic (or damping) and Kelvin signals (an example is shown in Figure 4.15).

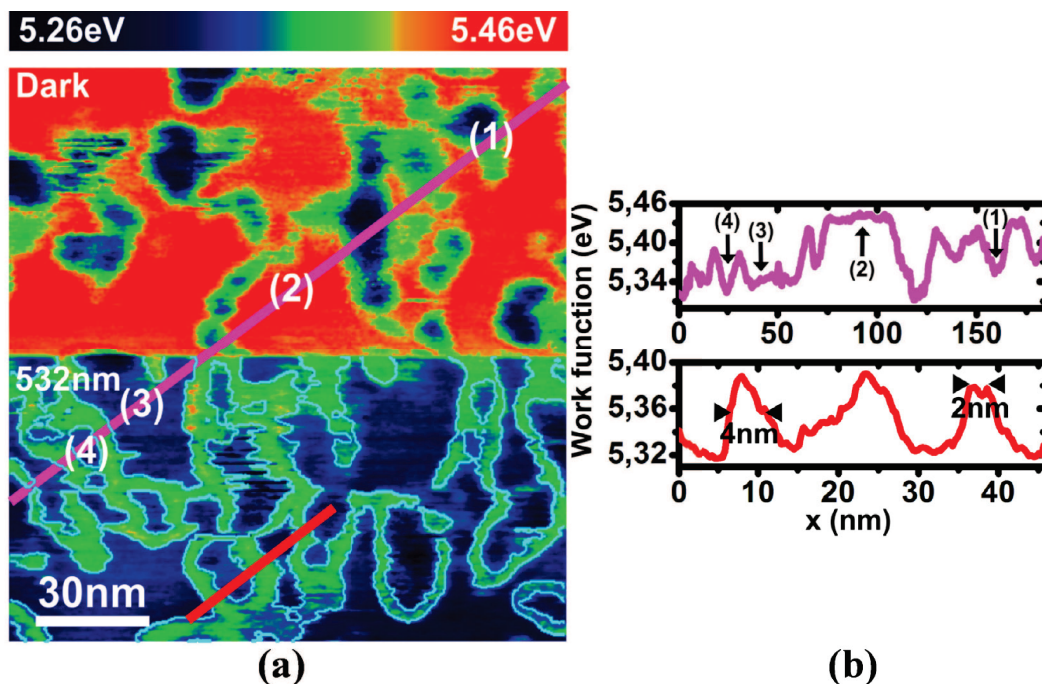


FIGURE 4.16: (a) FM-AFM (UHV, 300K) work function image ($150\text{ nm} \times 150\text{ nm}$, 600×600 pixels, $\Delta f = -17.6\text{ Hz}$, $A_{vib} = 43.4\text{ nm}$, scan speed = 35 ms per pixel) of the P3HT:PCBM sample recorded in dark (top half) and under 532 nm illumination (bottom half). The perimeters delimiting the levels higher than 5.35 eV are highlighted in light blue (under illumination only). (b) Work function profiles corresponding to the magenta and red cross sections in (a), four selected locations along the magenta path are indicated in the image (1 and 4 over P3HT, 2 and 3 over PCBM). The mean width of the “halos” at the D/A interface is estimated, either from the profiles or from an analysis of the area-perimeter ration based on the levels over 5.35 eV , to be ca. 4 nm .

4.3.4 Surface Photovoltage

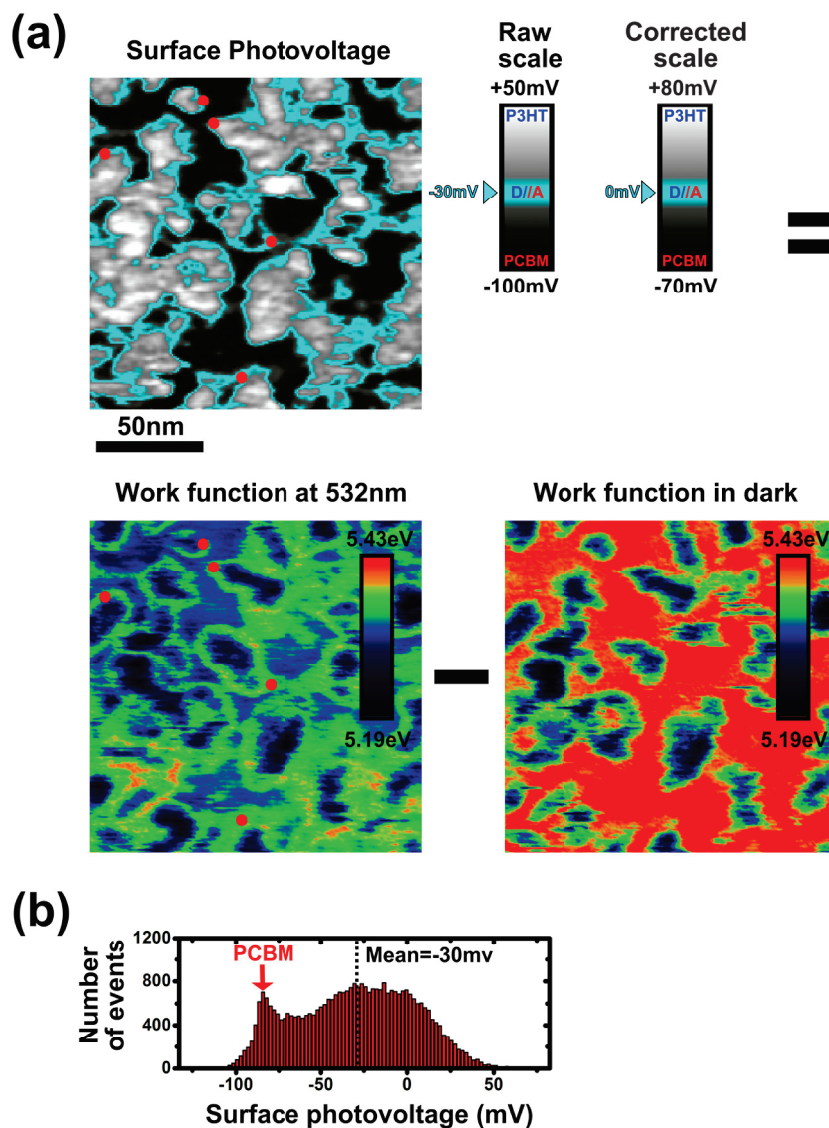


FIGURE 4.17: (a) Calculation of the surface photovoltage (SPV) image ($154 \text{ nm} \times 154 \text{ nm}$, 185×185 pixels) from the difference between the work function images under illumination and in dark of the P3HT-PCBM sample $\Delta f = -19 \text{ Hz}$, $A_{vib} = 44 \text{ nm}$, scan speed = 50 ms per pixel). (b) Histogram of the SPV values calculated from the SPV image, where the mean value is ca. -30 mV. The scale of the SPV image can be corrected by applying a global positive shift of +30 mV.

To clarify the origin of the work function changes, the surface photovoltage (SPV) has been calculated (Figure 4.17) as the difference between the work function under illumination and in dark.[16] This highlights that the PCBM network becomes negatively charged, while the SPV is only partially positive over P3HT crystallites. Remarkably, the mean level of the SPV histograms ($\sim -30 \text{ mV}$) corresponds exactly to the location of

the donor–acceptor interfaces (Figure 4.17), where a neutral potential would have been expected.

This result is confirmed by the analysis of KPFM images at the highest magnification, where local contrasts can be analyzed with a resolution of a few nm. Figure 4.19 was recorded over a P3HT crystallite while switching on the illumination at mid scan. An uninterrupted work function profile can be extracted at the donor-acceptor interface from the dark to illuminated states, revealing clearly the -30 mV shift, seen in figure 4.19. This suggests a better electrical and topological (as shown by TEM experiments [68]) connection between the P3HT and the bottom electrode, due to the HOMO alignment with the PEDOT:PSS Fermi level and to a favorable concentration gradient of the P3HT through the film thickness. The resulting net transfer of positive charges to the back contact (connected to the ground in our setup) leads to a global negative shift of the mean surface potential.[16] Such a scenario is commonly assumed as a vital ingredient for high power-conversion efficiency. An image combining the topography and the SPV, corrected from the negative shift, is presented in Figure 4.18.

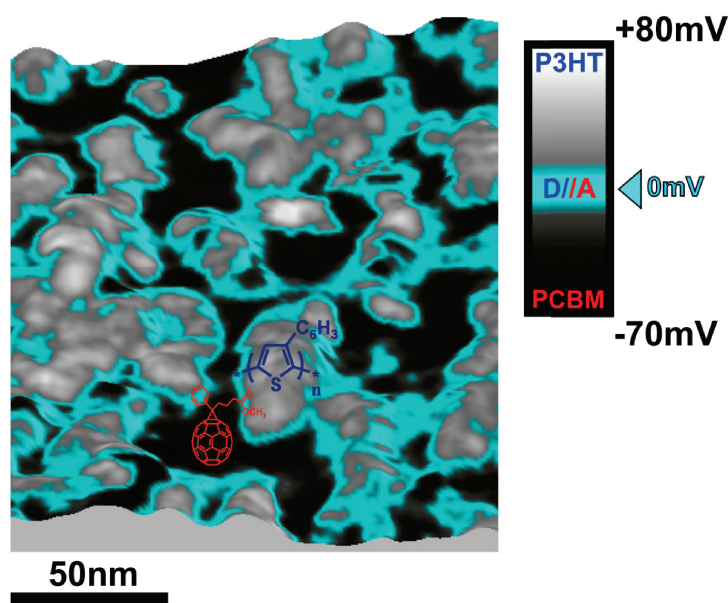


FIGURE 4.18: FM-AFM (UHV, 300K) composite image ($154 \text{ nm} \times 154 \text{ nm}$, 185×185 pixels) of topography (z levels) and surface photovoltage under illumination at 532 nm (gray scale color) encompassing the full 150 mV SPV bandwidth. PCBM clusters appear in dark (negative values) contrast, P3HT crystallites in bright (positive values), and the levels corresponding to the space charge area at the donor/acceptor interfaces are highlighted in light blue. The potential scale has been shifted by +30 mV according to the analysis of the surface photovoltage histogram in figure 4.17.

The zero level corresponds to the interfaces where the excitons generated in the P3HT are dissociated into holes and electrons, which are respectively transferred in the P3HT

and PCBM networks, becoming positively and negatively charged. Such a charged state can effectively be visualized under continuous irradiation since carrier recombination is a much slower process (time constant value ranging from 100 μs to 1 ms according to transient photovoltage measurements [190]) than carrier generation. Lastly, from the high-resolution work function images recorded under illumination (Figure 4.16), one can tentatively extract quantitative data related to the lateral extension of the space charge area at the donor–acceptor interface. While the mean half width of profiles crossing the “halos” is estimated to be 4 nm (Figure 4.16), the analysis of high-magnification images (Figure 4.19) suggests that a more realistic value probably falls below 2 nm. This corroborates that operating devices are subjected to very high interface potentials, reinforcing a picture of filamentary transport with current confinement effects in nanodomains.

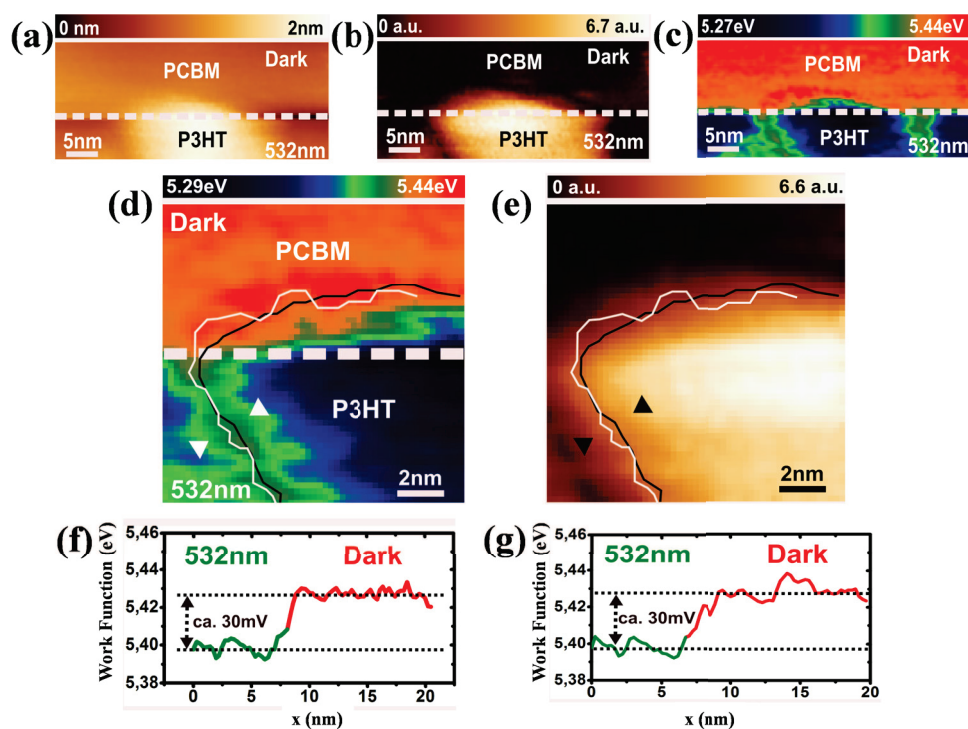


FIGURE 4.19: (a,b,c) FM-AFM images of the P3HT:PCBM sample recorded in dark (top half) and under illumination at 532nm (bottom half) of the (a) topography (b) damping and (c) work function. The white dotted lines indicate the separation between the parts recorded in dark and under illumination. (d,e) magnified work function (d) and damping (e) images. The distance between the two arrows in (d) and (e) is ca. 2 nm. (f,g) Work function profiles at the donor–acceptor interface corresponding to the paths underlined in white (f) and black (g) in image (d). The white path has been extracted by following manually potential levels in (d), while the black path has been objectively extracted by simultaneously following levels of nearly constant damping in image (e). The multiple profile function of WsXM software has been used for that purpose.[167] Both procedure yield the same value for the work function shift at the interface, ca. -30 mV.

4.4 Conclusions

This study clearly demonstrates that it is possible to investigate simultaneously the chemical phase separation and the electronic properties of organic bulk heterojunctions by KPFM at the sub-10 nm scale.

To the best of our knowledge, this experiment provides the first direct visualization of the carrier generation at the donor–acceptor interfaces in an optimally phase segregated P3HT:PCBM blend showing a PCE up to 4.25% using close tip-sample distances. Although we demonstrated exceptional resolution, we did not use specific cantilevers or dedicated electronic setup. The same approach can henceforth be applied in any standard commercial UHV NC-AFM setup. KPFM has the potential to become a routine tool for the characterization and optimization of nanophase separated organic and hybrid photovoltaic blends.

A 10-fold improvement in the KPFM lateral resolution has been achieved, making it possible to perform a chemical identification of the donor and acceptor phases at the surface and the near subsurface in addition to the high resolution topographic images. However, these contrasts have been obtained in a regime in which there may be a non-negligible contribution of short–range forces. As shown in the following chapter 5, the work function values deduced from the CPD images may deviate from the ones acquired out of the range of the short range forces. Nevertheless, our results are consistent with what is expected for the charge carrier generation under illumination at the donor-acceptor interfaces. In our opinion, this strongly supports the idea that single pass KPFM can be used at minimal tip-surface distances to qualitatively probe the charge carrier generation in BHJ thin films.

LCPD of Molecular Self-Assemblies:

Local Contact Potential Difference (LCPD)

Molecular CPD of π -Conjugated Edge-On Oligomers

Nous montrerons comment des contrastes aux échelles moléculaires peuvent être obtenus par microscopie à sonde de Kelvin en mode modulation d'amplitude. L'influence de la distance de séparation entre la pointe et la surface sur les signaux mesurés est discutée au regard des images en haute résolution, et des résultats des mesures de spectroscopie de distance. Particulièrement, nous montrerons que la distance pointe-surface en dessous de laquelle un contraste apparaît dans les images de dissipation, coïncide avec celle en dessous de laquelle les forces électrostatiques à courte portée contribuent au processus d'imagerie du potentiel mesuré par KPFM. Ces forces sont responsables de l'apparition de modulations dans les images du potentiel de surface, corrélées aux modulations topographiques.

In this chapter, contact potential differences at the molecular scale were achieved using amplitude modulation Kelvin probe force microscopy. The nature of the imaging contrast has been analyzed by combining high resolution imaging with distance-dependant spectroscopy measurements. It is shown that the apparition of a damping contrast characterizes the onset of the short range electrostatic forces, which are responsible for the occurrence of local contact potential difference modulations correlated with the molecular lattice.

5.1 Local Contact Potential Difference (LCPD)

For KPFM measurements, the contact potential difference (CPD) is recorded between the sample surface and the tip. At close tip-sample distances, the CPD can be influenced by the surface potential. Thus, it differs from the intrinsic CPD that is reliant upon on the macroscopic concept of work function. However, the physics that connects the magnitude of this so called LCPD and the surface potential still remains under debate.[128, 138, 142, 198–201] Understanding the origins of the CPD contrasts at the local scale and how they are related to the physical properties of the surface is critical for achieving single pass KPFM investigations at the nm or sub-nm scale.

Sub-nanometer LCPD resolution has been observed on a range of semiconductor surfaces including: Si(111)7×7 [20, 202–207], Si(111)5√3×5√3-Sb [208], GaAs(110) [209], InSb(001) [145], Ge(105)-(1×2) Si(105) [210], and on bulk dielectric surfaces including: TiO₂ [143, 211, 212]. It has been shown that in the short-range regime, neither AM nor FM-KPFM measurements reflect the true CPD or the local surface potential, but rather an effective value which is convoluted by the tip geometry. This indicates that polarization effects play a key role in the occurrence of SRE forces with two consequences in the nc-AFM and KPFM imaging process:

- (i) They contribute to the total interaction force and are thus involved in the Δf signal used to perform “topographical images” and,
- (ii) they must be considered for interpreting the LCPD contrast, owing to their cross-coupled distance and bias voltage dependence.

The CPD determined in equation 3.31 is based on the capacitive force between two macroscopic parallel metallic electrodes. At this scale, they do not exhibit a lateral electrostatic force distributions at the atomic-scale. During KPFM measurements of the total electrostatic force, atomic-scale LCPD contrasts are induced by a bias dependent short-range force.

The microscopic origin of the short-range electrostatic forces and the way they are coupled to the nc-AFM/KPFM imaging process remains unclear, which has triggered intensive experimental and theoretical efforts. In the following, we briefly discuss three models which have recently been proposed for analyzing the contribution of SRE forces to LCPD contrasts observed on semiconducting surfaces, ionic solids and metallic surface adatoms. Lastly, a brief introduction to molecular CPD contrast will be given.

LCPD of a semiconducting surface: Si(111)7×7 LCPD contrast on a Si(111)7×7 surface, previously reported by Shiota et al.[207], has been modeled by Okamoto et al.[213] The electrostatic force (F_{ES}) is separated from the topographical force (F_{top}),

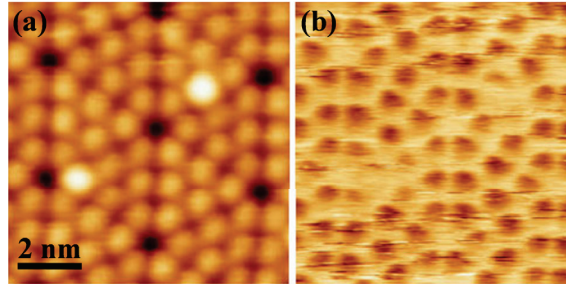


FIGURE 5.1: (a) Topography and (b) simultaneously measured KPFM image (256 pixels², $\Delta f = -8.6$ Hz, $V_s = 180$ mV, $V_{ac} = 0.5$ V, $f_{ac} = 1$ kHz, $f_0 = 161.4$ kHz, $A_{vib} = 93$ Å). Bright (dark) contrast in the CPD corresponds to 55.5 mV (-342.7 mV). Image adapted from reference [20].

where the F_{ES} is a function of frequency and F_{top} is a function of frequency and applied bias (V_{DC}). The sum of these two forces affects the measured LCPD. The topographical force F_{top} displays cubic-root-like dependence on $V_{applied}$. The resulting sum of the F_{ES} and F_{top} generates multiple stable LCPD values. The derived expression for the new stable values is:

$$V_{DC} = V_{CPD} \pm \frac{|f_{top}(\omega, \Delta V) \cos \Delta\theta|}{(\partial C/\partial z)V_{AC}}, \quad (5.1)$$

where f_{top} is the modulation component of the topographical force, V_{AC} is the applied AC potential, C is the capacitance, and $\Delta\theta$ is the phase difference between the F_{ES} and F_{top} signals.[213]

This model of the LCPD on semiconductors is supported by spectroscopy experiments on the Si(111)7×7 surface. Arai et al. revealed the presence of two separate minimums in the frequency shifts versus sample bias.[205] In the model, the LCPD contrast is due to the short-range force, denoted as $f_{top}(\omega)$. The short-range force is deduced from the interaction strength of the tip apex with the surface. On a semiconducting surface, the short-range force is characterized as a covalent bonding interaction. This is consistent with previous experimental studies of Au clusters on Si, in which the Au clusters show a higher potential than the underlying Si substrate. This is primarily due to a weaker bonding of Au-Si compared to Si-Si interactions.[204] The model has also been applied to experiments in which the LCPD is used for atom identification on a mixed Si-Sb surface.[208] Sadewasser et al. regarded the LCPD variation on a Si(111)7×7 surface is caused by the formation of a local surface dipole. This dipole forms from either a charge transfer between different surface atoms or from a tip induced charge redistribution at the surface.[20]

LCPD of ionic solids Bocquet et al. reported atomic resolution KPFM results on ionic solids such as KBr(001), as seen in figure 5.2.[146] Bocquet et al. also developed an analytical model describing the short range electrostatic force between a conductive

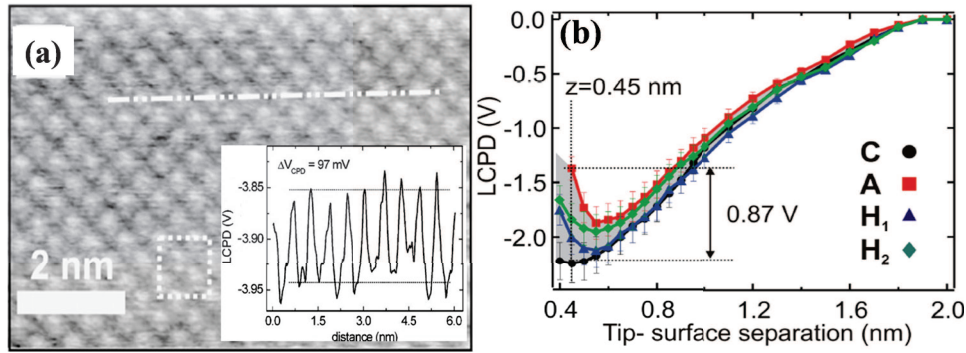


FIGURE 5.2: (a) Atomic resolution CPD image of a KBr(001) surface measured by AM-KPFM in UHV. Inset: Profile of the CPD indicated by the dash line in (a) where a 97 mV LCPD is clearly observed between K⁺ and Br⁻. The dashed box indicates a unit cell. Image (a) is adapted from reference [146]. (b) Calculated LCPD vs. Z spectroscopy curves on a NaCl surface. The distance dependence of the measured LCPD indicates an optimal tip-sample distance for LCPD contrast. Image (b) adapted from reference [21].

AFM tip and an ionic crystal. The LCPD is a result of the short-range electrostatic interaction between the tip apex and the local charge distribution on the ionic crystal surface. Based on the model developed by Bocquet et al., Nony et al. also developed an analytical model of short-range electrostatic forces to account for the LCPD contrast on ionic crystals by both AM and FM mode KPFM.[130] A lateral force distribution at the atomic scale is caused by the interaction of atoms on the tip apex with the surface provides. However, the LCPD has been shown to be dependant on the geometry of the tip, the tip-sample distance, and the tip-sample bias. The short-range electrostatic force (F_{sre}) is composed of two separate terms, where $F_{sre} = F_{m\mu}^{(1)} + F_{\mu}^{(2)}$. $F_{m\mu}^{(1)}$ represents the interaction between the tip apex (which acts as a capacitor with the sample surface) and the sample. In which case, it contributes to the atomic LCPD contrast. $F_{\mu}^{(2)}$ represents a static offset of the force between the tip apex at the mesoscopic scale and the surface charge density induced by the tip-sample bias. The full force expression, including both the short-range and long-range electrostatic interaction, is expressed as:

$$F_{es} = F_{m\mu}^{(1)} + F_{\mu}^{(2)} + F_M, \quad (5.2)$$

where where F_M is the macroscopic electrostatic force in terms of z (the direction normal to sample surface). F_M is defined by:

$$F_M = -\frac{1}{2} \frac{S \epsilon_0 \epsilon_d^2}{(z_M + z)^2} \left(V_{applied} + \frac{V_{cpd}}{e} \right)^2, \quad (5.3)$$

In summary, these results [130, 146, 204] have detailed how site-dependent SRE

forces may develop between a biased metallic tip carrying an atomic asperity such as a single atom or a small ionic cluster (figure 5.2c) and the (001) facet of a bulk alkali halide single crystal. The tip-sample distance and the chemical nature of the tip can both have an affect on the measured LCPD. The results indicate that the LCPD contrasts originate from the dynamic polarization of the atomic cluster and of surface atoms owing to the combined influence of the biased tip and of the Madelung surface potential of the ionic crystal.[99]

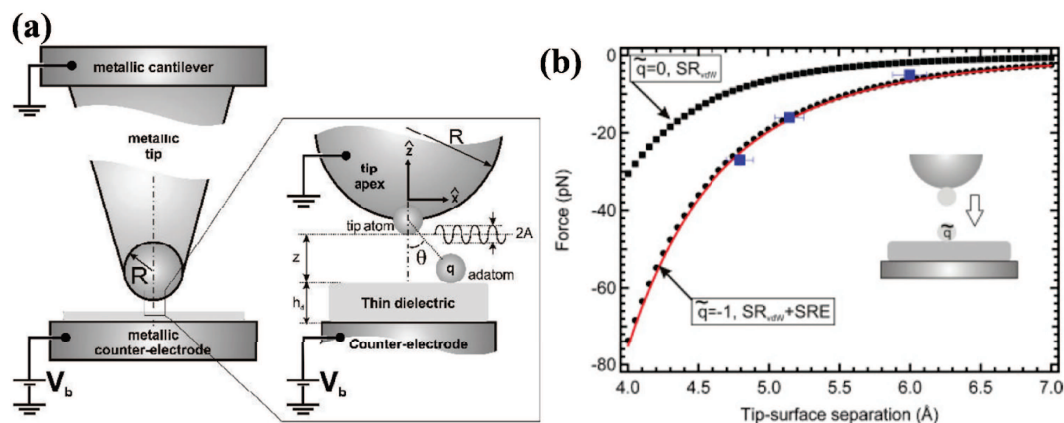


FIGURE 5.3: (a) Schematic proposed by Bocquet et al. [214] in which an AFM tip consists of a macroscopic metallic body with a conical shape. The tip apex is described by a sphere with a radius R . The tip is grounded with regard to the counter electrode on top of which lies a thin dielectric consisting of two monolayers of an ionic film. The tip apex carries a neutral, but polarizable single atom. On top of the dielectric lies an adatom that may carry a single-electron charge. The geometrical parameters of the problem are defined similarly to those in the work by Gross et al. [215] (b) Distance dependence of the tip-adatom SR force computed with $V_b=0$. The experimental values of the force derived from Gross et al. [215] are depicted with blue squares. The horizontal error bars depict a possible uncertainty in the z position of the tip of 2% only. The discrepancy between SRE and SR-vdW forces is well visible.

LCPD of metallic surface adatoms Bocquet et al. present a model depicting the influence of short-range electrostatic forces between the tip of an AFM and a surface carrying charged adatoms.[214] Their theoretical analysis is based upon the work by Gross et al.[215] Using a cryogenic qPlus TF-AFM, they investigated charge-switching of individual adsorbed gold and silver adatoms on ultrathin NaCl films on Cu(111).[215]

As explained in chapter 3, when the AFM tip is brought close enough to the surface, it becomes subject to forces of essentially two origins:

- (i) electrostatic forces (composed of capacitive, Coulombic, and short-range electrostatic, SRE, or dipolar forces), and
- (ii) van der Waals (vdW) forces (London dispersion forces without any permanent dipoles).

These forces have an intrinsic distinct decay length, which makes it possible to split them up into long-range (LR) and short-range (SR). Long-range forces typically dominate at tip-surface distances above 1 nm, while short-range forces may dominate below that. Nony et al. describes the total force as [214]:

$$\vec{F}_{tot} = \vec{F}_{LR} + \vec{F}_{SR} = [\vec{F}_{LR}^{el} + \vec{F}_{LR}^{vdW}] + [\vec{F}_{SR}^{el} + \vec{F}_{SR}^{vdW}]. \quad (5.4)$$

The vertical component of the short-range electrostatic force \vec{F}_{SR}^{el} can be broken down into the microscopic polarizable dipoles and electrostatic fields of the AFM tip apex and of the surface (in the case described by Bocquet et al., a metallic surface adatom [214, 215]):

$$\vec{F}_{SR}^{el} = -\frac{\partial}{\partial z} \left[-\frac{1}{2} \vec{p}_{tip} \cdot \vec{E}_{tip}^{ext} - \frac{1}{2} \vec{p}_{ad} \cdot \vec{E}_{ad}^{ext} \right]. \quad (5.5)$$

These results show that SRE forces decay almost as fast as SR-vdW, but their strength may prevail on the SR-vdW contribution upon the polarizability and/or the charge state of the interfacial atoms, as seen in figure 5.3b.

Molecular CPD Contrast Since more than 10 years, KPFM has been widely applied to investigate the local potential modification induced by self-assembled monolayers (SAMs) on various kinds of surfaces. These works [216–218] demonstrated that the molecular dipoles can strongly modify the CPD as measured by KPFM. It was concluded that the CPD signal directly reflects the surface potential modification induced by the molecular dipoles. The surface potential as a function of the area occupied by a molecule was also predicted by *ab-initio* calculations and compared to the experimental results, and a reasonable agreement was achieved in some cases.[218] However, we here underline that these earlier works were based on measurements performed at the mesoscopic scale.

On the other hand, LCPD contrasts at the molecular scale remain poorly investigated. Glatzel et al have investigated the dipole moment density variations within cyanoporphyrins molecular wires grown on KBr by AM-KPFM.[219] A semi-quantitative analysis of the dipole density was carried out, but the authors concluded that theoretical modeling would be needed to achieve a true quantitative analysis of the molecular dipoles. The authors also highlighted the possible existence of non conventional effects when performing KPFM measurements at very close tip-sample distances of the surface, hindering a straightforward absolute measurement of the molecular dipole intensity.

Ichii et al. have also recently reported molecular CPD contrasts using FM-KPFM on copper-phthalocyanine (CuPc) monolayers on Au(111) (see figure 5.4), suggesting that molecular electric dipoles may directly be imaged by KPFM. In that particular case, the

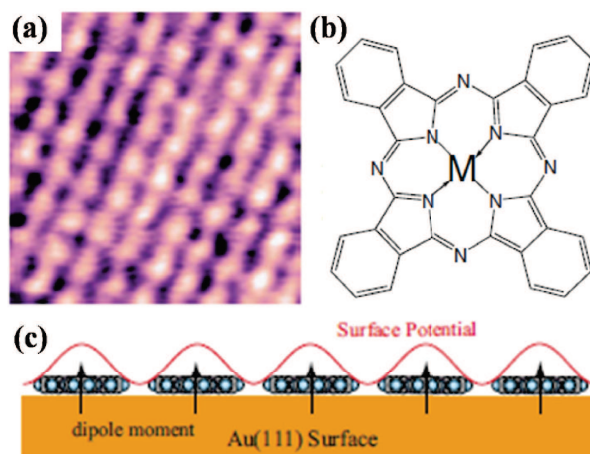


FIGURE 5.4: (a) CPD image using FM-AFM/KPFM of a CuPc monolayer on an Au(111) surface, $12 \times 12 \text{ nm}^2$, $\Delta f = -170 \text{ Hz}$. (b) Molecular structure of MPc, with $M = \text{Cu}$. (c) Dipole moment model to explain the molecular-scale SP contrast. Images modified from reference [220].

authors claimed [220] that the local dipoles may originate from a rearrangement of the electron cloud at the Au surface (keeping in mind that CuPc is a non polar molecule).

However, the exact nature of the forces involved in the KPFM imaging process at the molecular scale was not clearly established by the authors, who based all their conclusions on the modulation displayed by the CPD images. Especially, the dependence of the CPD magnitude and local contrast versus the tip-surface separation was not investigated. The relative contribution of both long range and short range electrostatic forces to the KPFM-compensated CPD was not established. At this stage, it is impossible to confirm that the reported contrast reflect the existence of local electric dipoles at the CuPc/Au(111) interface. The results may indeed as well be accounted by a local polarization of the underlying molecules induced by the proximity with the biased tip in the short range regime.

In summary, it is nowadays widely admitted that LCPD atomic contrasts originate from bias dependent SR interaction forces between the tip apex and the underlying sample surface. The mechanism behind this interaction force is dependent upon the sample. The short-range interaction on a semiconducting surface is likely due to covalent interactions similar to the one involved in the topographic imaging process in nc-AFM.[109] The measured LCPD is not a true representation of any one interaction but is a function of the bias dependent short-range force applied to a specific sample. The magnitude of the LCPD contrast depends both on the LR and SR interactions that are tip-surface distance dependent. Making a physical interpretation of the experimental results of LCPD measurements is difficult because the combination of these interactions may cause an

over-estimation of the true surface potential distribution. A model consistent of an accurate tip geometry and tip-sample separations, like the one described above for ionic solids and metallic adatoms, is needed for the extraction of physical values from the measured LCPD.

5.2 Molecular CPD of π -Conjugated Self-Assemblies

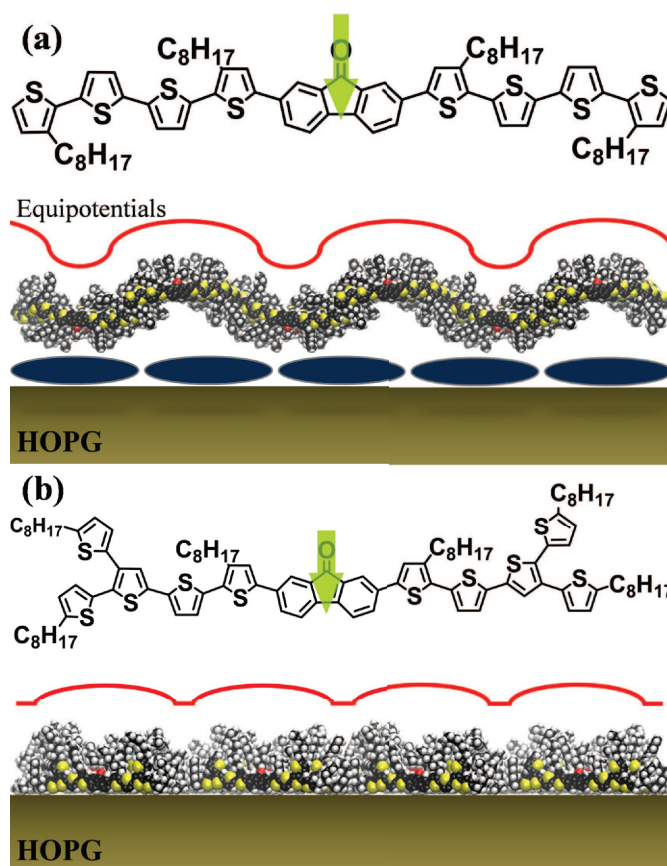


FIGURE 5.5: Chemical structures and dynamic simulations of edge-on stacks (side views) for (a) QTF8 (including face-on buffer layer) and (b) FG1 oligomers on a HOPG substrate. The main electric molecular dipoles at the fluorenone cores are indicated by green arrows. The red lines highlight that the electrostatic equipotential lines may display variations at the local scale, induced by the networks of the molecular dipoles.

In this work, the occurrence and nature of CPD contrasts at the molecular scale has been thoroughly investigated on two related model oligomers, labeled QTF8¹ [78] (seen in figure 5.5a) and FG1², [79] (seen in figure 5.5b), selected for their self-assembly

¹QTF8: 2,7-Bis(3,3'''-dioctyl-[2,2';5',2'';5'',2''']-quaterthiophen-5-yl)-fluoren-9-one

²FG1: 2,7-Bis(5-[3,5'''-dioctyl-4''-(5-octylthien-2-yl)-[2,2';5',2'';5'',2''']-quaterthiophene])-fluoren-9-one

properties. Both oligomers form self-assembled π -stacked edge-on nanowires on highly oriented pyrolytic graphite (HOPG).

Both molecules contain oligothiophene segments and a fluorenone central unit, the later group expected to carry the main molecular electric dipole at the C=O bond, as shown by figure 5.5. Calculations of the charge distribution and electric dipole of a fluorenone can be found in the work of Jozefowicz et al. [221] A dipole oriented perpendicular close to a surface induces a local change in the electrostatic potential of the substrate. Therefore, one may reasonably expect the existence of surface potential modulations correlated with the molecular dipoles at the fluorenone cores. For that reason, QTF8 and FG1 were chosen as model systems to probe the occurrence of CPD contrasts at the molecular scale.

Likewise to the case of atomic scale LCPD, we focus on the role of the SRE interactions and ask:

- (i) Is it possible to detect/image a CPD contrast at the molecular:submolecular scale?
- (ii) If so, are SRE forces alone responsible for the imaging process and are they related to the molecular dipoles?

5.2.1 Materials & Sample Fabrication

Fluorenone-based non-polymeric molecules are highly attractive materials for solution-processable solar cell applications due to the strong π -stacking interactions in the solid state.

The improved morphology could explain the good performances (ranking among the highest recorded for nonpolymeric materials) of OPV devices based on BHJ thin films where QTF and FG are used as the electron donor materials.[78, 79] The synthesis, characterization and photovoltaic properties (blended with PC₆₀BM and PC₇₀BM) of QTF8 and FG1 have been described elsewhere.[78, 79]

Thin deposits of QTF8 and FG1 were prepared by drop casting 10 mL of an anhydrous toluene solution (concentration 0.05 mg·mL⁻¹) on freshly cleaved HOPG substrates. The solvent was slowly evaporated under a toluene saturated atmosphere for 24h. A post deposition annealing was applied under UHV in the case of QTF8 (130°C for 3 hours). Both molecules self-assemble into edge-on π -conjugated nanowire stacks, which structural organization has been established by combining the results of NC-AFM with molecular mechanics (MM) and molecular dynamics (MD) simulations, briefly described hereafter.

5.2.2 QTF8 Topography on HOPG

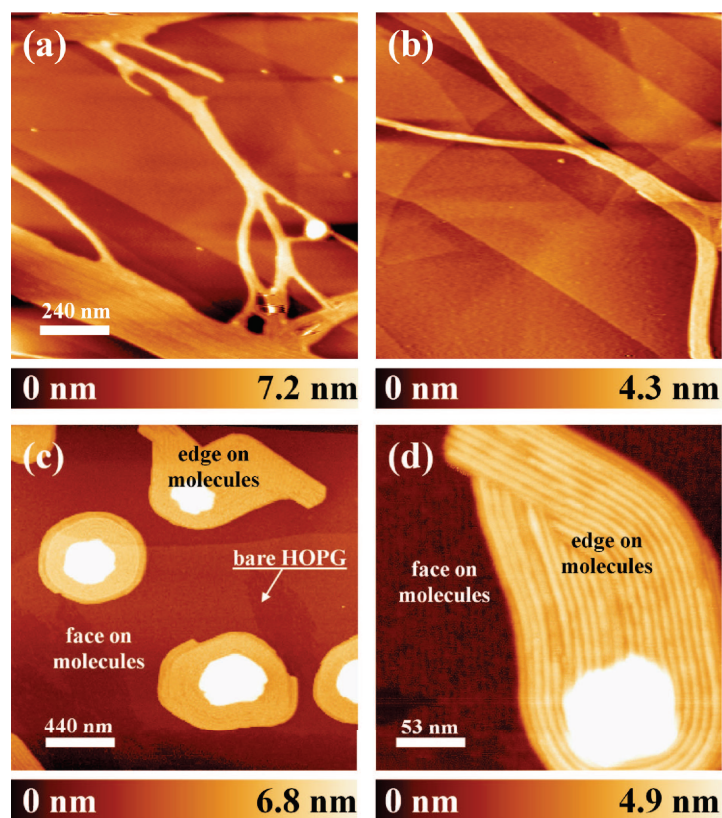


FIGURE 5.6: FM-AFM (UHV, 300K) 2D topography images of QTF8 thin films on HOPG. (a,b): 1200 nm \times 1200 nm, 600 \times 600 pixels, $\Delta f = -20$ Hz, $A_{vib} = 20$ nm, scan speed = 7 ms per pixel. (c): 2.2 $\mu\text{m}\times$ 2.2 μm . (d): 265 nm \times 265 nm. Edge-on stacks are formed on a buffer layer of face-on molecules, highlighted in (c) and (d). Images (c) and (d) have been modified from reference [33].

The QTF8 molecules form ordered aggregates in the form of fibrils (figure 5.6a,b) or stacks (figure 5.6c,d), with an effective stacking height of ~ 3 nm, consistent with previous FM-AFM [33] and TF-AFM [222] investigations. It is expected that the QTF8 π -conjugated system and its alkyl substituent will strongly interact with the underlying HOPG surface, giving rise to the formation of “face-on” 2D assemblies (described in chapter 2). However, considering the size of the QTF8 molecule (about 4 nm long, 2.5 nm wide, and 0.5 nm thick in its fully planar conformation), the value for the stack height clearly suggests that the molecular aggregates consist of π -stacked oligomers in the “edge-on” configuration, in which the plane of the conjugated system is perpendicular to the substrate and with fully extended octyl groups.[33]

The edge-on molecules (labeled in figure 5.6c,d) are in fact formed over of a monolayer of face-on molecules, adsorbed upon the HOPG surface. These face-on molecules provide a buffer layer that permits the formation of the edge-on supramolecular stacks,

and strongly attenuates the influence of the substrate on the stack nanostructure.[33] The role of a buffer monolayer has also been demonstrated on π -conjugated self-assembled oligo(p-phenylenevinylene) (OPV) on a Au surface, revealing that the presence of a monolayer can be a crucial factor for retaining the solution morphology and connectivity of fibrils on a surface.[223]

As explained in chapter 2, thermal or solvent annealing is known to improve the order of solid-state organic assemblies, by reducing the number of defects. This has been demonstrated in previous FM-AFM measurements, clearly revealing that under thermal annealing an improved ordering in the solid-state organic assemblies is observed.[33, 222]) Upon *in-situ* annealing, the apparent lateral periodicity becomes 7.0 ± 0.2 nm over most parts of the QTF8 stacks, which is slightly less than twice the length of a single oligomer.

5.2.3 QTF8 Modeling

The following molecular modeling has been performed by Dr. Mathieu Linares¹ in the Department of Computational Physics at Linköping University in Sweden. Molecular mechanics (MM) and molecular dynamics (MD) calculations have been carried out in order to investigate the organization of the QTF8 molecules in the assemblies. Further details about the molecular modeling packages and process can be found elsewhere.[33]

First, the most probable molecular conformers have been modeled:

- (i) by considering that the thiophene units within the two quarterthiophene segments are in an anti-conformation (which is the most stable situation in oligothiophenes) and,
- (ii) by examining the relative orientation of the two innermost thiophene rings with respect to the fluorenone unit; either in the *syn*-conformation or in the *anti*-conformation.

This gives rise to three conformers: *syn-syn*, *syn-anti*, and *anti-anti*, pictured in figure 5.7.

In a second step, assemblies consisting of edge-on π -stacked molecules (in the *syn-syn*, *syn-anti*, or *anti-anti* conformation) have been modeled, with the C=O bonds of the fluorenone units all pointing in the same direction within a given wire (this configuration being more stable than the one with alternating orientation of the fluorenone units along the wire). The three types of π -stacked nanowires are stable, with the *anti-anti* assembly more stable than the other two systems (by about $3.5 \text{ kcal}\cdot\text{mol}^{-1}$ per molecule), due to

¹Dr. Mathieu Linares: web.me.com/mathieulinaires

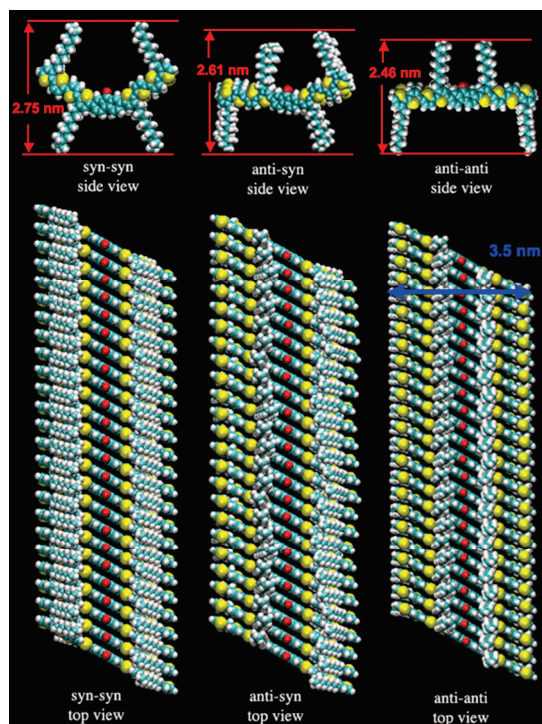


FIGURE 5.7: Molecular modeling calculations of edge-on π -stacked nanowires formed from QTF8 *syn-syn*, *anti-syn*, and *anti-anti* conformers (from left to right). Image adapted from reference [33].

a better π - π interaction between the core of the oligomers and a better van der Waals interaction between the alkyl chains. The results of the MD calculations indicate that the molecules within the three assemblies are slightly tilted in respect to the stacking axis. As a result, the width of the nanowires is slightly smaller than the length of the molecule (3.5 nm as opposed to 3.8 nm).

Finally, the assembly of adjacent nanowires in a 2D layer has been investigated starting from the most stable *anti-anti* wires. It is found that the most stable situation is with:

- (i) non-alternating tilting and,
- (ii) an alternating orientation of the fluorenone units.

This yields layers that are non-polar, because of the alternating orientation of the fluorenone unit (carrying the main molecular electric dipole, as seen in figure 5.5) from one wire (C=O bond pointing upward) to the next (C=O bond pointing downward), as illustrated by the oxygen atoms (in red) in figure 5.8. Upon optimization of these assemblies, a small displacement in the direction perpendicular to the layer occurs from one stack to the next. This improves the lateral interaction and the locking between the terminal-substituted thiophene units in adjacent nanowires (this clearly appears in the section through the layer shown in the top image of figure 5.8). As a result, the

lateral periodicity doubles, from around 3.5 nm to around 7.0 nm, consistent with the experimental observation.[33, 222]

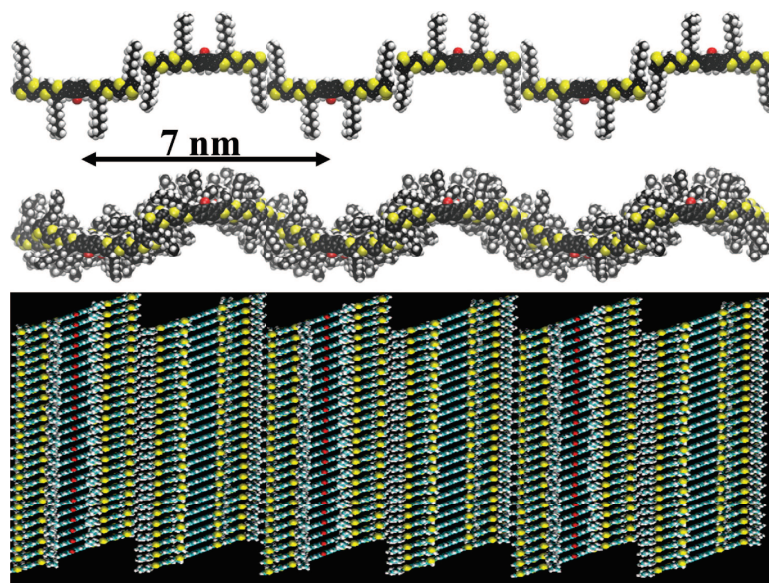


FIGURE 5.8: Molecular mechanics and dynamic simulations of the most stable supramolecular QTF8 stack, in the *anti-anti* conformation. (top: side view, bottom: top view).

5.2.4 FG1 Topography on HOPG

Like the QTF8 self-assembly, when drop-casted from solution onto a freshly cleaved HOPG substrate, FG1 forms edge-on π -stacked molecules. FM-AFM measurements revealed an average stacking height of $\sim 2.5 \pm 0.1$ nm. Contrary to the QTF8 self-assembly, NC-AFM investigations did not clearly reveal the presence of a face-on buffer layer. FM-AFM images (and corresponding damping images) of a FG1 molecular island self-assembled on a freshly cleaved HOPG substrate is seen in figure 5.9.

The FG1 self assemblies displayed an highly ordered morphology after direct deposition on HOPG without a thermal annealing treatment, unlike QTF8. In this case, the lattice periodicity was found to be slightly larger than the widths of a single molecule. In order to accurately determine the molecular lattice periodicity of FG1 stacks, a series of nc-AFM topographic images has been successively acquired, until reaching a complete stabilization of the apparent stripe to stripe distance (as deduced from FFT patterns: inset of figure 5.9f). This procedure ensures that the images are free from artifacts due to piezo creep or thermal drift. The mean lattice value deduced from these measurements is 4.55 ± 0.05 nm.

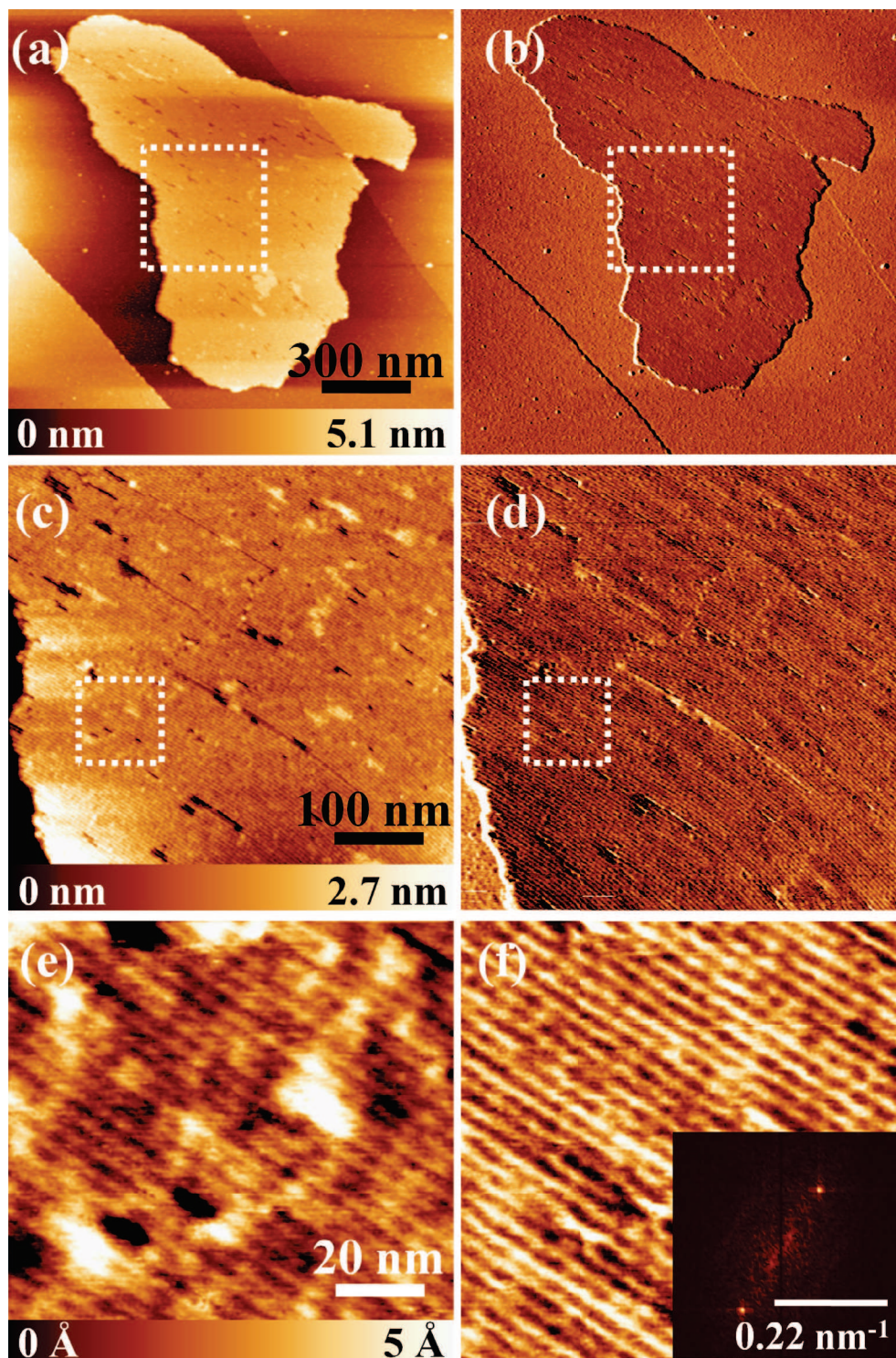


FIGURE 5.9: FM-AFM (UHV, 300K) 2D topography (a,c,e) and damping (b,d,f) images of a FG1 monolayer self-assembled on a HOPG substrate. (a,b): $1500 \text{ nm} \times 1500 \text{ nm}$, 600×600 pixels, $\Delta f = -13 \text{ Hz}$, $A_{vib} = 14.6 \text{ nm}$, scan speed = 5 ms per pixel. (c,d): Magnified images corresponding to the area delimited by the white box in (a,b). $500 \text{ nm} \times 500 \text{ nm}$, 600×600 pixels, $\Delta f = -25 \text{ Hz}$, $A_{vib} = 14.6 \text{ nm}$, scan speed = 5 ms per pixel. (e,f): Magnified images corresponding to the area delimited by the white box in (c,d). $100 \text{ nm} \times 100 \text{ nm}$, 400×400 pixels, $\Delta f = -25 \text{ Hz}$, $A_{vib} = 14.6 \text{ nm}$, scan speed = 5 ms per pixel.

5.2.5 FG1 Modeling

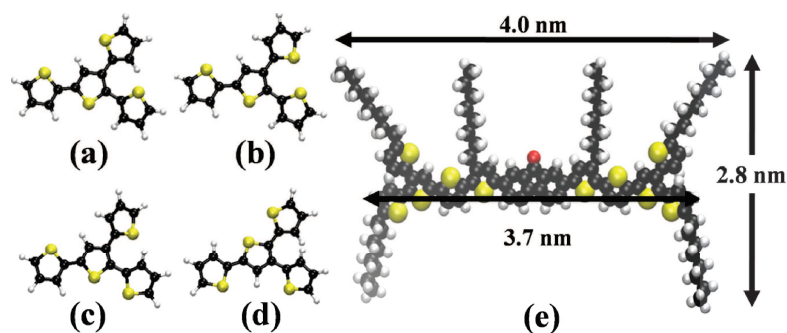


FIGURE 5.10: (a,d): Four possible conformations for the thiophenes at the extremity of the FG1 molecule. (e) Most stable conformation for the FG1 molecule.

Molecular mechanics (MM) and molecular dynamics (MD) calculations have been performed using the packages described for QTF8.[224–226] To separate the different effects that rule the self-assembly of the FG1 molecule, a conformational study of a model molecule containing 4 thiophenes (as seen in figure 5.10a-d) was performed in order to determine the most stable conformation of FG1. After the optimal conformation for the thiophenes was determined (figure 5.10d), it was necessary to determine the most stable conformation of the entire molecule.

It has been determined in a previous study that the thiophene chains attached to the fluorenone moiety preferred to adopt an all-trans configuration.[227] According to that and to the study of the extremity of the molecule, the most stable conformation for the FG1 molecule has been determined, seen in figure 5.10e.

Based on this, there are two ways to assemble the π -conjugated stacks, with the C=O bonds pointing in the same direction for all nanowires, or in an opposite direction from one wire to the next (figure 5.11 a and b, respectively). These assemblies display a lattice periodicity of 34.98 Å and 64.96 Å, respectively neither of which are consistent with the results from nc-AFM experiments.

Therefore, a new model was developed to account for the reported data, in which the alkyl chains at the extremity of the molecule interact with the underlying graphite substrate. It follows the absence of experimental evidence in favor of the existence of a face-on buffer layer. In order to favor the adsorption on the graphite surface, the alkyl chains at the extremity of the molecule are rotated. This situation favors the formation of CH- π interaction, and allows a full adsorption of the alkyl chains on the graphite surface (Figure 5.12). Following this assumption, the density of the stack assembly is now in agreement with the experiment. The configuration of the fluorenone unit (carrying the main molecular electric dipole, as seen in figure 5.5) does not alternate as in the case

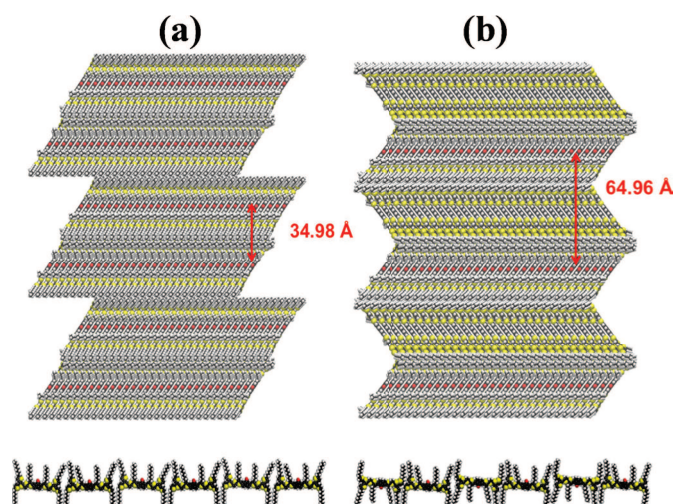


FIGURE 5.11: Two configurations to assemble the FG1 stack, with the C=O pointing in the same direction (a), or with the C=O pointing in opposite direction (b).

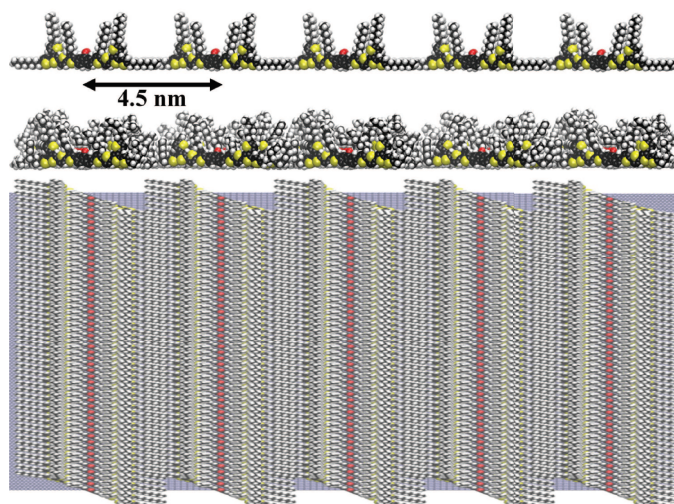


FIGURE 5.12: Molecular mechanics and dynamics simulations of the most stable supramolecular FG1 stack. Top: static side view. Middle: dynamic side view. Bottom: top view (static).

of QTF8, but remains in a single direction with the C=O bond pointing upward (figure 5.11a).

Considering the full assembly on the graphite surface, the intermolecular distance in the stacking direction is 4.42 \AA , and the distance between the rows is 45.7 \AA , in excellent agreement with nc-AFM topographical experiments. Finally, as shown by figure 5.12(middle), a dynamic during 500 ps has been performed on the system. The topographic profiles extracted from nc-AFM images in the direction of the modulation are in accordance with the shape simulated by the MD simulations. However, modeling

of the FG1 predicts a stacking height of ~ 1.8 nm, which is not in agreement with FM-AFM measurements ($\sim 2.5 \pm 0.1$ nm). Further optimization of the FG1 modeling will be needed in order to correlate more accurately with the experimental results.

5.2.6 Frequency Modulation KPFM

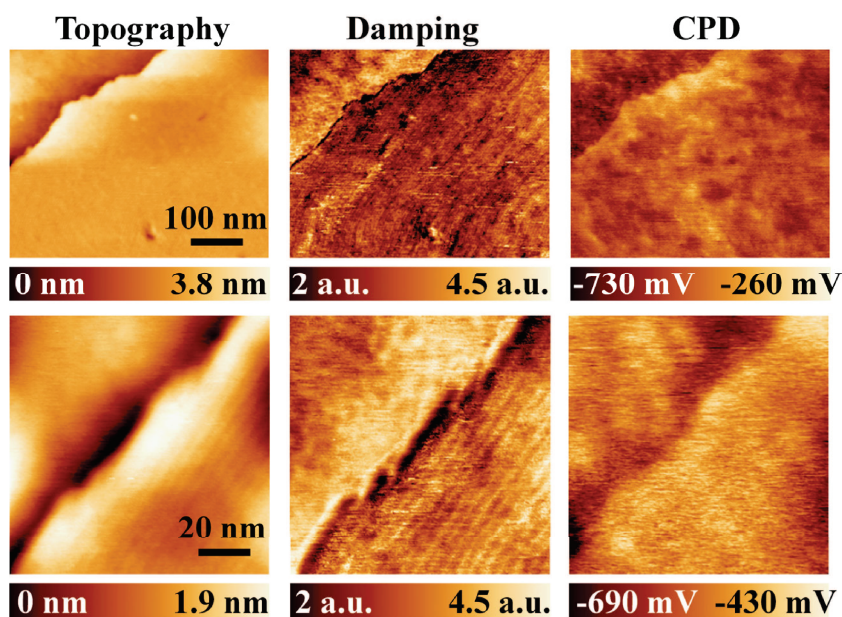


FIGURE 5.13: FM-AFM (UHV, 300K) 2D images of the topography, damping and CPD of a FG1 monolayer on a HOPG substrate using FM-KPFM. (top: $500 \text{ nm} \times 400 \text{ nm}$, 512×410 pixels, $\Delta f = -20 \text{ Hz}$, $A_{vib} = 40 \text{ nm}$, scan speed = 150 ms per pixel) (bottom: $100 \text{ nm} \times 100 \text{ nm}$, 250×250 pixels, $\Delta f = -30 \text{ Hz}$, $A_{vib} = 40 \text{ nm}$, scan speed = 50 ms per pixel)

As previously described in chapter 4 on the P3HT:PCBM BHJ blend, FM-KPFM was deployed using PtIr₅ coated Si cantilevers at a resonant frequency of 338 kHz, and a modulation frequency of 1.3 kHz. The scan speed (150 and 50 ms per pixel for figure 5.13 top and bottom, respectively) was limited primarily due to a rather low signal to noise ratio. Therefore, a relatively low frequency shift setpoint (close tip-sample distance) of -20 and -30 Hz was used in combination with a 20 dB damping attenuator in order to reduce the input amplitude. At higher magnification, the topography and damping images clearly reveal the molecular lattice of the FG1 assembly. Despite this, molecular resolution CPD was not obtained. Frequency shift setpoints below -30 Hz resulted in an instability (“jump to contact”) over the course of an entire image.

5.2.7 LCPD of QTF8 and FG1 Monolayers on HOPG

In the following, the results have been obtained using AM-KPFM. The data was recorded using PtIr₅ coated Si cantilevers (as described in table 3.2) at a resonant frequency (f_0) of ~ 62 kHz. As previously described, the scan speed in AM-KPFM was limited primarily due to the large quality factor of the cantilever in UHV, which means that the measured amplitude changes are slow (according to equation 3.15). The modulation frequency (f_{mod}) was tuned to the second resonance frequency at $\sim 6.3f_0 \approx 390$ kHz.

5.2.7.1 CPD Dependence vs. the Operating Set-Points

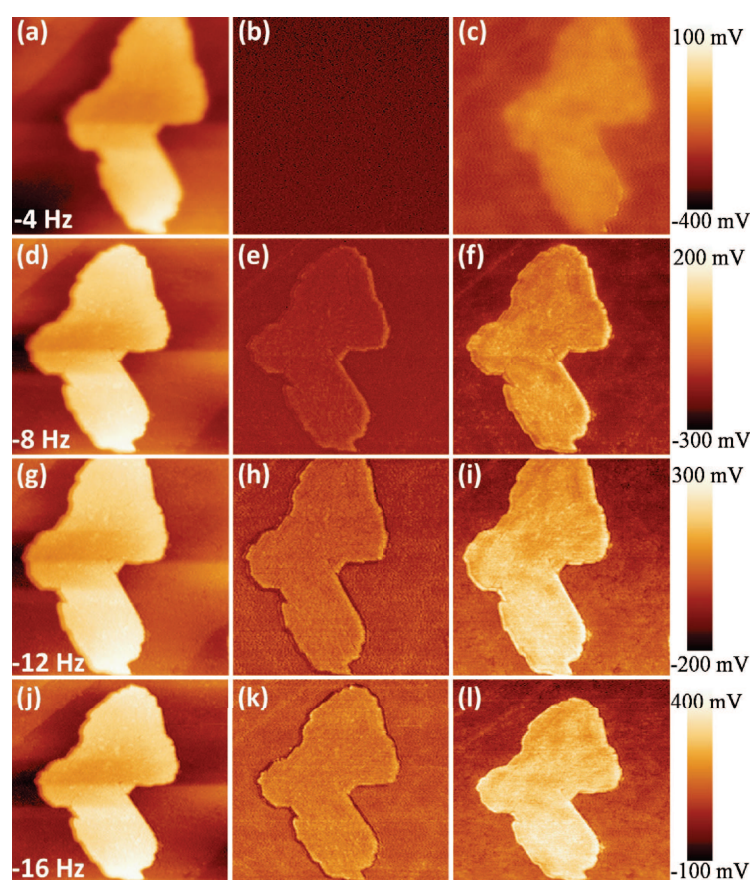


FIGURE 5.14: Topography [(a), (d), (g) and (j)], damping [(b), (e), (h) and (k)], and CPD [(c), (f), (i), and (l)] of a FG1 molecular island on an HOPG substrate using AM-KPFM (600 nm \times 600 nm, 512 \times 512 pixels, $A_{vib} = 55.7$ nm, scan speed = 20 ms per pixel). Images (a), (b) and (c) recorded at $\Delta f = -4$ Hz, (d), (e) and (f) at $\Delta f = -8$ Hz, (g), (h) and (i) at $\Delta f = -12$ Hz, and (j), (k) and (l) at $\Delta f = -16$ Hz.

To investigate the influence of the tip-surface separation on the KPFM signal, a first series of images (topography, damping and CPD) have been acquired at the mesoscopic scale on a FG1 thin film with sub-monolayer coverage while varying the frequency shift

set point (Δf) and keeping the vibration amplitude (A_{vib}) constant, as seen in figure 5.14.

The frequency shift dependence of the difference between the CPD levels (average values) measured over the oligomer stack and the substrate ($\Delta_{CPD} = CPD_{FG1} - CPD_{HOPG}$) has been plotted in figure 5.16b. The data points in figure 5.16a and b have been recorded from figure 5.15, where the behavior of the damping and CPD reveals an increasing contrast as a function of increasing Δf . Δ_{CPD} dramatically increases when lowering the set point (i.e. decreasing the tip-surface separation) below the value corresponding to the apparition of a contrast in the damping images ($\Delta f_{onset} \approx -5$ Hz), and a saturation plateau is reached below $\Delta f_{sat} \approx -10$ Hz. A similar behavior is seen while keeping the frequency shift constant ($\Delta f = -15$ Hz) but varying the amplitude A_{vib} from 39 to 66 nm, reaching a plateau at ~ 55 nm. The Δ_{CPD} correlation between the data acquired at variable Δf and variable A_{vib} is confirmed by the blue circles in figure 5.16b and c, which represents data points acquired with the same parameters ($\Delta f = -15$ Hz and $A_{vib} = 55.7$ nm). A $\Delta_{CPD} \simeq 170$ mV is observed in both cases.

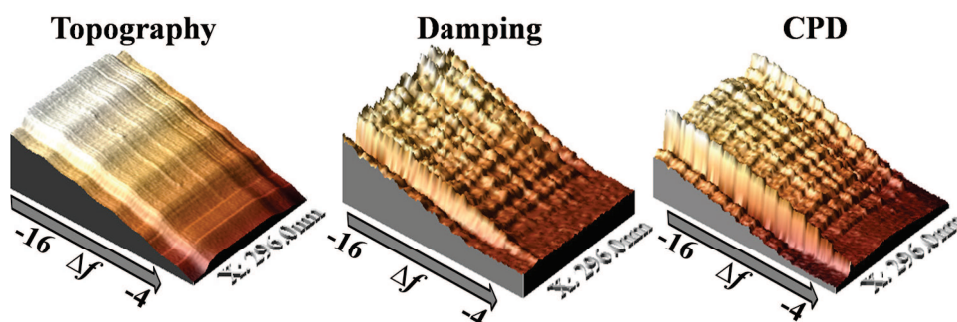


FIGURE 5.15: FM-AFM (UHV, 300K) 3D topography, damping and CPD of the same scan line of a monolayer of a FG1 molecule self-assembled on a HOPG substrate using AM-KPFM as a function of Δf from -4 Hz to -16 Hz every 30 lines (in constant line mode). (296 nm wide, 390×500 pixels, $A_{vib} = 56$ nm, scan speed = 15 ms per pixel).

In the large amplitude regime, the tip-surface distance d (at the lowest point of the cantilever oscillation cycle) is directly related to the normalized frequency shift γ , equation 3.20.[98] A second series of images (not shown) has been recorded at variable amplitudes, but keeping a constant $\gamma = -3.7 \text{ fN} \cdot \sqrt{m}$ by proper adjustments of the frequency shift. In that case, the CPD is nearly unchanged regardless of the amplitude set point (as seen in figure 5.16d), which confirms that the tip-surface separation is the key parameter in the above mentioned frequency shift dependence of the CPD contrast.

Before addressing more precisely the nature of the forces involved in the KPFM imaging, it is relevant to compare the measured CPD with what is expected for the surface potential induced by the molecular dipoles from simple considerations. Following earlier works [217, 219, 228], the difference of surface potential between the edge-on stack

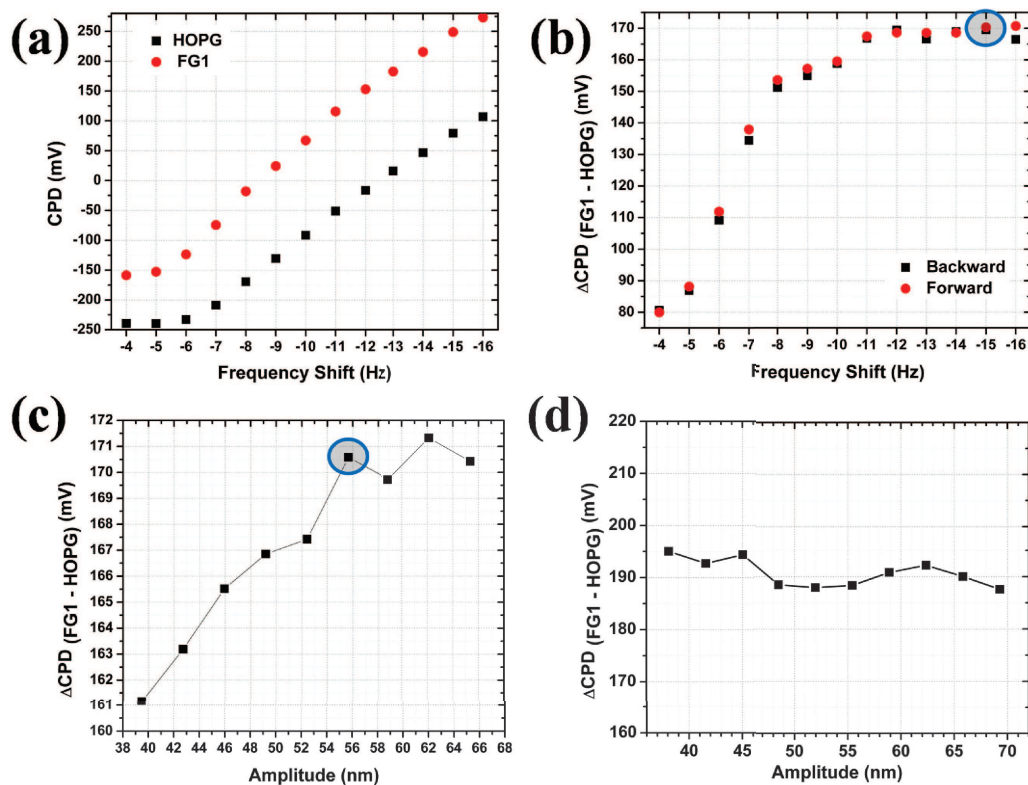


FIGURE 5.16: (a) CPD as a function of Δf for the FG1 monolayer and the HOPG substrate in the backward scan direction at a constant vibration amplitude ($A_{vib} = 55.7$ nm). (b) CPD difference between the FG1 monolayer and the HOPG substrate (Δ CPD = $CPD_{FG1} - CPD_{HOPG}$) as a function of Δf for the forward and backward scan directions at a constant $A_{vib} = 55.7$ nm. (c) CPD difference between the FG1 monolayer and the HOPG substrate as a function of A_{vib} in the backward scan direction at constant $\Delta f = -15$ Hz. (d) CPD difference between the FG1 monolayer and the HOPG substrate as a function of A_{vib} in the backward scan direction at constant normalized frequency shift $\gamma = -3.7$ fN $\cdot\sqrt{m}$. The blue circles in (b) and (c) represent data points acquired with the same parameters ($\Delta f = -15$ Hz and $A_{vib} = 55.7$ nm), where Δ CPD $\simeq 170$ mV.

and the substrate may be described as:

$$\Delta V_s = \frac{\mu \times \Gamma}{\varepsilon \times \varepsilon_0}, \quad (5.6)$$

where μ is the value of the dipole moment normal to the substrate for a molecule within the stack, Γ is the molecular surface concentration, ε the dielectric constant of the molecular layer and ε_0 the permittivity of free space. One shall keep in mind that the effective dipole μ differs from the one in the absence of depolarizing effects.[217, 219, 228]

In our experiments, the CPD difference between the stacks and the substrate reaches a maximum of 170 - 190 mV (depending of the normalized frequency shift setpoint, as

shown by figure 5.16). With an average area of ca. 2 nm^2 per FG1 molecule within the stacks and a relative dielectric constant ϵ of ca. 3 (which is a reasonable value for organic semiconductors), yields an effective molecular dipole on the order of 2.7 Debye per molecule, which is remarkably close to the values previously reported for fluorenones.[218, 221] Besides, the CPD increase over the stack corresponds to a reduction of the surface work function (the bias being applied to the tip in our setup), which has also been observed for porphyrins on HOPG.[228] Moreover, in both cases, the molecular dipole is expected to point downward from the molecule to the substrate.

In the case of QTF8, remarkably the CPD does not exceed a few tens of mV, even at the smallest tip-surface separations. This result seems consistent with the expected non polar nature of the QTF8 stacks, for which the dipole moment alternates from one nanowire to the next. However, the comparison between FG1 and QTF8 shall be carried out keeping in mind :

- (i) the possible differences induced by a buffer of face on molecules and,
- (ii) the open questions regarding the exact nature of FG1 assembly.

5.2.7.2 Molecular CPD Contrast

To check the occurrence of local CPD contrasts, another set of high magnification images (figure 5.17) has been recorded on the FG1 stack. First, we underline that topographic contrasts at the molecular wires scale are only achieved for tip-sample separations equal or less than the one corresponding to the onset of a contrast in the damping images ($\Delta f \leq \Delta f_{\text{onset}}$). For greater tip-surface distances ($\Delta f > \Delta f_{\text{onset}}$), the molecular network cannot be resolved in the topographic images (figure 5.17a, left panel). As expected, the lateral resolution of the CPD images improves noticeably when reducing the tip-sample separation as shown by the comparison between the CPD images presented in figure 5.17c and f. In figure 5.17f, features with lateral dimensions of a few nanometers are clearly resolved. However, CPD modulations correlated with the molecular lattice appear only after a further decrease of the tip-surface separation (figure 5.17i), for set points corresponding to the saturation plateau in figure 5.16b ($\Delta f \leq \Delta f_{\text{sat}}$).

Similar results have been achieved in the case of QTF8. In the following, the correlation between the topography, damping and CPD local contrast is briefly discussed by confronting the results achieved on both oligomers.

Topography, Damping, CPD Contrast Relationship Since the LCPD imaging mechanisms still remains unclear, it may be useful to correlate the topography, damping and CPD local contrast. This may help to establish a relation between the LCPD contrast and the molecular electric dipoles.

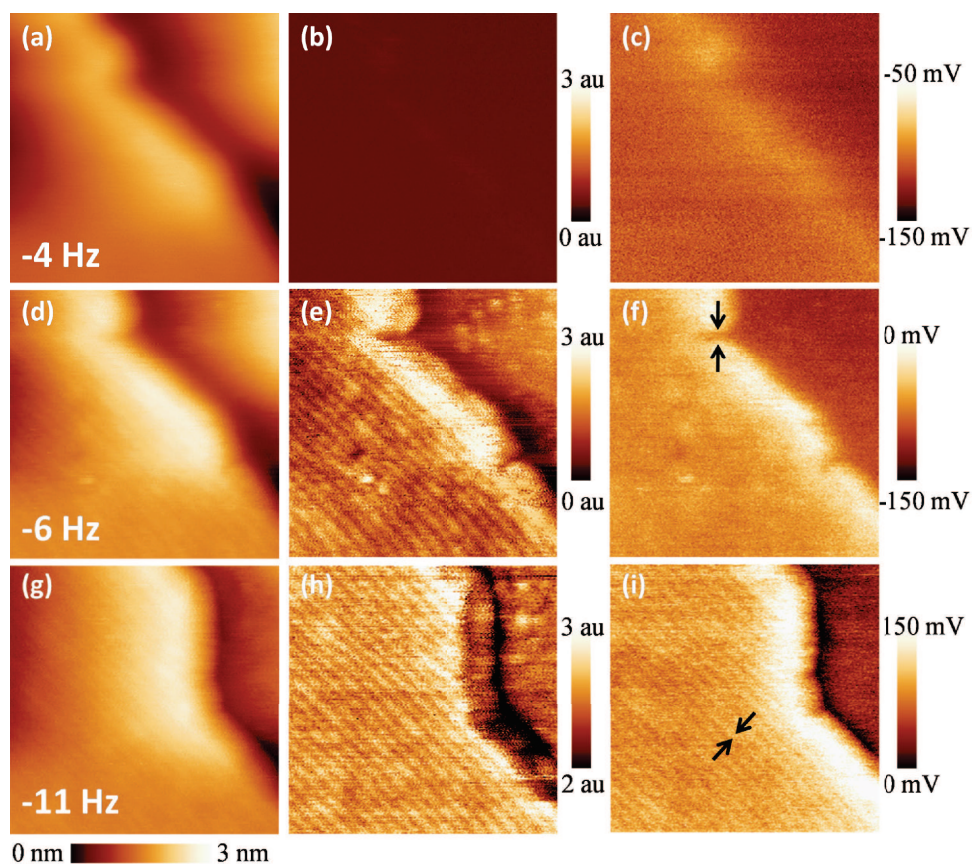


FIGURE 5.17: Topography [(a), (d), and (g)], damping [(b), (e), and (h)], and CPD [(c), (f), and (i)] of a FG1 monolayer on a HOPG substrate using AM-KPFM (100 nm \times 100 nm, 400 \times 400 pixels, $A_{vib} = 55$ nm, scan speed = 25 ms per pixel). Images (a, b, c) are at $\Delta f = -4$ Hz, (d, e, f) at $\Delta f = -6$ Hz, and (g, h, i) at $\Delta f = -11$ Hz. Arrows in image (f) and (i) indicate feature resolutions of ~ 5 nm and ~ 2.5 nm, respectively.

In the case of FG1, unfortunately it was not possible to definitely correlate the observed CPD and damping levels with those of the topography. However, the correlation between the CPD and damping levels is clearer. The CPD corresponds inversely to that of the dissipation signal, illustrated by the 3D CPD composite images in figure 5.20.

A tentative proposal is given in figure 5.18. Better results were achieved for QTF8 thanks to its larger lattice periodicity and the existence of a characteristic contrast in the damping images previously reported and confirmed in this work. Figures 5.19 and 5.21g,h,i clearly reveal that the topographic and dissipation images display opposite contrasts.

More precisely, the dissipation (figures 5.19b and 5.21b) is higher over the low topography regions, and vice versa. This is consistent with previous work using tuning-fork AFM (TF-AFM) in the qPlus configuration [114] carried out in the low amplitude

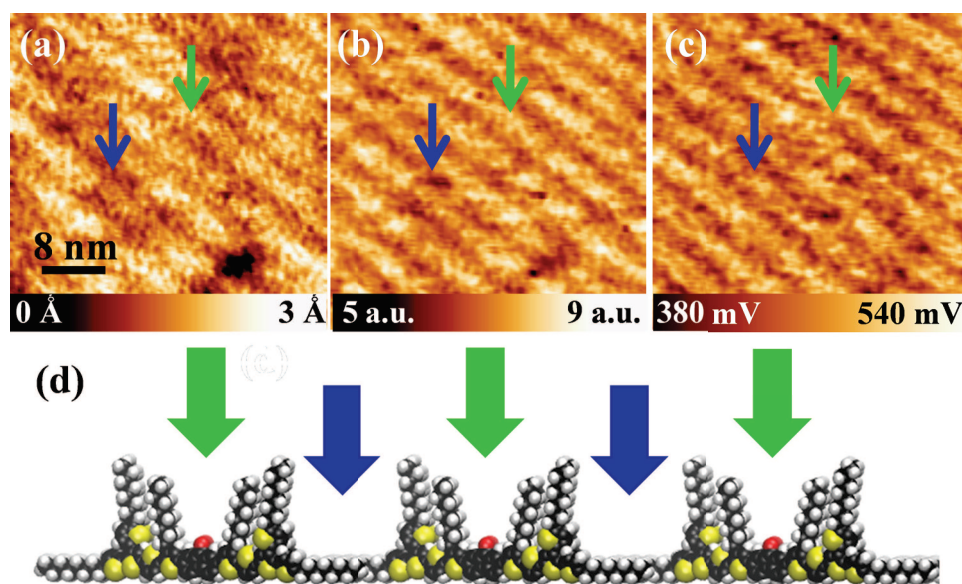


FIGURE 5.18: Topography (a), damping (b), and CPD (c) of FG1 self-assembled on HOPG using AM-KPFM. ($40\text{ nm}\times 40\text{ nm}$, 200×200 pixels, $\Delta f = -26\text{ Hz}$, $A_{vib} = 55\text{ nm}$, scan speed = 40 ms per pixel). Blue and green arrows in (a,b,c) indicate areas marked in (d).

regime ($A_{vib} < 0.5\text{ nm}$).^[33, 222] The CPD displays an opposite behavior being “in-phase” with the topography.

A former model to account for the local damping contrasts, proposed by Hayton et al., was based on the variation of the local mechanical properties within the stack at the sub-molecular scale.^[222] It was assumed that the stack may behave as a rigid object sustained by flexible pillars over which the damping is maximized, seen in figure 5.19g.

However, our data raises the question about the possible electrostatic origin of the damping. Such an effect could happen if the real tip-surface potential difference is not fully compensated by the KPFM feedback loop which can happen in the short range regime (similarly to the case of ionic crystals).

In that sense, it is remarkable that both QTF8 and FG1 display “out of phase” damping and CPD contrast. Since the “flexible pillars” are specific to the QTF8 stacks, the mechanistic model for the damping signal may be revised in favor of the electrostatic one.

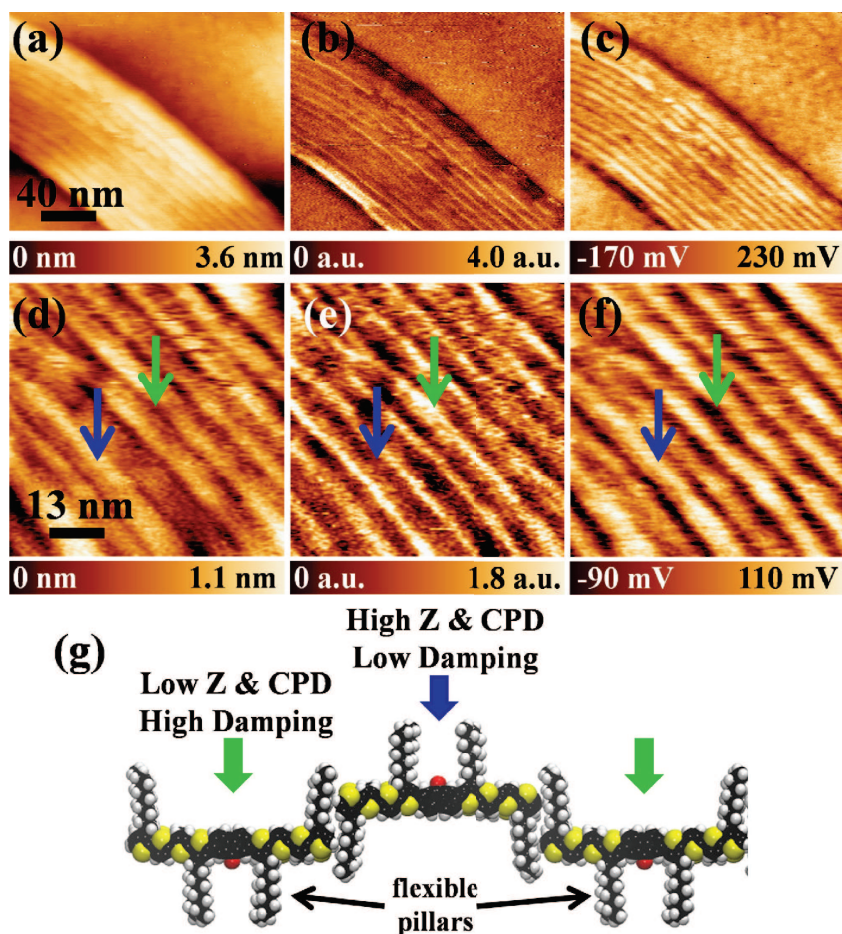


FIGURE 5.19: FM-AFM (UHV, 300K) 2D topography (a,d), damping (b,e) and CPD (c,f) images of a monolayer of a QTF8 molecular wire self-assembled on a HOPG substrate using AM-KPFM. (a,b,c): $200\text{ nm} \times 160\text{ nm}$, 600×480 pixels, $\Delta f = -30\text{ Hz}$, $A_{vib} = 20\text{ nm}$, scan speed = 16 ms per pixel. (d,e,f): $65\text{ nm} \times 65\text{ nm}$, 600×600 pixels, $\Delta f = -40\text{ Hz}$, $A_{vib} = 17\text{ nm}$, scan speed = 6 ms per pixel. Blue and green arrows in (d,e,f) indicate fluoronene orientation up and down, respectively, as marked in (g).

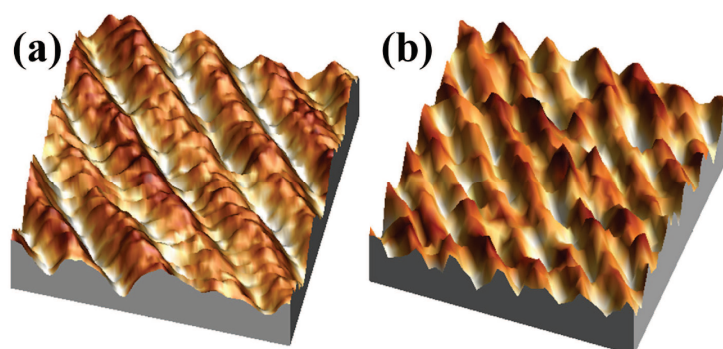


FIGURE 5.20: 3D composite images of the CPD (z-scale) with damping color code to illustrate the opposite contrast of the CPD and Damping signals on QTF8 (a) and FG1 (b) with bright indicating higher damping signals over lowest part of CPD. ($40\text{ nm} \times 40\text{ nm}$, 300×300 pixels, $\Delta f_{\text{HOPG}} = -40\text{ Hz}$, $\Delta f_{\text{FG1}} = -26\text{ Hz}$)

5.2.7.3 Distance Dependant Spectroscopy

Distance-spectroscopy measurements were performed by recording damping(z) and CPD(z) curves at selected locations on QTF8 molecular stacks (red and blue arrows labeled in figure 5.21), the feedback loop being disabled during the acquisition. For this data set, $z=0$ corresponds to the tip-surface distance at the regulated frequency shift set point before opening the feedback loop. Above all locations, the CPD shows a well marked drop from $z=0$ (regulated set point) to $z\approx 0.45$ (indicated by the green dash line in figure 5.22), and an almost constant value for greater tip-surface distances. This point characterizes the onset of the short range forces, as shown in the damping curves given as an inset in figure 5.22.

Above the threshold position marked in the spectroscopy curves in figure 5.22 at $\sim 4.5\text{\AA}$, the SRE forces do not contribute to the KPFM compensated CPD, which directly reflects the potential variations of the imaged surface. In that regime, the surface potential distribution may already be acquired with a resolution of a few nanometers, as the tip-surface separation can be on the order of 1 nm or less. This is almost the case of the data presented in figure 5.17(f), which has been acquired near the onset of the SRE forces. Reducing the tip surface separation, a crossover occurs between the LR and SR regimes, due to the increasing influence of SRE forces. At the smallest tip-surface separations, the “local” CPD becomes dominated by the contributions of SRE forces, accounting for the appearance of modulations correlated with the molecular lattice in CPD images. However, as in the case of atomic contrasts, these variations cannot be attributed directly to local changes in the surface potential, due to non conventional proximity effects between the tip apex and the surface.

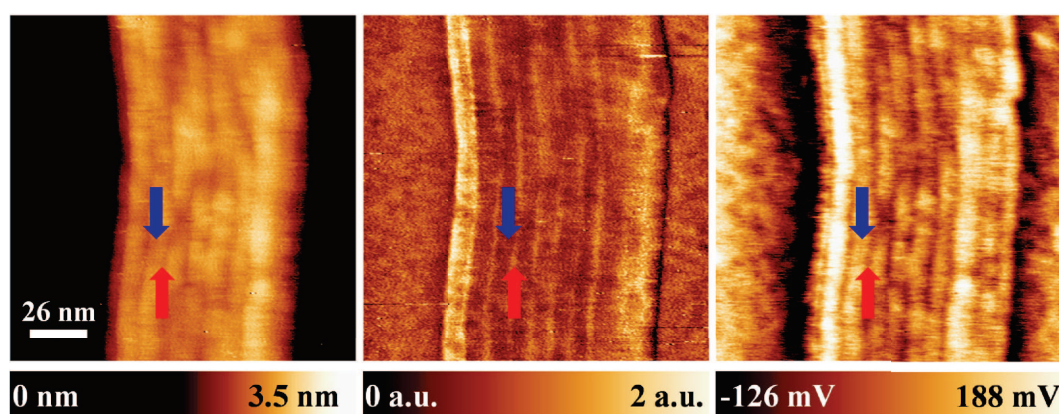


FIGURE 5.21: (a) Topographic, (b) damping, and (c) CPD images using AM-KPFM ($140\text{ nm}\times 140\text{ nm}$) of a QTF8 stack on HOPG recorded with $A_{vib} = 35\text{ nm}$ and $\Delta f = -20\text{ Hz}$. Arrows pointing up and down highlight the locations corresponding to the two different molecular orientations probed during z -spectroscopy measurements.

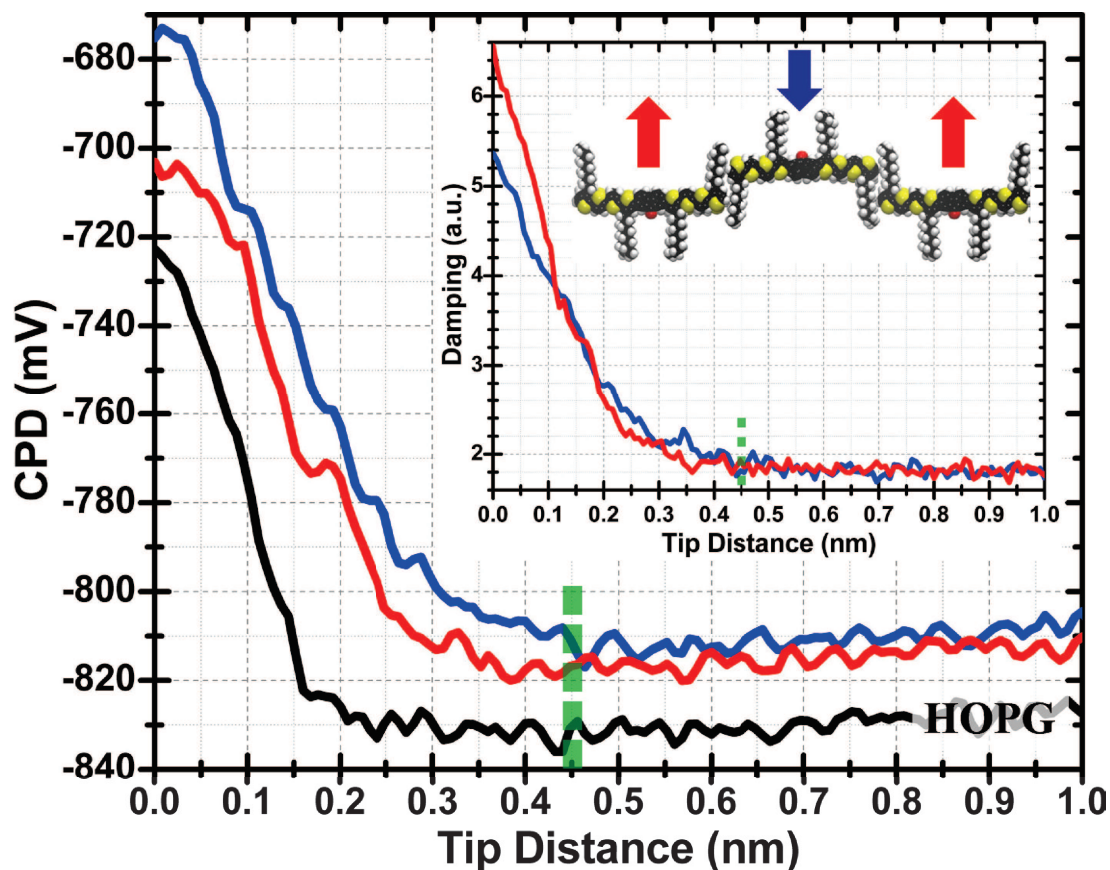


FIGURE 5.22: CPD as a function of tip-sample distance (curves averaged from 20 data points) ($\Delta f_{setpoint} = -25$ Hz, $A_{vib} = 41$ nm), recorded over the locations highlighted by the arrows in the inset. Inset: Damping signal as a function of tip-sample distance. The green dashed line indicates the onset of SR forces.

5.3 Conclusions

In summary, CPD contrast can be achieved at the molecular scale on edge-on π -stacked nanowires. The magnitude of the CPD is strongly dependent upon the tip-surface distance, and CPD contrasts correlated with the topography (i.e LCPD) are only achieved at minimal tip-surface separations. A crossover has been observed to occur between the LR and SR force regimes, in which SRE forces contribute to the measured CPD at a typical tip-sample separation on the order of 1 nm. This result is remarkably similar to the case of ionic crystals and metallic adatoms.[214, 215]

Unfortunately, in our case, the imaging mechanisms remain unclear, and it was not possible to establish a relation between the LCPD contrast and the lattice of the molecular electric dipoles. However, it is highly probable that a tip-induced proximity effect is involved in the CPD imaging process that would make a quantitative measurement of the local electric dipoles impossible. However, the LCPD may follow the periodicity of the surface potential, as in the the case of ionic crystals.[130, 146, 204]

Alternatively, our results demonstrate that the influence of the SRE forces can be minimized by working near the onset of the damping contrast. This provides an indication that by adjusting the tip-surface separation, an optimal lateral resolution can be achieved in “conventional” CPD images (i.e. images registered at tip-surface separation out of the range of SRE forces) on organic layers. This approach may be especially useful for further investigations of the surface photo-voltage of nano-phase segregated organic photovoltaic blends [189] and further investigations on organic layers for accurate work function measurements. Accurate measurements of the surface potential modification induced by polarized SAMs may also benefit from this procedure.

Novel Transparent Electrodes:

Introduction to Transparent Electrodes
Work Function Measurements
AM-KPFM/UPS of Functionalized CNTs

Ce chapitre présente les résultats d'une étude combinant plusieurs techniques, dans le but d'estimer la fonction de sortie d'électrodes transparentes à base de nanotubes de carbones mono-parois fonctionnalisés par des particules métalliques. Une série d'échantillons a été étudiée par microscopie à sonde de Kelvin en mode simple passe, par spectroscopie UPS et par spectroscopie XPS. Les valeurs de fonction de sortie estimées par microscopie à sonde de Kelvin sont comparées à celles déduites des mesures UPS.

In this chapter, a multitechnique interdisciplinary investigation was performed in order to characterize the work function of flexible transparent electrodes, based on functionalized carbon nanotubes using metallic nanoparticles. A series of single wall carbon nanotube networks was characterized by single pass Kelvin probe force microscopy, ultraviolet photoelectron spectroscopy, and X-ray photoelectron spectroscopy. The work function values obtained by KPFM are compared to the ones measured by UPS.

6.1 Novel Transparent Electrodes

Transparent conductive coatings are used in OPV device applications where it is necessary to transport electrical charges while not losing the optical properties of the particular substrate or optical component. For decades, transparent conductive oxides (TCO) have been developed and are still widely used.[229] For instance indium-tin oxide (ITO), $\text{In}_2\text{O}_3:\text{Sn}$, is still a “reference”, but it suffers from significant weaknesses such as the risky long term cost and limited supply of indium, the fragility or brittleness of ITO films, and the costly layer deposition requiring vacuum. In addition, ITO is not very compatible with polymer substrates due to its high deposition temperature of around 600°C . Therefore, alternatives are being sought such as graphene thin films, thin metal films and inherently conductive polymers (ICPs).

However, amongst the most promising materials currently under study for TCO replacement, carbon nanotubes (CNTs) demonstrate high potential.[230–234] Since carbon nanotubes (CNTs) were discovered by S. Iijima in 1991, they have attracted a great deal of interest from scientists in various research fields including electronics, optoelectronics and mechanics.[81–83] Carbon nanotubes can exhibit either metallic or semiconducting behavior depending on their band gap (which can range from 0 to about 2 eV) and electrical conductivity.

To form a flexible transparent conductive film using CNTs, researchers have focused on achieving a low sheet resistance (R_s) and a high transmittance (T).[232, 235] Although CNT-based conductive films of this type can be used to achieve flexible OLEDs and OPVs, their integration into operational devices poses many significant challenges. A major issue concerns the energy level alignment between the CNT thin film and the other active layers of the device. One approach to avoid these difficulties relies on modifying the effective work function of the conductive layer of the CNTs.[236, 237] The work function value plays a central role in determining efficiency and performance of the device, via control of the hole extraction process. In this way, the work-function engineering of the conductive layer can be used to integrate devices with controlled electronic energy levels. A previous report has shown that pristine SWCNT electrodes (a mixture of $1/3$ metallic and $2/3$ semiconducting tubes) have a work function of 4.8–4.9 eV.[238]

6.2 Work Function Measurements

Previous reports on ITO and TiO_2 have suggested that surface contaminants can significantly reduce the work function as deduced from the UPS measurements.[239–241] The work function is an extremely sensitive indicator of the state of a surface, and therefore of the environment surrounding it, since gases or other adsorbed species may induce substantial variations of the energy required to remove an electron from the Fermi level. In addition, the measured value is also known to be a function of the technique used. KPFM measures the local work function difference under the probe, whereas ultraviolet photoelectron spectroscopy UPS measures the lowest work function patch on the surface, even if it is only a small fraction of the surface area. Thus, KPFM work function values are often higher than those measured by UPS.

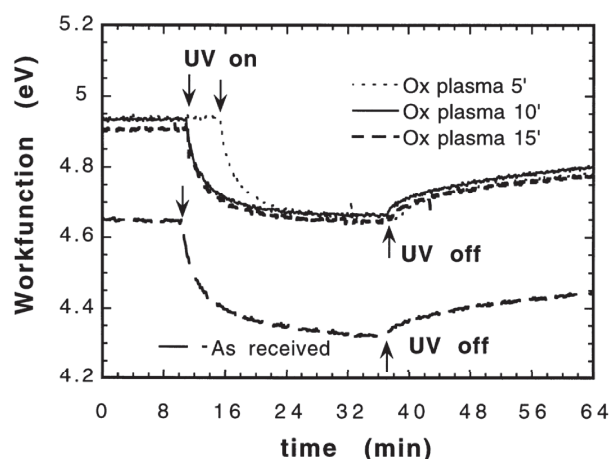


FIGURE 6.1: The shift in the contact potential difference of an ITO surface, induced by the UV irradiation. Image adapted from reference [241].

Furthermore, work function measurements using low intensity X-ray photoemission spectroscopy (LIXPS) suggest that the UV light used in UPS measurements may result in a lowering of the work function of an ITO surface during the measurement procedure itself.[239, 241, 242] These experiments showed that work function measurements (in this case using LIXPS) prior to standard UPS measurements yielded larger work function values, indicating a method to perform accurate work function measurement, as long as the photon flux is low enough to prevent significant photochemical changes of the ITO surface during the duration of the measurement. Exposing the ITO surface to the UV light used in UPS measurements can significantly induce a work function reduction. Examination of X-ray photoemission spectroscopy (XPS) core level line positions before and after UV exposure concludes that the effect is caused by the formation of a surface dipole.[239, 242] The reduction of the work function after UV exposure, as

seen in figure 6.1, can be attributed to a UV-induced desorption of surface contaminants, as reported Kim et al. on ITO.[241] Helander et al. have reported work function measurements using UPS and XPS for fluorine doped tin oxide (FTO), a commonly used transparent conducting oxide in optoelectronic device applications. They found that the presence of carbon contamination and UV exposure induces a work function reduction.[243]

Similarly, Song et al. reported lower UPS work function values compared to the one deduced from Kelvin probe measurements on NiAl(110). In addition, it was shown that the work function is dramatically reduced by the oxidation of the surface area.[244] They attribute that the formation of an interfacial dipole layer to be the main factor that determined the work function.

Strojnik et al. have reported similar results on MoSI nanowires, used in organic devices as a transparent electrode.[245] However, the difference between the UPS and KPFM measurements was reduced by heating the samples during the UPS measurement and thus, eliminating possible adsorbates that would lead to surface charges. In addition, as Sugiyama et al. have reported on ITO, surface treatments used to removed carbon contamination significantly changed the work function measurements. They have found that Ar⁺ sputtering reduced not only the carbon contamination but also the oxygen content on the ITO surface, leading to a decrease in the work function.[246]

There have been very few reports showing work function alteration of CNT based transparent electrodes. Friend and coworkers have reported work function values of multi-walled CNTs (MWNT), measured by UPS.[247] Using different techniques to oxidize the CNTs increases the work function by weakening or breaking the π -conjugation. In addition, Grujicic et al. have reported experimental observations of UV-light accelerated oxidation of carbon nanotubes.[248]

Recently, Kang et al. have reported the engineering of the work function of carbon nanotube (CNT) transparent conductive films on a flexible sheet of plastic.[249] UPS measurements reveal that a deposition of less than 0.5 nm of aluminum was enough to control the work function of the transparent conductive films of SWCNTs.

6.3 Functionalized CNTs

Carbon nanotubes (CNTs) have unique properties that make them highly attractive for transparent electrode device applications, such as their solution processability, electronic properties and flexibility. However, the intrinsic work function of CNT based electrodes might create a Schottky barrier, impeding electron transport with some active

materials within an OPV device. Therefore, due to their chemical inertness, CNTs have to be functionalized in order to acquire additional physicochemical properties. Since organic or hybrid materials developed for solar cells, organic electronics, or for many other applications generally have a work function value ranging from 4–6 eV, it would be very desirable to be able to tune the work function of the electrodes in order to align their energy levels with those of the active material(s).

Previously developed single wall carbon nanotube (SWNT) networks have generally consisted of a mixture of metallic and semiconducting CNTs, which yields to transparent electrodes with optoelectronic properties close to ITO.[250] However, their compatibility with other electronically active organic thin films can be improved to increase their optical and electronic properties. To achieve this goal, a good electronic homogeneity of the film will be necessary. Recently, much progress has been achieved in the separation of SWNTs by electronic type using density-gradient ultracentrifugation.[251] Metallic SWNTs rise great interest not only because they have a higher electrical conductivity compared to semiconducting SWNTs [252], but also because the resistance at metallic-metallic interconnects is much less than at metallic-semiconducting or semiconducting-semiconducting junctions.[253] As an example, the metallic fraction enhanced conductivity was demonstrated in nanocomposites with P3HT.[254]

In this work, we investigate the effect of the functionalization of metallic SWNTs by different metals and after nitric acid treatment by measuring the change in the work function. We compare values of work function measured by UPS and KPFM and show a good correlation between these measurements. We also show an effect of the UV and X-ray exposure on the work function of metallic SWNTs networks.

6.3.1 Materials & Sample Fabrication

The CNT networks in this work were fabricated (dispersion, spray coating and functionalization) by Dr. Karell Saint-Aubin and Dr. Jean-Pierre Simonato from LITEN (CEA, Grenoble).

Materials The SWNTs used in this work were 95% metallic, purchased from Nanointegris. These carbon nanotubes are produced using the electric arc discharge method and then purified by Density Gradient Ultracentrifugation (DGU) and used as received. Lengths of individual tubes range from 300 nm to 4 μm with an average diameter of

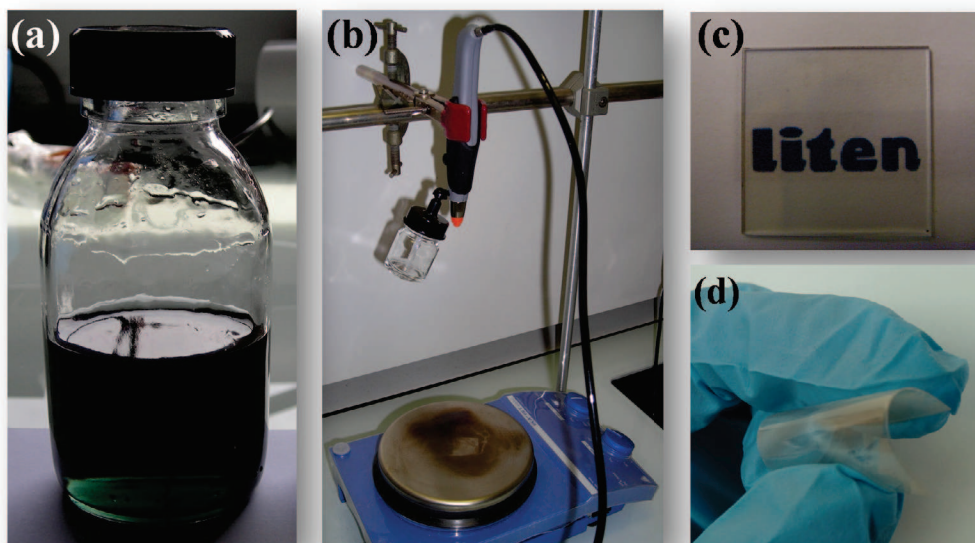


FIGURE 6.2: Photographs of the (a) CNT network dispersed in 100 mL solution of N-methylpyrrolidone (NMP), (b) the spray coating apparatus, (c) the CNT network deposited on a transparent substrate, and (d) demonstrating the flexibility of the network after deposition. Images taken by Dr. Karell Saint-Aubin.

1.5 nm. Nitric acid (HNO_3 , CAS#¹ 7697-32-7) and Sulfuric acid (H_2SO_4 , CAS# 7664-93-9) are used for SWNTs oxidation. The gold source is provided by Gold(III) Chloride trihydrate ($\text{HAuCl}_4 \cdot 3\text{H}_2\text{O}$, CAS# 27988-77-8), the palladium source is provided by Sodium Tetrachloropalladate(II) (Na_2PdCl_4 , CAS# 13820-53-6) and the platinum source from Potassium Tetrachloroplatinate(II) (K_2PtCl_4 , CAS# 10025-99-7). For the functionalization of SWNTs by silver particles, the following products are used Tin(II) Chloride (SnCl_2 , CAS# 7772-99-8), Palladium(II) Chloride (PdCl_2 , CAS# 7647-10-1), Hydrochloric acid (HCl , CAS# 7647-01-0), Silver nitrate (AgNO_3 , CAS# 7761-88-8), Ammonium hydroxide (NH_4OH , CAS# 1336-21-6) and Formaldehyde (HCHO , CAS# 50-00-0). All these products were purchased from Sigma Aldrich and used as received.

Dispersion Carbon nanotubes, as made, often exist as entangled agglomerates. In order to fully utilize the unique properties of the CNTs, an appropriate dispersion procedure has to be applied. In this work, SWCNT powder (5 mg) were dispersed by sonication in 100 mL of N-methylpyrrolidone (NMP), as seen in figure 6.2a, and bath sonicated for one hour and half at room temperature at a frequency of 53 kHz (180 W). The SWNTs bundles were separated from the solution by two consecutive centrifugation steps at 14,500 rpm where 80% of the supernatant were collected each time. The dispersions were used without any further treatment.

¹CAS registry number: a unique numerical identifier assigned by the “Chemical Abstracts Service” to every chemical described in scientific literature

Spray-Coating The dispersed SWNTs were spread on Si substrates using the spray coating technique. The spray coating technique is the simplest and quickest method for depositing CNT over surface. In addition, transparency of the samples can be tuned from 0% to 100%. A commercial airbrush (Aztek A4709 with large flow nozzle 0.7 mm) was used, as seen in figure 6.2b. In a typical experiment, the Si substrate was placed on a hot plate at 250°C in order to accelerate the drying of the small droplets on surface and facilitate uniform deposition. The solution was sprayed with the airbrush at a distance of 19 cm from the substrate at 2 bar air pressure. After spreading, the devices were washed with acetone and dried under nitrogen flux for 3 minutes. Figure 6.3 is a SEM image of the dispersed pristine, HNO₃ treated and functionalized SWNT networks after spray coated on a Si substrate for 30 seconds.

Functionalization The as-made electrodes were then used as a reference for further studies, specifically work function engineering. Then functionalization of the electrodes was realized with Ag, Au, Pd and Pt nanoparticles. The typical range for the work function ϕ of these metals are indicated in table 6.1.[255]

Ag	4.52–4.74 eV
Au	5.1–5.47 eV
Pd	5.22–5.6 eV
Pt	5.12–5.93 eV

TABLE 6.1: Electron work functions of metals, can change for crystalline elements based upon the orientation. For example Ag: 4.26, Ag(100): 4.64, Ag(110): 4.52, Ag(111): 4.74.[255]

The SWNT networks were functionalized post-deposition on the Si substrate. The oxidized m-SWNT sample was treated by immersion in a 10 mL 65% nitric acid bath for 24 hours. The functionalized m-SWNT networks were prepared using Au, Pd or Pt nanoparticles by immersing the sample in a 20 mL anhydrous ethanol solution, containing of 7.8 mg of H₂AuCl₄, 4.0 mg of Na₂PdCl₄, and 41.5 mg of K₂PtCl₄, respectively, for 24 hours. Each sample was washed with anhydrous ethanol and dried under nitrogen flux for 3 minutes. The functionalization of the m-SWNT network by Ag nanoparticles is done in four steps. In the first step, the m-SWNT network is oxidized by immersion in a mixture of H₂SO₄:HNO₃ (1:3) for 4 hours. Then, the sample is rinsed with deionized water and is immediately immersed in a 20 mL aqueous solution of 0.1 M SnCl₂ and 0.1 M HCl for 30 min. The electrode is then rinsed with deionized water and re-immersed in a 20 mL aqueous solution of 0.1 M PdCl₂ and 0.1 M HCl for 30 minutes. After rinsing the electrode with deionized water, the last step consists of immersing

the electrode in a 50 mL aqueous electroless bath containing 0.5 g AgNO_3 , 0.75 mL ammonium hydroxide and 1.5 mL formaldehyde at a pH of 8.5.

After functionalization, the sheet resistance (R_s) of the electrodes was observed to be lowered, which can be ascribed to metallic doping, as recently reported.[256] The m-SWNT network has also displayed a high transmittance, suitable for the use as a transparent conductive electrode. A chemical treatment was also carried out on pristine nanotubes with nitric acid (HNO_3) since this procedure is already known to modify significantly the work function of CNTs. Hatton et al. demonstrate a shift in the work function with the oxidation of the SWNTs.[257] Collins and co-workers have shown that the CNT oxidation efficiently induces chemical reactions at surface by monitoring the discrete change of CNT electrical conductance.[231]

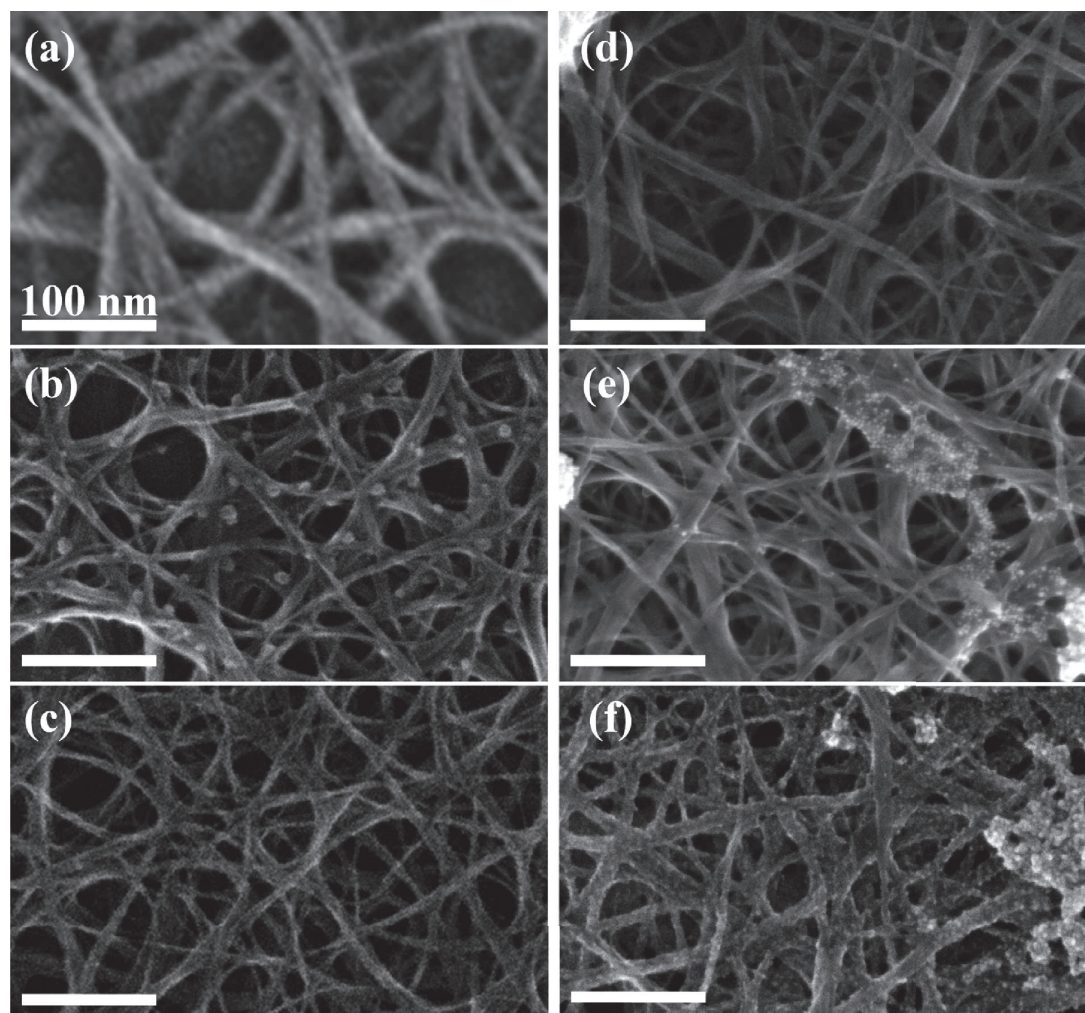


FIGURE 6.3: SEM images of the pristine metallic SWNT network (a) deposited by spray coating treated with nitric acid (b), functionalized by nanoparticles of gold (c), palladium (d), platinum (e), and silver (f). Image size $400\text{ nm} \times 250\text{ nm}$. Scale bar = 100 nm. Images taken by Dr. Karell Saint-Aubin.

6.3.2 KPFM of Functionalized CNTs

KPFM measurements were obtained using the same PtIr₅ coated Si cantilever as described in table 3.2. Topography was measured at the first resonant frequency (f_0) of 61.6 kHz and the CPD was recorded at the second resonant frequency (f_1) of 386.2 kHz. For the calculation of the absolute work function, the cantilever was calibrated on highly oriented pyrolytic graphite (HOPG, $\phi_{\text{HOPG}} = 4.6$ eV) before and after each set of measurements, which resulted in a tip work function ($\phi_{\text{tip}} = 5.1 \pm 0.1$ eV). However, tip changes occurred in between measurements, revealed by a variance of the mean CPD level over the HOPG. Therefore, the value of ϕ_{tip} was systematically calibrated over HOPG before and after each measurement. Last, with the aim to investigate the effect of the UV light on the surface, the KPFM data was acquired on each sample before and after carrying the *in-situ* UPS measurements (the XPS measurements were carried out in the same run). After calibration and adjustment, the histograms of all the CPD values, both before and after UV and X-ray exposure, can be seen in figure 6.5.

The full series of data was recorded with the same cantilever and operating parameters for the nc-AFM and KPFM detections. With the aim to minimize non-conventional contributions to the CPD due to SRE forces, we tried to “maximize” the tip-surface distance by using a relatively moderate frequency shift ($\Delta f = -10$ Hz). However, stable conditions were only achieved in a regime where damping images display a non-negligible contrast, as seen in figure 6.4. The KPFM-compensated CPD value may then deviate from the “pure” work function difference between the sample and the tip. In this study, our aim was therefore to take benefit of the comparison with the data acquired by using UPS, to confirm that single-pass KPFM can still be used for comparative investigations between different samples, even if SRE forces affect the measured CPD.

The results of KPFM investigations are presented in figures 6.4 and 6.5, which display the nc-AFM/KPFM images and histograms of the CPD levels, respectively.

After UV and X-ray exposure, the average surface potential increases by $\sim 95 \pm 15$ mV, consistent with the order of magnitude work function change on other surfaces.[239–244] It is highly likely that the surface potential variation is due to the surface contaminants exposure to the UV radiation.[239–244] Although, another possibility is that the relatively large increase in the surface potential of the SWNT networks is due to oxidation of the nanotubes from exposure to the UV radiation.[247, 248]

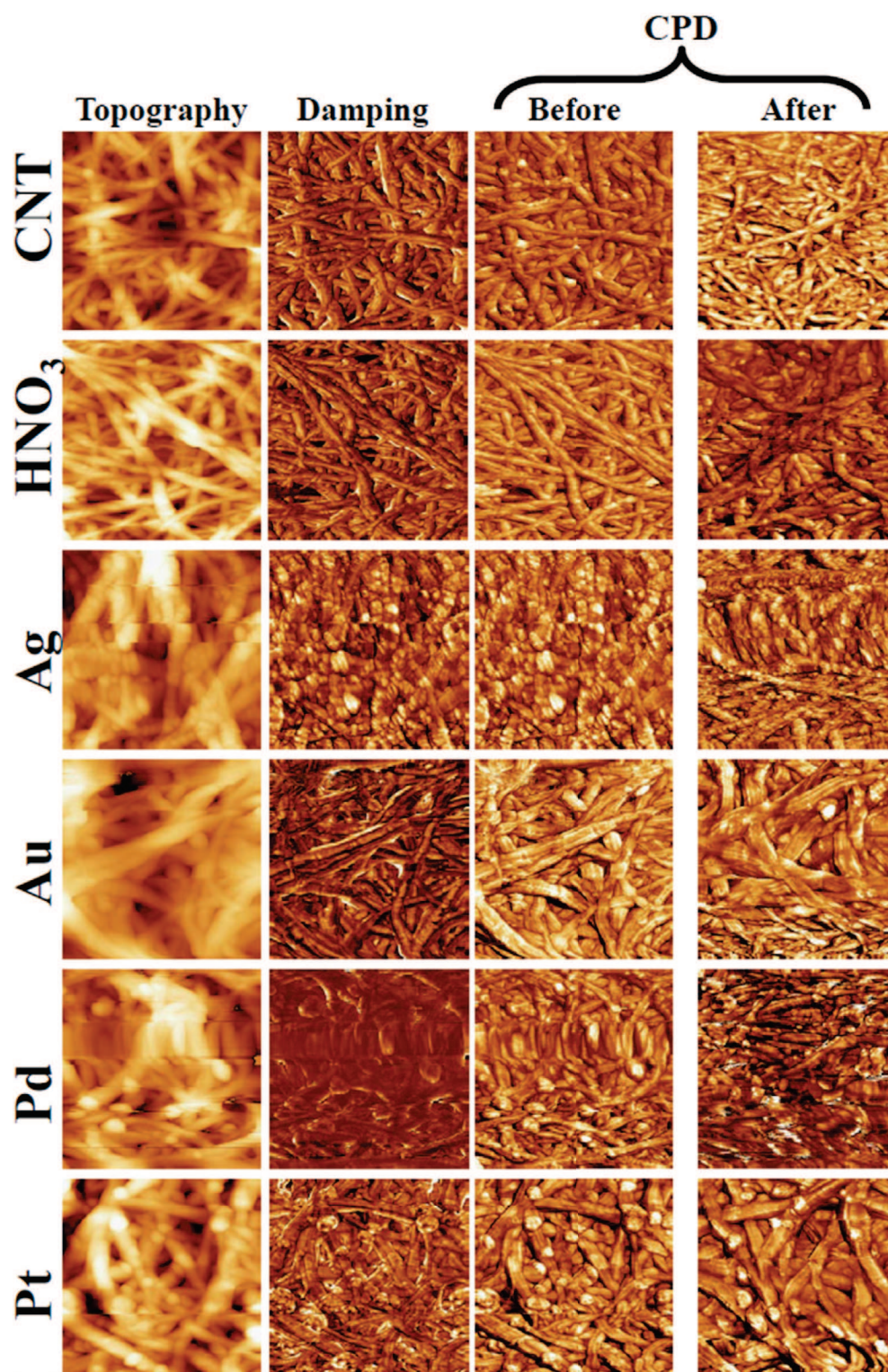


FIGURE 6.4: Topography, damping, and KPFM (before and after, at a different location, UV and X-ray exposure) of metallic SWNT networks deposited by spray coating of pristine CNTs, treated with nitric acid, functionalized by nanoparticles of silver, gold, palladium, and platinum. Z-scale for topography from 0 to 65 ± 10 nm. Image size $750 \text{ nm} \times 750 \text{ nm}$. $\Delta f = -10$ Hz. $A_{vib} = 57 \pm 10$ nm. Z-scale of the CPD is displayed by the histograms in figure 6.5.

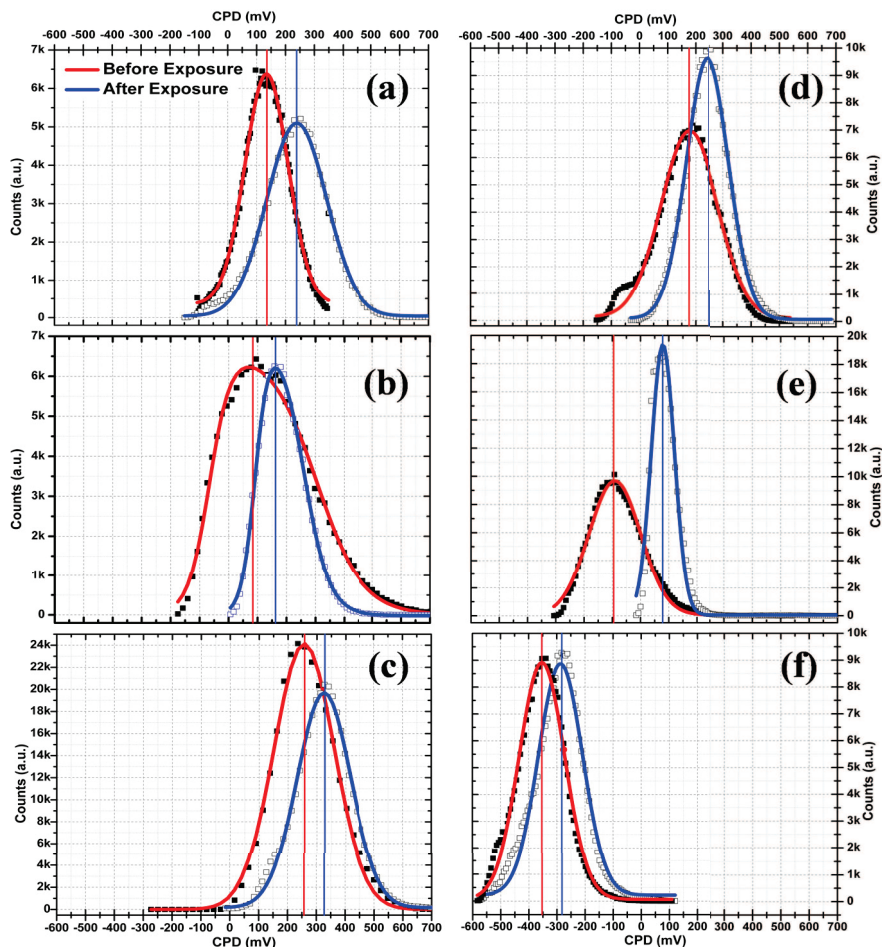


FIGURE 6.5: CPD histograms before and after UV and X-ray exposure (Gaussian fitting in red and blue for before and after, respectively) of metallic SWNT networks deposited by spray coating of pristine CNTs (a) treated with nitric acid (b), functionalized by nanoparticles of silver (c), gold (d), palladium (e), and platinum (f). Peak values indicated by vertical line. (x-axis scale: $-600 \text{ mV} \leq \text{CPD} \leq 700 \text{ mV}$). CPD histograms calculated from figure 6.4.

Material	CPD (mV)		$\Delta\text{CPD} (\%)$
	Before	After	
Pristine CNT	130	240	+110 = \uparrow 85%
HNO₃	80	160	+80 = \uparrow 100%
Ag	260	340	+80 = \uparrow 31%
Au	170	260	+90 = \uparrow 53%
Pd	-90	40	+130 = \uparrow 144%
Pt	-360	-280	+80 = \uparrow 33%

TABLE 6.2: Peak CPD values calibrated over HOPG and $\Delta\text{CPD}(\%)$ of the pristine CNT network, functionalized by nanoparticles of silver, gold, palladium, and platinum, based on CPD histograms in figure 6.5, before and after UV and X-ray exposure.

6.3.3 PES of Functionalized CNTs

Directly after the first KPFM measurement, the sample was transferred *in-situ* to the PES stage, located in the same UHV chamber as the AFM. In order to utilize the low pressure of chamber ($p = 10^{-10}$ mbar), XPS measurements were first taken, followed by UPS measurements, which due to the influx of the He gas can raise the pressure up to 10^{-7} mbar. After UPS measurements, the sample was transferred back to the AFM stage and the pressure recovered back to 10^{-10} mbar before recommencing KPFM measurements.

6.3.3.1 Ultraviolet photoelectron spectroscopy (UPS)

As mentioned in chapter 3, the work function of the concentric hemispherical analyzer (CHA) was calibrated with a clean Au(111) sample. This essentially gives a reference where the analyzer Fermi edge is on the energy (kinetic or binding) scale. The Au(111) UPS spectrum is calibrated in a way that the Fermi level is located at 0 eV binding energy, and therefore equilibrating the sample Fermi level with that of the CHA, i.e. the “internal” kinetic energy spectrum of the sample.

The Fermi level (or “edge”) manifests itself as a step, since it separates occupied and empty states. PES works only with occupied states, since there needs to be electrons that can be photoemitted, and therefore, states above the Fermi level do not emit electrons. In addition, there is the high binding energy cutoff (or “secondary edge”), where the spectrum ends. Electrons close to the edge are the slowest electrons of the spectrum (right at the edge they have a kinetic energy of zero after leaving the sample surface, i.e. they have barely enough energy to overcome the work function of the material). The electrons responsible for the secondary edge and the sloping up tail before the edge are inelastically scattered electrons, which were initially emitted from the valence bands states, but lost energy through scattering processes on their way to the sample surface. Since both the Fermi edge and the binding energy of the electrons right at the secondary edge is known, the work function of the sample can be determined (see equation 3.39), using $h\nu=21.22$ eV for He I radiation as the source.

Since the work function of the CNT networks is expected (from KPFM measurements) to be greater than the work function of the spectrometer ($\phi_{\text{sample}} > \phi_{\text{spectrometer}} = 4.28$ eV), the sample was grounded at earth potential, allowing the low energetic electrons coming from the sample to enter the detector. If on the contrary $\phi_{\text{spectrometer}} \geq \phi_{\text{sample}}$, then the sample would be negatively biased in order to facilitate the separation of the low energy electrons from the sample from those of the spectrometer. The ground was also necessary in order to prevent charging of the sample.

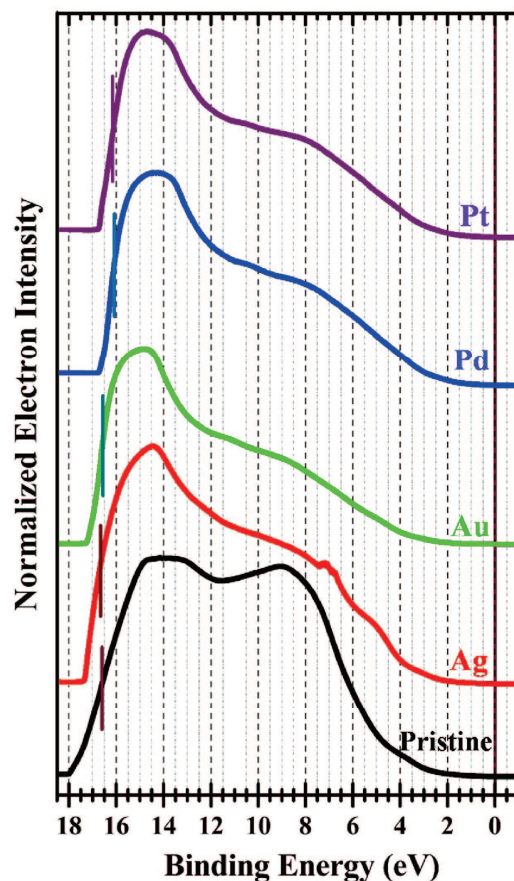


FIGURE 6.6: Full UPS spectra of the metallic SWNT network deposited by spray coating of pristine CNTs (black), functionalized by nanoparticles of silver (red), gold (green), palladium (blue), and platinum (purple). Spectra adjusted so that the Fermi edge is at 0 eV and the secondary cut-off is indicated by vertical line.

The UPS measurements were performed *in-situ* directly after XPS data acquisition, at a pressure of $\sim 2 \times 10^{-9}$ mbar, using a He I discharge lamp as the excitation source at $h\nu = 21.2$ eV. Typically, ten scans were acquired per sample with the UV light exposing a ~ 1 cm² area on the sample surface. Proper angle adjustment of $\sim 45^\circ$ was maintained in order to extract photoemitted electrons from the top few nm of the sample, as described in chapter 2 on AR-PES.

Calculating the work function of each CNT network sample is based on the location of the Fermi edge (at the $1/2$ intercept point) and of the secondary cut-off ($1/2$ maximum) [239, 240, 242, 258], seen in figure 6.7. Unfortunately, the locations of HNO₃ Fermi edge and secondary cut-off were not accurately determined and thus not pictured, as explained in the forthcoming XPS section.

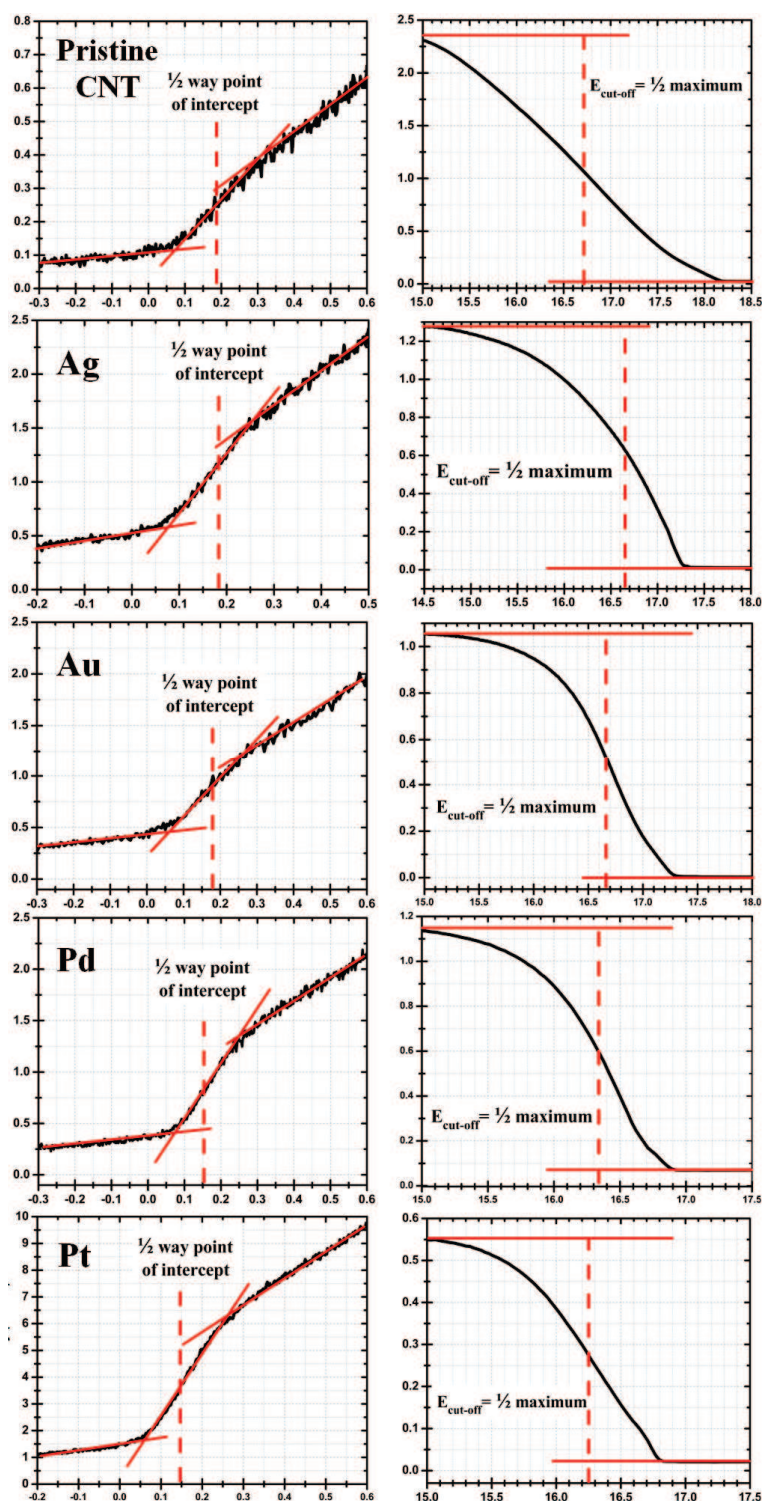


FIGURE 6.7: UPS spectra of the metallic SWNT networks deposited by spray coating of pristine CNTs, functionalized by nanoparticles of silver, gold, palladium, and platinum. Fermi edge (left column) and secondary cut-off (right column) indicated by vertical line. Y-axis: Electron Intensity (Fermi edge: counts $\cdot 10^3$, Secondary cut-off: counts $\cdot 10^6$). X-axis: Binding Energy (eV). Values seen in table 6.3.

Material	Fermi Edge	Secondary Cut-off	ΔE	ϕ_s
CNT	0.19	16.71	16.60	4.62
Ag	0.18	16.65	16.47	4.75
Au	0.17	16.67	16.50	4.72
Pd	0.15	16.32	16.17	5.05
Pt	0.15	16.25	16.10	5.12

TABLE 6.3: UPS Fermi edge, secondary cut-off, ΔE and ϕ_s values (in eV, determined from equation 3.39 using $h\nu=21.22$ eV for He I radiation) of the pristine CNT network, functionalized by nanoparticles of silver, gold, palladium, and platinum, based on UPS spectra in figure 6.7.

6.3.3.2 X-Ray photoelectron spectroscopy (XPS)

As discussed in chapter 3, XPS was used in constant analyzer energy (CAE) mode as quantification of the data is easier due to the fixed resolution of the spectrum. The particular binding energy peaks for each of the functionalized CNT networks were identified using values from the NIST XPS database². Generally, the peaks observed at higher binding energies, as seen in figure 6.8, are attributed to both Auger photoelectrons and “ghost” peaks, which arise from different X-ray excitation energies from contaminants on the anode. A “ghost” peak is seen for O $K\alpha$ at ~ 961 eV, indicating oxidation of the Al anode source filament, a condition that can also broaden the characteristic X-ray line width. However, a “ghost” peak is not observed for Cu $L\alpha$ at ~ 608 eV, which if present would indicate a degradation of the Al anode. However, due to the use of a twin anode source, cross-talk is often observed that can account for many of the smaller unknown peaks (which may also be a result of contaminants on the sample surface).[155, 158]

Not surprisingly, a strong C 1s peak (~ 288 eV) is observed throughout every sample, indicative of the CNT network. However, the additional presence of the O 1s peak (~ 533 eV), combined with the C 1s peak, may also indicate that the sample surface is not clean, as observed by the presence of extraneous peaks, that may also be indicative of the “ghost” peaks described above.

A Si 2p peak (~ 100 – 103 eV), due to the SiO_2 surface, is observed in the HNO_3 treated CNT network, indicating that the escape depth of the photoelectrons is greater than the thickness of the CNT networks. Therefore, the angle of emission was not properly optimized for this particular sample, as discussed in chapter 3 on AR-PES.

²National Institute of Standards and Technology (NIST) X-ray Photoelectron Spectroscopy Database srdata.nist.gov/xps

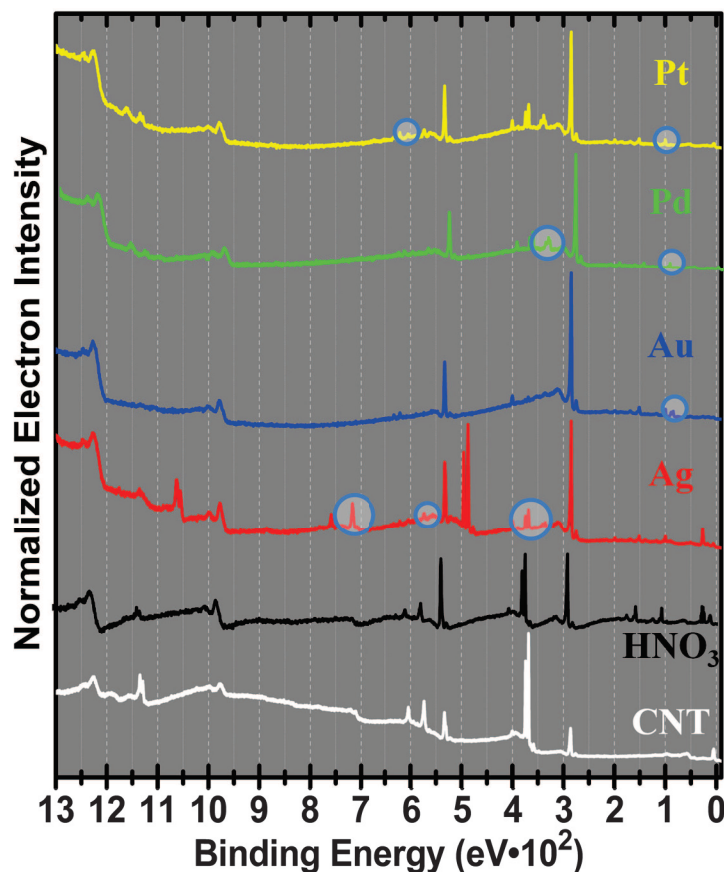


FIGURE 6.8: XPS spectra of the nanoparticle-functionalized CNT networks, circles indicated metallic peaks magnified in figure 6.9 of **Ag** 3s-1/2, 3p-3/2, 3d-7/2, 3s-5/2, **Au** 4f-5/2, 4f-7/2, **Pd** 4s-1/2, 3d-3/2, 3d-5/2, and **Pt** 5s-1/2, 4p-1/2.

However, the SiO₂ peak is not seen in the pristine CNT and functionalized networks, because careful angle adjustment was adapted in order to obtain photoemitted electrons from the top few nm of the sample surface. The analyzed region became more surface localized and the surface sensitivity was increased as the emission angle increased. Typically, the IMFP λ is approximately 10–35 Å for electron energies in the range of 10 eV < E_b < 1400 eV (within the Al K α source $h\nu$ range), indicating that most the photoemitted electrons had an escape depth ($\sim 3\lambda$) ranging from 3–10 nm, according to equation 3.36.[154, 157] The material dependant IMFP λ estimation was modeled using the IMFP calculator³. [259, 260]

A magnified view of the characteristic metallic peaks of the functionalized CNT networks is seen in figure 6.9. Within each functionalized CNT network, an XPS peak indicating the presence of the particular characteristic metallic nanoparticle is observed.

³IMFP calculator: www.lasurface.com/xps/imfpgrapher.php

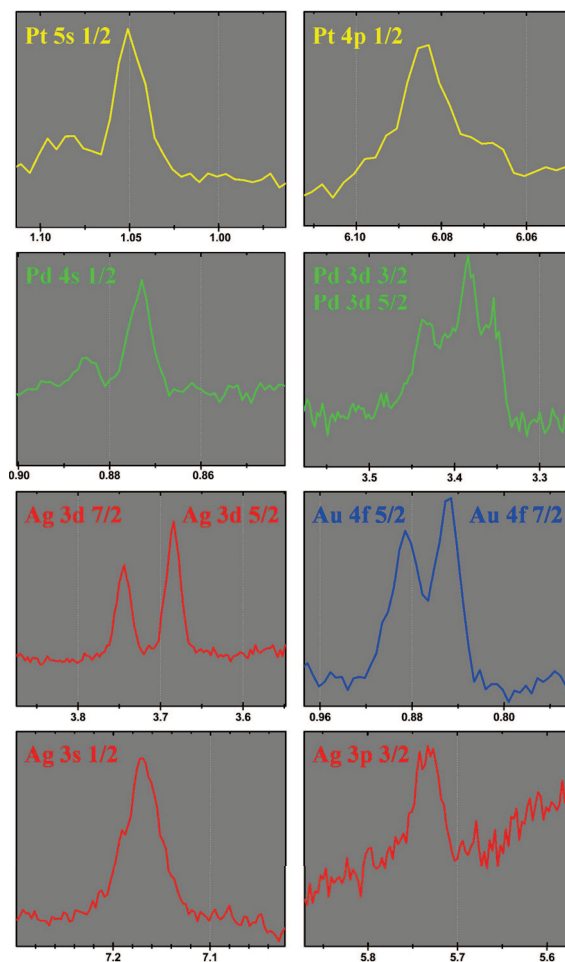


FIGURE 6.9: XPS Peaks of the nanoparticle-functionalized CNT networks magnified from figure 6.8: **Ag** 3s- $1/2$, 3p- $3/2$, 3d- $7/2$, 3s- $5/2$, **Au** 4f- $5/2$, 4f- $7/2$, **Pd** 4s- $1/2$, 3d- $3/2$, 3d- $5/2$, and **Pt** 5s- $1/2$, 4p- $1/2$.

In addition, a Ag 3d- $7/2$ and 3s- $5/2$ is observed not only in the Ag functionalized CNT network, but also in the pristine CNT and HNO₃ treated networks. This is due to the Ag paste used as a conductive adhesive of the sample onto the UHV stainless sample plate (escaping from the edges of the Si sample). Since the X-ray beam cannot be seen on the sample surface, unlike that from the UV lamp used for UPS, the XPS spectra for the pristine CNT and HNO₃ treated samples picked this up. Unfortunately, this was also the case for the UPS measurements on the HNO₃ treated sample, which heavily skewed the work function measurements. The UPS and XPS measurements for the remaining samples were adapted so that the Ag paste did not affect the results.

6.3.4 KPFM & UPS Work Function Values

Material	ϕ_s (eV)		
	KPFM		UPS
	Before	After	
Pristine CNT	4.97±0.07	4.86±0.10	4.62±0.10
HNO₃	5.02±0.16	4.94±0.07	...
Ag	4.84±0.10	4.76±0.09	4.75±0.10
Au	4.93±0.09	4.85±0.11	4.72±0.10
Pd	5.19±0.08	5.06±0.04	5.05±0.10
Pt	5.46±0.07	5.38±0.07	5.12±0.10

TABLE 6.4: Work function ϕ_s values in eV determined by KPFM (before and after UV and X-ray exposure) and UPS of the pristine CNT network, treated by HNO₃, functionalized by nanoparticles of silver, gold, palladium, and platinum. Values depicted in figure 6.10.

In summary, the work function of pristine SWNT networks, treated by HNO₃ and functionalized by nanoparticles of Ag, Au, Pd and Pt, deposited by spray coating on a Si(111) surface were investigated using KPFM and UPS. The work function values determined from KPFM and UPS are summed up in figure 6.10. The “error bars” for the work function values from KPFM were calculated from the first standard deviation σ of the CPD histograms, in which the FWHM = $2 \cdot \sqrt{2 \cdot \ln 2} \cdot \sigma$. The UPS error bars arise from the energy resolution of the analyzer.

As discussed, KPFM work function values are often higher than those measured by UPS. The KPFM data prior to UV exposure confirms a higher work function than what is expected. This is indicative of the experimental technique. KPFM measured the local work function values on a small section of the sample (in our case 600 nm²), while UPS measures the lowest work function value on a larger area of the sample (in our case 1 cm²).

XPS data clearly revealed the presence of the metallic nanoparticles which can account for the trend of the work function values. However, the presence of surface contamination indicates that the work function values are deviated from their true values, confirmed by the XPS measurements and the reduction of the KPFM data after exposure to UV and X-ray radiation. UPS measurements reveal a lower work function, induced by the exposure of the sample to UV light. KPFM after exposure to UV radiation confirms the work function reduction. The reduction of the work function is most likely brought about due to the surface contaminants exposure to UV light, as indicated by prior experiments on ITO, NaCl and TiO₂. [239–244] Although surface contaminants

affected the work function measurements, this effect can be reduced by a surface treatment such as Ar⁺ ion sputtering.[245, 246] However, as reported by Friend et al. [247] and Grujicic et al. [248] in the case of MWCNTs, another possible contribution to the work function reduction of the CNT networks is by oxidation by UV exposure.

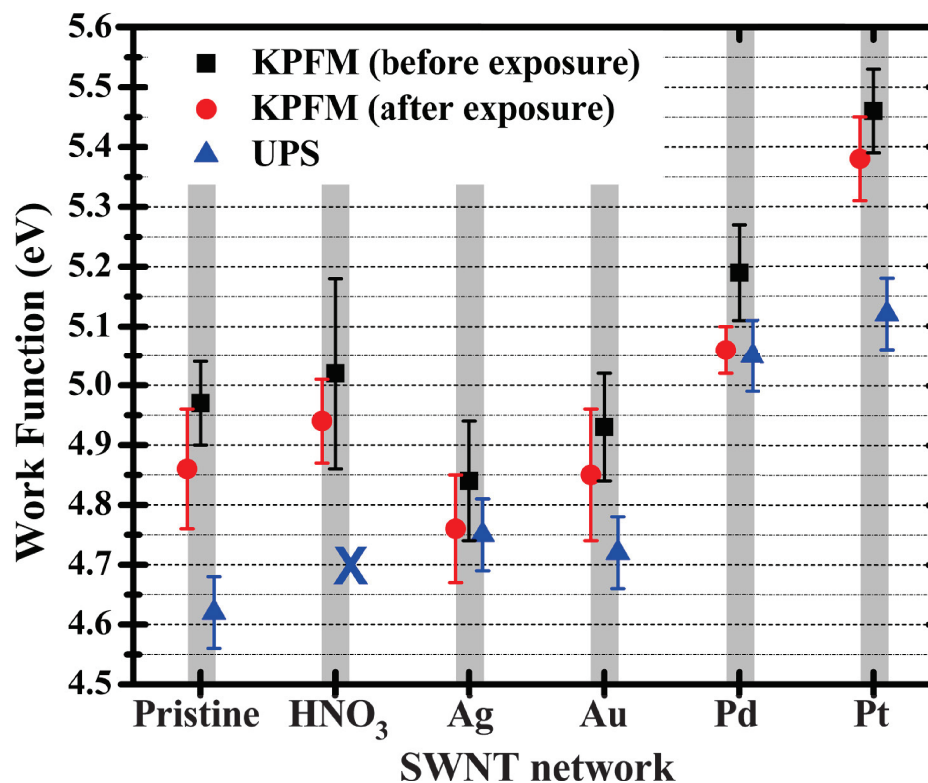


FIGURE 6.10: Work function values of the pristine CNT network, treated by HNO₃ (X indicates expecting UPS value), functionalized by nanoparticles of silver, gold, palladium, and platinum, determined by KPFM (before and after UV and X-ray exposure) and UPS. Values obtained from table 6.4.

6.4 KPFM Conclusions

In conclusion, KPFM has been used to characterize SWNT networks having different electronic properties. The work function values obtained from the KPFM measurements were compared to measurements obtained using UPS. Despite acquiring a modest level of damping contrast, the influence of SRE forces was minimized by working at a nominal frequency shift Δf setpoint of -10 Hz, as discussed in chapter 5. This approach ensured an accurate work function measurement of the SWNT network, taking into account evidence of surface contaminants by complimentary XPS measurements and UV induced work function reduction.

In conclusion, single pass AM-KPFM has been applied on a series of functionalized CNTs networks with different surface electronic properties. The work function values calculated from the CPD images have been compared to the ones deduced from UPS measurements, and a good agreement has been obtained between the results from both techniques. We attribute the quality of our results to two factors:

- (i) the full series of samples was investigated with the same operating set points (i.e. with the same tip-sample separation) and,
- (ii) the tip-surface separation was adjusted to minimize the contribution of SRE forces.

This confirms again that single pass KPFM can be, at least in some cases operated with small tip-surface separations, used for quantitative measurements of the surface properties.

Conclusion: Future Perspectives

In this thesis, high resolution noncontact atomic force microscopy (nc-AFM) and Kelvin probe force microscopy (KPFM), under ultrahigh vacuum, have been applied to investigate the structure and electronic surface properties of model organic materials and photovoltaic devices at the nanoscale. The series of samples investigated constitute key elements of an organic BHJ photovoltaic device, including:

- (i) the active BHJ layer,
- (ii) self-assembled electron donor π -conjugated oligomers and,
- (iii) the flexible transparent anode.

The chemical phase separation and the electronic properties of a highly efficient nanoscale phase segregated P3HT:PCBM bulk heterojunction photovoltaic device were simultaneously mapped by nc-AFM and KPFM at the sub-10 nm scale. Combining the topography images with the damping contrast revealed the interpenetrating percolating network of the donor and acceptor materials. However, further investigations are needed to establish the exact nature of the mechanisms responsible for the damping contrast.

The nanometer spatial resolution achieved represents a ten-fold improvement over previous reports on organic solar cells. Illuminating the surface revealed a net accumulation of negatively charged carriers at the surface, which is consistent with the better connection of the P3HT network to the bottom hole collecting PEDOT:PSS/ITO anode. In addition, the charge carrier generation at the donor-acceptor interfaces has been visualized by reconstructing 2-dimensional surface photovoltage images. The lateral extension of the space charge region at the donor-acceptor interfaces is estimated to be no more than 4 nm.

However, these results have been achieved at close tip-surface distances for which there may be non-negligible contributions of short range forces to the measured CPD. Further investigations are needed to determine to what extent the surface photovoltage measured at close tip-surface separation may differ from the one measured out of the range of SRE forces.

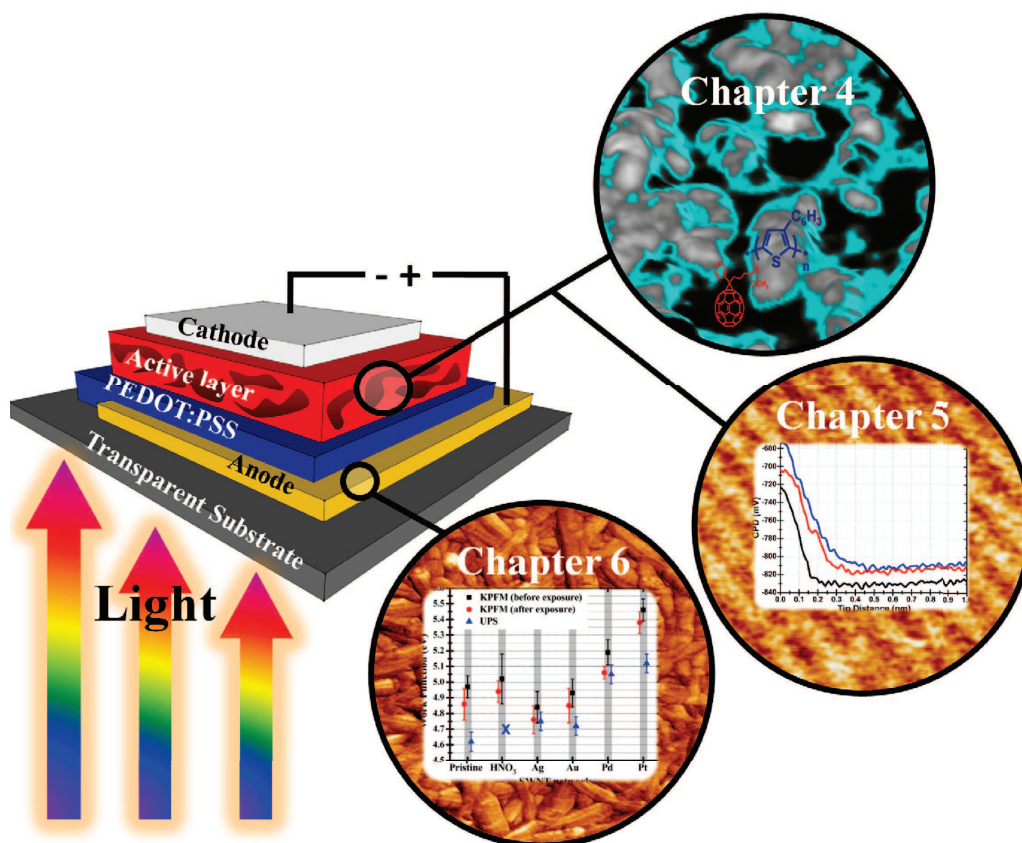


FIGURE 7.1

As a first step, the influence of the tip-surface separation on the CPD contrasts has been investigated for two related model oligomers (denoted as QTF8 and FG1) forming self-assembled π -stacked nanowires on HOPG. Distance dependant spectroscopy measurements revealed that the CPD is strongly dependent upon the tip-surface distance, and that CPD contrasts are correlated with the topography (i.e LCPD) at small tip-surface separations. In addition, a crossover has been observed to occur between the LR and SR regimes. SRE forces contribute to the measured CPD for typical tip-sample separations < 1 nm. While it was not possible to establish a direct relation between the LCPD contrast and the lattice of the molecular electric dipoles, it is highly probable that a tip-induced proximity effect is involved in the CPD imaging process. Therefore, a quantitative measurement of the local electric dipoles is unlikely. However, the influence of the SRE forces can be minimized by working near the onset of the damping contrast. This establishes an approach to perform single pass KPFM experiments at tip-surface separations out of the range of SRE forces on organic layers.

Following that idea, KPFM has been used to characterize SWNT networks having different electronic properties. An accurate work function measurement of the SWNT

networks has been confirmed by complementary UPS measurements, as well as taking into account surface contamination effects (as confirmed by complementary XPS measurements). The good agreement between the results of UPS and KPFM is attributed to the care taken to map the surface potential with the same tip-surface separation over the full series of samples.

In our opinion, our work clearly demonstrated that significant progress can still be made by nc-AFM investigations combined with KPFM in UHV on solution processed organic thin films and BHJ photovoltaic devices. However, our work does pinpoint some key issues that still remain to be addressed, specifically concerning the nature of the tip-sample forces at play in the nc-AFM/KPFM imaging process.

7.1 Future Perspectives

To address these issues, we propose the following roadmap for future investigations.

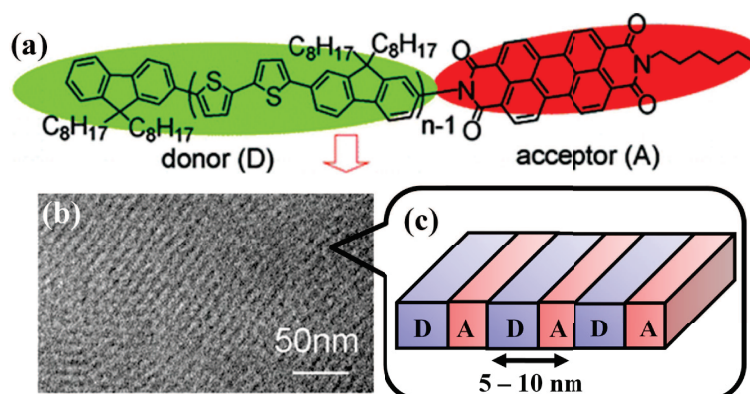


FIGURE 7.2: Chemical structure (a) and TEM image (b) of a co-oligomer donor-acceptor nanostructured film. (c) Schematic illustration of the lamellar nanostructures in films. Image modified from reference [261].

Obviously, there is now a crucial need to investigate donor/acceptor interfaces with a higher level of structural organization. Self-assembled material exhibiting these properties have been recently developed as an alternative to the solution processed blend for PV applications. For example, Bu and coworkers have designed and synthesized novel liquid crystalline conjugated co-oligomers, which are composed of donor and acceptor segments, as seen in figure 7.2.[261, 262] By tuning the molecular weight and post-treatment conditions, the length of each segment is customizable so that the films comprise ordered alternating D/A lamellae perpendicular to the substrate. Such samples would be ideal to investigate the nature of the damping and LCPD contrasts over the individual donor and acceptor components, as well as the carrier generation

at the interfaces. The possibility to tune the length of each segment will greatly help to identify the donor and acceptor groups when performing combined nc-AFM/KPFM experiments. Moreover, the surface morphology could be ideal to minimize possible crosstalk effects between the topography and CPD feedback loops. This would provide an interesting way to perform quasi-constant height measurements of the CPD contrast.

A complementary approach will consist in local investigations of the electronic transport under current flow in model systems. KPFM has already been widely used to investigate the voltage drop across the conducting channel in various kinds of devices. Here, the idea would be to check how the tip-surface distance effects the voltage drop measurement at the sub-10 nm scale. This can confirm that despite the contribution of short range electrostatic forces, KPFM can be used to probe the local electronic transport at the surface.

A model system could be provided by self-assembled Au networks, already investigated in our laboratory in collaboration with the group of Professor P. Moriarty at the University of Nottingham, as shown by figure 7.3.[263] They can form percolating self-organized domains on SiO₂ and would make ideal samples to probe voltage drops at the sub-10 scale.

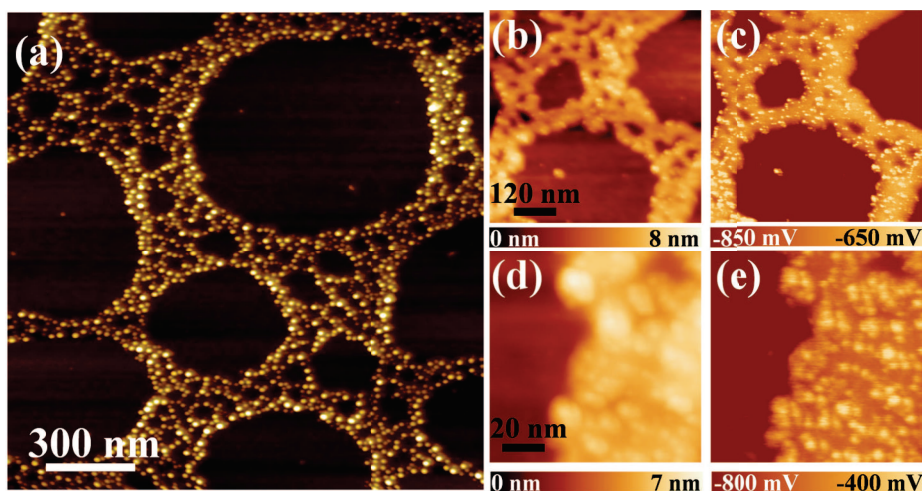


FIGURE 7.3: Topography (a,b,d) and CPD (c,e) of Au nanoparticle network. (a) 1500 nm \times 1500 nm, 500 \times 500 pixels, $\Delta f = -10$ Hz, $A_{vib} = 38$ nm $V_g = +0.6$ V. (b,c) 500 nm \times 500 nm, 300 \times 300 pixels, $\Delta f = -24$ Hz, $A_{vib} = 38$ nm, scan speed = 40 ms per pixel. (d,e) 100 nm \times 100 nm, 200 \times 200 pixels, $\Delta f = -31$ Hz, $A_{vib} = 38$ nm, scan speed = 40 ms per pixel. E. J. Spadafora, unpublished.

Lastly, following the recent results of the IBM group of G. Meyer demonstrating sub-nanometer resolution in charge mapping [215], it would be interesting to perform experiments in the regime of ultra-low tip oscillation amplitude by using cryogenic tuning-fork AFM.

KPFM on FG1:PC₇₀BM BHJ:

Morphology
SPV

A.1 Materials & Sample Fabrication

AM-KPFM has been applied to a BHJ blend consisting of a novel π -conjugated donor material (FG1, described in chapter 5) and PC₇₀BM as the electron acceptor. The sample used in this study was composed of a 350 to 400 nm thick active blend composing of FG1 and PC₇₀BM in a weight ratio of 1:1.5, respectively, and deposited on a PEDOT:PSS/ITO glass substrate. A post-deposition annealing was applied at 120°C for 5 min. The solution-processed bulk heterojunction FG1:PC₇₀BM solar cells showed a PCE as high as 0.78% when fabricated in a 1:2 weight ratio, respectively. However, the sample used for this study had a power conversion efficiency of 0.22%. The development and performance characteristics of the solar cell have been described in detail in a previous report.[79]

A.2 Topography

Initial FM-AFM inspection, using a SSS cantilever (details in table 3.2), revealed distinct rectangular shaped domains in the topography, see figure A.1, which proved to be an interesting characteristic of this particular sample. The aligned fibers within the rectangular shaped domains of the solar cell are donor-rich, while the light spots are attributed to acceptor-rich (PC₇₀BM) structures, seen in detail in figure A.1(b).[79] In the large scale image, figure A.1(a), PC₇₀BM clusters of around 10–20 nm are apparent, as depicted by the red arrows in figure A.1(a) and circled in figure A.1(b). However, the higher magnification image reveals more acceptor-rich areas that cannot be seen at larger scales, as depicted by the red arrows in figure A.1(b). Furthermore, it is clearly seen that within the grains of the blend there exists an ordered fibril-like structure of the FG1 oligomer. This order is clearly revealed in the damping image, figure A.2(b).

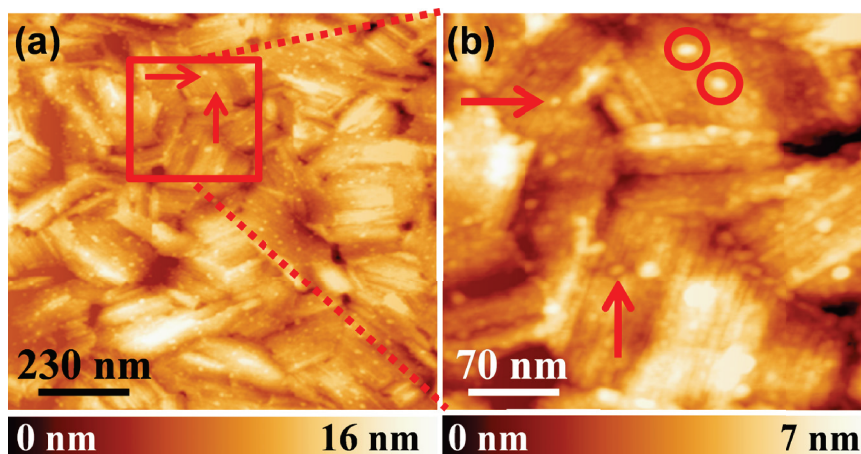


FIGURE A.1: FM-AFM (UHV, 300K) 2D topography images of the FG1-PCBM sample ($\Delta f = -25$ Hz, $A_{vib} = 34$ nm). (a): 1150 nm \times 1150 nm, 512 \times 512 pixels. (b) Zoomed region outlined in red in (a). (b): 350 nm \times 350 nm, 512 \times 512 pixels. Red arrows and circles indicate PCBM clusters.

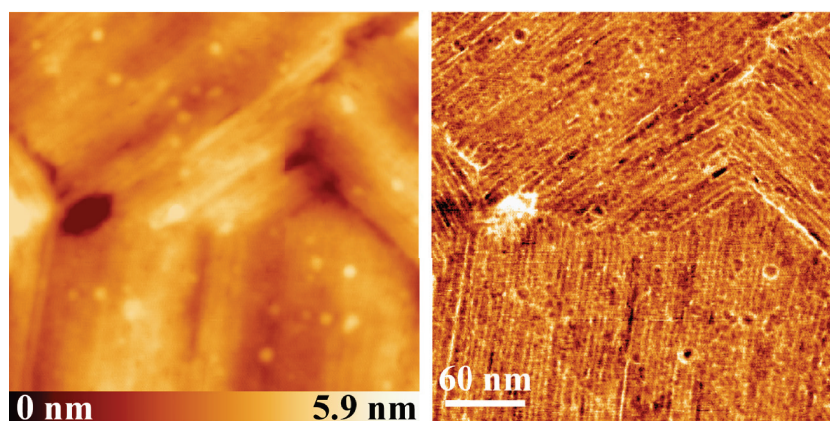


FIGURE A.2: FM-AFM (UHV, 300K) 2D topography (left) and damping (right) images of the FG1-PCBM sample (300 nm \times 300 nm, 512 \times 512 pixels, $\Delta f = -40$ Hz, $A_{vib} = 22$ nm).

As described in chapter 5, pure FG1 self assemblies displayed an highly ordered morphology after direct deposition on HOPG. The molecular lattice periodicity of FG1 stacks was determined to be 4.55 ± 0.05 nm, as seen in figure A.3(a) and (b). Remarkably, a similar molecular lattice periodicity of FG1 stacks is also observed in the 350-400 nm thick BHJ blend, as seen in the magnified damping image A.3(d). Furthermore, it is clearly seen that within the FG1 stacks of the BHJ blend, small PC₇₀BM clusters (<10 nm diameter) emerge at the surface, highlighted by yellow circles in A.3(d).

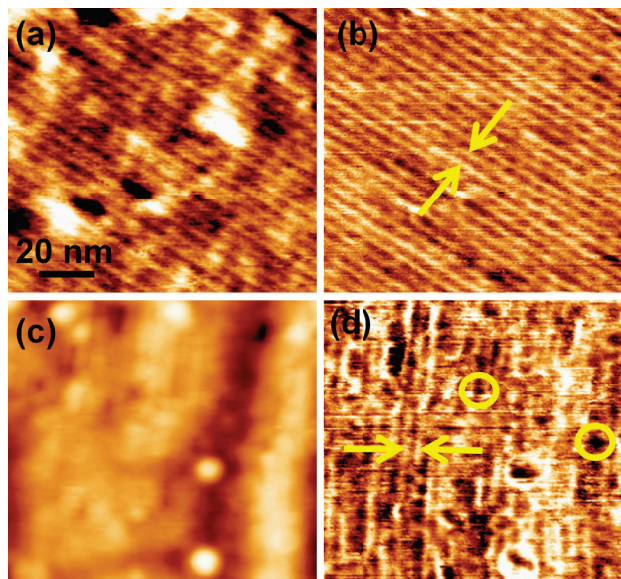


FIGURE A.3: FM-AFM (UHV, 300K) 2D topography (a,c) and damping (b,d) images of pure FG1 on a HOPG substrate (a,b) and the FG1-PCBM blend (c,d). (a,b): 100 nm × 100 nm, 400 × 400 pixels, $\Delta f = -25$ Hz, $A_{vib} = 14.6$ nm. (c,d): 100 nm × 100 nm, 500 × 500 pixels, $\Delta f = -30$ Hz, $A_{vib} = 27$ nm. Yellow arrows indicating equivalent lattice periodicity and yellow circles outlining PCBM cluster.

A.3 Contact Potential Difference

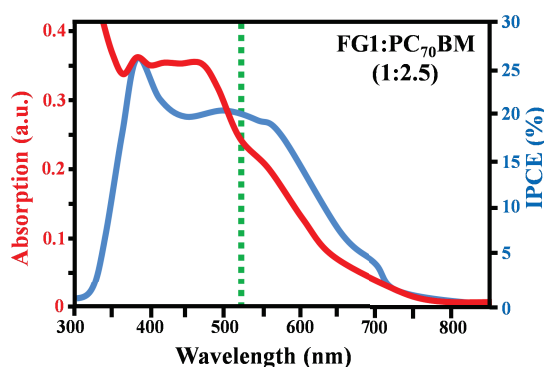


FIGURE A.4: Absorption spectra (red) and IPCE (blue) of FG1:PC₇₀BM in a weight ratio of 1:2.5. Laser illumination at 532 nm (green-dashed line). Image modified from reference [79].

Like in the P3HT:PCBM investigation, a 532 nm cw laser was used, since both components of the blend showed a high absorbance between 350 and 600 nm, as seen in figure A.4.[79] At the global scale, as seen in figure A.5, the topography from the in dark to the illuminated state remained unchanged, proving the absence of artifacts by illuminating the surface by the 532 nm laser. However, the CPD from the in dark to the illuminated state changed significantly. In dark, a histogram plot, as shown in figure

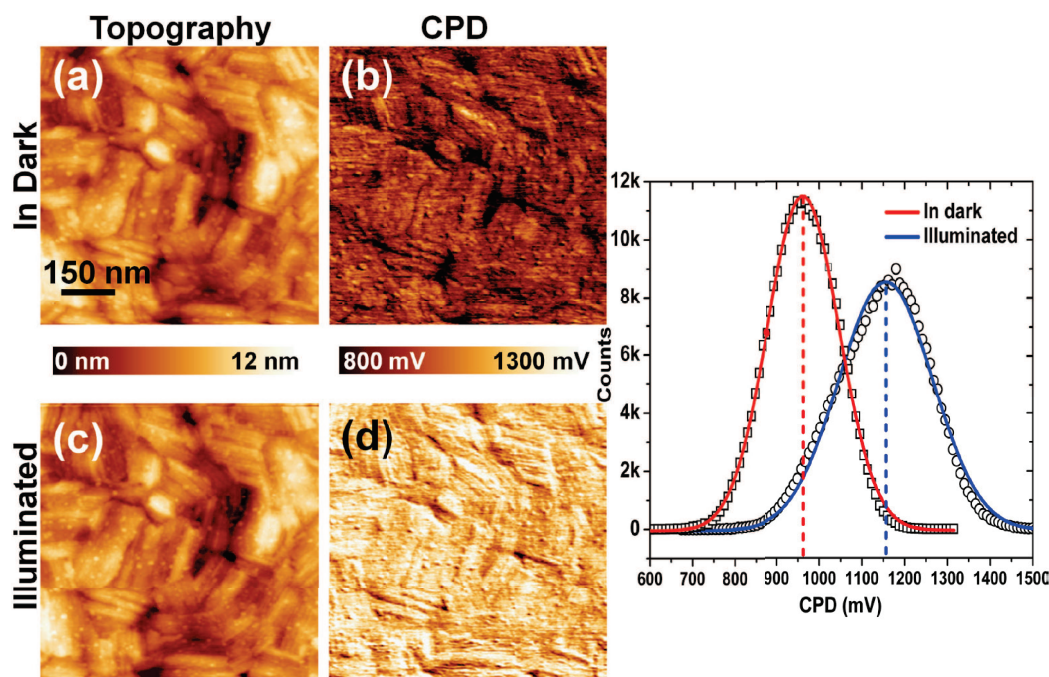


FIGURE A.5: FM-AFM (UHV, 300K) 2D topography (a,c) and CPD (b,d) images of the FG1-PCBM blend in dark (a,b) and under 532 nm illumination (c,d). 750 nm \times 750 nm, 512 \times 512 pixels, $\Delta f = -18$ Hz, $A_{vib} = 45$ nm, scan speed = 50 ms per pixel. Histogram of the CPD in dark and under illumination shown in graph.

A.5, shows an average CPD of around +950 mV, while under illumination the average CPD increases to almost +1150 mV, an increase of approximately 200 mV. Since the CPD is proportional to the difference of the work function of the tip and sample, equation 3.31, this corresponds to a negative change in the work function of the sample. This indicates a net accumulation of negative carriers at the surface. This has also been observed in the P3HT:PCBM blend described in chapter 4.

Considering that the basic operating principle of a BHJ organic solar cell is that exciton dissociation takes place at the donor/acceptor interface and the electrons are transferred at the fullerene, PC₇₀BM, acceptors, a closer examination of the PC₇₀BM structures was performed. Figure A.6(a)-(d) is a higher magnification (250 nm²) of the FG1:PC₇₀BM blend. At this scale, there is a small x-y displacement (<50 nm) between the in dark and illuminated images, most likely due to piezoelectric creep over the course of several hours of scanning. Nonetheless, the same features are clearly present in both images, such as the PC₇₀BM cluster highlighted by the red and blue squares in figure A.6(b) and (d), respectively. It is clearly apparent that the same positive shift of the CPD takes place at local scale as it did at the global scale, as seen in figure A.5. However, at this scale, it is evident that this change is not uniform throughout the entire FG1:PC₇₀BM blend. One area in particular was examined to quantify the local CPD

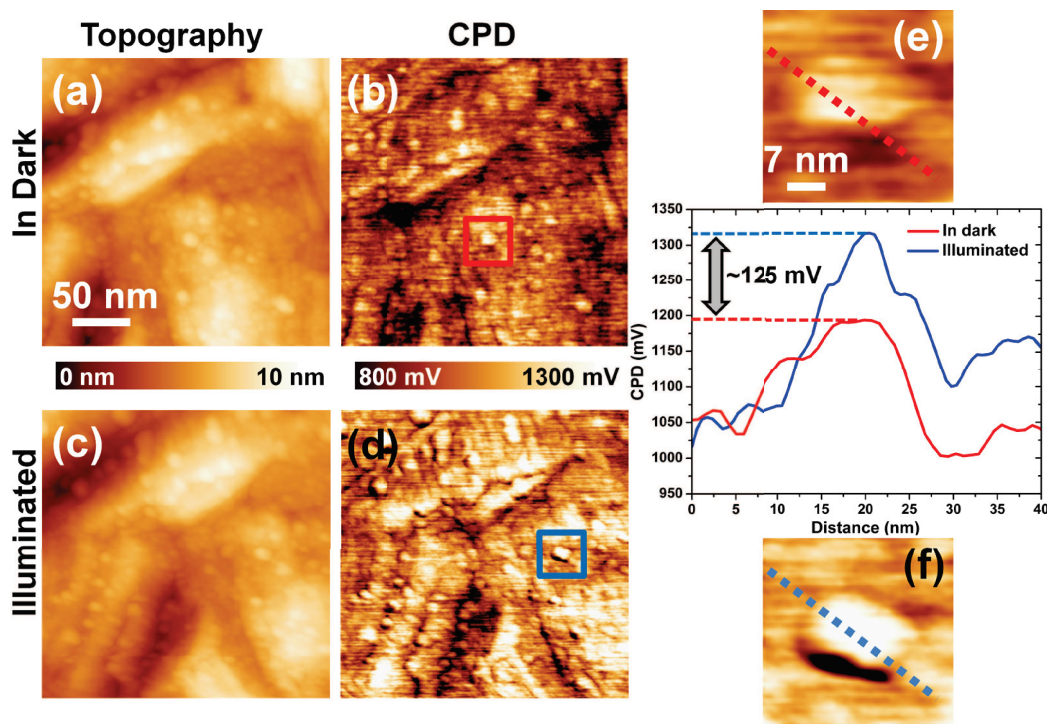


FIGURE A.6: FM-AFM (UHV, 300K) 2D topography (a,c) and CPD (b,d) images of the FG1-PCBM blend in dark (a,b) and under 532 nm illumination (c,d). 250 nm \times 250 nm, 500 \times 500 pixels, $\Delta f = -20$ Hz, $A_{vib} = 45$ nm, scan speed = 50 ms per pixel. CPD profile of the same magnified PCBM cluster in dark (e) and under illumination (f) shown in graph.

change, as outlined by the red and blue squares in figure A.6(b) and (d) and shown in figure A.6(e) and (f), respectively. This area encompasses a ~ 14 nm wide PC₇₀BM cluster emerging from the surrounding FG1 matrix. A typical profile of the same area is shown in the graph of figure A.6. While numerous profiles were taken, this is shown as an example of the typical response of the PC₇₀BM structure displayed under illumination. A predominate increase of approximately 125 mV from the in dark to the illuminated state is seen in the PC₇₀BM acceptor material, indicating a clear build up of negative charges. However, due to the complex nature of the topography and CPD signal, the π -conjugated molecular periodic stacks, as seen in figure A.3(c,d), are not visible in the CPD signal. Further investigations will have to be performed to increase the resolution at this scale.

Bibliography

- [1] Martin A. Green, Keith Emery, Yoshihiro Hishikawa, Wilhelm Warta, and Ewan D. Dunlop. Solar cell efficiency tables (Version 38). *Progress in Photovoltaics: Research and Applications*, 19(5): 565–572, 2011. URL <http://dx.doi.org/10.1002/pip.1150>.
- [2] Russell Gaudiana and Christoph Brabec. Organic materials: Fantastic plastic. *Nat Photonics*, 2(5):287–289, 2008.
- [3] Alex C. Mayer, Shawn R. Scully, Brian E. Hardin, Michael W. Rowell, and Michael D. McGehee. Polymer-based solar cells. *Materials Today*, 10(11):28 – 33, 2007. URL <http://www.sciencedirect.com/science/article/pii/S1369702107702766>.
- [4] Gang Li, Vishal Shrotriya, Jinsong Huang, Yan Yao, Tom Moriarty, Keith Emery, and Yang Yang. High-efficiency solution processable polymer photovoltaic cells by self-organization of polymer blends. *Nature Materials*, 4(11):864–868, 2005. URL <http://dx.doi.org/10.1038/nmat1500>.
- [5] W. Ma, C. Yang, X. Gong, K. Lee, and A.J. Heeger. Thermally stable, efficient polymer solar cells with nanoscale control of the interpenetrating network morphology. *Advanced Functional Materials*, 15(10):1617–1622, 2005. URL <http://dx.doi.org/10.1002/adfm.200500211>.
- [6] J. Peet, J. Y. Kim, N. E. Coates, W. L. Ma, D. Moses, A. J. Heeger, and G. C. Bazan. Efficiency enhancement in low-bandgap polymer solar cells by processing with alkane dithiols. *Nature Materials*, 6(7):497–500, 2007. URL <http://dx.doi.org/10.1038/nmat1928>.
- [7] Hsiang-Yu Chen, Jianhui Hou, Shaoqing Zhang, Yongye Liang, Guanwen Yang, Yang Yang, Luping Yu, Yue Wu, and Gang Li. Polymer solar cells with enhanced open-circuit voltage and efficiency. *Nature Photonics*, 3(11):649–653, 2009. URL <http://dx.doi.org/10.1038/nphoton.2009.192>.
- [8] Martin A. Green, Keith Emery, Yoshihiro Hishikawa, and Wilhelm Warta. Solar cell efficiency tables (version 37). *Progress in Photovoltaics: Research and Applications*, 19(1):84–92, 2011. URL <http://dx.doi.org/10.1002/pip.1088>.
- [9] F. A. Kekulé. Sur la constitution des substances aromatiques. *Bulletin de la Société Chimique de Paris*, 3:98–110, 1865.
- [10] Leo Gross, Fabian Mohn, Nikolaj Moll, Peter Liljeroth, and Gerhard Meyer. The chemical structure of a molecule resolved by atomic force microscopy. *Science*, 325(5944):1110–1114, 2009. URL <http://www.sciencemag.org/content/325/5944/1110.abstract>.

- [11] S. Morita, R. Wiesendanger, and E. Meyer. *Noncontact Atomic Force Microscopy*. Springer, Berlin, Germany, 2002. ISBN 978-3-540-43117-6. URL <http://www.springer.com/materials/nanotechnology/book/978-3-540-43117-6>.
- [12] S. Morita, F. J. Giessibl, and R. Wiesendanger. *Noncontact Atomic Force Microscopy*, volume 2. Springer, Berlin, Germany, 2009. ISBN 978-3-642-01494-9. URL <http://www.springer.com/materials/nanotechnology/book/978-3-642-01494-9>.
- [13] Franz J. Giessibl. Advances in atomic force microscopy. *Reviews of Modern Physics*, 75(3):949–983, July 2003. URL <http://link.aps.org/doi/10.1103/RevModPhys.75.949>.
- [14] Kanan P. Puntambekar, Paul V. Pesavento, and C. Daniel Frisbie. Surface potential profiling and contact resistance measurements on operating pentacene thin-film transistors by kelvin probe force microscopy. *Applied Physics Letters*, 83(26):5539–5541, 2003. URL <http://link.aip.org/link/doi/10.1063/1.1637443>.
- [15] Y. Luo, F. Gustavo, J.-Y. Henry, F. Mathevet, F. Lefloch, M. Sanquer, P. Rannou, and B. Grévin. Probing local electronic transport at the organic single-crystal/dielectric interface. *Advanced Materials*, 19(17):2267–2273, 2007. URL <http://dx.doi.org/10.1002/adma.200700913>.
- [16] H. Hoppe, T. Glatzel, M. Niggemann, A. Hinsch, M. Ch. Lux-Steiner, and N. S. Sariciftci. Kelvin probe force microscopy study on conjugated polymer/fullerene bulk heterojunction organic solar cells. *Nano Letters*, 5(2):269–274, 2005. URL <http://pubs.acs.org/doi/abs/10.1021/nl048176c>.
- [17] Marco Chiesa, Lukas Bürgi, Ji-Seon Kim, Rafi Shikler, Richard H. Friend, and Henning Sirringhaus. Correlation between surface photovoltage and blend morphology in polyfluorene-based photodiodes. *Nano Letters*, 5(4):559–563, 2005. URL <http://pubs.acs.org/doi/abs/10.1021/nl047929s>.
- [18] Klára Maturová, Martijn Kemerink, Martijn M. Wienk, Dimitri S. H. Charrier, and René A. J. Janssen. Scanning Kelvin probe microscopy on bulk heterojunction polymer blends. *Advanced Functional Materials*, 19(9):1379–1386, 2009. URL <http://dx.doi.org/10.1002/adfm.200801283>.
- [19] Piotr Matyba, Klara Maturova, Martijn Kemerink, Nathaniel D. Robinson, and Ludvig Edman. The dynamic organic p-n junction. *Nature Materials*, 8(8):672–676, 2009. URL <http://dx.doi.org/10.1038/nmat2478>.
- [20] Sascha Sadewasser, Pavel Jelinek, Chung-Kai Fang, Oscar Custance, Yusaku Yamada, Yoshiaki Sugimoto, Masayuki Abe, and Seizo Morita. New insights on atomic-resolution frequency-modulation Kelvin-probe force-microscopy imaging of semiconductors. *Phys. Rev. Lett.*, 103(26):266103, December 2009.
- [21] Laurent Nony, Adam S. Foster, Franck Bocquet, and Christian Loppacher. Understanding the atomic-scale contrast in Kelvin probe force microscopy. *Phys. Rev. Lett.*, 103(3):036802, July 2009.
- [22] C. K. Chiang, C. R. Fincher, Y. W. Park, A. J. Heeger, H. Shirakawa, E. J. Louis, S. C. Gau, and Alan G. MacDiarmid. Electrical conductivity in doped polyacetylene. *Phys. Rev. Lett.*, 39(17):1098–1101, October 1977. URL <http://link.aps.org/doi/10.1103/PhysRevLett.39.1098>.

- [23] Hideki Shirakawa, Edwin J. Louis, Alan G. MacDiarmid, Chwan K. Chiang, and Alan J. Heeger. Synthesis of electrically conducting organic polymers: halogen derivatives of polyacetylene, $(\text{CH})_x$. *J. Chem. Soc., Chem. Commun.*, pages 578–580, 1977. URL <http://dx.doi.org/10.1039/C39770000578>.
- [24] *Advanced Information on the Nobel Prize of Chemistry 2000*. The Royal Swedish Academy of Sciences. URL http://nobelprize.org/nobel_prizes/chemistry/laureates/2000.
- [25] György Inzelt. Historical background (Or: There is nothing new under the sun). In *Conducting Polymers*, Monographs in Electrochemistry, pages 265–269. Springer Berlin Heidelberg, 2008. URL http://dx.doi.org/10.1007/978-3-540-75930-0_8.
- [26] Noel S. Hush. An overview of the first half-century of molecular electronics. *Annals of the New York Academy of Sciences*, 1006(1):1–20, 2003. URL <http://dx.doi.org/10.1196/annals.1292.016>.
- [27] Stephen R. Forrest and Mark E. Thompson. Introduction: Organic electronics and optoelectronics. *Chemical Reviews*, 107(4):923–925, 2007. URL <http://pubs.acs.org/doi/abs/10.1021/cr0501590>.
- [28] Serap Günes, Helmut Neugebauer, and Niyazi Serdar Sariciftci. Conjugated polymer-based organic solar cells. *Chemical Reviews*, 107(4):1324–1338, 2007. URL <http://pubs.acs.org/doi/abs/10.1021/cr050149z>.
- [29] Yen-Ju Cheng, Sheng-Hsiung Yang, and Chain-Shu Hsu. Synthesis of conjugated polymers for organic solar cell applications. *Chemical Reviews*, 109(11):5868–5923, 2009. URL <http://pubs.acs.org/doi/abs/10.1021/cr900182s>.
- [30] Tommie W. Kelley, Paul F. Baude, Chris Gerlach, David E. Ender, Dawn Muyres, Michael A. Haase, Dennis E. Vogel, and Steven D. Theiss. Recent progress in organic electronics: Materials, devices, and processes. *Chemistry of Materials*, 16(23):4413–4422, 2004. URL <http://pubs.acs.org/doi/abs/10.1021/cm049614j>.
- [31] Vellaiappillai Tamilavan, Myungkwan Song, Sung-Ho Jin, and Myung Ho Hyun. Synthesis of conjugated polymers with broad absorption bands and photovoltaic properties as bulk heterojunction solar cells. *Polymer*, 52(11):2384–2390, 2011. URL <http://www.sciencedirect.com/science/article/pii/S0032386111002461>.
- [32] Gilles Horowitz. Organic thin film transistors: From theory to real devices. *Journal of Materials Research*, 19(7):1946–1962, 2004. URL <http://www.mrs.org/publications/jmr/jmra/2004/jul/0266.html>.
- [33] Benjamin Grévin, Renaud Demadrille, Mathieu Linares, Roberto Lazzaroni, and Philippe Leclère. Probing the local conformation within π -conjugated one-dimensional supramolecular stacks using frequency modulation atomic force microscopy. *Advanced Materials*, 21(41):4124–4129, 2009. URL <http://dx.doi.org/10.1002/adma.200803762>.
- [34] Lorette Scifo. *Structuration et Propriétés Électroniques de Matériaux π -Conjugés Modèles Sondées à l'Échelle Moléculaire par Microscopie en Champ Proche*. PhD thesis, Université Joseph Fourier, 2007.

- [35] R. Joseph Kline, Michael D. McGehee, and Michael F. Toney. Highly oriented crystals at the buried interface in polythiophene thin-film transistors. *Nature Materials*, 5:222–228, 2006. URL <http://dx.doi.org/10.1038/nmat1590>.
- [36] H. Sirringhaus, R. J. Wilson, R. H. Friend, M. Inbasekaran, W. Wu, E. P. Woo, M. Grell, and D. D. C. Bradley. Mobility enhancement in conjugated polymer field-effect transistors through chain alignment in a liquid-crystalline phase. *77(3)*:406–408, 2000. URL <http://dx.doi.org/doi/10.1063/1.126991>.
- [37] Karl R. Amundson, B. Joyce Sapjeta, Andrew J. Lovinger, and Zhenan Bao. An in-plane anisotropic organic semiconductor based upon poly(3-hexyl thiophene). *Thin Solid Films*, 414(1):143 – 149, 2002. URL <http://www.sciencedirect.com/science/article/pii/S0040609002003383>.
- [38] L. Kinder, J. Kanicki, and P. Petroff. Structural ordering and enhanced carrier mobility in organic polymer thin film transistors. *Synthetic Metals*, 146(2):181 – 185, 2004. URL <http://www.sciencedirect.com/science/article/pii/S0379677904002802>.
- [39] H. Sirringhaus, P. J. Brown, R. H. Friend, M. M. Nielsen, K. Bechgaard, B. M. W. Langeveld-Voss, A. J. H. Spiering, R. A. J. Janssen, E. W. Meijer, P. Herwig, and D. M. de Leeuw. Two-dimensional charge transport in self-organized, high-mobility conjugated polymers. *Nature*, 401: 685–688, 1999. URL <http://dx.doi.org/10.1038/44359>.
- [40] Jean-Marie Lehn. Supramolecular chemistry – scope and perspectives molecules, supermolecules, and molecular devices (nobel lecture). *Angewandte Chemie International Edition in English*, 27(1):89–112, 1988. ISSN 1521-3773. URL <http://dx.doi.org/10.1002/anie.198800891>.
- [41] Jean-Marie Lehn. Perspectives in supramolecular chemistry – from molecular recognition towards molecular information processing and self-organization. *Angewandte Chemie International Edition in English*, 29(11):1304–1319, 1990. ISSN 1521-3773. URL <http://dx.doi.org/10.1002/anie.199013041>.
- [42] Jean-Marie Lehn. *Supramolecular Chemistry: Concepts and Perspectives*. George Fisher Baker Lectures in Chemistry. Wiley-VCH, 1995. ISBN 3-527-29311-6.
- [43] Jean-Marie Lehn. Toward self-organization and complex matter. *Science*, 295(5564):2400–2403, 2002. URL <http://www.sciencemag.org/content/295/5564/2400.abstract>.
- [44] Jean Roncali. Molecular bulk heterojunctions: An emerging approach to organic solar cells. *Accounts of Chemical Research*, 42(11):1719–1730, 2009. URL <http://pubs.acs.org/doi/abs/10.1021/ar900041b>.
- [45] Barry C. Thompson and Jean M. J. Fréchet. Polymer-Fullerene composite solar cells. *Angewandte Chemie International Edition*, 47(1):58–77, 2008. URL <http://dx.doi.org/10.1002/anie.200702506>.
- [46] James R. Heath and Mark A. Ratner. Molecular electronics. *Physics Today*, 56(5):43–49, 2003. URL <http://link.aip.org/link/?PTO/56/43/1>.
- [47] N. S. Sariciftci, L. Smilowitz, A. J. Heeger, and F. Wudl. Photoinduced electron transfer from a conducting polymer to buckminsterfullerene. *Science*, 258(5087):1474–1476, 1992. URL <http://www.sciencemag.org/content/258/5087/1474.abstract>.

- [48] C. W. Tang. Two-layer organic photovoltaic cell. *Applied Physics Letters*, 48(2):183–185, 1986. URL <http://link.aip.org/link/doi/10.1063/1.96937>.
- [49] Dieter Wöhrle and Dieter Meissner. Organic solar cells. *Advanced Materials*, 3(3):129–138, 1991. URL <http://dx.doi.org/10.1002/adma.19910030303>.
- [50] G. Yu, J. Gao, J. C. Hummelen, F. Wudl, and A. J. Heeger. Polymer photovoltaic cells: Enhanced efficiencies via a network of internal donor-acceptor heterojunctions. *Science*, 270(5243):1789–1791, 1995. URL <http://www.sciencemag.org/content/270/5243/1789.abstract>.
- [51] M. Granstrom, K. Petritsch, A. C. Arias, A. Lux, M. R. Andersson, and R. H. Friend. Laminated fabrication of polymeric photovoltaic diodes. *Nature*, 395:257–260, 1998. URL <http://dx.doi.org/10.1038/26183>.
- [52] H. Antoniadis, B.R. Hsieh, M.A. Abkowitz, S.A. Jenekhe, and M. Stolka. Photovoltaic and photoconductive properties of aluminum/poly(p-phenylene vinylene) interfaces. *Synthetic Metals*, 62(3):265–271, 1994. URL <http://www.sciencedirect.com/science/article/pii/0379677994902151>.
- [53] J. J. M. Halls, C. A. Walsh, N. C. Greenham, E. A. Marseglia, R. H. Friend, S. C. Moratti, and A. B. Holmes. Efficient photodiodes from interpenetrating polymer networks. *Nature*, 376:498–500, 1995. URL <http://dx.doi.org/10.1038/376498a0>.
- [54] G. Yu and A. J. Heeger. Charge separation and photovoltaic conversion in polymer composites with internal donor/acceptor heterojunctions. *Journal of Applied Physics*, 78(7):4510–4515, 1995. URL <http://dx.doi.org/doi/10.1063/1.359792>.
- [55] Samson A. Jenekhe and Shujian Yi. Efficient photovoltaic cells from semiconducting polymer heterojunctions. *Applied Physics Letters*, 77(17):2635–2637, 2000. URL <http://dx.doi.org/doi/10.1063/1.1320022>.
- [56] A. J. Breeze, A. Salomon, D. S. Ginley, B. A. Gregg, H. Tillmann, and H.-H. Hörhold. Polymer-erylene diimide heterojunction solar cells. *Applied Physics Letters*, 81(16):3085–3087, 2002. URL <http://dx.doi.org/doi/10.1063/1.1515362>.
- [57] Sean E. Shaheen, Christoph J. Brabec, N. Serdar Sariciftci, Franz Padinger, Thomas Fromherz, and Jan C. Hummelen. 2.5 percent efficient organic plastic solar cells. *Applied Physics Letters*, 78(6):841–843, 2001. URL <http://dx.doi.org/doi/10.1063/1.1345834>.
- [58] J. J. Dittmer, E. A. Marseglia, and R. H. Friend. Electron trapping in dye/polymer blend photovoltaic cells. *Advanced Materials*, 12(17):1270–1274, 2000. URL [http://dx.doi.org/10.1002/1521-4095\(200009\)12:17<1270::AID-ADMA1270>3.0.CO;2-8](http://dx.doi.org/10.1002/1521-4095(200009)12:17<1270::AID-ADMA1270>3.0.CO;2-8).
- [59] Brian O'Regan and Michael Gratzel. A low-cost, high-efficiency solar cell based on dye-sensitized colloidal TiO_2 films. *Nature*, 353:737–740, 1991. URL <http://dx.doi.org/10.1038/353737a0>.
- [60] N. C. Greenham, Xiaogang Peng, and A. P. Alivisatos. Charge separation and transport in conjugated-polymer/semiconductor-nanocrystal composites studied by photoluminescence quenching and photoconductivity. *Phys. Rev. B*, 54(24):17628–17637, December 1996.

- [61] H. Hoppe, N. S. Sariciftci, and D. Meissner. Optical constants of conjugated polymer/fullerene based bulk-heterojunction organic solar cells. *Molecular Crystals and Liquid Crystals*, 385(1): 113–119, 2002. URL <http://www.tandfonline.com/doi/abs/10.1080/713738799>.
- [62] Alex C. Mayer, Shawn R. Scully, Brian E. Hardin, Michael W. Rowell, and Michael D. McGehee. Polymer-based solar cells. *Materials Today*, 10(11):28 – 33, 2007. URL <http://www.sciencedirect.com/science/article/pii/S1369702107702766>.
- [63] Serap Günes, Helmut Neugebauer, and Niyazi Serdar Sariciftci. Conjugated polymer-based organic solar cells. *Chemical Reviews*, 107(4):1324–1338, 2007. URL <http://pubs.acs.org/doi/abs/10.1021/cr050149z>.
- [64] Kevin M. Coakley and Michael D. McGehee. Conjugated polymer photovoltaic cells. *Chemistry of Materials*, 16(23):4533–4542, 2004. URL <http://pubs.acs.org/doi/abs/10.1021/cm049654n>.
- [65] V.D. Mihaileti, H.X. Xie, B. de Boer, L.J.A. Koster, and P.W.M. Blom. Charge transport and photocurrent generation in poly(3-hexylthiophene): Methanofullerene bulk-heterojunction solar cells. *Advanced Functional Materials*, 16(5):699–708, 2006. URL <http://dx.doi.org/10.1002/adfm.200500420>.
- [66] F. Padinger, R.S. Rittberger, and N.S. Sariciftci. Effects of postproduction treatment on plastic solar cells. *Advanced Functional Materials*, 13(1):85–88, 2003. URL <http://dx.doi.org/10.1002/adfm.200390011>.
- [67] Peter Peumans, Soichi Uchida, and Stephen R. Forrest. Efficient bulk-heterojunction photovoltaic cells using small-molecular-weight organic thin films. *Nature*, 425:158–162, 2003. URL <http://dx.doi.org/10.1038/nature01949>.
- [68] Svetlana S. van Bavel, Erwan Sourty, Gijsbertus de With, and Joachim Loos. Three-dimensional nanoscale organization of bulk heterojunction polymer solar cells. *Nano Letters*, 9(2):507–513, 2009. URL <http://pubs.acs.org/doi/abs/10.1021/nl8014022>.
- [69] Steffan Cook, Ruyzi Katoh, and Akihiro Furube. Ultrafast studies of charge generation in pcbm:p3ht blend films following excitation of the fullerene pcbm. *The Journal of Physical Chemistry C*, 113(6):2547–2552, 2009. URL <http://pubs.acs.org/doi/abs/10.1021/jp8050774>.
- [70] Vishal Shrotriya, Jianyong Ouyang, Ricky J. Tseng, Gang Li, and Yang Yang. Absorption spectra modification in poly(3-hexylthiophene):methanofullerene blend thin films. *Chemical Physics Letters*, 411(1-3):138 – 143, 2005. URL <http://www.sciencedirect.com/science/article/pii/S0009261405008729>.
- [71] C.J. Brabec, V. Dyakonov, J. Parisi, and N.S. Sariciftci. *Organic photovoltaics: concepts and realization*. Springer series in materials science. Springer, 2003. ISBN 3-540-00405-9.
- [72] C. Deibel, A. Wagenpfahl, and V. Dyakonov. Origin of reduced polaron recombination in organic semiconductor devices. *Phys. Rev. B*, 80(7):075203, August 2009.
- [73] Maria Hilczler and M. Tachiya. Unified theory of geminate and bulk electron-hole recombination in organic solar cells. *The Journal of Physical Chemistry C*, 114(14):6808–6813, 2010. URL <http://pubs.acs.org/doi/abs/10.1021/jp912262h>.

- [74] Christoph J. Brabec, Gerald Zerza, Giulio Cerullo, Sandro De Silvestri, Silvia Luzzati, Jan C. Hummelen, and Serdar Sariciftci. Tracing photoinduced electron transfer process in conjugated polymer/fullerene bulk heterojunctions in real time. *Chemical Physics Letters*, 340(3-4):232 – 236, 2001. URL <http://www.sciencedirect.com/science/article/pii/S0009261401004316>.
- [75] Ivan Montanari, Ana F. Nogueira, Jenny Nelson, James R. Durrant, Christoph Winder, Maria Antonietta Loi, Niyazi Serdar Sariciftci, and Christoph Brabec. Transient optical studies of charge recombination dynamics in a polymer/fullerene composite at room temperature. *Applied Physics Letters*, 81(16):3001–3003, 2002. URL <http://link.aip.org/link/doi/10.1063/1.1512943>.
- [76] Ton Offermans, Stefan C. J. Meskers, and René A. J. Janssen. Charge recombination in a poly(para-phenylene vinylene)-fullerene derivative composite film studied by transient, nonresonant, hole-burning spectroscopy. *Journal of Chemical Physics*, 119(20):10924–10929, 2003. URL <http://link.aip.org/link/doi/10.1063/1.1619946>.
- [77] M.-C. Scharber, D. Mühlbacher, M. Koppe, P. Denk, C. Waldauf, A.-J. Heeger, and C.-J. Brabec. Design rules for donors in bulk-heterojunction solar cells: towards 10 percent energy-conversion efficiency. *Advanced Materials*, 18(6):789–794, 2006. URL <http://dx.doi.org/10.1002/adma.200501717>.
- [78] Frédéric Lincker, Nicolas Delbosc, Séverine Bailly, Rémi De Bettignies, Martial Billon, Adam Pron, and Renaud Demadrille. Fluorenone-based molecules for bulk-heterojunction solar cells: Synthesis, characterization, and photovoltaic properties. *Advanced Functional Materials*, 18(21):3444–3453, 2008. URL <http://dx.doi.org/10.1002/adfm.200800366>.
- [79] Frederic Lincker, Benoit Heinrich, Remi De Bettignies, Patrice Rannou, Jacques Pecaut, Benjamin Grevin, Adam Pron, Bertrand Donnio, and Renaud Demadrille. Fluorenone core donor-acceptor-donor [small pi]-conjugated molecules end-capped with dendritic oligo(thiophene)s: synthesis, liquid crystalline behaviour, and photovoltaic applications. *J. Mater. Chem.*, 21:5238–5247, 2011. URL <http://dx.doi.org/10.1039/C0JM02437F>.
- [80] Jan C. Hummelen, Brian W. Knight, F. LePeq, Fred Wudl, Jie Yao, and Charles L. Wilkins. Preparation and characterization of fulleroid and methanofullerene derivatives. *The Journal of Organic Chemistry*, 60(3):532–538, 1995. URL <http://pubs.acs.org/doi/abs/10.1021/jo00108a012>.
- [81] Sumio Iijima. Helical microtubules of graphitic carbon. *Nature*, 354(6348):56–58, 1991. URL <http://dx.doi.org/10.1038/354056a0>.
- [82] Seong Jun Kang, Coskun Kocabas, Taner Ozel, Moonsub Shim, Ninad Pimparkar, Muhammad A. Alam, and John A. Rotkin, Slava V. and Rogers. High-performance electronics using dense, perfectly aligned arrays of single-walled carbon nanotubes. *Nature Nanotechnology*, 2(4):230–236, 2007. URL <http://dx.doi.org/10.1038/nnano.2007.77>.
- [83] Kenji Hata, Don N. Futaba, Kohei Mizuno, Tatsunori Namai, Motoo Yumura, and Sumio Iijima. Water-assisted highly efficient synthesis of impurity-free single-walled carbon nanotubes. *Science*, 306(5700):1362–1364, 2004. URL <http://www.sciencemag.org/content/306/5700/1362.abstract>.

- [84] G. Binnig, H. Rohrer, Ch. Gerber, and E. Weibel. Surface studies by scanning tunneling microscopy. *Physical Review Letters*, 49(1):57–61, April 1982. URL <http://link.aps.org/doi/10.1103/PhysRevLett.49.57>.
- [85] G. Binnig, H. Rohrer, Ch. Gerber, and E. Weibel. Tunneling through a controllable vacuum gap. *Applied Physics Letters*, 40(2):178–180, January 1982. URL <http://link.aip.org/link/doi/10.1063/1.92999>.
- [86] G. Binnig and H. Rohrer: U.S. Patent 4, 343, 993. Scanning tunneling microscope, 1982.
- [87] G. Binnig, H. Rohrer, C. F. Quate, and Ch. Gerber. 7×7 reconstruction on Si(111) resolved in real space. *Physical Review Letters*, 50(2):120–123, January 1983. URL <http://link.aps.org/doi/10.1103/PhysRevLett.50.120>.
- [88] Franz J. Giessibl. AFM's path to atomic resolution. *Materials Today*, 8(5):32–41, April 2005. URL <http://www.sciencedirect.com/science/article/pii/S1369702105008448>.
- [89] Roland Wiesendanger. *Scanning Probe Microscopy and Spectroscopy: Methods and Applications*. Cambridge University Press, Cambridge, United Kingdom, 1994. ISBN 0-521-42847-5. URL <http://dx.doi.org/10.2277/0521428475>.
- [90] S. Morita. *Roadmap of Scanning Probe Microscopy*. Springer, Berlin, Germany, 2007. ISBN 978-3-540-34314-1. URL <http://www.springer.com/materials/nanotechnology/book/978-3-540-34314-1>.
- [91] Peter W. Hawkes and John C. H. Spence. *Science of Microscopy*, volume 2. Springer, Berlin, Germany, 2007. ISBN 978-0-387-25296-4. URL <http://www.springer.com/materials/characterization+26+evaluation/book/978-0-387-25296-4>.
- [92] H.-J. Güntherodt, D. Anselmetti, and E. Meyer. *Forces in Scanning Probe Methods*. Kluwer Academic Publishers, 1995. ISBN 978-0-7923-3406-4. URL <http://www.springer.com/materials/book/978-0-7923-3406-4>.
- [93] David G. Rickerby, Giovanni Valdrè, and Ugo Valdrè. *Impact of Electron and Scanning Probe Microscopy on Materials Research*. Kluwer Academic Publishers, 1999. ISBN 978-0-7923-5940-1. URL <http://www.springer.com/materials/characterization+26+evaluation/book/978-0-7923-5940-1>.
- [94] G. Binnig: U.S. Patent 4, 724, 318. Atomic force microscope and method for imaging surfaces with atomic resolution, 1986.
- [95] G. Binnig, C. F. Quate, and Ch. Gerber. Atomic force microscope. *Physical Review Letters*, 56(9):930–933, March 1986. URL http://prl.aps.org/abstract/PRL/v56/i9/p930_1.
- [96] A. L. Weisenhorn, P. K. Hansma, T. R. Albrecht, and C. F. Quate. Forces in atomic force microscopy in air and water. *Applied Physics Letters*, 54(26):2651–2653, 1989. URL <http://link.aip.org/link/?APL/54/2651/1>.
- [97] Y. Martin, C. C. Williams, and H. K. Wickramasinghe. Atomic force microscope force mapping and profiling on a sub-100Å scale. *Journal of Applied Physics*, 61(10):4723–4729, May 1987. URL <http://link.aip.org/link/doi/10.1063/1.338807>.

- [98] Franz J. Giessibl. Forces and frequency shifts in atomic-resolution dynamic-force microscopy. *Physical Review B*, 56(24):16010–16015, December 1997. URL <http://link.aps.org/doi/10.1103/PhysRevB.56.16010>.
- [99] F. J. Giessibl. Theory for an electrostatic imaging mechanism allowing atomic resolution of ionic crystals by atomic force microscopy. *Phys. Rev. B*, 45(23):13815–13818, June 1992. URL <http://link.aps.org/doi/10.1103/PhysRevB.45.13815>.
- [100] Dror Sarid, Todd G. Ruskell, Richard K. Workman, and Dong Chen. Driven nonlinear atomic force microscopy cantilevers: From noncontact to tapping modes of operation. *J. Vac. Sci. Technol. B*, 14(2):864–867, 1996. URL <http://link.aip.org/link/?JV/B/14/864/1>.
- [101] Neil W. Ashcroft and N. David Mermin. *Solid State Physics*. Brooks Cole, Pacific Grove, California, United States, 1976. ISBN 0-030-83993-9.
- [102] Jacob N. Israelachvili. *Intermolecular and Surface Forces: With Applications to Colloidal and Biological Systems*, volume 2. Academic Press, 1992. ISBN 0-123-75181-0.
- [103] David Tabor. *Gases, Liquids and Solids*, volume 2. Cambridge University Press, 1980. ISBN 0-521-29466-5.
- [104] M. Guggisberg, M. Bammerlin, Ch. Loppacher, O. Pfeiffer, A. Abdurixit, V. Barwich, R. Bennewitz, A. Baratoff, E. Meyer, and H.-J. Güntherodt. Separation of interactions by noncontact force microscopy. *Phys. Rev. B*, 61(16):11151–11155, April 2000. URL <http://link.aps.org/doi/10.1103/PhysRevB.61.11151>.
- [105] Seizo Morita and Yasuhiro Sugawara. Atomically resolved imaging of Si(100)2×1, 2×1:h and 1×1:2h surfaces with noncontact atomic force microscopy. *Japanese Journal of Applied Physics*, 41:4857–4862, July 2002. URL <http://jjap.jsap.jp/link?JJAP/41/4857/>.
- [106] Singiresu S. Rao. *Mechanical Vibrations 4th Edition*. Prentice Hall, 2003. ISBN 0-130-48987-5.
- [107] John E. Sader, Ian Larson, Paul Mulvaney, and Lee R. White. Method for the calibration of atomic force microscope cantilevers. *Review of Scientific Instruments*, 66(7):3789–3798, 1995. URL <http://link.aip.org/link/?RSI/66/3789/1>.
- [108] John E. Sader, James W. M. Chon, and Paul Mulvaney. Calibration of rectangular atomic force microscope cantilevers. *Review of Scientific Instruments*, 70(10):3967–3969, 1999. URL <http://link.aip.org/link/?RSI/70/3967/1>.
- [109] Ricardo García and Rubén Pérez. Dynamic atomic force microscopy methods. *Surface Science Reports*, 47(6–8):197–301, September 2002. URL [http://dx.doi.org/10.1016/S0167-5729\(02\)00077-8](http://dx.doi.org/10.1016/S0167-5729(02)00077-8).
- [110] T. R. Albrecht, P. Grütter, D. Horne, and D. Rugar. Frequency modulation detection using high-Q cantilevers for enhanced force microscope sensitivity. *Journal of Applied Physics*, 69(2):668–673, January 1991. URL http://jap.aip.org/resource/1/japiau/v69/i2/p668_s1?bypassSS0=1.
- [111] Franz J. Giessibl, Hartmut Bielefeldt, Stefan Hembacher, and Jochen Mannhart. Calculation of the optimal imaging parameters for frequency modulation atomic force microscopy. *Applied Surface Science*, 140(3-4):352 – 357, 1999. URL <http://www.sciencedirect.com/science/article/pii/S0169433298005534>.

- [112] Franz J. Giessibl and Marco Tortonese. Self-oscillating mode for frequency modulation noncontact atomic force microscopy. *Applied Physics Letters*, 70(19):2529–2531, 1997. URL <http://link.aip.org/link/?APL/70/2529/1>.
- [113] J.S. Beasley and G.M. Miller. *Modern Electronic Communication: 9th Edition*. Pearson/Prentice Hall, 2008. ISBN 0-132-25113-6.
- [114] Franz J. Giessibl. Atomic resolution on Si(111)-(7×7) by noncontact atomic force microscopy with a force sensor based on a quartz tuning fork. *Applied Physics Letters*, 76(11):1470–1472, 2000. URL <http://link.aip.org/link/?APL/76/1470/1>.
- [115] Bharat Bhushan. *Springer Handbook of Nanotechnology*. Springer, 2010. ISBN 3-642-02524-2.
- [116] A. S. Foster, C. Barth, A. L. Shluger, and M. Reichling. Unambiguous interpretation of atomically resolved force microscopy images of an insulator. *Phys. Rev. Lett.*, 86(11):2373–2376, March 2001. URL http://prl.aps.org/abstract/PRL/v86/i11/p2373_1.
- [117] Byung I. Kim. Direct comparison between phase locked oscillator and direct resonance oscillator in the noncontact atomic force microscopy under ultrahigh vacuum. *Review of Scientific Instruments*, 75(11):5035–5037, 2004. URL <http://link.aip.org/link/?RSI/75/5035/1>.
- [118] Z. Khan, C. Leung, B. A. Tahir, and B. W. Hoogenboom. Digitally tunable, wide-band amplitude, phase, and frequency detection for atomic-resolution scanning force microscopy. *Review of Scientific Instruments*, 81(7):073704, 2010. URL <http://link.aip.org/link/?RSI/81/073704/1>.
- [119] H. Diesinger, D. Deresmes, J.-P. Nys, and T. Mélin. Kelvin force microscopy at the second cantilever resonance: An out-of-vacuum crosstalk compensation setup. *Ultramicroscopy*, 108(8):773 – 781, 2008. URL <http://www.sciencedirect.com/science/article/pii/S0304399108000132>.
- [120] R. Garcia, C. J. Gómez, N. F. Martinez, S. Patil, C. Dietz, and R. Magerle. Identification of nanoscale dissipation processes by dynamic atomic force microscopy. *Phys. Rev. Lett.*, 97(1):016103, July 2006.
- [121] John E Sader, Takayuki Uchihashi, Michael J Higgins, Alan Farrell, Yoshikazu Nakayama, and Suzanne P Jarvis. Quantitative force measurements using frequency modulation atomic force microscopy - theoretical foundations. *Nanotechnology*, 16(3):S94, 2005. URL <http://stacks.iop.org/0957-4484/16/i=3/a=018>.
- [122] Noriaki Oyabu, Pablo Pou, Yoshiaki Sugimoto, Pavel Jelinek, Masayuki Abe, Seizo Morita, Rubén Pérez, and Óscar Custance. Single atomic contact adhesion and dissipation in dynamic force microscopy. *Phys. Rev. Lett.*, 96(10):106101, March 2006.
- [123] M A Venegas de la Cerda, J Abad, A Madgavkar, D Martrou, and S Gauthier. Step-induced tip polarity reversal investigated by dynamic force microscopy on KBr(001). *Nanotechnology*, 19(4):045503, 2008. URL <http://stacks.iop.org/0957-4484/19/i=4/a=045503>.
- [124] J. Erskine-Murray. On contact electricity of metals. *Proceedings of the Royal Society of London*, 63(389-400):113–146, 1898. URL <http://rsp1.royalsocietypublishing.org/content/63/389-400/113.short>.

- [125] W. A. Zisman. A new method of measuring contact potential differences in metals. *Review of Scientific Instruments*, 3(7):367–370, 1932. URL <http://link.aip.org/link/?RSI/3/367/1>.
- [126] M. Nonnenmacher, M. P. O’Boyle, and H. K. Wickramasinghe. Kelvin probe force microscopy. *Applied Physics Letters*, 58(25):2921–2923, April 1991. URL <http://link.aip.org/link/APPLAB/v58/i25/p2921/s1&Agg=doi>.
- [127] Ch. Sommerhalter, Th. W. Matthes, Th. Glatzel, A. Jager-Waldau, and M. Ch. Lux-Steiner. High-sensitivity quantitative Kelvin probe microscopy by noncontact ultra-high-vacuum atomic force microscopy. *Applied Physics Letters*, 75(2):286–288, 1999. URL <http://link.aip.org/link/?APL/75/286/1>.
- [128] K. Wandelt. The local work function: Concept and implications. *Applied Surface Science*, 111:1 – 10, 1997. URL <http://www.sciencedirect.com/science/article/pii/S0169433296006927>. Proceedings of the International Vacuum Electron Sources Conference 1996.
- [129] R. Shikler, T. Meoded, N. Fried, B. Mishori, and Y. Rosenwaks. Two-dimensional surface band structure of operating light emitting devices. *Journal of Applied Physics*, 86(1):107–113, 1999. URL <http://link.aip.org/link/?JAP/86/107/1>.
- [130] Laurent Nony, Franck Bocquet, Christian Loppacher, and Thilo Glatzel. On the relevance of the atomic-scale contact potential difference by amplitude-modulation and frequency-modulation Kelvin probe force microscopy. *Nanotechnology*, 20(26):264014, 2009. URL <http://iopscience.iop.org/0957-4484/20/26/264014>.
- [131] S. Hudlet, M. Saint Jean, C. Guthmann, and J. Berger. Evaluation of the capacitive force between an atomic force microscopy tip and a metallic surface. *Eur. Phys. J. B*, 2(1):5–10, 1998. URL <http://dx.doi.org/10.1007/s100510050219>.
- [132] S. Hudlet, M. Saint Jean, B. Roulet, J. Berger, and C. Guthmann. Electrostatic forces between metallic tip and semiconductor surfaces. *Journal of Applied Physics*, 77(7):3308–3314, 1995. URL <http://link.aip.org/link/?JAP/77/3308/1>.
- [133] S. V. Kalinin and A. Gruverman. *Scanning Probe Microscopy: Electrical and Electromechanical Phenomena at the Nanoscale*. Springer, Berlin, Germany, 2007. ISBN 978-0-387-28667-9. URL <http://www.springer.com/materials/characterization+26+evaluation/book/978-0-387-28667-9>.
- [134] Yves Martin, David W. Abraham, and H. Kumar Wickramasinghe. High-resolution capacitance measurement and potentiometry by force microscopy. *Applied Physics Letters*, 52(13):1103–1105, 1988. URL <http://link.aip.org/link/?APL/52/1103/1>.
- [135] M. Saint Jean, S. Hudlet, C. Guthmann, and J. Berger. Charge dynamics and time evolution of contact potential studied by atomic force microscopy. *Phys. Rev. B*, 56(23):15391–15395, December 1997. URL http://prb.aps.org/abstract/PRB/v56/i23/p15391_1.
- [136] Atsushi Kikukawa, Sumio Hosaka, and Ryo Imura. Silicon pn junction imaging and characterizations using sensitivity enhanced Kelvin probe force microscopy. *Applied Physics Letters*, 66(25):3510–3512, 1995. URL <http://link.aip.org/link/?APL/66/3510/1>.

- [137] Atsushi Kikukawa, Sumio Hosaka, and Ryo Imura. Vacuum compatible high-sensitive Kelvin probe force microscopy. *Review of Scientific Instruments*, 67(4):1463–1467, 1996. URL <http://link.aip.org/link/?RSI/67/1463/1>.
- [138] Th. Glatzel, S. Sadewasser, and M. Ch. Lux-Steiner. Amplitude or frequency modulation-detection in Kelvin probe force microscopy. *Applied Surface Science*, 210(1-2):84 – 89, 2003. URL <http://www.sciencedirect.com/science/article/pii/S0169433202014848>. 5th International Conference on non-contact AFM in Montreal, Canada.
- [139] R. Shikler, T. Meoded, N. Fried, and Y. Rosenwaks. Potential imaging of operating light-emitting devices using Kelvin force microscopy. *Applied Physics Letters*, 74(20):2972–2974, 1999. URL <http://link.aip.org/link/?APL/74/2972/1>.
- [140] R. Shikler, T. Meoded, N. Fried, B. Mishori, and Y. Rosenwaks. Two-dimensional surface band structure of operating light emitting devices. *Journal of Applied Physics*, 86(1):107–113, 1999. URL <http://link.aip.org/link/?JAP/86/107/1>.
- [141] Ch. Sommerhalter, Th. Glatzel, Th. W. Matthes, A. Jäger-Waldau, and M. Ch. Lux-Steiner. Kelvin probe force microscopy in ultra high vacuum using amplitude modulation detection of the electrostatic forces. *Applied Surface Science*, 157(4):263 – 268, 2000. URL <http://www.sciencedirect.com/science/article/pii/S0169433299005371>.
- [142] Ulrich Zerweck, Christian Loppacher, Tobias Otto, Stefan Grafström, and Lukas M. Eng. Accuracy and resolution limits of Kelvin probe force microscopy. *Phys. Rev. B*, 71(12):125424, March 2005. URL <http://link.aps.org/doi/10.1103/PhysRevB.71.125424>.
- [143] G. H. Enevoldsen, T. Glatzel, M. C. Christensen, J. V. Lauritsen, and F. Besenbacher. Atomic scale Kelvin probe force microscopy studies of the surface potential variations on the $TiO_2(110)$ surface. *Phys. Rev. Lett.*, 100(23):236104, June 2008. URL <http://link.aps.org/doi/10.1103/PhysRevLett.100.236104>.
- [144] Wilhelm Melitz, Jian Shen, Andrew C. Kummel, and Sangyeob Lee. Kelvin probe force microscopy and its application. *Surface Science Reports*, 66(1):1 – 27, 2011. URL <http://www.sciencedirect.com/science/article/pii/S0167572910000841>.
- [145] F. Krok, K. Sajewicz, J. Konior, M. Goryl, P. Piatkowski, and M. Szymonski. Lateral resolution and potential sensitivity in Kelvin probe force microscopy: Towards understanding of the sub-nanometer resolution. *Phys. Rev. B*, 77(23):235427, June 2008. URL <http://link.aps.org/doi/10.1103/PhysRevB.77.235427>.
- [146] Franck Bocquet, Laurent Nony, Christian Loppacher, and Thilo Glatzel. Analytical approach to the local contact potential difference on (001) ionic surfaces: Implications for Kelvin probe force microscopy. *Phys. Rev. B*, 78(3):035410, July 2008. URL <http://prb.aps.org/abstract/PRB/v78/i3/e035410>.
- [147] Wilhelm Melitz, Jian Shen, S. Lee, J.S. Lee, J.E. Royer, Steven Bentley, Douglas Macintyre, Martin Holland, Iain Thayne, and Andrew C. Kummel. (Invited) Tip cleaning and sample design for high resolution MOSCAP x-KPFM. *ECS Transactions*, 33(3):97–103, 2010. URL <http://link.aip.org/link/abstract/ECSTF8/v33/i3/p97/s1>.

- [148] T. Arai and M. Tomitori. Removal of contamination and oxide layers from UHV-AFM tips. *Applied Physics A: Materials Science & Processing*, 66:S319–S323, 1998. URL <http://dx.doi.org/10.1007/s003390051154>.
- [149] Masahiko Tomitori and Toyoko Arai. Tip cleaning and sharpening processes for noncontact atomic force microscope in ultrahigh vacuum. *Applied Surface Science*, 140(3-4):432 – 438, 1999. URL <http://www.sciencedirect.com/science/article/pii/S0169433298005698>.
- [150] H. Hertz. Ueber einen einfluss des ultravioletten lichtes auf die electriche entladung (On the influence of ultraviolet light on the electric discharge). *Annalen der Physik*, 267(8):983–1000, 1887. URL <http://dx.doi.org/10.1002/andp.18872670827>.
- [151] P. Lenard. Ueber die lichtelektrische wirkung (On the photoelectric effect). *Annalen der Physik*, 313(5):149–198, 1902. URL <http://dx.doi.org/10.1002/andp.19023130510>.
- [152] A. Einstein. Über einen die erzeugung und verwandlung des lichtes betreffenden heuristischen gesichtspunkt (Generation and transformation of light). *Annalen der Physik*, 322(6):132–148, 1905. URL <http://dx.doi.org/10.1002/andp.19053220607>.
- [153] H. P. Bonzel and Ch. Kleint. On the history of photoemission. *Progress in Surface Science*, 49(2):107–153, 1995. URL <http://www.sciencedirect.com/science/article/pii/007968169500035W>.
- [154] Stefan Hüfner. *Photoelectron spectroscopy: principles and applications*. Springer series in solid-state sciences. Springer, 2003. ISBN 3-540-41802-4. URL <http://books.google.com/books?id=Wf0w6jP9-oIC>.
- [155] Omicron Nanotechnology. *EA 125 Energy Analyser: User Guide Version 2.3*, July 2005.
- [156] D. Briggs. *Surface analysis of polymers by XPS and static SIMS*. Cambridge solid state science series. Cambridge University Press, 1998. ISBN 0-521-35222-3. URL http://books.google.com/books?id=pzj_6n0tEuwC.
- [157] D. Briggs and M.P. Seah. *Practical Surface Analysis: Auger and X-ray photoelectron spectroscopy*. Practical Surface Analysis. Wiley, 1990. ISBN 0-471-92081-9. URL <http://books.google.com/books?id=D9pTAAAMAAJ>.
- [158] CasaXPS. *Introduction to XPS with Examples of Spectra: User Guide Version 2.3.14*.
- [159] J.H. Moore, C.C. Davis, and M.A. Coplan. *Building scientific apparatus: a practical guide to design and construction*. Advanced Book Program. Westview Press, 2002. ISBN 0-813-34006-3. URL <http://books.google.com/books?id=D48NFxh68IIC>.
- [160] G. Margaritondo, D. L. Huber, and C. G. Olson. Photoemission spectroscopy of the high-temperature superconductivity gap. *Science*, 246(4931):770–775, 1989. URL <http://www.sciencemag.org/content/246/4931/770.abstract>.
- [161] K. Siegbahn, C. Nordling, R. Fahlman, R. Nordberg, K. Hamrin, J. Hedman, G. Johansson, T. Bergmark, S.-E. Karlsson, I. Lindgren, and B. Lindberg. *ESCA; atomic, molecular and solid state structure studied by means of electron spectroscopy*, volume 20 of *Nova Acta Regiae Soc. Sci.* Almqvist & Wiksells, 1967.

- [162] D. W. Turner and M. I. Al Jobory. Determination of ionization potentials by photoelectron energy measurement. *The Journal of Chemical Physics*, 37(12):3007–3008, 1962. URL <http://link.aip.org/link/?JCP/37/3007/1>.
- [163] J.W. Rabalais. *Principles of ultraviolet photoelectron spectroscopy*. Wiley Monographs in Chemical Physics. Wiley, 1977. ISBN 0-471-70285-4. URL <http://books.google.com/books?id=zkl5AAAAIAAJ>.
- [164] J S Kim, B Lagel, E Moons, N Johansson, I D Baikie, W R Salaneck, R H Friend, and F Cacialli. Kelvin probe and ultraviolet photoemission measurements of indium tin oxide work function: a comparison. *Synthetic Metals*, 111-112(1-2):311–314, 2000. URL <http://linkinghub.elsevier.com/retrieve/pii/S0379677999003549>.
- [165] G. Ertl and J. Küppers. *Low energy electrons and surface chemistry*. VCH, 1985. ISBN 3-527-26056-0.
- [166] Weijie Song and Michiko Yoshitake. A work function study of ultra-thin alumina formation on NiAl(110) surface. *Applied Surface Science*, 251(1-4):14 – 18, 2005. URL <http://www.sciencedirect.com/science/article/pii/S0169433205005349>. The 5th International Vacuum Electron Sources Conference – IVESC 2004.
- [167] I. Horcas, R. Fernandez, J. M. Gomez-Rodriguez, J. Colchero, J. Gomez-Herrero, and A. M. Baro. Wsxn: A software for scanning probe microscopy and a tool for nanotechnology. *Review of Scientific Instruments*, 78(1):013705, 2007. URL <http://link.aip.org/link/?RSI/78/013705/1>.
- [168] P.A. Redhead, J.P. Hobson, and E.V. Kornelsen. *The physical basis of ultrahigh vacuum*. American Vacuum Society classics. American Institute of Physics, 1993. ISBN 1-563-96122-9.
- [169] Leeor Kronik and Yoram Shapira. Surface photovoltage phenomena: theory, experiment, and applications. *Surface Science Reports*, 37(1-5):1 – 206, 1999. URL <http://www.sciencedirect.com/science/article/pii/S0167572999000023>.
- [170] Dieter K Schroder. Surface voltage and surface photovoltage: history, theory and applications. *Measurement Science and Technology*, 12(3):R16, 2001. URL <http://stacks.iop.org/0957-0233/12/i=3/a=202>.
- [171] Thilo Glatzel, Harald Hoppe, Niyazi S. Sariciftci, Martha Ch. Lux-Steiner, and Masaharu Komiyama. Kelvin probe force microscopy study of conjugated polymer/fullerene organic solar cells. *Japanese Journal of Applied Physics*, 44(7B):5370–5373, 2005. URL <http://jjap.jsap.jp/link?JJAP/44/5370/>.
- [172] Th. Glatzel, D. Fuertes Marrón, Th. Schedel-Niedrig, S. Sadewasser, and M. Ch. Lux-Steiner. CuGaSe₂ solar cell cross section studied by Kelvin probe force microscopy in ultrahigh vacuum. *Applied Physics Letters*, 81(11):2017–2019, 2002. URL <http://link.aip.org/link/doi/10.1063/1.1506205>.
- [173] Dieter Wöhrle and Dieter Meissner. Organic solar cells. *Advanced Materials*, 3(3):129–138, 1991. URL <http://dx.doi.org/10.1002/adma.19910030303>.

- [174] C. J. Brabec, N. S. Sariciftci, and J. C. Hummelen. Plastic solar cells. *Advanced Functional Materials*, 11(1):15–26, 2001. URL [http://dx.doi.org/10.1002/1616-3028\(200102\)11:1<15::AID-ADFM15>3.0.CO;2-A](http://dx.doi.org/10.1002/1616-3028(200102)11:1<15::AID-ADFM15>3.0.CO;2-A).
- [175] Rajiv Giridharagopal and David S. Ginger. Characterizing morphology in bulk heterojunction organic photovoltaic systems. *The Journal of Physical Chemistry Letters*, 1(7):1160–1169, 2010. URL <http://pubs.acs.org/doi/abs/10.1021/jz100100p>.
- [176] Vincenzo Palermo, Matthijs B. J. Otten, Andrea Liscio, Erik Schwartz, Pieter A. J. de Witte, Maria Angela Castriciano, Martijn M. Wienk, Fabian Nolde, Giovanna De Luca, Jeroen J. L. M. Cornelissen, Renet' A. J. Janssen, Klaus Müllen, Alan E. Rowan, Roeland J. M. Nolte, and Paolo Samori. The relationship between nanoscale architecture and function in photovoltaic multichromophoric arrays as visualized by Kelvin probe force microscopy. *Journal of the American Chemical Society*, 130(44):14605–14614, 2008. URL <http://pubs.acs.org/doi/abs/10.1021/ja804069n>.
- [177] Andrea Liscio, Vincenzo Palermo, and Paolo Samori. Nanoscale quantitative measurement of the potential of charged nanostructures by electrostatic and Kelvin probe force microscopy: Unraveling electronic processes in complex materials. *Accounts of Chemical Research*, 43(4):541–550, 2010. URL <http://pubs.acs.org/doi/abs/10.1021/ar900247p>.
- [178] Andrea Liscio, Vincenzo Palermo, Oliver Fenwick, Slawomir Braun, Klaus Müllen, Mats Fahlman, Franco Cacialli, and Paolo Samori. Local surface potential of π -conjugated nanostructures by Kelvin probe force microscopy: Effect of the sampling depth. *Small*, 7(5):634–639, 2011. URL <http://dx.doi.org/10.1002/smll.201001770>.
- [179] Andrea Liscio, Giovanna De Luca, Fabian Nolde, Vincenzo Palermo, Klaus Müllen, and Paolo Samori. Photovoltaic charge generation visualized at the nanoscale: a proof of principle. *Journal of the American Chemical Society*, 130(3):780–781, 2008. URL <http://pubs.acs.org/doi/abs/10.1021/ja075291r>.
- [180] Tom Martens, Zjef Beelen, Jan D'Haen, Tom Munters, Ludwig Goris, Jean Manca, Marc D'Olieslaeger, Dirk Vanderzande, Luc De Schepper, and Ronn Andriessen. Morphology of MDMO-PPV:PCBM bulk heterojunction organic solar cells studied by AFM, KFM, and TEM. *Organic Photovoltaics III; Proceedings of the SPIE-The International Society for Optical Engineering*, 4801(1):40–47, 2003. URL <http://dx.doi.org/doi/10.1117/12.452453>.
- [181] H. Hoppe, M. Niggemann, C. Winder, J. Kraut, R. Hiesgen, A. Hinsch, D. Meissner, and N.S. Sariciftci. Nanoscale morphology of conjugated polymer/fullerene-based bulk- heterojunction solar cells. *Advanced Functional Materials*, 14(10):1005–1011, 2004. ISSN 1616-3028. URL <http://dx.doi.org/10.1002/adfm.200305026>.
- [182] Harald Hoppe and Niyazi Serdar Sariciftci. Morphology of polymer/fullerene bulk heterojunction solar cells. *J. Mater. Chem.*, 16:45–61, 2006. URL <http://dx.doi.org/10.1039/B510618B>.
- [183] Tsung-Wei Zeng, Fang-Chi Hsu, Yu-Chieh Tu, Tsung-Han Lin, and Wei-Fang Su. Kelvin probe force microscopy study on hybrid P3HT:titanium dioxide nanorod materials. *Chemical Physics Letters*, 479(1-3):105 – 108, 2009. URL <http://www.sciencedirect.com/science/article/pii/S0009261409009610>.

- [184] Ming-Chung Wu, Yi-Jen Wu, Wei-Che Yen, Hsi-Hsing Lo, Ching-Fuh Lin, and Wei-Fang Su. Correlation between nanoscale surface potential and power conversion efficiency of P3HT/TiO₂ nanorod bulk heterojunction photovoltaic devices. *Nanoscale*, 2:1448–1454, 2010. URL <http://dx.doi.org/10.1039/B9NR00385A>.
- [185] Liming Liu and Guangyong Li. Electrical characterization of single-walled carbon nanotubes in organic solar cells by Kelvin probe force microscopy. *Applied Physics Letters*, 96(8):083302, 2010. URL <http://link.aip.org/link/doi/10.1063/1.3332489>.
- [186] Liming Liu and Guangyong Li. Scanning Kelvin probe force microscopy for investigation of charge transport in carbon-nanotube enhanced organic photovoltaics. In *Proceedings of 10th IEEE International Conference on Nanotechnology (IEEE-NANO)*, pages 1145–1148, August 2010. URL http://ieeexplore.ieee.org/xpls/abs_all.jsp?arnumber=5697875.
- [187] Ming-Chung Wu, Yun-Yue Lin, Sharon Chen, Hsueh-Chung Liao, Yi-Jen Wu, Chun-Wei Chen, Yang-Fang Chen, and Wei-Fang Su. Enhancing light absorption and carrier transport of P3HT by doping multi-wall carbon nanotubes. *Chemical Physics Letters*, 468(1-3):64–68, 2009. URL <http://www.sciencedirect.com/science/article/pii/S000926140801614X>.
- [188] Minh Trung Dang, Lionel Hirsch, and Guillaume Wantz. P3ht:pcbm, best seller in polymer photovoltaic research. *Advanced Materials*, 2011. ISSN 1521-4095. URL <http://dx.doi.org/10.1002/adma.201100792>.
- [189] Evan J. Spadafora, Renaud Demadrille, Bernard Ratier, and Benjamin Grévin. Imaging the carrier photogeneration in nanoscale phase segregated organic heterojunctions by Kelvin probe force microscopy. *Nano Letters*, 10(9):3337–3342, 2010. URL <http://pubs.acs.org/doi/abs/10.1021/nl101001d>.
- [190] R Radbeh, E Parbaile, J Bouclé, C Di Bin, A Moliton, V Coudert, F Rossignol, and B Ratier. Nanoscale control of the network morphology of high efficiency polymer fullerene solar cells by the use of high material concentration in the liquid phase. *Nanotechnology*, 21(3):035201, 2010. URL <http://stacks.iop.org/0957-4484/21/i=3/a=035201>.
- [191] S A Burke, J M LeDue, Y Miyahara, J M Topple, S Fostner, and P Grütter. Determination of the local contact potential difference of ptcda on nacl: a comparison of techniques. *Nanotechnology*, 20(26):264012, 2009. URL <http://stacks.iop.org/0957-4484/20/i=26/a=264012>.
- [192] T. Heim, K. Lmimouni, and D. Vuillaume. Ambipolar charge injection and transport in a single pentacene monolayer island. *Nano Letters*, 4(11):2145–2150, 2004. URL <http://pubs.acs.org/doi/abs/10.1021/nl0487673>.
- [193] T. M. Brown, J. S. Kim, R. H. Friend, F. Cacialli, R. Daik, and W. J. Feast. Built-in field electroabsorption spectroscopy of polymer light-emitting diodes incorporating a doped poly(3,4-ethylene dioxythiophene) hole injection layer. *Applied Physics Letters*, 75(12):1679–1681, 1999. URL <http://link.aip.org/link/doi/10.1063/1.124789>.
- [194] Y. Park, V. Choong, Y. Gao, B. R. Hsieh, and C. W. Tang. Work function of indium tin oxide transparent conductor measured by photoelectron spectroscopy. *Applied Physics Letters*, 68(19):2699–2701, 1996. URL <http://link.aip.org/link/doi/10.1063/1.116313>.

- [195] M. Kemerink, J. M. Kramer, H. H. P. Gommans, and R. A. J. Janssen. Temperature-dependent built-in potential in organic semiconductor devices. *Applied Physics Letters*, 88(19):192108, 2006. URL <http://link.aip.org/link/doi/10.1063/1.2205007>.
- [196] H. Ishii, N. Hayashi, E. Ito, Y. Washizu, K. Sugi, Y. Kimura, M. Niwano, Y. Ouchi, and K. Seki. Kelvin probe study of band bending at organic semiconductor/metal interfaces: examination of fermi level alignment. *physica status solidi (a)*, 201(6):1075–1094, 2004. URL <http://dx.doi.org/10.1002/pssa.200404346>.
- [197] M. Pfeiffer, K. Leo, and N. Karl. Fermi level determination in organic thin films by the Kelvin probe method. *Journal of Applied Physics*, 80(12):6880–6883, 1996. doi: DOI:10.1063/1.363757. URL <http://link.aip.org/link/doi/10.1063/1.363757>.
- [198] H. O. Jacobs, P. Leuchtmann, O. J. Homan, and A. Stemmer. Resolution and contrast in Kelvin probe force microscopy. *Journal of Applied Physics*, 84(3):1168–1173, 1998. URL <http://link.aip.org/link/doi/10.1063/1.368181>.
- [199] J. Colchero, A. Gil, and A. M. Baró. Resolution enhancement and improved data interpretation in electrostatic force microscopy. *Phys. Rev. B*, 64(24):245403, November 2001.
- [200] A Gil, J Colchero, J Gómez-Herrero, and A M Baró. Electrostatic force gradient signal: resolution enhancement in electrostatic force microscopy and improved Kelvin probe microscopy. *Nanotechnology*, 14(2):332, 2003. URL <http://stacks.iop.org/0957-4484/14/i=2/a=345>.
- [201] Krzysztof Sajewicz, Franciszek Krok, and Jerzy Konior. Bias potential for tip–plane systems in Kelvin probe force microscopy imaging of non-uniform surface potential distributions. *Japanese Journal of Applied Physics*, 49(2):025201, 2010. URL <http://jjap.jsap.jp/link?JJAP/49/025201/>.
- [202] Shin'ichi Kitamura and Masashi Iwatsuki. High-resolution imaging of contact potential difference with ultrahigh vacuum noncontact atomic force microscope. *Applied Physics Letters*, 72(24):3154–3156, 1998. URL <http://link.aip.org/link/doi/10.1063/1.121577>.
- [203] Shinichi Kitamura, Katsuyuki Suzuki, and Masashi Iwatsuki. High resolution imaging of contact potential difference using a novel ultrahigh vacuum non-contact atomic force microscope technique. *Applied Surface Science*, 140(3-4):265 – 270, 1999. URL <http://www.sciencedirect.com/science/article/pii/S0169433298005388>.
- [204] Shin'ichi Kitamura, Katsuyuki Suzuki, Masashi Iwatsuki, and C. B. Mooney. Atomic-scale variations in contact potential difference on Au/Si(111) 7×7 surface in ultrahigh vacuum. *Applied Surface Science*, 157(4):222 – 227, 2000. ISSN 0169–4332. URL <http://www.sciencedirect.com/science/article/pii/S0169433299005309>.
- [205] T. Arai and M. Tomitori. Observation of electronic states on Si(111)7×7 through short-range attractive force with noncontact atomic force spectroscopy. *Phys. Rev. Lett.*, 93(25):256101, December 2004.
- [206] Kenji Okamoto, Yasuhiro Sugawara, and Seizo Morita. The elimination of the ‘artifact’ in the electrostatic force measurement using a novel noncontact atomic force microscope/electrostatic force microscope. *Applied Surface Science*, 188(3-4):381 – 385, 2002. URL <http://www.sciencedirect.com/science/article/pii/S0169433201009539>.

- [207] Tadashi Shiota and Keiji Nakayama. Atom-resolved imaging of the potential distribution at Si (111) 7×7 surfaces. *Japanese Journal of Applied Physics*, 41(Part 2, No. 10B):L1178–L1180, 2002. URL <http://jjap.jsap.jp/link?JJAP/41/L1178/>.
- [208] Kenji Okamoto, Kentaro Yoshimoto, Yasuhiro Sugawara, and Seizo Morita. KPFM imaging of Si(111)-Sb surface for atom distinction using NC-AFM. *Applied Surface Science*, 210(1-2):128 – 133, 2003. URL <http://www.sciencedirect.com/science/article/pii/S0169433202014927>. 5th International Conference on non-contact AFM in Montreal, Canada.
- [209] Yasuhiro Sugawara, Takayuki Uchihashi, Masayuki Abe, and Seizo Morita. True atomic resolution imaging of surface structure and surface charge on the GaAs(110). *Applied Surface Science*, 140(3-4):371 – 375, 1999. URL <http://www.sciencedirect.com/science/article/pii/S0169433298005571>.
- [210] T. Eguchi, Y. Fujikawa, K. Akiyama, T. An, M. Ono, T. Hashimoto, Y. Morikawa, K. Terakura, T. Sakurai, M. G. Lagally, and Y. Hasegawa. Imaging of all dangling bonds and their potential on the Ge/Si(105) surface by noncontact atomic force microscopy. *Phys. Rev. Lett.*, 93:266102, December 2004. URL <http://link.aps.org/doi/10.1103/PhysRevLett.93.266102>.
- [211] Akira Sasahara, Chi Lun Pang, and Hiroshi Onishi. Probe microscope observation of platinum atoms deposited on the TiO₂(110)-(1×1) surface. *The Journal of Physical Chemistry B*, 110(27):13453–13457, 2006. URL <http://pubs.acs.org/doi/abs/10.1021/jp062000c>.
- [212] Akira Sasahara, Hiroshi Uetsuka, and Hiroshi Onishi. Individual adatoms on TiO₂(110)-(1×1) surface observed using Kelvin probe force microscope. *Japanese Journal of Applied Physics*, 43(7B):4647–4650, 2004. URL <http://jjap.jsap.jp/link?JJAP/43/4647/>.
- [213] Kenji Okamoto, Yasuhiro Sugawara, and Seizo Morita. The imaging mechanism of atomic-scale Kelvin probe force microscopy and its application to atomic-scale force mapping. *Japanese Journal of Applied Physics*, 42(Part 1, No. 11):7163–7168, 2003. URL <http://jjap.jsap.jp/link?JJAP/42/7163/>.
- [214] Franck Bocquet, Laurent Nony, and Christian Loppacher. Polarization effects in noncontact atomic force microscopy: A key to model the tip-sample interaction above charged adatoms. *Phys. Rev. B*, 83(3):035411, January 2011. URL <http://link.aps.org/doi/10.1103/PhysRevB.83.035411>.
- [215] Leo Gross, Fabian Mohn, Peter Liljeroth, Jascha Repp, Franz J. Giessibl, and Gerhard Meyer. Measuring the charge state of an adatom with noncontact atomic force microscopy. *Science*, 324(5933):1428–1431, June 2009. URL <http://www.sciencemag.org/content/324/5933/1428.abstract>.
- [216] Shigeki Hattori, Shinya Kano, Yasuo Azuma, and Yutaka Majima. Surface potential of 1,10-decanedithiol molecules inserted into octanethiol self-assembled monolayers on au(111). *The Journal of Physical Chemistry C*, 114(18):8120–8125, 2010. doi: 10.1021/jp101998q. URL <http://pubs.acs.org/doi/abs/10.1021/jp101998q>.
- [217] N. Saito, K. Hayashi, H. Sugimura, O. Takai, and N. Nakagiri. Surface potentials of patterned organosilane self-assembled monolayers acquired by kelvin probe force microscopy and ab initio molecular calculation. *Chemical Physics Letters*, 349(3-4):172 – 177, 2001. URL <http://www.sciencedirect.com/science/article/pii/S0009261401010971>.

- [218] N. Saito, K. Hayashi, H. Sugimura, O. Takai, and N. Nakagiri. Surface potential images of self-assembled monolayers patterned by organosilanes: ab initio molecular orbital calculations. *Surface and Interface Analysis*, 34(1):601–605, 2002. URL <http://dx.doi.org/10.1002/sia.1369>.
- [219] Th. Glatzel, L. Zimmerli, S. Koch, S. Kawai, and E. Meyer. Molecular assemblies grown between metallic contacts on insulating surfaces. *Applied Physics Letters*, 94(6):063303, 2009. URL <http://link.aip.org/link/doi/10.1063/1.3080614>.
- [220] Takashi Ichii, Takeshi Fukuma, Tadashi Yoda, Kei Kobayashi, Kazumi Matsushige, and Hirofumi Yamada. Submolecular-scale investigations on metal-phthalocyanine monolayers by frequency modulation atomic force microscopy. *Journal of Applied Physics*, 107(2):024315, 2010. URL <http://link.aip.org/link/doi/10.1063/1.3284094>.
- [221] Marek Józefowicz and Janina R. Heldt. Dipole moments studies of fluorenone and 4-hydroxyfluorenone. *Spectrochimica Acta Part A: Molecular and Biomolecular Spectroscopy*, 67(2):316 – 320, 2007. URL <http://www.sciencedirect.com/science/article/pii/S1386142506004161>.
- [222] James Hayton, Frédéric Lincker, Renaud Demadrille, Mathieu Linares, Mickael Brun, and Benjamin Grevin. Pi-conjugated molecular nanowire stacks investigated by frequency-modulation atomic force microscopy in the qplus configuration. *Applied Physics Express*, 2(9):091501, 2009. URL <http://apex.jsap.jp/link?APEX/2/091501/>.
- [223] Martin Wolffs, Mantas Malisauskas, Inge De Cat, Zeljko Tomovic, Jeroen van Herikhuyzen, Christianus M. A. Leenders, Evan J. Spadafora, Benjamin Grevin, Steven De Feyter, E. W. Meijer, Albertus P. H. J. Schenning, and Philippe Leclere. On the transfer of cooperative self-assembled π -conjugated fibrils to a gold substrate. *Chem. Commun.*, 47:9333–9335, 2011. URL <http://dx.doi.org/10.1039/C1CC12799C>.
- [224] Pengyu Ren and Jay W. Ponder. Polarizable atomic multipole water model for molecular mechanics simulation. *The Journal of Physical Chemistry B*, 107(24):5933–5947, 2003. URL <http://pubs.acs.org/doi/abs/10.1021/jp0278152B>.
- [225] Norman L. Allinger, Young H. Yuh, and Jenn Huei Lii. Molecular mechanics. the mm3 force field for hydrocarbons. 1. *Journal of the American Chemical Society*, 111(23):8551–8566, 1989. URL <http://pubs.acs.org/doi/abs/10.1021/ja00205a001>.
- [226] H. J. C. Berendsen, J. P. M. Postma, W. F. van Gunsteren, A. DiNola, and J. R. Haak. Molecular dynamics with coupling to an external bath. *Journal of Chemical Physics*, 81(8):3684–3690, 1984. URL <http://link.aip.org/link/doi/10.1063/1.448118>.
- [227] Mathieu Linares, Lorette Scifo, Renaud Demadrille, Patrick Brocorens, David Beljonne, Roberto Lazzaroni, and Benjamin Grevin. Two-dimensional self-assemblies of thiophene-fluorenone conjugated oligomers on graphite: A joint stm and molecular modeling study. *The Journal of Physical Chemistry C*, 112(17):6850–6859, 2008. URL <http://pubs.acs.org/doi/abs/10.1021/jp711047x>.
- [228] Maxim P. Nikiforov, Ulrich Zerweck, Peter Milde, Christian Loppacher, Tae-Hong Park, H. Tetsuo Uyeda, Michael J. Therien, Lukas Eng, and Dawn Bonnell. The effect of molecular orientation

- on the potential of porphyrin-metal contacts. *Nano Letters*, 8(1):110–113, 2008. URL <http://pubs.acs.org/doi/abs/10.1021/nl072175d>.
- [229] Huiyong Liu, V. Avrutin, N. Izyumskaya, Ü. Özgür, and H. Morkoç. Transparent conducting oxides for electrode applications in light emitting and absorbing devices. *Superlattices and Microstructures*, 48(5):458 – 484, 2010. URL <http://www.sciencedirect.com/science/article/pii/S0749603610001795>.
- [230] David S. Hecht, Liangbing Hu, and Glen Irvin. Emerging transparent electrodes based on thin films of carbon nanotubes, graphene, and metallic nanostructures. *Advanced Materials*, 23(13):1482–1513, 2011. URL <http://dx.doi.org/10.1002/adma.201003188>.
- [231] Brett R. Goldsmith, John G. Coroneus, Vaikunth R. Khalap, Alexander A. Kane, Gregory A. Weiss, and Philip G. Collins. Conductance-controlled point functionalization of single-walled carbon nanotubes. *Science*, 315(5808):77–81, 2007. URL <http://www.sciencemag.org/content/315/5808/77.abstract>.
- [232] Daihua Zhang, Kounghmin Ryu, Xiaolei Liu, Evgueni Polikarpov, James Ly, Mark E. Tompson, and Chongwu Zhou. Transparent, conductive, and flexible carbon nanotube films and their application in organic light-emitting diodes. *Nano Letters*, 6(9):1880–1886, 2006. URL <http://pubs.acs.org/doi/abs/10.1021/nl0608543>.
- [233] Miguel A. Contreras, Teresa Barnes, Jao van de Lagemaat, Garry Rumbles, Timothy J. Coutts, Chris Weeks, Paul Glatkowski, Igor Levitsky, Jorma Peltola, and David A. Britz. Replacement of transparent conductive oxides by single-wall carbon nanotubes in cu(in,ga)se₂-based solar cells. *The Journal of Physical Chemistry C*, 111(38):14045–14048, 2007. URL <http://pubs.acs.org/doi/abs/10.1021/jp075507b>.
- [234] Andriy V Kyrylyuk, Marie Claire Hermant, Tanja Schilling, Bert Klumperman, Cor E Koning, and Paul Van Der Schoot. Controlling electrical percolation in multicomponent carbon nanotube dispersions. *Nature Nanotechnology*, 6(April):364–369, 2011. URL <http://www.nature.com/doi/10.1038/nnano.2011.40>.
- [235] Quinton L. Williams, Xi Liu, Jr. Wilbur Walters, Jian-Ge Zhou, Tylvia Y. Edwards, Franchesca L. Smith, Gregory E. Williams, and Brenitra L. Mosley. Boron-doped carbon nanotube coating for transparent, conducting, flexible photonic devices. *Applied Physics Letters*, 91(14):143116, 2007. URL <http://link.aip.org/link/doi/10.1063/1.2795343>.
- [236] Satoru Suzuki, Chris Bower, Yoshio Watanabe, and Otto Zhou. Work functions and valence band states of pristine and Cs-intercalated single-walled carbon nanotube bundles. *Applied Physics Letters*, 76(26):4007–4009, 2000. URL <http://dx.doi.org/doi/10.1063/1.126849>.
- [237] Amit K Chakraborty, Karl S Coleman, and Vinod R Dhanak. The electronic fine structure of 4-nitrophenyl functionalized single-walled carbon nanotubes. *Nanotechnology*, 20(15):155704, 2009. URL <http://stacks.iop.org/0957-4484/20/i=15/a=155704>.
- [238] Jao van de Lagemaat, Teresa M. Barnes, Garry Rumbles, Sean E. Shaheen, Timothy J. Coutts, Chris Weeks, Igor Levitsky, Jorma Peltola, and Paul Glatkowski. Organic solar cells with carbon nanotubes replacing In₂O₃:Sn as the transparent electrode. *Applied Physics Letters*, 88(23):233503, 2006. URL <http://link.aip.org/link/doi/10.1063/1.2210081>.

- [239] M.M. Beerbom, B. Lagel, A.J. Cascio, B.V. Doran, and R. Schlaf. Direct comparison of photoemission spectroscopy and in situ Kelvin probe work function measurements on indium tin oxide films. *Journal of Electron Spectroscopy and Related Phenomena*, 152(1-2):12 – 17, 2006. URL <http://www.sciencedirect.com/science/article/pii/S0368204806000077>.
- [240] S. Gutmann, M. A. Wolak, M. Conrad, M. M. Beerbom, and R. Schlaf. Effect of ultraviolet and x-ray radiation on the work function of TiO₂ surfaces. *Journal of Applied Physics*, 107(10):103705, 2010. URL <http://link.aip.org/link/doi/10.1063/1.3410677>.
- [241] J. S. Kim, B. Lagel, E. Moons, N. Johansson, I. D. Baikie, W. R. Salaneck, R. H. Friend, and F. Cacialli. Kelvin probe and ultraviolet photoemission measurements of indium tin oxide work function: a comparison. *Synthetic Metals*, 111-112:311 – 314, 2000. URL <http://www.sciencedirect.com/science/article/pii/S0379677999003549>.
- [242] R. Schlaf, H. Murata, and Z. H. Kafafi. Work function measurements on indium tin oxide films. *Journal of Electron Spectroscopy and Related Phenomena*, 120(1-3):149 – 154, 2001. URL <http://www.sciencedirect.com/science/article/pii/S0368204801003103>.
- [243] M. G. Helander, M. T. Greiner, Z. B. Wang, W. M. Tang, and Z. H. Lu. Work function of fluorine doped tin oxide. *J. Vac. Sci. Technol. A*, 29(1):011019, 2011. URL <http://dx.doi.org/10.1116/1.3525641>.
- [244] Weijie Song and Michiko Yoshitake. A work function study of ultra-thin alumina formation on NiAl(110) surface. *Applied Surface Science*, 251(1-4):14 – 18, 2005. URL <http://www.sciencedirect.com/science/article/pii/S0169433205005349>.
- [245] Martin Strojnik, Ales Omerzu, Aleksej Majkic', Peter M. Mihailovic, Junos Lukan, Gregor Bavdek, Gvido Bratina, Dean Cvetko, Peter Topolovsek, and Dragan Mihailovic. Ionization energy and energy gap structure of mosi molecular wires: Kelvin probe, ultraviolet photoelectron spectroscopy, and cyclic voltammetry measurements. *Langmuir*, 27(8):4296–4299, 2011. URL <http://pubs.acs.org/doi/abs/10.1021/la1050767>.
- [246] Kiyoshi Sugiyama, Hisao Ishii, Yukio Ouchi, and Kazuhiko Seki. Dependence of indium-tin-oxide work function on surface cleaning method as studied by ultraviolet and x-ray photoemission spectroscopies. *Journal of Applied Physics*, 87(1):295–298, 2000. URL <http://link.aip.org/link/doi/10.1063/1.371859>.
- [247] Hiroki Ago, Thomas Kugler, Franco Cacialli, William R. Salaneck, Milo S. P. Shaffer, Alan H. Windle, and Richard H. Friend. Work functions and surface functional groups of multiwall carbon nanotubes. *The Journal of Physical Chemistry B*, 103(38):8116–8121, 1999. URL <http://pubs.acs.org/doi/abs/10.1021/jp991659y>.
- [248] M. Grujicic, G. Cao, A. M. Rao, T. M. Tritt, and S. Nayak. UV-light enhanced oxidation of carbon nanotubes. *Applied Surface Science*, 214(1-4):289 – 303, 2003. URL <http://www.sciencedirect.com/science/article/pii/S0169433203003611>.
- [249] Seong Jun Kang, Yoojin Song, Yeonjin Yi, Won Mook Choi, Seon-Mi Yoon, and Jae-Young Choi. Work-function engineering of carbon nanotube transparent conductive films. *Carbon*, 48(2):520 – 524, 2010. URL <http://www.sciencedirect.com/science/article/pii/S000862230900654X>.

- [250] Qingfeng Liu, Tsuyohiko Fujigaya, Hui-Ming Cheng, and Naotoshi Nakashima. Free-standing highly conductive transparent ultrathin single-walled carbon nanotube films. *Journal of the American Chemical Society*, 132(46):16581–16586, 2010. URL <http://pubs.acs.org/doi/abs/10.1021/ja1067367>.
- [251] Michael S. Arnold, Alexander A. Green, James F. Hulvat, Samuel I. Stupp, and Mark C. Hersam. Sorting carbon nanotubes by electronic structure using density differentiation. *Nature Nanotechnology*, 1(1):60–65, 2006. URL <http://dx.doi.org/10.1038/nnano.2006.52>.
- [252] Roderick K. Jackson, Andrea Munro, Kenneth Nebesny, Neal Armstrong, and Samuel Graham. Evaluation of transparent carbon nanotube networks of homogeneous electronic type. *ACS Nano*, 4(3):1377–1384, 2010. URL <http://pubs.acs.org/doi/abs/10.1021/nn9010076>.
- [253] M. Stadermann, S. J. Papadakis, M. R. Falvo, J. Novak, E. Snow, Q. Fu, J. Liu, Y. Fridman, J. J. Boland, R. Superfine, and S. Washburn. Nanoscale study of conduction through carbon nanotube networks. *Phys. Rev. B*, 69:201402, May 2004. URL <http://link.aps.org/doi/10.1103/PhysRevB.69.201402>.
- [254] Wei Wang, K. A. Shiral Fernando, Yi Lin, Mohammed J. Meziani, L. Monica Veca, Li Cao, Puyu Zhang, Martin M. Kimani, and Ya-Ping Sun. Metallic single-walled carbon nanotubes for conductive nanocomposites. *Journal of the American Chemical Society*, 130(4):1415–1419, 2008. URL <http://pubs.acs.org/doi/abs/10.1021/ja0768035>.
- [255] D.R. Lide. *CRC Handbook of chemistry and physics*. Taylor and Francis, 2009. ISBN 9781420090840.
- [256] Daeseob Shim, Seung-Ho Jung, Song Yi Han, Kwonwoo Shin, Kun-Hong Lee, and Jong Hun Han. Improvement of SWCNT transparent conductive films via transition metal doping. *Chem. Commun.*, 47:5202–5204, 2011. URL <http://dx.doi.org/10.1039/C1CC10190K>.
- [257] Ross A. Hatton, N.P. Blanchard, Li Wei Tan, Gianluca Latini, Franco Cacialli, and S. Ravi P. Silva. Oxidised carbon nanotubes as solution processable, high work function hole-extraction layers for organic solar cells. *Organic Electronics*, 10(3):388 – 395, 2009. URL <http://www.sciencedirect.com/science/article/pii/S1566119908002619>.
- [258] S. Schramm, S. Dantscher, C. Schramm, O. Autzen, C. Wesenberg, E. Hasselbrink, and W. Pfeiffer. Photoinduced interface charging in multiphoton photoemission from ultrathin ag films on si(100). *Applied Physics A: Materials Science & Processing*, 88:459–464, 2007. URL <http://dx.doi.org/10.1007/s00339-007-4048-z>.
- [259] M. P. Seah and W. A. Dench. Quantitative electron spectroscopy of surfaces: A standard data base for electron inelastic mean free paths in solids. *Surface and Interface Analysis*, 1(1):2–11, 1979. URL <http://dx.doi.org/10.1002/sia.740010103>.
- [260] P. J. Cumpson and M. P. Seah. Elastic scattering corrections in AES and XPS. II. Estimating attenuation lengths and conditions required for their valid use in overlayer/substrate experiments. *Surface and Interface Analysis*, 25(6):430–446, 1997. URL [http://dx.doi.org/10.1002/\(SICI\)1096-9918\(199706\)25:6<430::AID-SIA254>3.0.CO;2-7](http://dx.doi.org/10.1002/(SICI)1096-9918(199706)25:6<430::AID-SIA254>3.0.CO;2-7).

- [261] Laju Bu, Xiaoyang Guo, Bo Yu, Yao Qu, Zhiyuan Xie, Donghang Yan, Yanhou Geng, and Fosong Wang. Monodisperse co-oligomer approach toward nanostructured films with alternating donor-acceptor lamellae. *Journal of the American Chemical Society*, 131(37):13242–13243, 2009. URL <http://pubs.acs.org/doi/abs/10.1021/ja905980w>.
- [262] Laju Bu, Xiaoyang Guo, Bo Yu, Yingying Fu, Yao Qu, Zhiyuan Xie, Donghang Yan, Yanhou Geng, and Fosong Wang. Donor-acceptor liquid crystalline conjugated cooligomers for the preparation of films with the ideal morphology for bulk heterojunction solar cells. *Polymer*, 52(19):4253 – 4260, 2011. URL <http://www.sciencedirect.com/science/article/pii/S0032386111006045>.
- [263] Adam Sweetman. *Forces at the nanoscale: interactions in atomic force microscopy and dielectrophoresis*. PhD thesis, University of Nottingham, 2009.